Spectroscopic Studies of Ligand Migration in Myoglobin

Dissertation zur Erlangung des Doktorgrades Dr. rer. nat.
der Fakultät für Naturwissenschaften
der Universität Ulm

vorgelegt von Karin Nienhaus
Rhede
2002

Amtierender Dekan: Prof. Dr. Wolfgang Witschel

Erstgutachter: Prof. Dr. Peter Bäuerle

Zweitgutachter: Prof. Dr. Hartmut Seliger

Tag der Promotion: 13.02.2003

Contents:

1. Introduction 1

1.1 Protein Structure, Function, Dynamics 1

1.2 Myoglobin, the Hydrogen Atom of Biology 3

Brief Historical Overview 3

1.2.1 Structure and Function 3

1.2.2 Ligand Binding and Protein Dynamics 5

1.2.3 Infrared Spectroscopy 13

1.2.4 Outline of this work 17

2. Materials and Methods 19

2.1 Protein Expression and Purification 19

2.1.1 Transformation and Multiplication 19

2.1.2 Lysis and Purification 19

2.2 Mutagenesis 20

2.3 Sample Preparation 22

2.4 Absorption Spectroscopy 23

2.4.1 Introduction 23

2.4.2 UV/Visible Spectroscopy 25

2.4.2.1 Survey Spectra in the Visible 25

2.4.2.1 Flash Photolysis 25

2.5 Cryospectroscopy in the Infrared 25

2.6 Fourier Transform Infrared (FTIR) Techniques 26

2.6.1 FTIR Absorbance Difference Spectra 27

2.6.2 Isothermal Kinetic Measurements 29

2.6.3 Temperature Derivative Spectroscopy (TDS) 29

2.6.3.1 Theoretical Background 33

2.6.3.2 Kinetic Hole Burning in the TDS Map 35

2.6.3.2.1 Temperature-dependent Transmission Spectra and TDS Maps 36

2.6.4 Illumination Protocols 39

3. Results and Interpretation 41

3.1 WT and Related Mutants 41

3.1.1 Probing Active Site and Initial Docking Site 41

3.1.1.1 FTIR Absorbance Spectra after Short Illumination 41

3.1.1.2 TDS Contour Maps after Short Illumination 46

3.1.1.3 Discussion: Bound State A and Initial Docking Site B 52

3.1.2 Probing Intermediates within the Xe non cavities 55
3.1.2.1 FTIR Absorbance Spectra after Slow Cooling from 160 to 3 55
3.1.2.2 TDS after Slow Cooling from 160 to 3 K 59
3.1.2.3 Interpretation and Discussion:
TDS after Slow Cooling from 160 to 3 K 64

3.1.3 Probing Intermediates above the Dynamic Transition Temperature 72
3.1.3.1 FTIR Absorbance Spectra at 160 K 72
3.1.3.2 TDS after Illumination at 185 K and
Slow Cooling from 185 to 160 K 74
3.1.3.3 Interpretation and Discussion: Intermediate States above
the Dynamic Transition Temperature 76

3.2 Mutant L29W and Related Double Mutants 78

3.2.1 Probing Taxonomic Substates A_I and A_{II} 79
3.2.1.1 FTIR Absorbance Difference Spectra at 3 K 79
3.2.1.2 Interpretation and Discussion: Interconversion between
Taxonomic Substates A_I and A_{II} 83

3.2.2 Probing the Initial Docking Site B 86
3.2.2.1 FTIR Absorbance Difference Spectra after Short Illumination
for 1 s at 3 K 86
3.2.2.2 TDS after Short Illumination at 3 K 88
3.2.2.3 Interpretation and Discussion:
Probing the Initial Docking Site B 91

3.2.3 Remote Intermediates: Site C' 93
3.2.3.1 Isothermal Illumination at 3 K 93
3.2.3.2 TDS Experiment after Isothermal Illumination at 3 K 94
3.2.3.3 Isothermal Illumination at 80 K 95
3.2.3.4 Interpretation and Discussion:
Structural Interpretation of Intermediate S ite C' 96

3.2.4 Detailed Investigations of Photoproduct State C' reveal an Additional
Photoproduct State C'' 101
3.2.4.1 Isothermal Illumination at 120 K 101
3.2.4.2 FTIR Absorbance Difference Spectra after Slow Cooling
from 160 to 3 K 102
3.2.4.3 TDS after Slow Cooling from 160 to 3 K 104
3.2.4.4 Isothermal Illumination at 160 K 108
3.2.4.5 TDS after Isothermal Illumination at 160 K 109
3.2.4.6 TDS after Slow Cooling from 160 to 100 K 110
3.2.4.7 Interpretation and Discussion: Structural Interpretation of
Intermediate Site C'' 111

3.2.5 Intermediate D, the Photoproduct in a Fluctuating Protein 114
3.2.5.1 TDS under Illumination 114
3.2.5.2 Isothermal Kinetics at 180 K 115
3.2.5.3 FTIR Absorbance Difference Spectra after Illumination
at 185 K and Slow Cooling under Light to 160 K 117
3.2.5.4 TDS after Illumination at 185 K and Slow Cooling to 160 K 119

3.2.5.5 Interpretation and Discussion: Photoproducts in a Fluctuating Protein 122

4. The Role of Internal Cavities in Physiological Ligand Binding 126

4.1 Migration and Recombination in WT MbCO 126

4.1.1 The Primary Docking Site B 126

4.1.2 Ligand Migration across a One-dimensional Energy Landscape 127

4.1.3 Physiological Ligand Binding in WT MbCO 133

4.2 Ligand Migration and Recombination in L29W MbCO 141

4.2.1 Ligand Dynamics in a Frozen Protein 141

4.2.2 Physiological Ligand Binding in L29W MbCO 144

4.3 Conclusion 147

Appendix A: Intrinsic Absorbance Changes of Photoproduct Bands i

Appendix B: CO Stretch Frequencies viii

Appendix C: List of Figures ix

Bibliography xiv

Summary xix

Zusammenfassung xxii

List of Publications xxvi

Acknowledgements xxviii

Curriculum Vitae xxix

1. Introduction

1.1 Protein Structure, Dynamics and Function

Proteins are the working machines of all living systems. Antibodies, for example, protect from disease. Enzymes function as biological catalysts. Hemoglobin (Hb) acts as an oxygen carrier in the blood of vertebrates. Molecules like collagen or elastin are important in maintaining the physical form of an organism.

The primary structure of all proteins is a sequence of amino acids connected by covalent peptide bonds. The secondary structure describes how the amino acid chain is organized into a regular structure stabilized by hydrogen bonds; for example the α-helix or the β-pleated sheet. The relative arrangement of secondary structure elements with respect to each other is called the tertiary structure. Hydrophobic and van der Waals interactions as well as hydrogen bonds and, less frequently, disulfide bridges stabilize this so-called native 3D structure. Sometimes the tertiary structure is associated with non-polypeptide groups like the heme in myoglobin (Mb). Such a unit is called a prosthetic group.

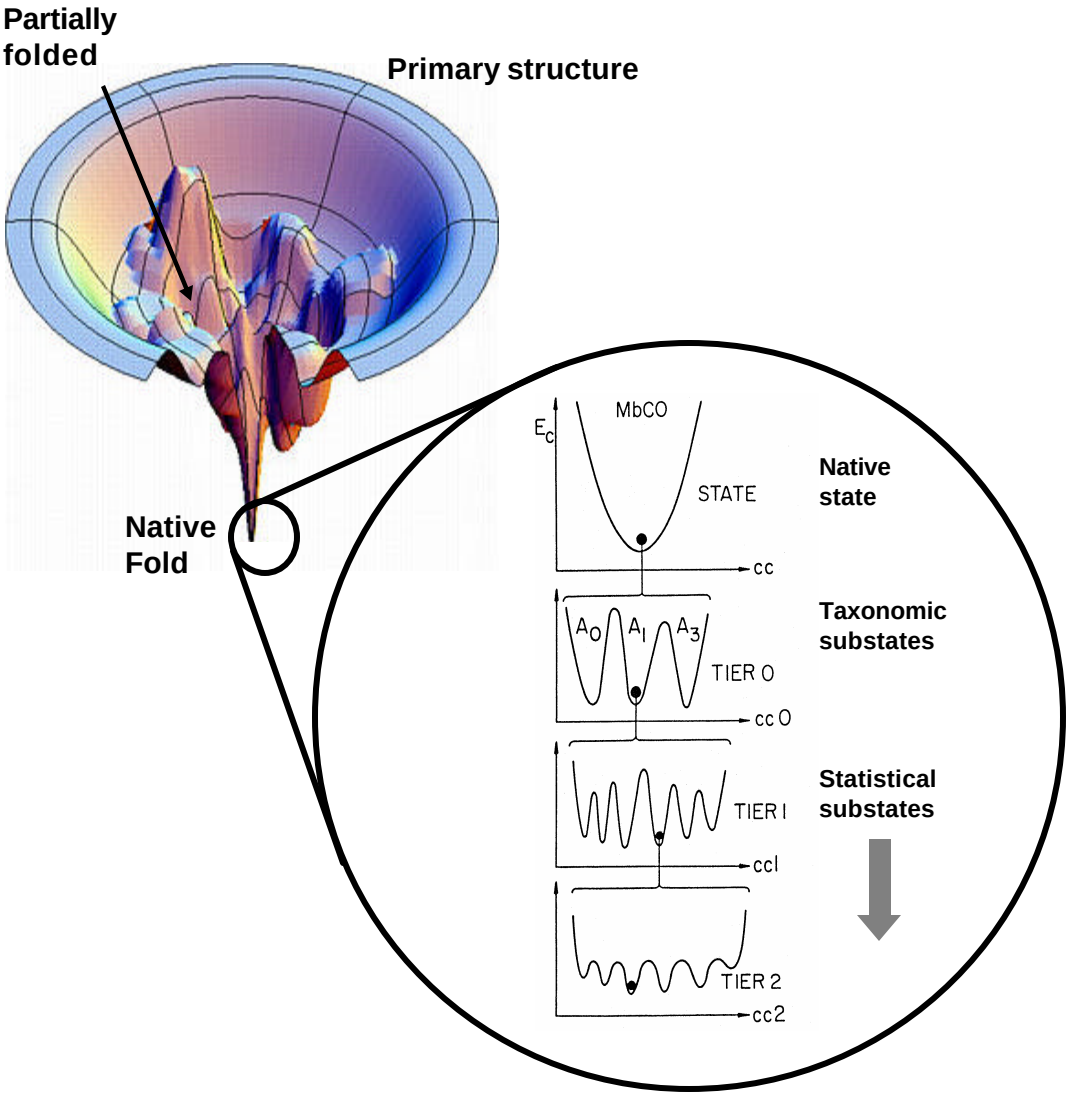

Fig. 1.1: Schematic representation of the rugged energy landscape guiding the protein toward the native fold; and hierarchy of conformational substates within the native fold.

Since the work of Anfinsen in the 1960s (1), it has been known that proteins normally fold into a state of minimal free energy which is completely determined by the primary sequence. Extensive efforts are under way to understand how proteins fold spontaneously into their native functional structure. The now generally accepted 'new view' recognizes the statistical aspects of the folding problem (2-6). It considers ensembles of conformations evolving toward the native state by biased diffusion over a rough energy landscape. The concept of an energy landscape is common to complex systems, e.g. glass-forming liquids, spin glasses or synthetic polymers. All these systems are characterized by distributed physical parameters, a non-linear response to perturbations and non-Arrhenius temperature dependence. Fig. 1.1 shows that the energy landscape has the shape of a funnel which guides the diffusion from many non-native states towards the native fold. The wide rim represents the many configurations that the unfolded chain can assume. Formation of native contacts lowers the enthalpy of the protein, and protein molecules start to slip down the funnel. This motion will continue as long as the decrease in enthalpy overcomes the unfavorable decrease in entropy that goes along with forming the more ordered folded state. The folding funnel will in general be rugged, as represented by the elevated areas within the funnel slopes. This can lead to folding traps, metastable intermediates along the folding pathway. Eventually, the protein will reach the state of minimal free energy in the tip of the funnel. Introduction of a folding funnel solves the so-called Levinthal paradox, which suggests that a protein randomly searching all of its configurational space will never be able to fold on physiological time scales (7).

The dense packing in the interior of the protein results in a competition of groups of atoms for the same space. Frustrated interactions occur. Thus, the final native fold is not unique, but contains a large number of slightly different conformations called conformational substates. These can be presented by local minima at the bottom of the folding funnel, separated by energy barriers with widely differing heights. Already in 1985, Frauenfelder and coworkers have suggested that conformational substates are arranged in a hierarchical fashion (8). A few individual substates in the highest tier 0 can be characterized spectroscopically and structurally; they are called taxonomic substates (Fig. 1.1). Every taxonomic substate consists of a large number of statistical substates of lower tiers separated by successively smaller energy barriers. Transitions between these local minima are essential for proteins to perform their specific functions.

Normal 3D structure determinations by x-ray crystallography reveal only average structures around the global free energy minimum. Functional processes, however, often involve transient species not evident from the diffraction data. In order to perform their individual tasks, proteins need to undergo specific conformational changes finely tuned to bring about their function. At physiological temperatures, these conformational rearrangements span a large range of time scales, from femtoseconds to seconds and even longer. This situation poses an immense challenge to the researcher. She has to identify and temporally resolve these functionally important motions. Intermediate species, however, are difficult to characterize with diffraction methods. By contrast, spectroscopic methods are very powerful tools, and dynamic processes can be studied with high sensitivity and time resolution provided that a suitable marker is available. Unfortunately, it is often difficult to interpret the observed spectral changes in terms of the underlying structural changes. To elucidate structural aspects, spectroscopy can be combined with genetic engineering. By introducing specific alterations in the primary sequence, particular intermediates can be enhanced, and free energies of transient species and barriers between them can be modified. Functional studies at cryogenic temperatures often allow one to separate different dynamic processes. Below ~180 K, each protein molecule is frozen in a particular substate. Reaction intermediates can often be trapped and thus become accessible to investigation. Above the dynamic transition temperature of ~180 K, the protein performs large-scale fluctuations. Sampling individual conformations allows the protein to perform its biological function. A

molecular movie presents itself in front of the observer's eyes, if she has the right camera equipment.

Due to the complexity of the interplay among structure, dynamics and function, a detailed investigation of the energy landscape is only feasible for a few well-selected model systems. Myoglobin, a small monomeric heme protein, has proven particularly suitable. Since all proteins are built according to the same design principles, their energy landscapes may show universal features. Myoglobin is simple enough that its substates and motions can be studied in great detail yet complex enough that the concepts found may be of general validity (9, 10).

1.2 Myoglobin, the Hydrogen Atom of Biology

1.2.1 Brief Historical Overview

Myoglobin (Mb), the hydrogen atom of Biology (11), has been in the center of protein structure-dynamics-function studies for more than 40 years. This small globin reversibly binds diatomic ligands like oxygen (MbO_2) or carbon monoxide (MbCO). Almost fifty years ago, its three-dimensional average structure was resolved in atomic detail and has been refined ever since (12). The diffraction data revealed an amino acid chain tightly wrapped around a heme group, leaving no direct pathway from the outside to the central heme-iron where the ligands bind. Therefore, it became evident early on that protein motions are essential for Mb to perform its function.

Initially, ligand binding was assumed to be a simple one-step process (13). This view had to be refined when flash photolysis experiments showed non-exponential recombination and multi-step kinetics (14). Over the years an intricate picture of ligand binding has emerged. In this model, the ligand has to overcome a sequence of energy barriers to migrate from the solvent to the active site. For a long time, the underlying structural determinants of these barriers remained a topic of controversial discussion, until researchers obtained direct structural evidence from x-ray studies of photoproduct intermediates, showing photolyzed CO within various hydrophobic internal cavities of Mb (15-18).

Using nanosecond time-resolved x-ray crystallography at room temperature, Moffat and coworkers (19-22) recently confirmed that these cavities play a role as transient ligand docking sites in the physiological binding process. The emerging picture implies that the highly conserved hydrophobic cavities have functional significance either as ligand storage sites and/or as modulators of ligand dynamics and internal protein reactions.

1.2.2 Structure and Function

J. C. Kendrew was the first to provide insights into the impressive architecture of an alpha helical globular protein. He solved the three-dimensional structure of Mb in atomic detail (12):

> *" The choice of material was not simple. One looked for a protein of low molecular weight, easily prepared in quantity, readily crystallized, and not already been studied. Myoglobin seemed to satisfy these criteria. … The search (for the right species) took us far and wide, through the world and through the animal kingdom, and eventually led us to the choice of the sperm whale."*
>
> *J. C. Kendrew, 1963 (23)*

Myoglobin is a small monomeric heme protein of 18 kDa. 153 amino acids form eight α-helices that are wrapped around a heme prosthetic group (24). The latter is covalently linked to the proximal histidine (H93) through its central Fe^{2+} ion (Fig. 1.2). Small ligands like O_2, CO or NO bind reversibly from an internal cavity, the distal heme pocket, to the iron. Ligand release can be triggered by light (25). Although Mb appears to be a very compact molecule, it has long been known to have four internal cavities spacious enough to accommodate a xenon atom, the so-called Xe cavities (26-28).

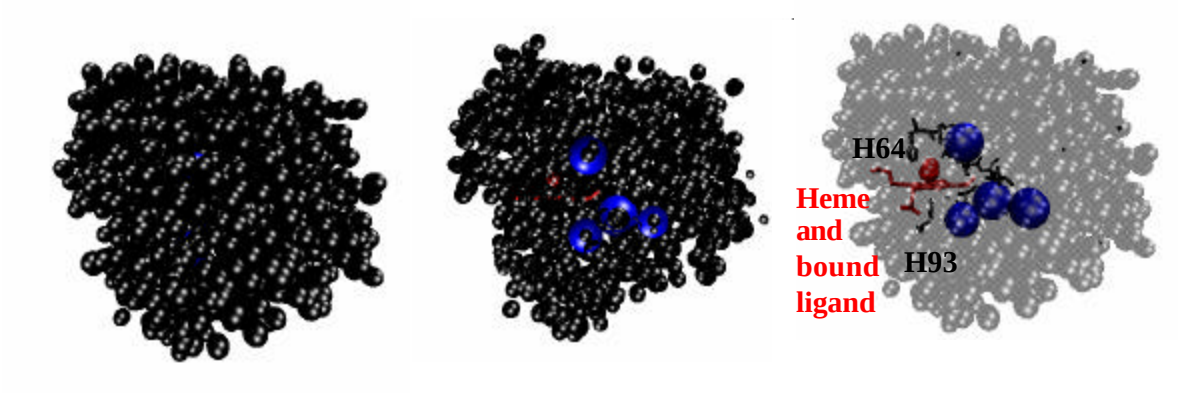

Fig. 1.2: Left: van der Waals representation of myoglobin; center: partial view into the core; right: active site of myoglobin; blue spheres: xenon cavities; red: heme group and bound ligand; black lines: residues H64 and H93.

The van der Waals representation in Fig. 1.2 (left) shows the densely packed protein globule. The heme group, depicted in red, is not visible from the outside. A partial view into the core (Fig. 1.2, center) reveals that there are no open channels to the inside. The xenon cavities (blue spheres) are visible, the position of the heme group can be guessed. On the right hand side, the protein moiety is displayed as a gray background, heme plane and bound CO are shown in red, blue spheres represent the Xe cavities. Two key residues in the vicinity of the active site, H64 and H93, are shown as black lines.

Textbooks state that myoglobin's function is oxygen storage and delivery in heart and skeletal muscle (24). It facilitates oxygen diffusion from the periphery of the cell to the mitochondria for respiration. Ferrous Mb is known to bind several other small molecules, among them CO and NO. Very recently, it was proposed that oxymyoglobin may also have a role of scavenging NO in the red muscle (29-31). NO is known to inhibit mitochondrial respiration (32), and the reaction of MbO_2 with NO may protect the energy-producing machinery and thus prevent muscle failure.

An isolated heme group has an intrinsically high affinity for CO; it prefers CO to O_2 by about a factor of ~10^4. The presence of the protein chain reduces this factor to about 200. The decreased ratio of affinities of myoglobin for CO versus O_2 is biologically important because CO is produced endogenously in the breakdown of heme. It normally blocks about 1% of the available sites in myoglobin. If the relative affinity of myoglobin for CO were similar to that of free heme, active myoglobin sites would be blocked quantitatively. The textbook explanation for Mb's decreased preference for CO versus O_2 is that the H64 sidechain forces CO, which for electronic reasons prefers to bind along the heme normal, to bind at an angle (24). Dioxygen, on the other hand, binds in a bent fashion, and thus the steric hindrance due to the H64 imidazole is absent. This explanation is wrong, as shown by ligand binding studies with mutant myoglobins that have H64 replaced by other residues (33). The correct explanation of the effect involves formation of an additional hydrogen bond to the bound ligand, which increases the binding free energy for O_2 (und thus decreases the O_2 dissociation rate). For electronic reasons, this hydrogen bond can only form with O_2 and not CO.

1.2.3 Ligand Binding and Protein Dynamics

The heme group gives rise to intense absorption bands in the visible that are sensitive to its local environment (34-36). These bands can be used to monitor oxidation state and ligation of the protein, as demonstrated in Fig. 1.3.

In his pioneering experiments, Gibson took advantage of the photosensitivity of the bond between heme iron and ligand. He monitored the ligand-rebinding kinetics of CO to Mb and Hb after photodissociation induced by a microsecond pulse of white light (25, 37). These were among the first applications of flash technology, an approach that paved the way for a dynamic view of structural biology that became prolific after the introduction of pulsed laser

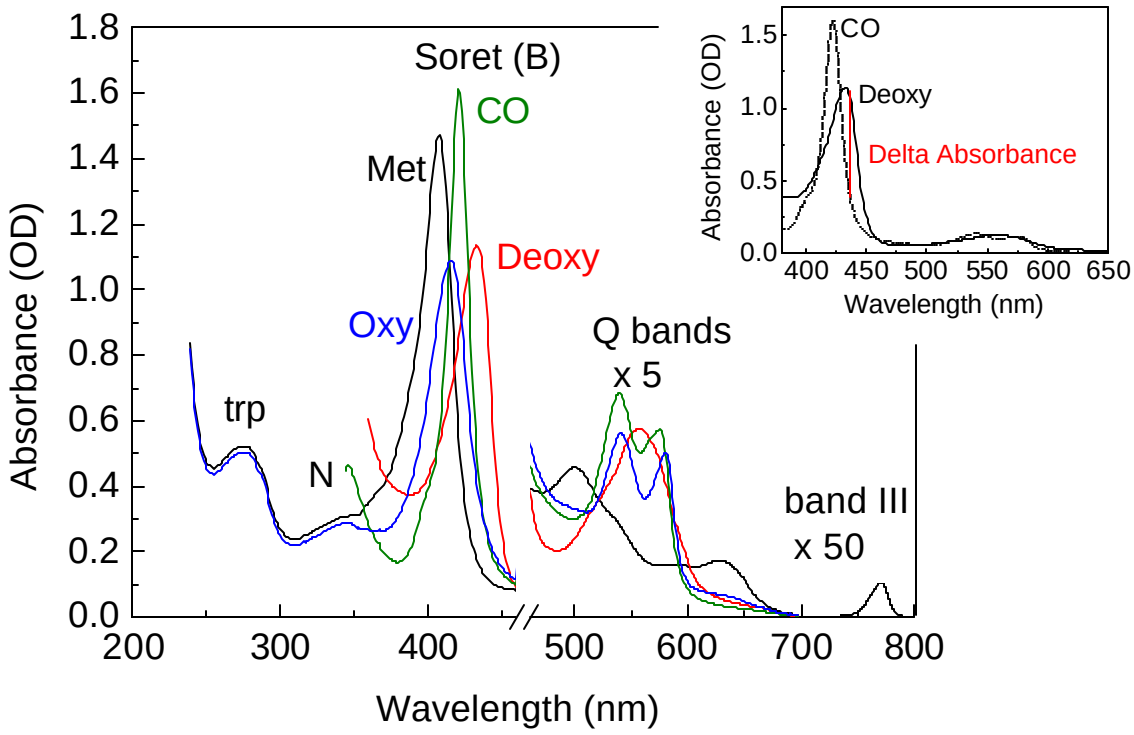

Fig. 1.3: Absorbance spectra of L29W mutant Mb in the UV-visible region of the spectrum. Soret, Q and N are $\pi \rightarrow \pi^*$ transitions, band III is a charge-transfer band, and the band indicated trp is due to absorption of aromatic residues like tryptophan; inset: absorbance change induced by illumination of L29W MbCO at 12 K; ligation states at the sixth position: Oxy: ligand O_2, CO: ligand CO, Deoxy: no ligand; Met: ligand H_2O/OH^- binding to Fe^{3+}).

technology.

Up to the early seventies, ligand binding was considered a simple one-step reaction. Antonini and Brunori described this particular case by a one-step scheme $Mb + CO \rightleftarrows MbCO$:

> *" The results on myoglobin (Mb) present no problem; indeed, they are just what would be expected for a simple one-site molecule that undergoes no conformational change on ligand binding, has no Bohr effect, and, of course, no cooperativity."*
>
> *Maurizio Brunori, 1972 (13)*

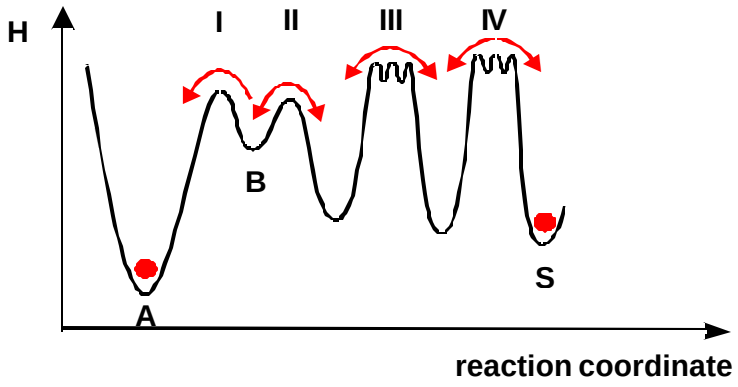

Fig. 1.4: Five-well-model to describe ligand recombination; consecutive barriers are labeled I through IV.

In 1975, flash photolysis experiments on MbCO and MbO_2 over a wide temperature range (40 - 350 K) by Frauenfelder and coworkers (14) revealed a surprising complexity of the recombination process. Multiple intermediate steps were resolved, as schematically depicted in Fig. 1.4. Below 180 K, rebinding from a photoproduct state called B to the bound state A was observed. This process was found to be non-exponential and independent of ligand concentration. To explain non-exponential rebinding, a static distribution of the innermost enthalpy barrier at the heme iron, $g(H_{BA})$, was invoked. The fraction of molecules still in the photodissociated state B at time t after the photolysis pulse was modeled by

$$N_B(t) = \int g(H_{BA}) \exp[-k_{BA}(T)t] dH_{BA}, \tag{1.1}$$

where the temperature dependence of the rate coefficient k_{BA} is governed by the Arrhenius law,

$$k_{BA}(T) = A_{BA} \frac{T}{T_0} \exp\left(-\frac{H_{BA}}{RT}\right) \tag{1.2}$$

Here, the pre-exponential A_{BA} was determined as ~10^9 s^{-1}, T_0 is a reference temperature set to 100 K and R is the universal gas constant. We note that the Arrhenius prefactor A_{BA} is exceptionally small. It has been shown by detailed quantum-chemical (DFT) calculations by Mc Mahon *et al.* (38) that the small pre-exponential arises from the fact that the CO, the heme iron, and the distal histidine have to move in concert to enable the CO to form the bond with the heme iron. To explain the distribution of enthalpy barriers, Frauenfelder and coworkers postulated that proteins do not possess a unique structure of minimal free energy, but exist in a huge number of conformational substates (CS) with markedly different rate coefficients.

At intermediate temperatures (180 - 280 K), at least two additional rebinding processes could be resolved that were also independent of ligand concentration. Therefore, they also have to be attributed to ligands that rebind from the interior of the protein after photodissociation, which is called geminate rebinding. Above 280 K, however, a simple exponential process remained which was found to be proportional to ligand concentration, hence it is attributed to bimolecular binding of ligands from the surrounding solvent. The authors suggested that four sequential barriers governed the rates of the four processes. The barriers were associated with specific ligand motions. Mounting the inner barriers was

identified as transitions of the ligand among different sites within the protein, while the hydration shell between solvent and protein entrance was assumed to form the outermost barrier. The structural assignment, however, was mere speculation at that time. The model reproduced the data well, although it was essentially static, with a temperature-independent reaction enthalpy surface.

In 1983, Henry *et al.* (39) performed flash photolysis experiments on MbCO in the Soret band with nanosecond time resolution at room temperature. Their kinetic curves were biphasic. The fast process was proposed to represent ligand recombination from within the protein, whereas the slow process was associated with bimolecular rebinding from the solvent. At room temperature, separate geminate processes were not observable, and the simpler three-well model in Fig. 1.5 was sufficient to model the data.

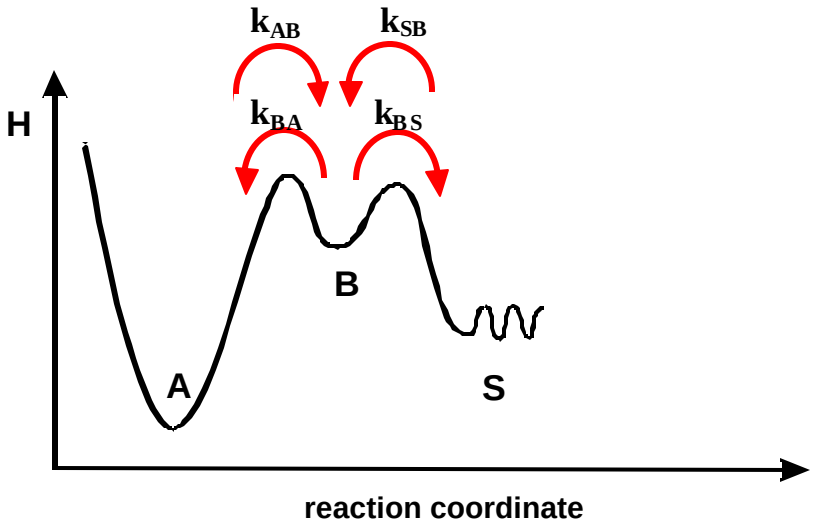

Fig. 1.5: Three-well model introduced by Eaton and coworkers (39) to describe the recombination kinetics of MbCO after flash photolysis at room temperature.

Besides the bound state A, there is the unbound state B, which is characterized by the ligand in the heme pocket. In state S, the ligand has escaped into the solvent. These states are interconnected by four microscopic rate coefficients k_{AB}, k_{BA}, k_{BS} and k_{SB} according to the sketch in Fig. 1.5. The total CO population within the sample is normalized to 1. Subsequent to photolysis, all ligands are found at site B. Thus, the initial condition of the sample directly after the flash is described by

$$N_A(0) = 0, \quad N_B(0) = 1, \quad N_S(0) = 0. \tag{1.3}$$

where N_i denotes the fraction of ligands in state i. Three differential equations describe the kinetics of the system,

$$\begin{aligned} \frac{dN_A}{dt} &= -k_{AB}N_A + k_{BA}N_B, \\ \frac{dN_B}{dt} &= -k_{BA}N_B - k_{BS}N_B + k_{AB}N_A + k_{SB}N_S, \\ \frac{dN_S}{dt} &= -k_{SB}N_S + k_{BS}N_B. \end{aligned} \tag{1.4}$$

Rate coefficient k_{AB} is much smaller than all the other rate coefficients. Thus, for simplicity, we set $k_{AB} \sim 0$. Furthermore, we assume that the internal and the bimolecular recombination process are sufficiently separated in time, which implies $k_{SB} << k_{BA}, k_{BS}$. The temporal development of the photodissociated population *N(t)* is determined by two macroscopic rate coefficients l_I and l_S,

$$\begin{aligned} N(t) &= 1 - N_A(t) = N_B(t) + N_S(t) \\ &= N_I \exp(l_I \cdot t) + N_S \exp(l_S \cdot t) \end{aligned} \tag{1.5}$$

with

$$\begin{aligned} N_I &= \frac{k_{BA}}{k_{BA} + k_{BS}} \\ N_S &= \frac{k_{BS}}{k_{BA} + k_{BS}} \\ l_I &= k_{BA} + k_{BS} = \frac{k_{BA}}{N_I} \\ l_S &= l_{on} = k_{SB} \cdot N_I = k_{SB} \frac{k_{BA}}{k_{BA} + k_{BS}} = k_{BA} \cdot \frac{k_{SB}}{k_{BS}} \cdot \frac{k_{BS}}{k_{BA} + k_{BS}} \\ &= k_{BA} \cdot P_B \cdot N_{out}. \end{aligned} \tag{1.6}$$

where N_I denotes the fraction of ligands that rebind internally (geminately) and N_S those that recombine from the solvent. Whereas l_I describes the depletion of state B, l_S refers to bimolecular rebinding from the solvent.

The pocket occupation factor P_B represents the equilibrium coefficient for binding CO at site B, if there were no recombination at the heme iron. N_{out} denotes the probability for ligands at site B to exit the protein. We can discuss two limiting cases for l_S:

(i) $N_S \sim 1$ implies that essentially all ligands escape into the solvent. Consequently, $k_{BA} << k_{BS}$ and thus

$$l_S = k_{BA} \cdot \frac{k_{SB}}{k_{BS}} = k_{BA} \cdot P_B . \tag{1.7}$$

Therefore, the inner barrier governs rebinding; the rate coefficient k_{BA} is scaled down by the pocket occupation factor.

(ii) $N_S << 1$ implies that most ligands recombine directly from site B. Hence $k_{BA} >> k_{BS}$ and

$$l_S = k_{SB}. \tag{1.8}$$

Here, the outer barrier governs the rebinding rate. At 300 K, case (i) holds for WT MbCO; case (ii) describes recombination between 200 and 250 K.

With reference to the structural differences known to exist between the bound and unbound states, Agmon and Hopfield (40) postulated in 1983 a dynamic model that involves a conformational relaxation towards the deoxy structure after photolysis, which leads to a time-dependent increase of the inner barrier at the heme iron. They proposed a two-dimensional energy surface spanned by a reaction coordinate (x-axis in Fig 1.6) and a conformational coordinate (y-axis). Whereas photodissociation propels the system along the reaction coordinate, an additional conformational relaxation along the conformational coordinate towards the deoxy structure was assumed to occur over time. Below the dynamic transition temperature, protein motions are arrested so that the conformational coordinate remains constant. Only when large-scale protein motions are activated, the relaxation occurs which leads to a concomitant barrier increase.

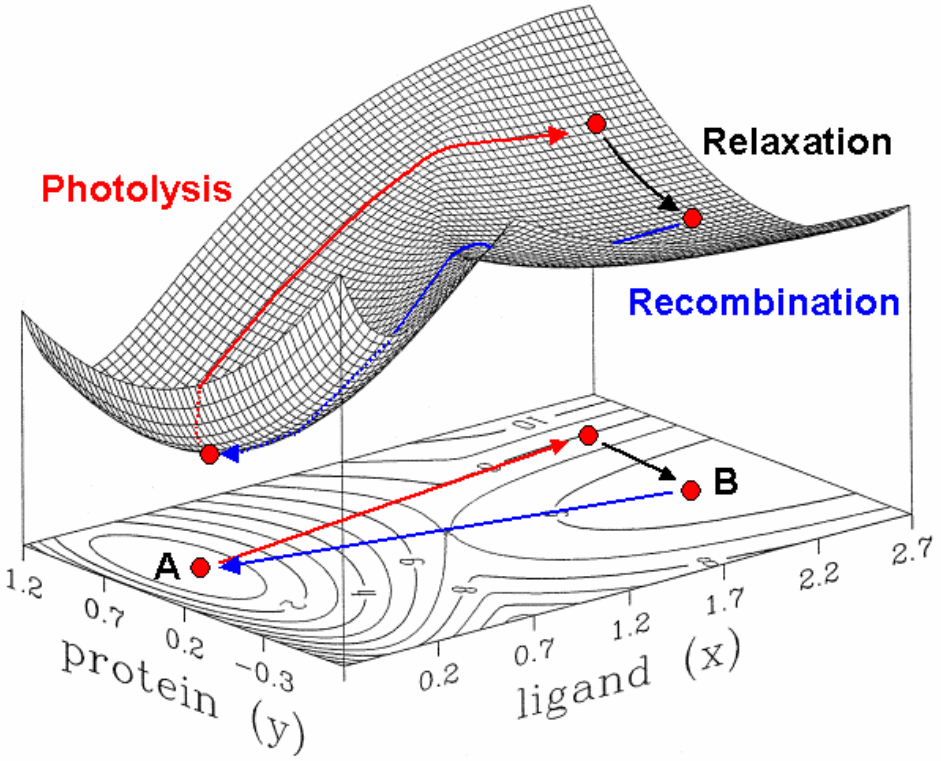

Fig. 1.6: Schematic representation of the two-dimensional reaction surface proposed by Agmon/Hopfield, the enthalpy H is included as third axis (adopted from (40)).

In the mid 1980s, Powers, Chance and coworkers (41, 42) found that extended illumination slows rebinding in MbCO at cryogenic temperatures. They called the effect 'pumping' and explained it with ligand motion to more slowly rebinding sites along the reaction pathway. While this interpretation turned out to be essentially correct, they stated erroneously that rebinding from each of these states was exponential. Subsequent flash-photolysis experiments on MbCO by Ansari *et al.* (43) confirmed that rebinding can be slowed by extended illumination, but they also showed that rebinding remained non-exponential. In 1991, Champion and coworkers presented further evidence from Raman and absorption measurements that extended exposure of MbCO to cw laser light alters the rebinding kinetics (44). These data were interpreted by a significantly increased population of a specific long-lived state C. Two possible assignments were made for the two geminate states

B and C. In the first model, state B corresponds to a contact pair where the ligand has experienced just a slight motion away from the bound-state position and state C to a separated geminate pair with the CO further away from the iron. In the alternative model, state B corresponds to a CO molecule in the heme pocket and state C to a CO molecule that became trapped in another cavity while migrating through the protein.

In 1991, Steinbach *et al.* (45) studied ligand binding by monitoring band III, a charge-transfer band at ~760 nm (Fig. 1.3), characteristic of 5-coordinated heme. The authors noticed that the internal process of recombination from B to A slowed at temperatures above 170 K. Furthermore, they observed that band III of photolyzed Mb*CO, where the ligand is still inside the pocket in state B, was red-shifted compared with band III for relaxed, non-ligated deoxyMb. Moreover, Steinbach *et al.* showed that band III is inhomogeneously broadened in a very peculiar way: A linear relation exists between the position of a homogeneous component of band III and the barrier height H_{BA}. Such couplings between spectral and functional parameters arise when they both originate from a common structural coordinate. This effect is frequently denoted as "kinetic hole burning" (KHB). From these studies, it was concluded that ligands face a higher barrier in relaxed deoxyMb than in the low-temperature photoproduct Mb*CO. Thus, they interpreted the slowing of the kinetics at temperatures above the dynamic transition temperature with a relaxation process from Mb*CO to deoxyMb along a conformational coordinate, thus following the model of Agmon and Hopfield (40).

To further elucidate the assumed Agmon-Hopfield relaxation, Nienhaus *et al.* (46) performed Fourier transform infrared (FTIR) spectroscopy on MbCO with monitoring band III under continuous illumination. They found that, below 200 K, the area of band III in the photoproduct increased with time even over several hours. This behavior was interpreted as change in the distribution of activation enthalpy barriers associated with a relaxation of the protein at the heme iron. These studies were subsequently extended to the stretch bands of CO ligands in the mid-infrared in 1994 (47) because the CO bands are sensitive to the local environment. Therefore, the authors hoped to be able to distinguish between the two models of slowed ligand rebinding, conformational relaxation of the protein according to Agmon and Hopfield and ligand migration to other sites. As they did not observe any significant change in the IR bands upon extended illumination, they again came to the conclusion that light-induced relaxation processes are the underlying cause for the shift of recombination barriers to higher values.

Starting in 1994, x-ray crystallography contributed new pieces to the ligand binding puzzle by revealing so-called photoproduct structures (48-51). Illumination of MbCO crystals at liquid-helium temperatures produced stable light-induced intermediates, characterized by photodissociated CO ligands trapped in the heme pocket. Diffraction data all depicted the ligands above pyrrol C parallel to the heme plane in the vicinity of the active site as proposed earlier by spectroscopic studies (52). The protein fold was found essentially unchanged. Anfinrud and coworkers named this position sketched in Fig. 1.7 the 'initial docking site B' (53, 54). Infrared spectroscopy gives a more complex picture and shows that the CO ligand can assume two opposite orientations in this site, denoted as B_1 and B_2 (55).

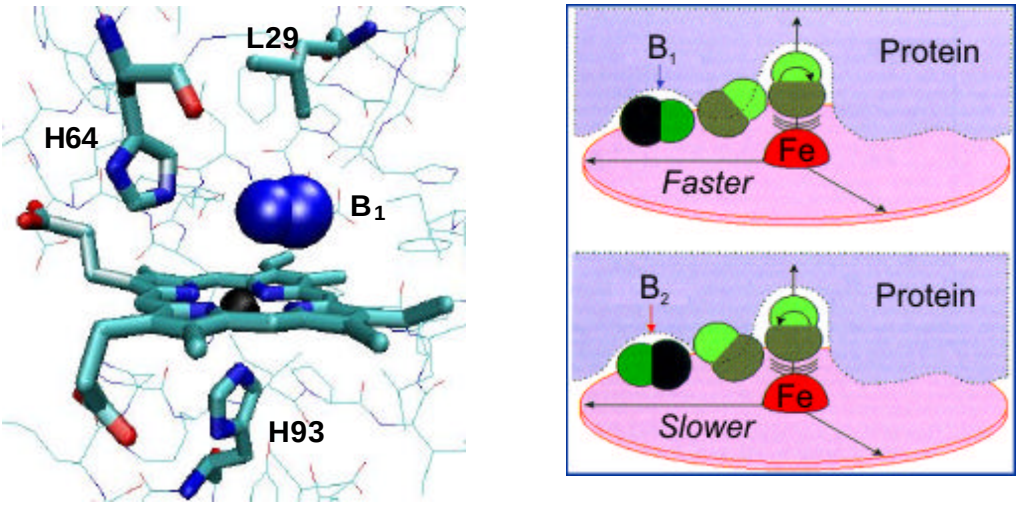

Fig. 1.7: Schematic representation of the initial docking site B (pdb code 1ABS) in WT; E_1 and B_2 represent opposite orientations of the CO ligand at the same location (adapted from Lim *et al.* ((54)

In 1997, Scott and Gibson (56) performed flash photolysis experiments on a large variety of myoglobin mutants at room temperature and followed the geminate rebinding of oxygen in the presence and absence of xenon. To explain the nature of the observed kinetic intermediates, they developed a model that contained the initial docking site B and the internal cavities (Xe cavities) as additional secondary docking places for the photolyzed ligands. More research was reported in 1998, when both short flash and extended illumination protocols were applied to MbCO crystals at cryogenic temperatures (57). The subsequent temperature-derivative spectroscopy (TDS) experiments revealed that extended illumination had produced discrete populations with higher barriers within the crystals. This result was anticipated from earlier investigations on solutions of myoglobin (46, 47), but it is not *a priori* self-evident because proteins in crystals might respond very differently due to packing forces. Also reported were slight band shifts that were interpreted in terms of CO migrating to alternative locations in the protein. The low-temperature pumping studies spawned the development of intricate illumination protocols to enhance specific, spectroscopically distinguishable intermediate populations to a large extent, large enough to perform x-ray crystallography. The development culminated in the x-ray structural characterization of new photoproducts showing that the ligands can indeed migrate away from their initial docking site into other internal cavities (15-17). The clearest results, however, were not obtained with the wild type protein (WT), but on mutants L29W[1], YQR (L29F/H64Q/T67R) and YQRF (with an additional I107F mutation). After these structure analyses it became clear that the light-induced slowing of the rebinding at low temperatures is essentially caused by ligand migration. Agmon-Hopfield type conformational relaxation may occur in addition, but is definitely not the dominant effect responsible for the altered rebinding behavior that was observed.

[1] The nomenclature L29W indicates that amino acid leucine (L) at position 29 in the primary structure of WT is replaced by tryptophan (W).

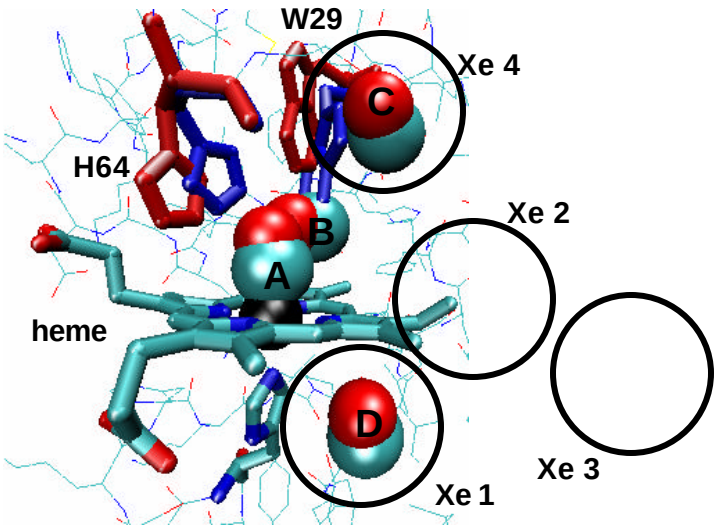

Fig. 1.8: Three-dimensional sketch of mutant L29W MbCO; the CO ligand is depicted at binding site A and intermediate docking sites B, C, D; residues H64 and W29 of taxonomic substates A_I and A_{II} are shown in red and blue; circles indicate the locations of the Xe cavities.

Fig. 1.8 shows the three-dimensional structure of mutant L29W MbCO around the active site. We have superimposed the CO ligands at the initial docking site B and inside xenon cavities 4 (site C) and 1 (site D). The Xe cavities are numbered from highest (site 1) to lowest (site 4) affinity for xenon (27, 28).

The migration of the photodissociated CO within the protein at cryogenic temperatures is likely to be related to the earliest states of ligand migration at room temperature. Thus, a detailed study of intermediate states and the transitions between them will yield valuable information about the energy landscape that governs the physiological ligand binding process in myoglobin.

> *" One major achievement in the study of any protein would be the establishment of convincing connections among structure, kinetics, energy landscape, dynamics, and function. We believe that this goal has not yet been reached in any protein, but the present knowledge of Mb gives some hope that the end is near in this case."*
>
> *Hans Frauenfelder (58)*

1.2.4 Infrared Spectroscopy

Structural and chemical interpretations of bonding in transition metal carbonyls have been based on the studies of the CO stretch frequency $n_{C\text{-}O}$ (59). These investigations suggested that measurements of the CO stretch bands would be of great value for the understanding of interactions between CO and the protein in heme proteins. Alben and Caughey performed pioneering room temperature IR measurements on substituted deutero pyridine hemes (60). The bond order found for the CO molecules could be rationalized in terms of differences in the electron density at the heme iron. Furthermore, the authors measured CO stretch bands in red blood cells and confirmed the sensitivity of the stretch frequency in hemoglobin on the environment. They introduced difference infrared spectroscopy as a method to selectively observe certain molecular vibrations in the presence of massive background absorption.

While crystallographic studies showed only one location for the heme-bound CO, the appearance of several stretch bands was explained by different ways in which the CO binds to myoglobin (61, 62). These conformers were expected to differ appreciably since the frequencies ranged from ~1930 to ~1965 cm^{-1}. In 1982, the effect of pH on the CO stretch bands was investigated by Shimada *et al.* (63). While the frequencies were found to remain identical, the intensities changed with pH. Therefore, the authors proposed that the conformers could interconvert, indicative of a flexible protein. The presence of independent conformers was also predicted to be important for the function.

In 1982, Alben *et al.* (55) collected IR spectra over a large temperature range, from 5 to 350 K. They cooled an MbCO sample down to 5 K and collected a transmission spectrum I_{dark}. Subsequently, the sample was illuminated to photodissociate the bound ligands before a second transmission spectrum I_{light} was measured. The absorbance spectra were computed as $\log(I_{light}/I_{dark})$. At 5 K, the CO ligands cannot leave the heme pocket and rebind geminately. Thus, two states are involved in low-temperature recombination: state A, in which CO is bound, and state B, in which the CO is photodissociated from the heme and remains in the heme pocket. Both states were found to contribute to the absorbance spectrum (Fig. 1.9 a). Several strong bands between 1900 and 2000 cm^{-1} arise from different structural environments that affect the bond order of the heme-bound ligand. These A substate bands represent the 'taxonomic' conformational substates in tier 0 of the substate hierarchy (64). They are connected with much weaker bands between 2100 and 2200 cm^{-1} representative of different photoproduct states B (65).

The bands of heme-bound CO in WT myoglobin are denoted A_0 ($\nu_{C\text{-}O}$ = 1969 cm^{-1}), A_1 ($\nu_{C\text{-}O}$ = 1945 cm^{-1}), and A_2 ($\nu_{C\text{-}O}$ = 1927 cm^{-1}); B_0 at 2149 cm^{-1}, B_1 at 2131 cm^{-1} and B_2 at 2119 cm^{-1} are the peaks for the photolyzed CO (55). The absorbance bands were found to be heterogeneously broadened, indicative of a large number of slightly different statistical substates within every taxonomic (66). Below 180 K, conformational interconversions between taxonomic substates cannot be observed because protein motions are frozen in. By contrast, transitions from B_2 to B_1 do occur even at ~13 K (55). Initial photolysis was proposed to lead to a statistical distribution between photoproduct states B_1 and B_2. Only above ~13 K the populations can adjust towards equilibrium. Lim *et al.* proposed to assign B_1 and B_2 to opposite orientations of the CO ligand at the docking site B (53, 54). Therefore, this exchange process at 13 K is interpreted as reorientation of CO in a frozen protein.

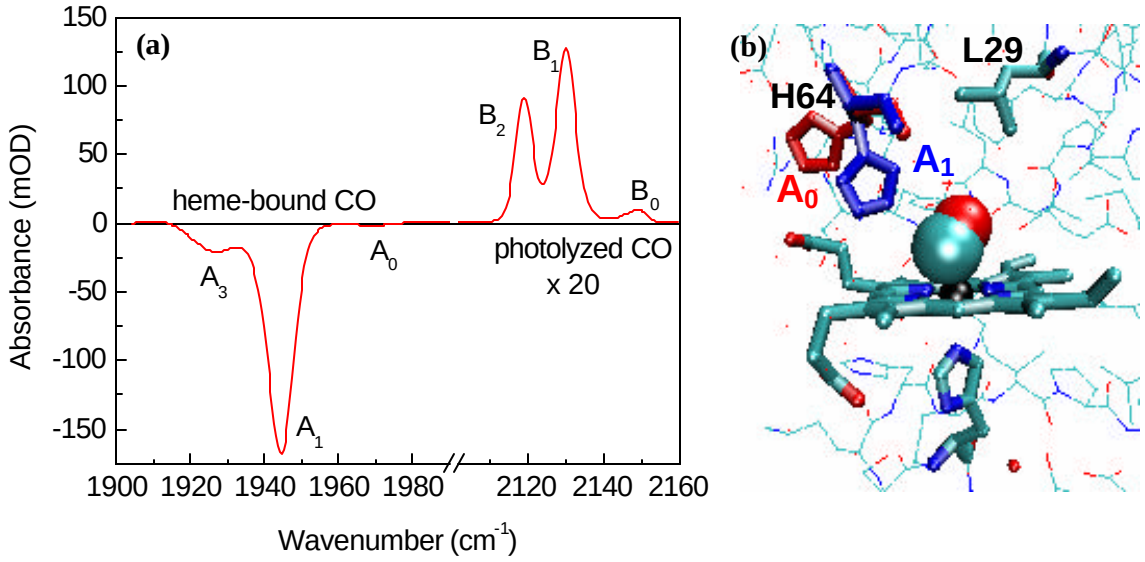

Fig. 1.9: (a) FTIR photolysis difference spectrum of WT MbCO; (b) sketch of the three-dimensional structure of taxonomic substates A_1 and A_0 at the active site; residues 29 and 64 are marked.

Later on, four stretch bands A_0 to A_3 at ~1966, ~1946, ~1941 and ~1930 cm^{-1} were introduced for MbCO (43). Whereas A_2 was found to be relevant for hemoglobin (67), it was later dropped from the list of taxonomic substates in MbCO for lack of evidence. Over the years, the remaining three taxonomic substates A_1, A_3 and A_0 have been investigated extensively. The CO binding kinetics after photodissociation at cryogenic temperatures are markedly different when monitored in the A state bands (68). The relative populations of the A states depend on environmental variables like pH (69), pressure (70), temperature (68) or solvent (this work). Two examples are given in Fig. 1.10. Above the solvent glass transition temperature of ~180 K, large-scale protein motions are activated and allow dynamic substate interconversion (68). Recently, it was shown that the same set of taxonomic substates exists also in MbO_2 (71).

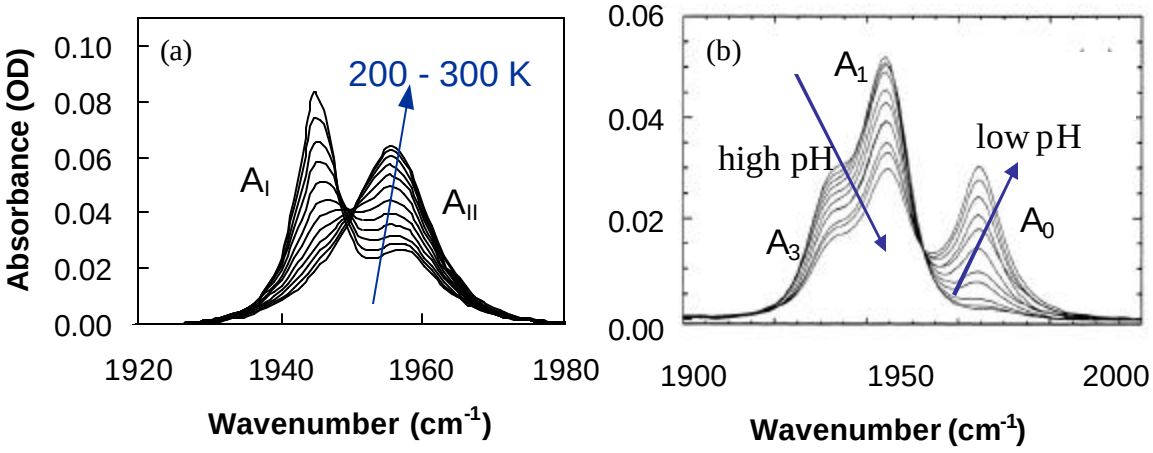

Fig. 1.10: (a) Temperature dependence of FTIR spectra of mutant L29W MbCO; (b) pH dependence of FTIR spectra of WT MbCO.

Studies of the pH dependence of the A state bands have given clues about the structural determinants that give rise to the individual A states. Müller *et al.* (69) observed that A_1 and A_3 predominate at high pH. With decreasing pH, the population of A_0 grows at the expense of A_1 and A_3. The pH dependence implies that protonation processes are responsible for the spectral change. These IR bands have been associated with specific three-dimensional structures (Fig. 1.9 b). The A states differ mainly in the position of the distal histidine H64 (72). At low pH, the imidazole sidechain is protonated and swings towards the solvent to better solvate the charge. The resulting 'open' conformation is associated with A_0, whereas the 'closed' conformation is related to A_1 and A_3. In 1999, Vojtechovsky *et al.* determined the x-ray structure of MbCO to a resolution better than 1.2 A (73). They refined their structure with multiple occupancies of H64 and obtained – besides 20% occupancy for A_0 – two positions of the imidazole sidechain inside the pocket, occupied to 60 and 20%. They suggested assigning these two conformations to A_1 and A_3, with the distal histidine positioned slightly deeper in the distal pocket in A_3.

Among all amino acids, the distal histidine H64 plays a special role, not only in defining taxonomic substates. Perutz and Matthews (74) proposed already more than thirty years ago that the pathway for ligand entry and exit involves rotation of the H64 imidazole sidechain, which opens a short and direct channel between heme pocket and solvent. Since then, experimental evidence has emerged in favor of this histidine gate mechanism, for instance the significant increase in O_2 association rates at low pH (72, 75) or the large increase in the rate of ligand binding when H64 is mutated to smaller apolar residues (76-78). However, we need to mention that the impact of the distal histidine on the binding process is twofold. Its 'absence' from the distal heme pocket not only opens the gate and thus allows easier access into the pocket, but is also lowers the barrier at the active site and thus enhances recombination. Moreover, several groups have argued that the histidine gate may not be the primary pathway into and out of the protein (27, 79, 80). Instead, ligands may escape through the interior of the protein by multiple transiently formed hydrophobic channels.

In recent years, site-directed mutagenesis has become an important tool in protein structure-function studies because it enables the researcher to modify the structure with surgical precision. For example, the interesting relation between the Fe-C and C-O stretch bands in different myoglobin mutants and their structural determinants became the target of extensive studies (81-86). Fig. 1.11 explains the inverse correlation between $n_{FE\text{-}C}$ and $n_{C\text{-}O}$ for the heme-bound ligand based on the valence bond formalism of Caughey and Alben (60). The bond between the heme iron and the ligand is formed by two major contributions: σ-donation from a weakly antibonding 5σ MO of CO to the iron 4s and $3d_{z^2}$ orbitals and π-backbonding from the iron $3d_{\pi}$ orbitals to the strongly antibonding CO $2\pi^*$ orbital. Changes in backbonding result from electron-donating or electron-withdrawing influences of polar molecules in the vicinity of the bound CO (84). The appearance of a positive charge in the CO vicinity attracts electron density to the CO and causes a decrease in σ-donation and an increase in backbonding. The bond order C-O is decreased, the frequency shifts to lower values. A negative charge has the opposite effect and moves the frequency to higher values. Even protonation of H97 on the proximal side of the heme plane was found to slightly shift the frequencies (69). The truly double bonded CO displays a frequency of 1600 cm^{-1}, the triple bonded CO absorbs at 2200 cm^{-1}. Free CO shows a stretch band at ~2143 cm^{-1} (87, 88).

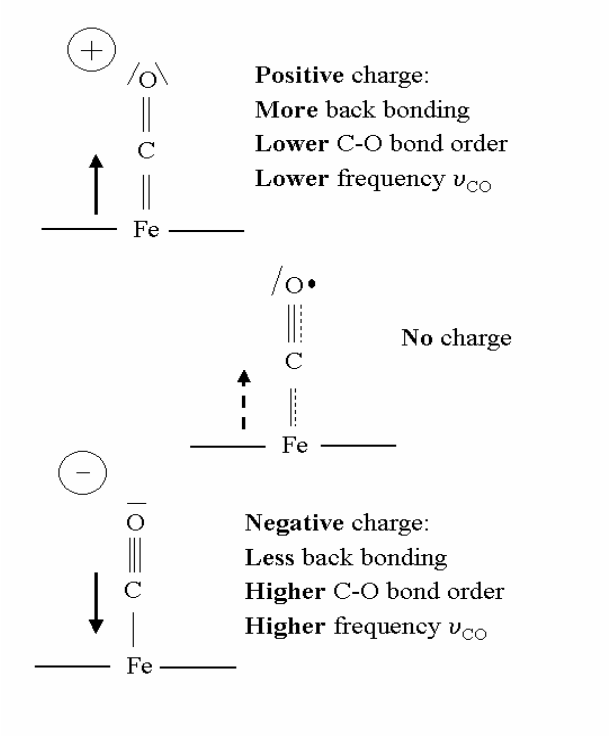

Fig. 1.11: Sketch of the back-bonding mechanism based on the valence bond formalism of Alben and Caughey (60).

As of yet, much less emphasis has been put on the study of the stretch bands of photolyzed CO. These peaks between 2100 and 2200 cm^{-1} are more than 20 times weaker than the A bands. With steady-state FTIR spectrometers, they can be easily studied at cryogenic temperatures (3 to ~200 K) under photodissociating conditions. They show surprisingly narrow line shapes, indicative of a constrained orientation at the intermediate site. With femto-second IR spectroscopy of MbCO, Anfinrud and co-workers have observed these bands also at room temperature (89). In analogy to the A state bands, the individual stretch frequencies are affected by the local environment, mainly through Stark effects of the local electric field acting on the CO dipole. Above the glass transition temperature of the cryo-solvent, protein fluctuations are activated that diminish the steric constraints on the photolyzed ligands in the protein interior and even enable them to escape from the protein matrix. As a consequence, the observed IR photoproduct bands get wider and lose intensity.

First IR studies of photolyzed MbCO crystals of mutant L29W revealed three kinetic states associated with well-defined photoproduct spectra (15, 90). X-ray diffraction experiments performed in parallel recovered photodissociated CO ligands within sites Xe 4 and Xe 1. Thus, this study provided a first coherent correlation between results obtained by crystallography and infrared spectroscopy. While comparable IR investigations on WT MbCO crystals have shown a number of discrete photoproduct states (57), x-ray studies have only in part succeeded to associate these states with photolyzed ligands at their secondary sites (16).

Initially, mutant L29W was chosen for ligand binding studies because of an extremely low ligand association rate. In the spectral range of heme-bound CO, the ligated protein displays two CO stretch bands, denoted A_I (1945 cm^{-1}) and A_{II} (1955 cm^{-1}) associated with two taxonomic substates (Fig. 1.12). The new nomenclature was introduced to emphasize that these substates are not related to the substates A_1, A_3 and A_0 of the native protein. The spectrum of the photodissociated ligands after 1-s illumination at 3 K displays one major band

B_2 at 2122 cm^{-1} and a minority species B_1 at 2131 cm^{-1}. Here we have retained the WT nomenclature. At low temperature, A_I is the dominant conformation, whereas at temperatures above 180 K, the population in A_{II} grows at the expense of A_I. At room temperature, essentially the total population resides in A_{II}. Contrary to native sperm whale myoglobin, this shift in population is not due to protonation of the distal histidine. Only below pH 6, we observe in L29W MbCO the additional band assigned to A_0 in WT.

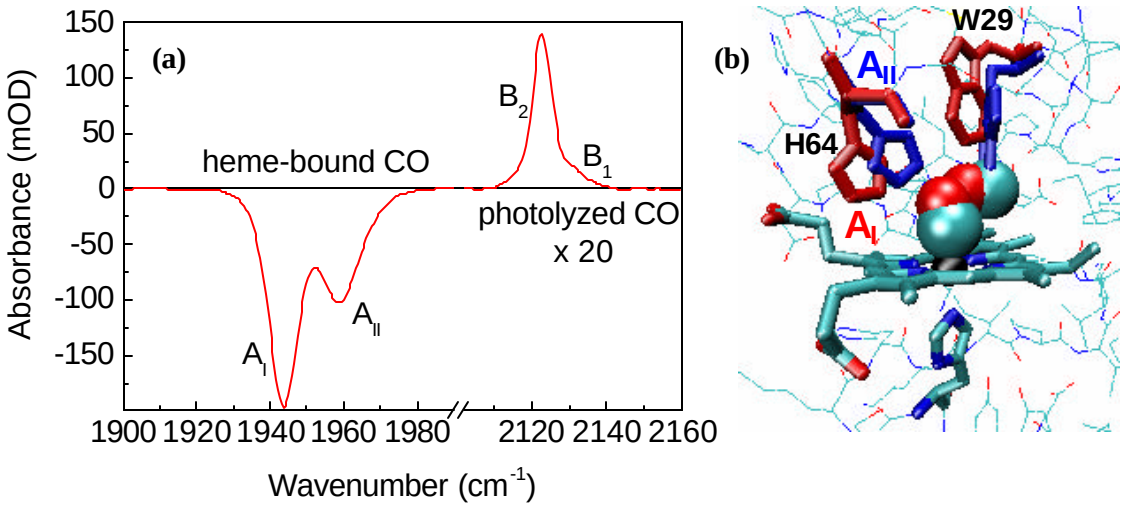

Fig. 1.12: (a) FTIR absorbance difference spectrum of L29W MbCO at 3 K after 1-s illumination; (b) three-dimensional structure of L29W around the active site.

1.2.5 Outline of this work

In this chapter, we have summarized the present knowledge about ligand binding to myoglobin. Identification and characterization of the intermediate states are important first steps toward understanding the dynamic aspects of the binding process, i. e. the temporal sequence of ligand transitions among the various sites as well as the accompanying protein fluctuations and relaxations.

Monitoring transitions among the various intermediate docking sites in real time has proven very difficult. Time-resolved diffraction experiments still lack time resolution and sensitivity. FTIR spectroscopy, however, is a remarkable tool to monitor not only the heme-bound ligands, but also the photodissociated CO molecules within the protein matrix. Even small subpopulations, down to ~2% of the total, can easily be resolved. Special illumination protocols in combination with temperature ramps allow us to trap photolyzed ligands in different intermediate sites in a frozen protein. Subsequently, kinetic protocols at constant temperature and TDS experiments can be applied to observe ligand recombination and migration as a function of time and temperature.

To influence the occupancy of intermediate sites and migration pathways in a specific fashion, we performed site-directed mutagenesis on WT and L29W. This strategy involves the implicit assumption (which we found to be valid in most of the cases) that single mutations do not disturb the general architecture of the Mb molecules. Consequently, if ligands occupy specific sites during migration, only mutations near those sites will have an influence. Furthermore, we equilibrated mutant MbCO samples with 1 atmosphere of xenon gas. If

intermediate CO docking sites are also xenon binding sites, the xenon and the photolyzed CO are expected to compete for them.

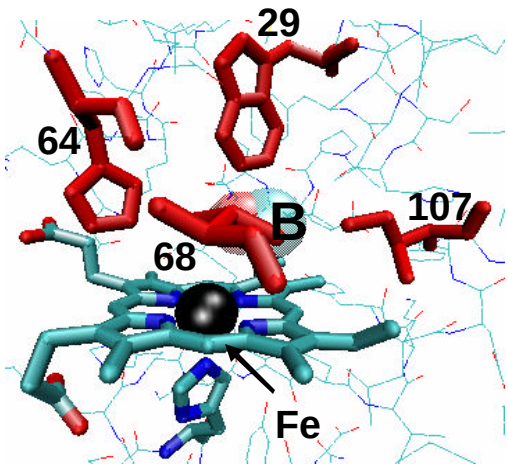

Fig. 1.13: Mutated residues in the close vicinity of the binding site A and the initial docking site B in L29W MbCO.

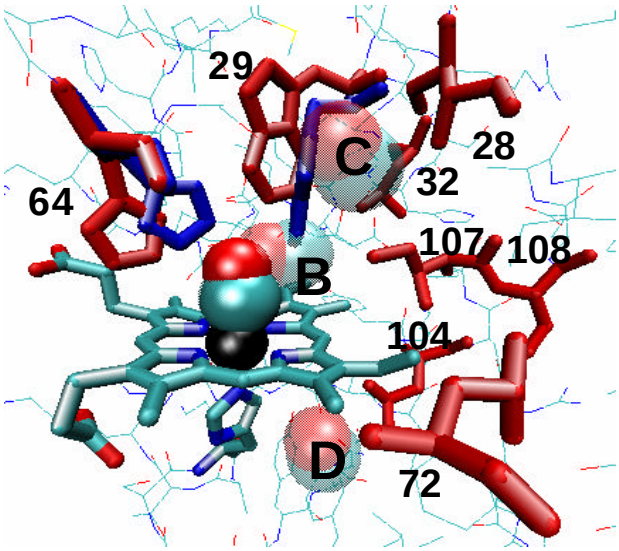

Fig. 1.14: Mutated residues lining the Xe cavities of L29W MbCO; CO ligand is sketched at docking sites B, C and D.

The choice of mutants was based in part on results of molecular dynamics simulations of Elber and Karplus (79). In these calculations, ligands collide many times with the walls of the heme pocket after photolysis before escaping. In the heme pocket, most collisions were observed to occur with residues L29, V68, and I107 and, outside of the heme pocket, with amino acids L104, L72, and S108. In Figs. 1.13 and 1.14, all amino acids that have been modified in this work are marked. Miniaturized sketches similar to Fig. 1.14 will accompany us throughout this thesis for easier residue recognition.

In the first part of Chapter 2, we will describe the biochemical techniques, protein expression, purification and site-directed mutagenesis. In the second part, we will give a detailed introduction into Fourier transform infrared (FTIR) and temperature-derivative (TDS) spectroscopy. We will also present a meticulous description of the data treatment.

The results will be presented in Chapter 3. It is divided into two main parts. As WT myoglobin is the target protein, Section 3.1 describes the results obtained on WT MbCO and related mutants. Section 3.2 summarizes the results on mutant L29W and related double mutants. Mutant L29W was found to give a high yield of specific photoproducts. Moreover, it exhibits large frequency shifts of the photoproduct CO bands, thus providing a sensitive marker of the local CO environments (15, 90). As the amount of data presented here is perplexing, discussion sections are interleaved with the description of the data.

In Chapter 4, the results obtained at cryogenic temperatures will be connected to the physiological ligand binding process. We will present a general scheme that explains ligand migration and recombination in myoglobin using simple, one-dimensional reaction energy landscapes. The thesis concludes with an appendix containing additional data on the temperature dependence of CO photoproduct bands, a list of figures, bibliography and summary.

2. Materials and Methods

2.1 Protein Expression and Purification

2.1.1 Transformation and Multiplication

The plasmids pUC19 carrying the sperm whale myoglobin genes of mutants I28F/W, L29W, V68S/F/W and H64L/V were kindly provided by Prof. John S. Olson (Rice University, Houston, Texas). All double mutants of L29W were constructed on the basis of this vector. The plasmid pUC19 hos ting the gene to express recombinant 'native' sperm whale myoglobin was a gift from Prof. Steve Sligar (University of Illinois, Urbana, Illinois). This myoglobin will be called 'native' or wild type (WT) throughout this work, although it differs in two positions from the actual sperm whale myoglobin extracted from sperm whale skeletal muscle: it contains an additional methionine at position 1 due to the recombinant production, and mutation D122N due to a typing error in the source of the sequence (36). Strain Tb 1 of *Escherichia coli* was employed as a host. This strain carries a streptomycin resistance and the following genotypes: F- ara ?(lac-proAB) stra thi φ80?lacZ ?m15 hsdR17($r_k^-m_k^+$).

Tb 1 cells were prepared by growing a 5 ml culture in LB medium (per liter: 10 g tryptone, 5 g yeast extract, 10 g NaCl) in the presence of 25 µg/ml streptomycin overnight at 37 °C while shaking at 220 rpm. 50 ml of LB were inoculated with 500 µl of overnight culture and shaken at 37°C for 3-4 h. The culture was centrifuged at 5000 rpm (Sigma rotor 19776) for 5 min at 4°C. The supernatant was discarded. The cell pellet was resuspended in 25 ml 0.1 M ice-cold sterile $CaCl_2$ and incubated for 45 min. The suspension was centrifuged again for 5 min. The cells were resuspended in 4 ml $CaCl_2$ and stored on ice for up to 24 h. This treatment of bacterial cells with $CaCl_2$ induces a transient state of 'competence' in the recipient bacteria, during which they are able to take up DNA from various sources.

2-5 µg of plasmid containing the myoglobin gene were added to 200 µl of competent Tb 1, incubated on ice for 30 min and subjected to a heat shock at 37°C for 2 min. Cells were put back on ice for 5 min, 1 ml of LB was added. The cell suspension was incubated for 1 h at 37°C. 200 µl of the suspension were streaked on LB agar plates containing 50 µg/ml ampicillin. Colonies appeared within 24 h at 37°C. 5 ml of LB were inoculated with one colony and shaken overnight at 37°C in the presence of ampicillin. 500 µl of overnight culture were transferred into 50 ml of LB and grown to mid log phase (3-4 h). Then 1.5 l of 2xYT (per liter: 16 g tryptone, 10 g yeast extract, 5 g NaCl) were inoculated with 15 ml of culture and grown overnight at 37°C. Since an additional tryptophan amino acid was introduced in most mutants, medium 2xYT was used for the final multiplication step. Cells were not able to express sufficiently in LB.

2.1.2 Lysis and Purification

The following purification procedure is based on the protocol developed by Springer and Sligar (91) and was modified to meet our needs. Cells were harvested by centrifugation at 4°C for 10 min at 6500 rpm (Heraeus rotor 14.290). The cell cake was resuspended in CO-saturated lysis buffer (50 mM Tris (pH 8.2), 1 mM EDTA, 100 mM NaCl; 3 ml per gram cells) and lysozyme was added (0.8 mg/g cells). The suspension was stirred for 30 min at 4°C. Then 4 mg of deoxycholic acid per gram cells were added and the lysis solution was stirred for another 15 min at 37°C. Finally, DNAse was added (40 U/ml) before stirring for 30 min at room temperature. Cell debris was removed by centrifugation at 20,000 rpm (Sorval rotor SS34) for 30 min at 4°C.

The clear, reddish-brown lysate was decanted into a clean beaker. Its pH was adjusted to 5.8 with solid NaH_2PO_4. The total volume was doubled by adding cold H_2O before loading the protein solution onto a CM Sephadex C50 cation exchange column (Amersham Biosciences, Freiburg) equilibrated with 10 mM sodium phosphate buffer, pH 6. The column was washed with at least 4 volumes of 10 mM sodium phosphate buffer, pH 6. Changing the buffer to 20 mM sodium phosphate buffer, pH 8 eluted the myoglobin. Mutant L29W/S108L was eluted from the CM Sephadex C50 column with 20 mM sodium phosphate buffer, pH 9.2. All mutations at position 32 caused the isoelectric point of the protein to change markedly. The CM Sephadex C50 column had to be replaced by a DEAE anion exchange column (Amersham Biosciences, Freiburg). The protein was loaded in 20 mM Tris/HCl buffer, pH 8, and eluted with the same buffer while a large fraction of protein impurities were retained.

Appropriate fractions were pooled and concentrated to 5 ml using an Amicon concentrating cell with a YM 10 membrane. The concentrated protein solution was loaded onto a sephacryl S 200 gel chromatography column (Amersham Biosciences, Freiburg) equilibrated with 150 mM sodium phosphate buffer pH 7.4 and eluted with the same buffer. The grade of purity was determined by taking the ratio R_z between the absorbance at the maximum of the Soret peak and the protein specific absorbance at 280 nm. Suitable fractions with an $R_z > 3$ were pooled and dialyzed extensively against water before freeze-drying. The lyophilized protein was stored at -20°C until further use.

2.2 Mutagenesis

All mutants and double mutants were produced using the Quikchange mutagenesis kit provided by Stratagene (Stratagene Europe, Amsterdam). Custom designed primers were ordered from MWG (MWG-Biotech GmbH, Ebersberg, Germany). In Table 2.1, the sequences of the oligonucleotides used to generate the mutants are listed.

Table 2.1: Primer sequences

Mutant	**Oligonucleotide Primer I**
(L29W) / L104W	5' – CCC GAT CAA ATA CTG GGA ATT CAT CTC TGA AGC G – 3'
(L29W) / I107W	5' – CCC GAT CAA ATA CCT GGA ATT CTG GTC TGA AGC G – 3'
L29W / L72F	5' – CCG TGT TAA CTG CCT TCG GTG CTA TCC –3'
L29W / S108L	5' – CCC GAT CAA ATA CCT GGA ATT CAT CCT TGA AGC G – 3'
L29W / L32T	5' – GGA CAT CTG GAT TCG AAC GTT CAA ATC TCA TCC –3'
L32H	5' – GGA CAT CTT GAT TCG ACA TTT CAA ATC TCA TCC –3'

The table contains primer I; primer II is the oligonucleotide complementary to primer I. Whenever L29W is put in parentheses, the same mutation has also been performed on WT myoglobin using the identical primer. Underlined are the base triplets that code for the new amino acid.

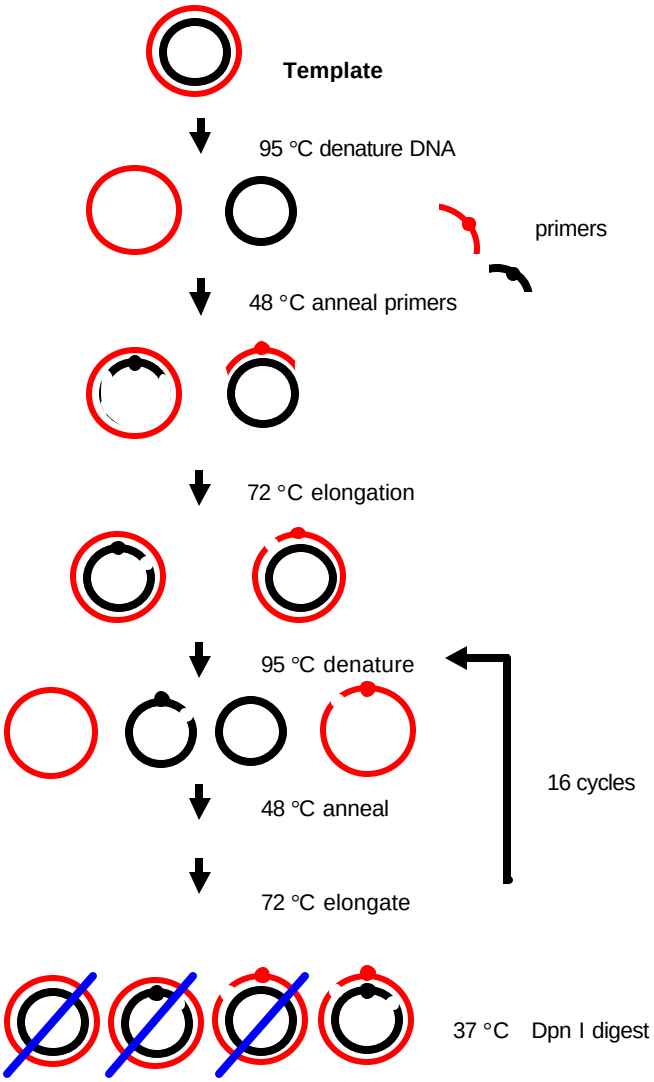

Fig. 2.1: Schematic presentation of the PCR (polymerase chain reaction) temperature protocol used for site-directed mutagenesis.

The polymerase chain reaction (PCR) is a method to produce large amounts of DNA in just a few hours. PCR is not only able to reproduce any given DNA but also a convenient tool for introducing point mutations into a protein gene to alter the code for a particular amino acid. The basic procedure utilizes a double-stranded DNA vector with the gene of interest as insert and two oligonucleotide primers containing the desired mutation. The oligonucleotide primers, each complementary to opposite strands of the vector, are extended during temperature cycling by *PfuTurbo* polymerase (Stratagene). Fig. 2.1 summarizes the PCR protocol.

The reaction itself was set up as a batch. The following reaction mixture was prepared in a small reaction vial (total volume 200 µl):

5 µl reaction buffer (10 x)
5 – 50 ng template DNA (plasmid pUC19 carrying the myoglobin gene)
125 ng primer I
125 ng primer II
1 µl dNTP-mix
sterile H_2O to a total volume of 50 µl

(10 x reaction buffer: 100 mM KCl, 100 mM $(NH_4)_2SO_4$, 200 mM Tris-HCl (pH 8.8), 20 mM $MgSO_4$, 1% Triton X-100, 1 mg/ml BSA).

The reaction mixture was placed into a thermocycler (Primus, MWG-Biotech GmbH, Ebersberg, Germany) and incubated at 95°C for 2 min to denature the template double stranded DNA plasmid to obtain two complementary single stranded templates (Fig. 2.1). 1 µl of *PfuTurbo* polymerase (2.5 U) was added to the hot vial. After another 45 s at the denaturing temperature of 95°C the temperature was decreased to 48°C for 60 s to allow primers I and II to anneal to their complementary single strand of template DNA. Subsequently, the temperature was raised to 72°C for 8 min to provide ideal conditions for the *PfuTurbo* polymerase to use the annealed primers as starting points to replicate the whole DNA strand. At this point the original DNA had doubled. Subsequently, heating the reaction mixture for 45 s to 95°C started the next temperature cycle. A total of 16 cycles were performed.

After cycling, the reaction mixture was cooled to 37°C. 1µl of restriction enzyme Dpn I (10 U) was added to digest the original template DNA. The Dpn I endonuclease (target sequence: 5'-G(CH_3-A)TC-3') is specific for methylated DNA and used to digest the parental DNA. DNA isolated from *E. coli* strain Tb 1 is methylated and therefore susceptible to Dpn I digestion.

2.3 Sample Preparation

To prepare a sample for a FTIR experiment, lyophilized myoglobin was dissolved in 75%/25% (vol./vol.) glycerol/buffer (1 M potassium phosphate, pH 8) to a final concentration of 20 mM. The solution was equilibrated with 1 atmosphere of CO for 1 hour. A twofold excess of sodium dithionite was added anaerobically before stirring for another 15 min under CO. To equilibrate MbCO samples with xenon gas (MbCO(Xe)), the solutions were stirred for an additional hour at 0°C under 1 atm of xenon. To remove any undissolved protein, the sample solution was centrifuged at 5,000 rpm (Eppendorf table top centrifuge) for 15 min prior to loading it into the sample cell. The final pH values of all samples are listed in Table 2.2.

The L29W trehalose sample was prepared by dissolving lyophilized myoglobin to a final concentration of 20 mM in 250 mM potassium phosphate buffer, pH 8. Solid trehalose was added until saturation. Afterwards, the sample was equilibrated with CO and sodium dithionite was added. A few microliters of this sample were dried under a CO atmosphere at 70°C overnight to obtain the sample that we will refer to as dried trehalose.

The UV/visible data were taken on dilute sample, prepared by dissolving lyophilized protein in 100 mM potassium phosphate buffer, pH 8, to a final concentration of 10 µM. The

solution was equilibrated with 1 atm of CO. A tenfold excess of sodium dithionite was added anaerobically. The pH of the buffer determined the final pH of the dilute sample.

Table 2.2: pH values of the IR-samples employed in this work.

Sample	pH	Sample	pH
L29W	7.8	I107W	7.2
L29W / L104W	7.5	L32H	7.1
L29W / I107W	7.5	H64V	9.2
L29W / S108L	7.4	H64L	9.1
L29W / L32T	7.2	V68F	9.3; 5.4
L29W / L72F	7.3	V68S	8.9
WT	7.0; 5.6	V68W	7.4
I28F	7.6	L104W	7.3
I28W	7.6	L29W (trehalose)	7.6

2.4. Absorption Spectroscopy

2.4.1 Introduction

In the classical approach, the interaction of matter and radiation is treated as induction of oscillating dipoles by the oscillating electric field of the light wave. In absorption spectroscopy, the loss of light from an incident beam is measured as a function of the frequency (or wavelength) of the radiation. To derive the law that governs absorption, the sample of thickness l is assumed to be homogeneous, rectangular and cut up in slices of thickness dl perpendicular to the beam (Fig. 2.2).

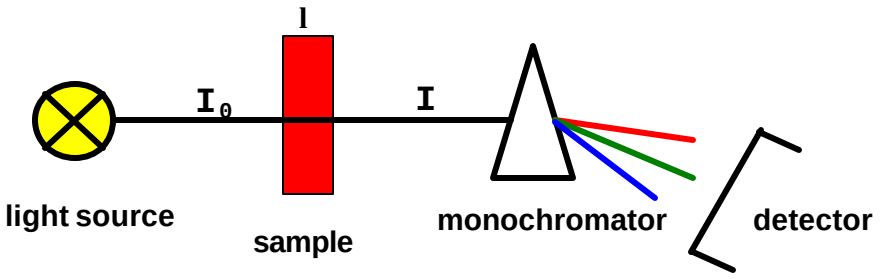

Fig. 2.2: Principle of absorption spectroscopy.

The loss of intensity dI by a slice dl is given by

$$-dI = e' \cdot I \cdot c \cdot dl \tag{2.1}$$

with incident light intensity I, path length dl, concentration c and extinction coefficient e'. Integration yields

$$\ln I - \ln I_0 = -e' \cdot c \cdot l \tag{2.2}$$

Conversion of the natural logarithm to base 10 gives Beer's law:

$$A(l) = \log\left(\frac{I_0}{I}\right) = e(l) \cdot c \cdot l \tag{2.3}$$

with $e = e'/2.303$.

The quantity A is called absorbance or optical density.

The range of wavelengths used in the spectroscopy of biological molecules is impressive. It spans more than ten orders of magnitude, from long radio waves with a typical wavelengths of ~1 m employed in NMR to very short γ-rays of 10^{-11} cm in Mössbauer spectroscopy. Visible light is confined to a narrow window from $3 - 6 \cdot 10^{-5}$ cm. Absorption of visible or ultraviolet light excites a molecule from its electronic ground state S_0 to the first excited singlet state S_1. In heme proteins, we observe electronic absorption bands of three internal chromophors. The peptide bond itself absorbs weakly around 220 nm. Aromatic amino acids like tyrosine, tryptophan or histidine contribute with bands between 230 – 300 nm. The heme prosthetic group has its strongest bands in the visible region of the spectrum.

By contrast, transitions between vibrational levels of the electronic ground state are of much lower energy than the electronic transitions. The absorption bands from these vibrational transitions generally occur between 4,000 and 200 cm^{-1}. These bands typically arise from vibrations that are localized at a specific part of a biomolecule.

In heme-proteins, the external ligand CO absorbs strongly in the infrared region of the spectrum. CO has a permanent dipole moment along its molecular axis. Stretch vibrations can be treated in the simplest way using a harmonic oscillator model (92). The potential energy V as a function of the interatomic distance R is given by

$$V(R) = \frac{1}{2} k \left(R - R_e\right)^2 \ , \tag{2.4}$$

with the equilibrium bond length R_e and force constant k of the bond. A quantum mechanical analysis yields equidistant energy levels given by

$$E_n = \left(n + \frac{1}{2}\right) \hbar w \quad , \tag{2.5}$$

with $n = w/2p$, and $n = 0, 1, 2, \ldots$ is the quantum number associated with the energy level E_n.

The gross selection rule demands that vibrations have to be accompanied by a changing dipole moment to be excited. The specific selection rule asks for $Dn = +/- 1$. According to the selection rules, the following transitions are allowed:

$$\Delta E = \hbar w = \hbar \sqrt{\frac{k}{m}} . \qquad (2.6)$$

Here μ represents the reduced mass of the vibrating system. For a diatomic molecule, with atomic masses m_1 and m_2,

$$m = \frac{m_1 m_2}{m_1 + m_2} . \qquad (2.7)$$

Eq. 2.7 implies that different isotopes will yield different reduced masses and consequently different IR stretch frequencies. In fact, isotopic substitution of $C^{12}O^{16}$ with $C^{13}O^{16}$ and $C^{13}O^{18}$ has been an important tool for band assignment. From measurements of the vibrational frequency, the bond strength can be calculated. The individual local environment of a CO ligand will influence the bond strength and thus shift the IR stretch frequency. Although vibrational spectroscopy cannot give direct structural information, it is an exceedingly sensitive gauge of the interactions between ligand and protein. Once these interactions are understood, precise structural information can be inferred.

2.4.2 UV/Visible Spectroscopy

2.4.2.1 Survey Spectra in the UV/Visible

Three milliliters of dilute sample were sealed in an airtight 1 x 1 x 3 cm^3 quartz cuvette. The absorbance in the wavelength range from 240 to 700 nm was monitored in a commercial UV/Visible spectrometer (Cary 1E, Varian).

2.4.2.2 Flash Photolysis

Experiments were carried out in a home-built flash photolysis apparatus, using a 6-ns (full width at half maximum) pulse from a frequency doubled Nd:YAG laser (model Surelite, Continuum, Santa Clara, CA) for photodissociation. Ligand binding was monitored with light from a tungsten source which was passed through a monochromator set at 436 nm. A photomultiplier tube (model R5600U, Hamamatsu Corp., Middlesex, NJ) measured the intensities. These data were recorded with a digital storage oscilloscope from 10 ns to 50 µs (model TDS 520, Tektronix, Wilsonville, OR) and a home-built logarithmic time-base digitizer (Wondertoy II) from 2 µs to 100 s.

2.5 Cryospectroscopy in the Infrared

A few microliters of the protein solution were kept between two CaF_2 windows (diameter 25.4 mm) separated by a 75 µm thick mylar washer. The windows were sandwiched inside a block of oxygen-free high-conductivity copper mounted on the cold-finger of a closed-cycle helium refrigerator (model SRDK-205AW, Sumitomo, Tokyo, Japan). The sample temperature - variable from 3 to 320 K - was measured with a silicon temperature sensor

diode and regulated by a digital temperature controller (model 330, Lake Shore Cryotronics, Westerville, OH). A continuous wave, frequency-doubled Nd-YAG laser (model Forte 530-300, Laser Quantum, Manchester, UK), emitting 300 mW output power at 532 nm, was used to photolyze the sample. The laser beam was split and focused with lenses on the sample from both sides. The standard photolysis rate k_L was determined as ~20 s^{-1} at low temperatures. A Fourier transform infrared (FTIR) spectrometer (IFS 66v/S, Bruker, Karlsruhe, Germany) was employed to collect transmission spectra in the mid-infrared between 1800 and 2400 cm^{-1} at a resolution of 2 cm^{-1}.

The 'heart' of this instrument, the Michelson interferometer, introduces several advantages over disperse instruments: (i) all frequencies are measured simultaneously, (ii) no slits and apertures are necessary, therefore larger throughput meaning a better signal to noise ratio and (iii) high wavenumber stability due to a He Ne reference laser (93, 94).

2.6 Fourier Transform Infrared (FTIR) Techniques

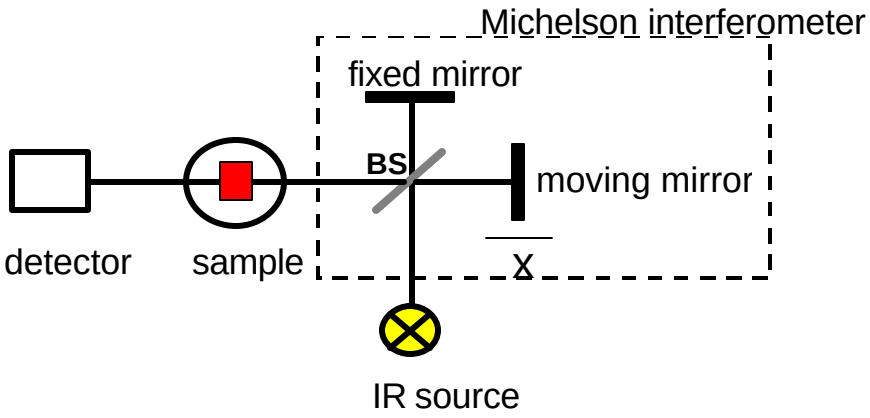

Fig. 2.3: Basic instrumentation of the FTIR spectrometer.

Fourier transform infrared (FTIR) spectroscopy is a well established method to record FTIR data. Polychromatic radiation from an infrared source is divided by a beamsplitter (BS). One part is directed onto a fixed mirror, the other part is passed onto a moving mirror (Fig. 2.3). The reflected beams are recombined and give rise to a complex interference pattern, with the highest intensity in the center burst (x = 0) and decreasing intensities to either side. After passing the sample, the detector measures the intensity *I(x)* as a function of the mirror position *x*. The beam of a He/Ne-laser takes the same path. The monochromatic laser light produces a sine shaped interferogram. The distance between two zero crossing points is half the wavelength of the laser light. Thus, the laser light is used as internal distance calibration. The relation between the intensity *I'(x)* at mirror position *x* and the intensity of a monochromatic spectral line *S(n)* at the wavenumber *n* is given by

$$I'(x) = S(n)\cos(2\pi n x). \tag{2.8}$$

The Fourier transform yields the transmission spectrum $I(\nu)$:

$$I(\nu) = const. \int_0^\infty [I'(x) - I(0)] \cos(2\pi\nu x) dx \qquad (2.9)$$

The negative logarithm of the ratio between two transmission spectra gives an absorption difference spectrum A(ν).

2.6.1 FTIR Absorbance Difference Spectra

Fig. 2.4 shows three different transmission spectra labeled 'met', 'dark' and 'light'. The spectrum 'met' is taken from a sample without any diatomic ligand. The overall shape of this line reflects the spectral behavior of a protein sample and serves as a baseline. MbCO yields the spectrum labeled 'dark'. A dominant band due to bound CO is visible. After photolysis (spectrum 'light') at 3 K, only a residual fraction of ligands remains bound to the heme iron. Most ligands are photolyzed and trapped in the protein interior. They give rise to a new band labeled 'photolyzed CO' in Fig. 2.4.

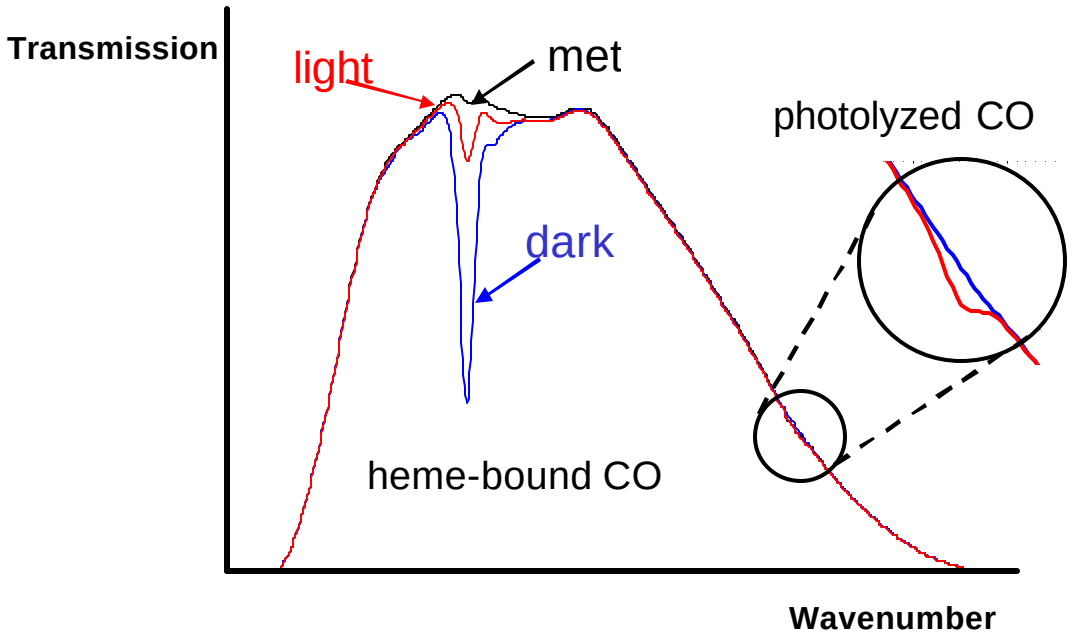

Fig. 2.4: Transmission spectra: The blue line represents the transmission of an MbCO sample with CO bound to the heme. The spectrum recorded in red shows a residual fraction of ligands still bound to the heme; the photodissociated ligands give rise to a new band. The black curve labeled 'met' is taken from a protein sample with no CO.

From these three transmission spectra, different absorbance difference spectra can be calculated:

(i) total bound population: $-\log\left(\frac{I(dark)}{I(met)}\right)$

(ii) actually bound population at any given time: $-\log\left(\frac{I(light)}{I(met)}\right)$

(iii) photolyzed population: $-\log\left(\frac{I(light)}{I(dark)}\right)$

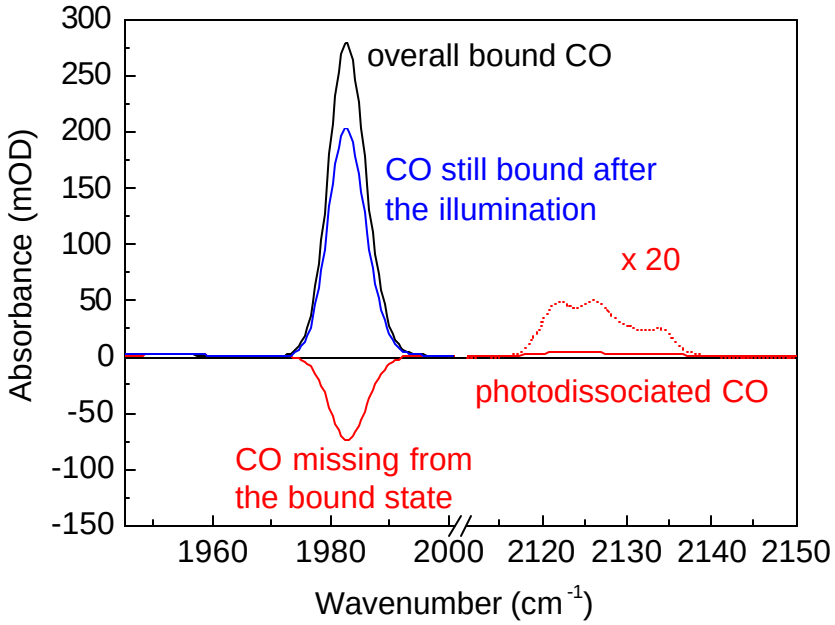

Fig. 2.5: FTIR absorbance difference spectra: The black line represents the overall concentration of CO bound to the heme within the MbCO sample. The sample recorded in red shows the photolyzed fraction, a negative band for ligands missing from the bound state and a positive band from the photodissociated ligands. The blue curve gives the residual bound population after illumination.

Fig. 2.5 shows exemplary absorbance difference spectra. Originally, this particular sample protein shows a single A state band for bound CO (black line), indicative of only one taxonomic substate. After incomplete photolysis, a large fraction of CO ligands is still bound (blue line). The photodissociated ligands give rise to a negative band for bound CO (red line), since CO is missing from the bound state. Simultaneously, these same photolyzed ligands produce a new band with a positive sign (red line) that represents these ligands at the intermediate site. The extinction coefficient for this type of bands is much smaller. For better presentation, we expand the scale by multiplying the absorbance with a factor of 20 (red dotted line).

FTIR absorbance spectra are calculated for every new sample. The dark/met difference spectrum gives information about the number of taxonomic substates within the sample. Moreover, the light/dark spectrum shows the photolyzable CO fraction and allows a first look at the photoproduct bands.

2.6.2 Isothermal Kinetics Measurements

Isothermal perturbation and relaxation spectroscopy monitors IR absorbance changes in the sample during and subsequent to illumination. The sample is exposed to laser light for an extended period of time (e.g., 15,000 s) at selected fixed temperatures to produce a non-equilibrium state while FTIR transmission spectra are collected continuously. In a first approximation, we assume that two only states, the bound state A and the photodissociated intermediate state B are involved. The rate coefficient k_L for the transition from A $\rightarrow$ B is determined by the intensity of the illumination. The recombination B $\rightarrow$ A is characterized by the rate coefficient k_{BA}. The photolyzed fraction N within the sample at a temperature T is given by

$$N(T) = \int \frac{k_L}{k_L + k_{BA}} g(H_{BA})\, dH_{BA} \tag{2.10}$$

with the recombination barrier distribution $g(H_{BA})$ (47). This relation implies that the sample should reach a steady state after an illumination time $t = 1/(k_L + k_{BA})$. Instead, it was observed by Nienhaus *et al.* that the photolyzed fraction increases logarithmically (46, 47). Thus, a more complex 'pumping' model is necessary to explain that the photolyzed fraction $N(T,t)$ is time-dependent on long time scales. In this model, ligands become initially trapped in intermediate B. Subsequently, these ligands are excited again, and they explore longer-lived states with higher recombination barriers and, therefore, slower reaction pathways. Relaxation towards a new metastable dark state is observed at the same temperature over 50,000 s.

2.6.3 Temperature Derivative Spectroscopy (TDS)

2.6.3.1 Theoretical Background

Temperature Derivative Spectroscopy (TDS) is an experimental protocol designed to investigate thermally activated rate processes that are characterized by distributed enthalpy barriers (47, 65, 95). It has proven to be particularly useful for detailed investigations of ligand recombination, because this 2D technique allows to separate populations not only by their spectral components (wavenumber n), but also by their rebinding properties (recombination temperature T).

Within the sample, a non-equilibrium intermediate state is created by photolysis. The subsequent TDS measurement records the relaxation of the sample back to equilibrium while the temperature is ramped up linearly with time in the dark at a rate $b = 5$ mK/s, starting at the initial temperature T_i:

$$T = T_i + bt\,. \tag{2.11}$$

The recombination reaction is a unimolecular process (like an isomerization reaction) and thus described by a first-order rate process:

$$\frac{dN}{dt} = -kN\,, \tag{2.12}$$

where k is the rate coefficient and N the photodissociated population. Integration yields

$$N = N_i \exp\left[-\int_0^t k\, dt'\right]. \tag{2.13}$$

After substitution of time t by temperature T according to equation (2.11) we obtain

$$\frac{dN}{dT} = \frac{-N_i}{b} k \exp\left[-\int_{T_i}^{T} \frac{k}{b}\, dT'\right] = \frac{-N_i}{b} k \exp(-q) \tag{2.14}$$

with resolution function $k \exp(-q)$.

The integral over temperature, q, can be quantified if we take the rate coefficient k to be given by the Arrhenius relation,

$$k = A\left(\frac{T}{T_0}\right)\exp\left(-H/RT\right), \tag{2.15}$$

with pre-exponential A, temperature T and reference temperature T_0 set to 100 K:

$$q = \frac{AT_0}{b}\left[\left(\frac{T}{T_0}\right)^2 E_3\left(\frac{H}{RT}\right) - \left(\frac{T_i}{T_0}\right)^2 E_3\left(\frac{H}{RT_i}\right)\right]. \tag{2.16}$$

Here, E_3 denotes the exponential integral of order 3,

$$E_3(x) = \int_1^{\infty} \frac{e^{-xt}}{t^3}\, dt. \tag{2.17}$$

Next, we take into account that each protein molecule within the ensemble rebinds by overcoming a unique activation enthalpy barrier, but that there is a distribution of barriers $g(H)$ within the ensemble:

$$\frac{dN}{dT} = -\frac{N_i}{b}\int_0^{\infty} k \exp(-q)\, g(H) dH \tag{2.18}$$

with the probability $g(H)dH$ that a given protein molecule has an activation enthalpy barrier between H and $H + dH$ (normalized to 1). The temperature ramp protocol ensures that rebinding occurs sequentially with respect to the height of the activation enthalpy barrier. It can be shown that the barrier height is approximately proportional to the ramp temperature; the temperature axis can be cast into an enthalpy axis (95).

During the TDS experiment, FTIR transmission spectra $I(n,T)$ are taken every kelvin. The integrated absorbance A of the spectral band taken at the lowest temperature represents the total photolyzed population N. The change in integral absorbance $\int \Delta A dn$ is taken proportional to the population ΔN that changes its state during the acquisition of two successive spectra. Distributed barrier heights and, therefore, recombination rates are a universal feature of protein ensembles at low temperatures. We expect small changes in the

absorbance at low temperatures, because only a few molecules can surmount the barrier for recombination. At higher temperatures $\int \Delta A d\nu$ will increase, since more and more molecules are able to rebind. At even higher temperatures $\int \Delta A d\nu$ will decrease again, the population N has been depleted.

For a quantitative modeling of the TDS data, the derivative of the population with respect to temperature, *dN/dT*, is approximated by calculating absorbance difference spectra from transmission spectra at successive temperatures. This is done technically by one of two equivalent procedures: Either one subtracts absorbance spectra, calculated against the same arbitrary reference spectrum, or one takes the ratio of two transmission spectra. This is shown by the following calculation:

$$\begin{aligned}
\Delta A(\nu, T) &= A(\nu, T - \tfrac{1}{2}K) - A(\nu, T + \tfrac{1}{2}K) \\
&= -\log\left(\frac{I(\nu, T - \tfrac{1}{2}K)}{I_{ref}(\nu)}\right) + \log\left(\frac{I(\nu, T + \tfrac{1}{2}K)}{I_{ref}(\nu)}\right) \\
&= -\log I(\nu, T - \tfrac{1}{2}K) + \log I_{ref}(\nu) + \log I(\nu, T + \tfrac{1}{2}K) - \log I_{ref}(\nu) \qquad (2.19) \\
&= -\log I(\nu, T - \tfrac{1}{2}K) + \log I(\nu, T + \tfrac{1}{2}K) \\
&= -\log\left(\frac{I(\nu, T - \tfrac{1}{2}K)}{I(\nu, T + \tfrac{1}{2}K)}\right)
\end{aligned}$$

We emphasize that two assumptions are implicit in this procedure: (i) The change in absorbance is proportional to the rebinding population, and (ii) there is no intrinsic temperature dependence in the measured spectra. The first assumption is well fulfilled for A-state spectra, as shown from the agreement of kinetic experiments in the Soret band and the A substate bands. For the IR bands of the photodissociated CO, there is clear experimental evidence for an intrinsic temperature dependence of the infrared band areas, and therefore, absorbance changes cannot - *a priori* – be set proportional to population changes. The second assumption is not strictly fulfilled either. IR bands can shift and broaden with temperature, which will give rise to difference signals. Referencing procedures that compensate for these effects will be discussed below.

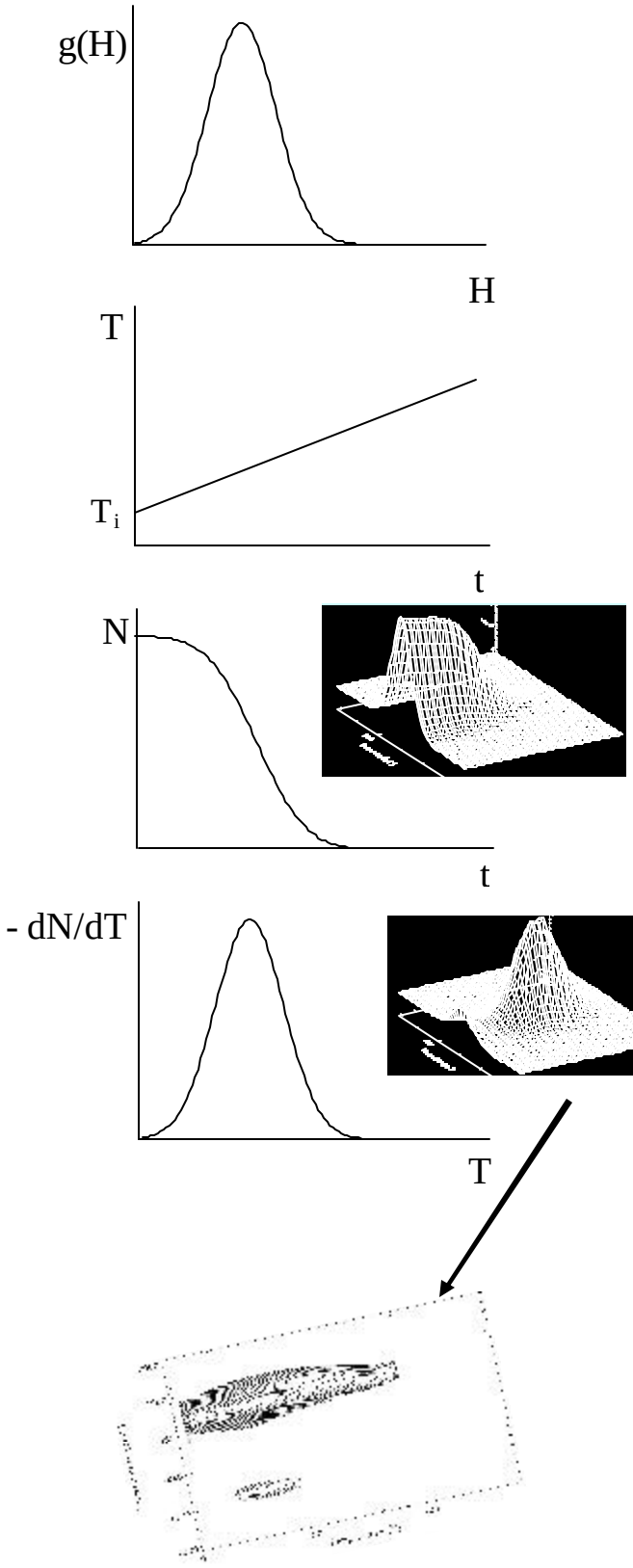

Overview of the TDS Technique:

Distributed recombination rates due to distributed recombination barriers H are a universal feature of protein ensembles, arising from conformational differences.

After photolysis, the temperature is ramped up linearly in time from the initial temperature T_i at a rate $b = 5$ mK/s.

$$T = T_i + bt.$$

Spectra are taken every kelvin. Our observable O is a spectral band with an integrated absorbance assumed to be proportional to the photolyzed population N. Due to the linear temperature ramp, the time axis is cast into a temperature axis. Thus, the change in band area versus time is proportional to the change in photolyzed population versus temperature:

$$\frac{dO}{dt} \propto b \frac{dN}{dT}$$

At low temperatures, the change of dN/dT will be small: Only those few ligands that encounter a low recombination barrier can surmount it. At higher temperatures, dN/dT will increase as more and more ligands have enough energy to overcome their rebinding barriers, and at even higher temperatures, the change dN/dT will decrease again because the population N has been depleted.

Contour plots are a convenient means of presenting the data.

2.6.3.2 Representation of TDS Data in Contour Maps

TDS data are conveniently presented as (linearly or logarithmically scaled) contour plots of the absorbance change on a surface spanned by the wavenumber (n) and temperature (T) axes. Linearly scaled contour plots mediate a distinct impression of the actual recombining population. Logarithmic spacing, however, favors minority species and provides an important tool to present intermediates of low occupancy. In Fig. 2.6, we plot the same data set using contours with linear spacing (left panel) and logarithmic spacing (right panel).

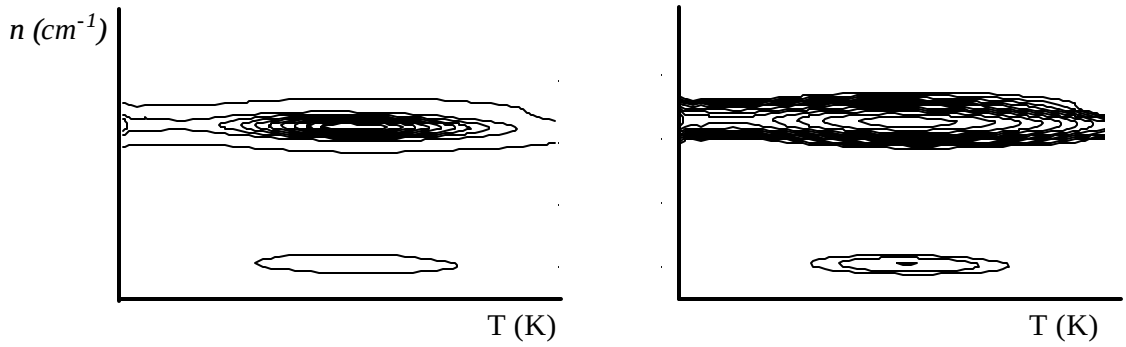

Fig. 2.6: FTIR absorbance difference spectra presented as linearly spaced (left panel) and logarithmically spaced (right panel) contour plots on a temperature versus wavenumber surface.

Fig. 2.7 a shows a typical twin set of TDS contour maps. The upper map records the FTIR absorbance changes in the bands of heme-bound CO, the bottom map refers to the bands of photolyzed CO. In general, solid contour lines indicate an absorbance gain, whereas dotted lines represent a decrease in absorbance. Consequently, solid lines in the contour plot of heme-bound CO denote recombination, whereas dashed lines depict a decrease in a particular bound population. The assignment is opposite in the contour maps of photodissociated CO. A concurrent increase in heme-bound CO and decrease in photolyzed CO (blue arrows) connects specific intermediates to taxonomic substates. To point this out explicitly, we include panel c on the lower right; we plot a temperature set of FTIR transmission spectra referenced against a 'met' transmission spectrum.

Increase and decrease of absorbance within the same map (red arrow), however, indicate an exchange within one of the ligand populations. In our example, the exchange occurs among photolyzed intermediates. This particular exchange is explained by a rotation of the CO ligands at the initial docking site B (55). We again display FTIR absorbance difference spectra in the panels b on the lower left, now exclusively for the photodissociated ligands. The red line represents the initial distribution of CO ligands between the two dominant intermediate states. After raising the TDS temperature by 20 K, the distribution has changed significantly (blue line). We monitor an increase in the band at 2131 cm^{-1}, while the band at 2119 cm^{-1} has lost area. The consecutive differences of the FTIR/TDS absorbance difference spectra (or FTIR derivative spectra) in the bottom panel clarify the exchange.

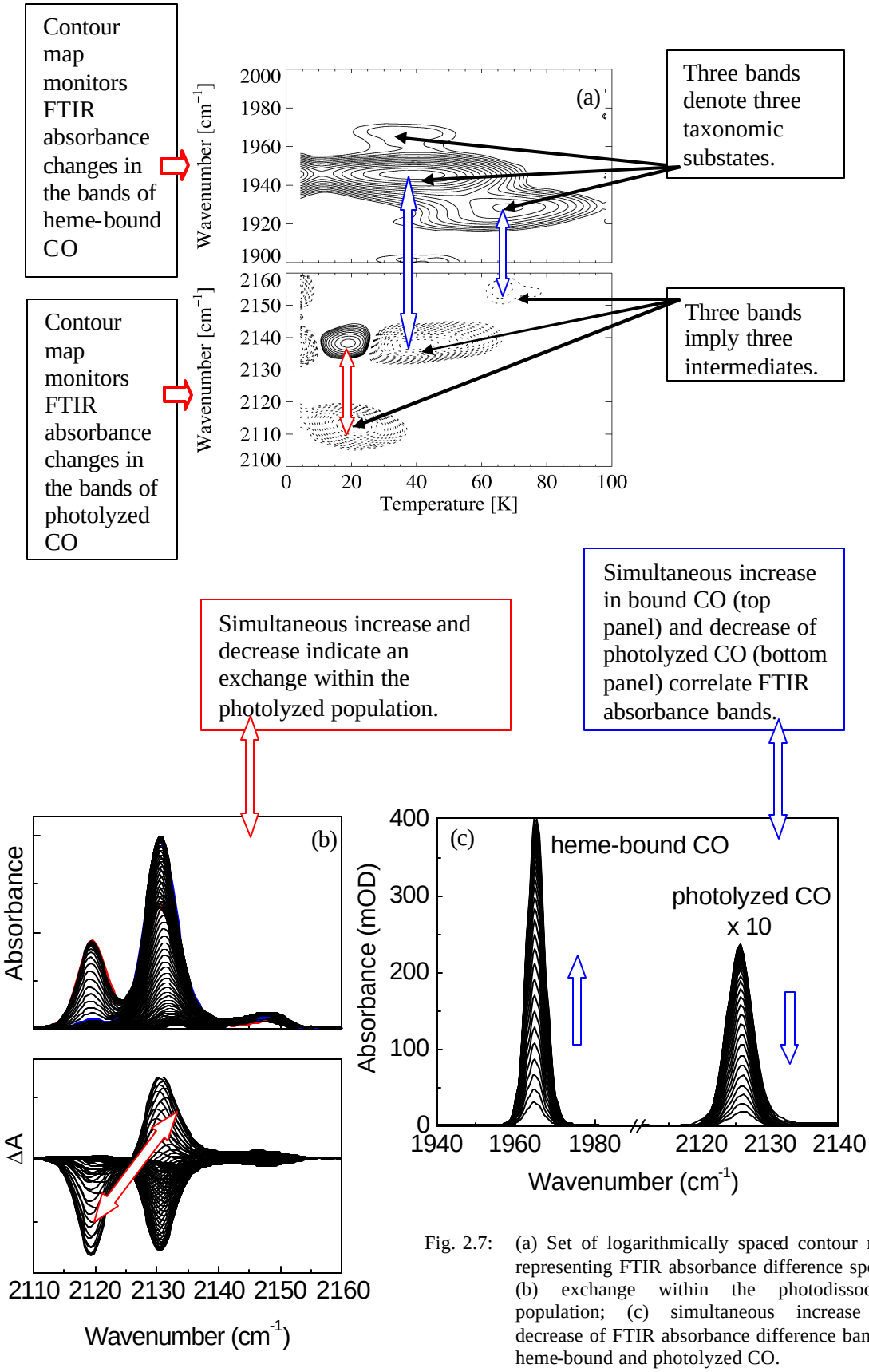

Fig. 2.7: (a) Set of logarithmically spaced contour maps representing FTIR absorbance difference spectra; (b) exchange within the photodissociated population; (c) simultaneous increase and decrease of FTIR absorbance difference bands of heme-bound and photolyzed CO.

2.6.3.3 Kinetic Hole Burning (KHB) in the TDS Map

An artificial TDS data set is presented in Fig. 2.8 to explain the impact of KHB on the TDS maps, assuming a fictional inhomogeneous sample with one taxonomic substate A. Due to recombination the band loses intensity non-uniformly (panel a). A contour map of the integral FTIR absorbance difference spectra (panel b) clearly shows KHB indicated by the red line. Note that this is *not* a derivative map. The peak frequency of the remaining band shifts approximately linearly with increasing temperature. The effect is much more pronounced when plotting successive differences of FTIR absorbance difference spectra (panel c). Especially the inset depicting the normalized FTIR derivative spectra accentuates the correlation between recombining subpopulation and peak frequency. The corresponding TDS map displays more distinct KHB (panel d). All FTIR absorbance difference spectra were calculated using a 'met' transmission spectrum as reference.

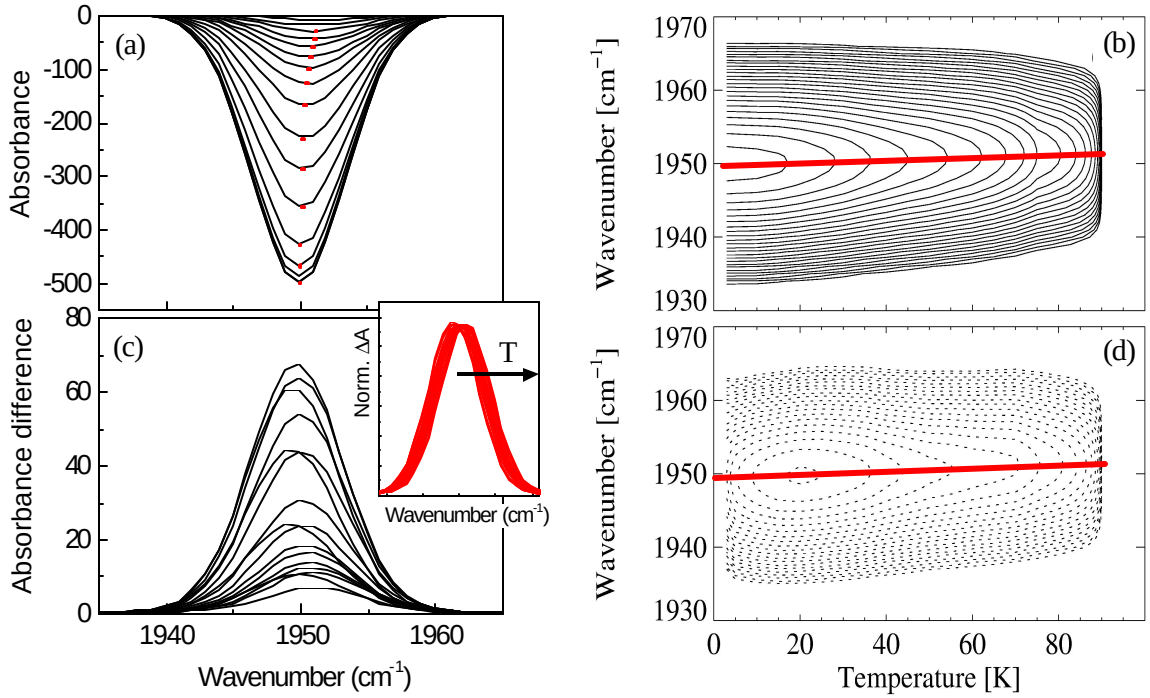

Fig. 2.8: (a) FTIR absorbance difference spectra showing kinetic hole burning; (b) contour plot of the data in panel a showing a peak shift with increasing temperature typical for KHB; (c) successive differences of FTIR absorbance difference spectra represent the bands for the individual homogeneous components; the phenomenon is most clearly visible in the normalized spectra; (d) TDS map representing the data in panel c.

2.6.3.4. Temperature-dependent Transmission Spectra and TDS

FTIR transmission spectra of heme-bound CO intrinsically change shape and intensity. The WT spectra in Fig. 2.9 illustrate this problem. In panel a, we plot the integral FTIR absorbance difference spectra of heme-bound CO from 160 to 300 K, in panel b the same data in a contour map. To calculate the spectra, we used a set of 'met' transmission spectra. Because these 'met' spectra lack a CO-related peak, the FTIR absorbance difference spectra reflect exclusively the intrinsic temperature dependence. The calculation of consecutive differences (panel c) yields positive (solid) and negative (dotted) signals in the contour plot in panel d, although no reaction occurs.

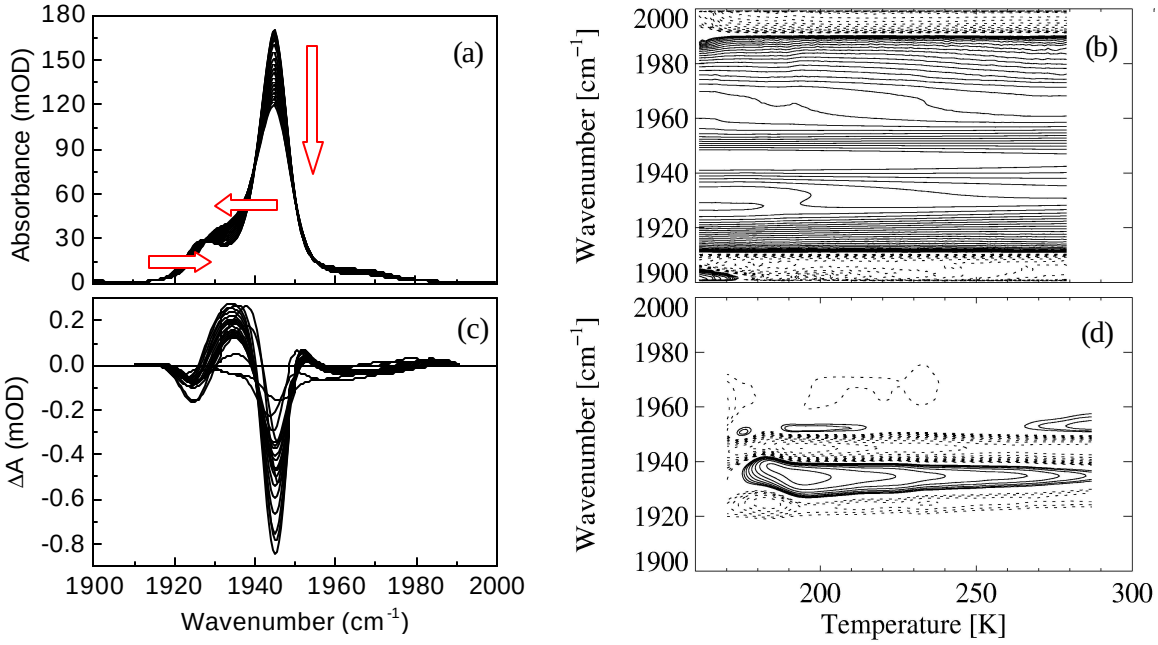

Fig. 2.9: (a) FTIR absorbance difference spectra showing an intrinsic temperature dependence; (b) same data as in panel a in a contour plot; (c) successive differences of the FTIR absorbance difference spectra reveal positive and negative bands; (d) the corresponding TDS map.

To avoid TDS signals from these intrinsic band changes, the referencing procedure (Eq. 2.19) for calculating FTIR/TDS absorbance difference spectra was modified. Reference transmission spectra $I_{ref}(n,T)$ were recorded every kelvin on a fully ligated sample, spanning the entire TDS temperature range. We emphasize that these reference spectra display the total absorbance from *all* heme-bound ligands within the sample. Subsequent to illumination, FTIR/TDS transmission spectra $I_{light}(n,T)$ were collected. These exhibit absorbance signals of only a subpopulation of ligands, namely those that have already rebound at a given temperature T. Therefore, while both reference spectra and TDS spectra exhibit an intrinsic temperature dependence, only the TDS transmission spectra show the additional spectral change due to the reaction.

To correctly compensate for intrinsic temperature-induced band changes at any given temperature, a set of reference transmission spectra $I_{refc}(n,T)$ was calculated as a linear

combination of the initial transmission spectrum $I_{ref}(n,T_i)$ taken at the TDS starting temperature T_i and the temperature-dependent reference transmission spectra $I_{ref}(n,T)$,

$$I_{refc}(n,T) = x \cdot I_{ref}(n,T_i) + (1-x) \cdot I_{ref}(n,T). \tag{2.20}$$

The factor $x(T)$ is given by the fraction of molecules that have not yet rebound their ligand at temperature T. The FTIR/TDS derivative spectra $DA(n,T)$ were calculated as:

$$\begin{aligned}
\Delta A(n,T) &= A(n,T-\tfrac{1}{2}K) - A(n,T+\tfrac{1}{2}K) \\
&= -\log\left(\frac{I_{light}(n,T-\frac{1}{2}K)}{I_{refc}(n,T-\frac{1}{2}K)}\right) + \log\left(\frac{I_{light}(n,T+\frac{1}{2}K)}{I_{refc}(n,T+\frac{1}{2}K)}\right) \\
&= -\log\left(\frac{I_{light}(n,T-\frac{1}{2}K)}{x \cdot I_{ref}(n,T_i) + (1-x) \cdot I_{ref}(n,T-\frac{1}{2}K)}\right) \\
&\quad + \log\left(\frac{I_{light}(n,T+\frac{1}{2}K)}{x \cdot I_{ref}(n,T_i) + (1-x) \cdot I_{ref}(n,T+\frac{1}{2}K)}\right)
\end{aligned} \tag{2.21}$$

We discuss the two extreme cases: (i) In the beginning of the TDS experiment, $x(T)$ is close to one. Most ligands are still photodissociated. Thus, equation 2.21 yields:

$$\begin{aligned}
\Delta A(n,T) &= A(n,T-\tfrac{1}{2}K) - A(n,T+\tfrac{1}{2}K) \\
&= -\log\left(\frac{I_{light}(n,T-\frac{1}{2}K)}{I_{light}(n,T+\frac{1}{2}K)}\right) \quad .
\end{aligned} \tag{2.22}$$

Consequently, the derivative spectra are given by the ratio of consecutive transmission spectra according to Eq. 2.19.

(ii) As recombination becomes complete, $x(T)$ approaches 0. TDS spectra as well as reference spectra show identical intrinsic temperature dependencies:

$$\begin{aligned}
\Delta A(n,T) &= A(n,T-\tfrac{1}{2}K) - A(n,T+\tfrac{1}{2}K) \\
&= -\log\left(\frac{I_{light}(n,T-\frac{1}{2}K)}{I_{ref}(n,T-\frac{1}{2}K)}\right) + \log\left(\frac{I_{light}(n,T+\frac{1}{2}K)}{I_{ref}(n,T+\frac{1}{2}K)}\right)
\end{aligned} \tag{2.23}$$

Between these two cases, it is important to calculate the reference according to Eq. 2.20. In Fig. 2.10, we plot TDS maps of heme-bound CO as an example for these referencing procedures. In panel a, we calculated the FTIR absorbance difference spectra according to the extreme case in Eq. 2.22. Above 210 K, the map displays solid lines in combination with dashed lines. These contours do *not* represent recombination, but temperature-induced band changes between the reference spectrum recorded at 160 K and the TDS data collected at temperatures above 210 K. After utilizing the other extreme method described by Eq. 2.23, the temperature induced combination of solid and dashed contours appears in the lower temperature region (panel b). Panel c shows the contours after referencing according to Eq. 2.21.

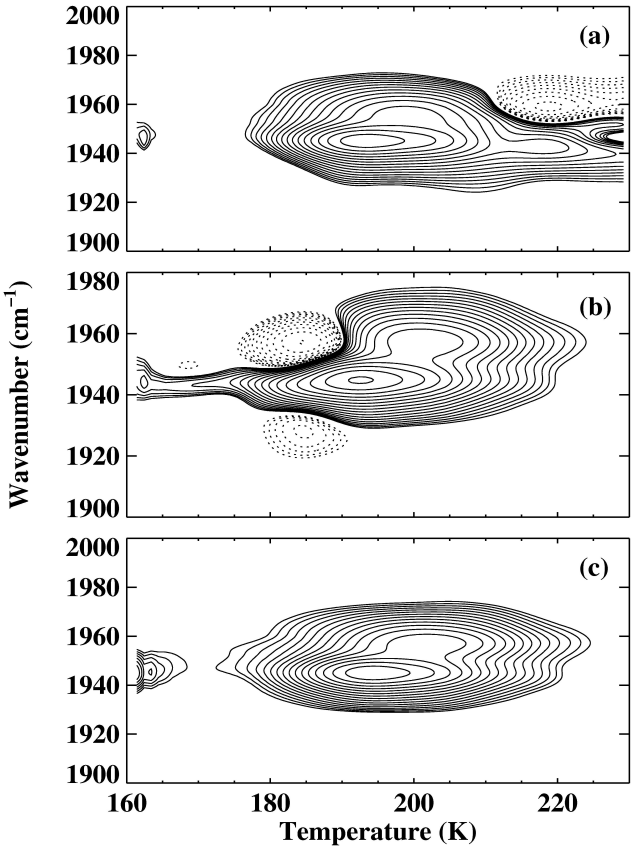

Fig. 2.10: Comparison of contour plots of TDS data, employing different referencing procedures; (a) referenced against a *unique* transmission spectrum taken without prior illumination at the lowest temperature of the TDS experiment (here: 160 K); (b) referenced against a complete dark data set; (c) referenced against a linear combination of (a) and (b).

2.6.4 Illumination Protocols

Every TDS experiment monitors the recombination of photodissociated ligands sorted by their recombination temperatures. The sample is prepared by especially designed illumination protocols to selectively populate intermediate states. Fig. 2.11 gives an overview of the different protocols. The illumination procedure is marked in red, black lines describe the TDS protocol. Five different protocols, labeled 1 through 5, have been used in this thesis.

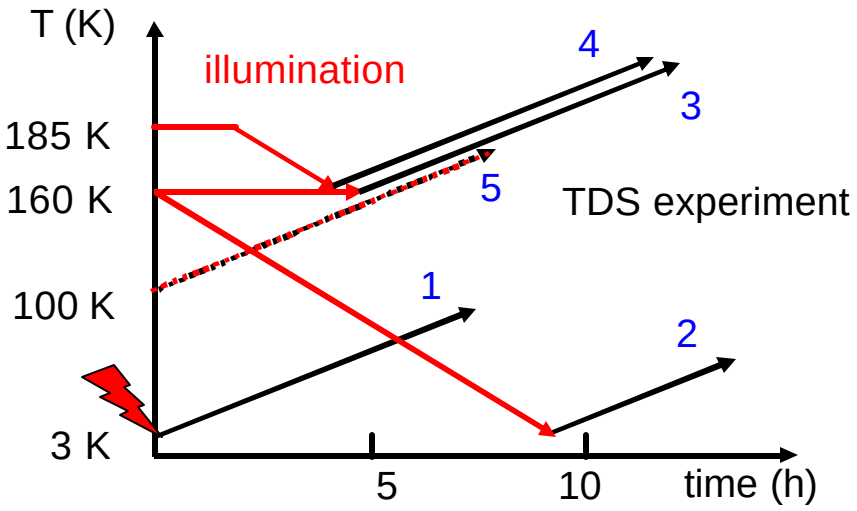

Fig. 2.11: Overview of different illumination protocols to prepare specific intermediates. Their recombination characteristics are monitored in the TDS experiment.

Whereas protocol 1 measures rebinding from states that can be populated at 3 K, the following protocols monitor rebinding from states that can (only) be populated at higher temperatures. In protocol 1, the sample is illuminated for 1 s at 3 K (protocol 1). Immediately afterwards, the TDS experiment is started. We expect to mainly observe recombination from the initial docking site B. To sample higher recombination barriers, the slow cool protocol (protocol 2) is applied. The laser light is kept on while the sample is cooled from 160 to 3 K. At 160 K, essentially all ligands are photolyzed. At high temperature, ligands may rebind and are photolyzed again. Because the temperature is ramped down, rebinding will be slowed continuously. At one point, ligands with high recombination barriers within the barrier distribution $g(H_{BA})$ cannot overcome these anymore; they become trapped at an intermediate site. Afterwards, ligands with successively smaller energy barriers will be trapped in the protein. In Fig. 2.12, we schematically explain the process for the intermediate B.

In protocol 3, we illuminate the sample at 160 K for 15,000 s. A steady state situation under illumination is achieved. The subsequent TDS experiment records the recombination of only those few ligands that can still be kept photodissociated at 160 K; it monitors only very long-lived intermediate states.

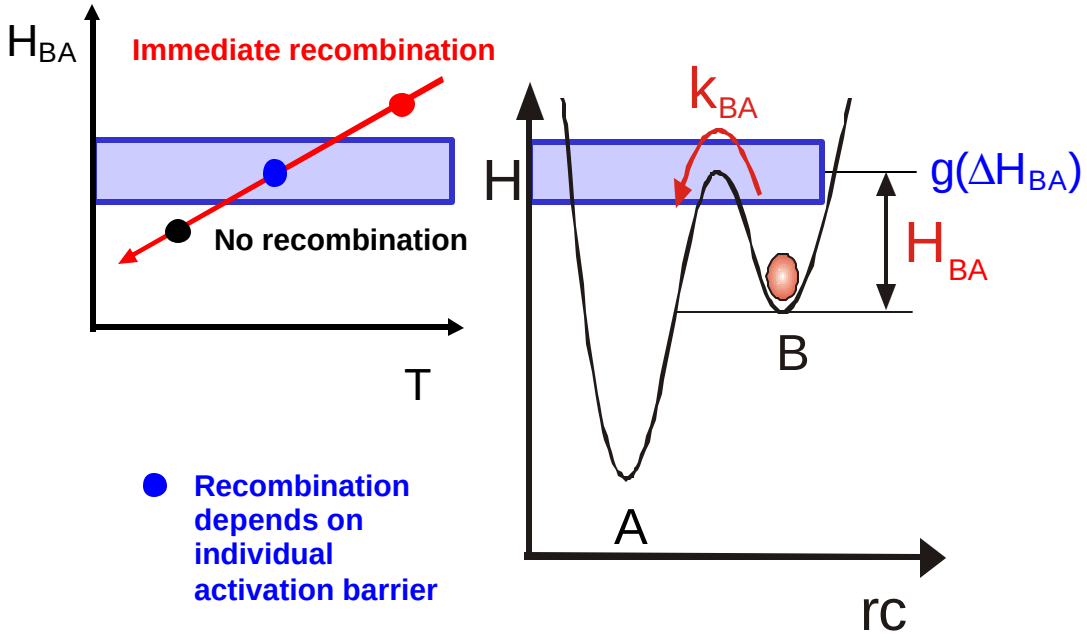

Fig. 2.12: The principle of the slow-cool protocol.

To explore intermediates above the dynamic transition temperature, the sample is illuminated for 2 h at 185 K before cooling to 160 K (protocol 4). At 185 K, the protein can perform large-scale motions. The taxonomic substates interconvert. The illumination protocol enables ligands to either populate new intermediates with very high recombination barriers or to escape into the solvent. Whenever a ligand leaves the protein moiety, it experiences an individual electrostatic environment provided by the solvent molecules. Therefore, each CO molecule will give rise to a homogeneous line with an individual FTIR stretch frequency. All these ligands will give rise to a very broad FTIR band of low amplitude that cannot be detected anymore.

Protocol 5 differs from the rest insofar as the TDS ramp (100 – 220 K) is performed while the photolysis light is switched on. The equilibrium between bound and photodissociated ligands is governed by the competition between photolysis and recombination. Initially, all ligands are photolyzed. Some will become trapped at an intermediate site. Others will recombine and are photolyzed again. Because the temperature is ramped up, the trapped ligands will be able to return to the heme iron at a particular temperature. Moreover, recombination will become increasingly faster. At higher temperatures, ligands might become trapped at another intermediate site with higher recombination barriers. Therefore, this protocol samples all available intermediate sites from the one with the lowest barriers to the ones with the highest barriers for recombination within the temperature interval of the TDS experiment.

3. Results and Interpretation

After more than forty years of intense research, uncovering the detailed mechanism of ligand binding to myoglobin resembles an unfinished puzzle. We have studied the ligand binding process with kinetic and temperature ramp protocols over wide temperature ranges, using the IR stretch bands of CO ligands as exquisitely sensitive reporters of the structural environment of the ligands. This approach, together with site-directed mutagenesis has allowed us to fill in some of the crucial pieces of the puzzle. The following section describes our results on WT myoglobin and related mutants. In section 3.2, we will report on mutant L29W and related double mutants.

3.1 WT MbCO and Related Mutants

In 1994, more than 35 years after the first structure analysis of myoglobin (12, 23), x-ray diffraction experiments performed below 40 K revealed the first photoproduct structures of WT (49, 50). Subsequent to photolysis of MbCO crystals at liquid-helium temperatures, the CO ligands were recovered very near to the active site on top of the heme group, oriented parallel to the heme plane above pyrrole C. This position is called the primary docking site B. A subsequent structure analysis at ~160 K has also detected a small fraction of CO molecules in the Xe 1 cavity of horse heart myoglobin MbCO crystals after extended illumination (16). As of yet, no direct structural evidence of ligand migration into other hydrophobic cavities exists for WT. In mutants L29W and YQR (L29Y/H64Q/T67R), however, photodissociated CO ligands have also been observed in the Xe 4 pocket (15, 18). To examine the structural determinants that influence ligand binding and migration, we have investigated WT and related mutants with FTIR/TDS techniques in great detail. In Table 3.1 in Appendix B, we have compiled the IR stretch frequencies of the CO ligands, both heme-bound and photodissociated, of all samples discussed in this section.

3.1.1 Probing the Active Site and Initial Docking Site

3.1.1.1 FTIR Absorbance Difference Spectra after Short Illumination

To obtain a first impression of the influence of specific residues on the IR stretch bands of heme-bound and photodissociated CO, we have measured the FTIR absorbance difference spectra at 3 K. Each MbCO sample was cooled to 3 K in the dark, a transmission spectrum I_{dark} and, after illumination for 1 s, a second transmission spectrum I_{light} were taken. The difference spectrum, was calculated as $-\log(I_{light}/I_{dark})$; it reflects the changes within the sample caused by the laser light.

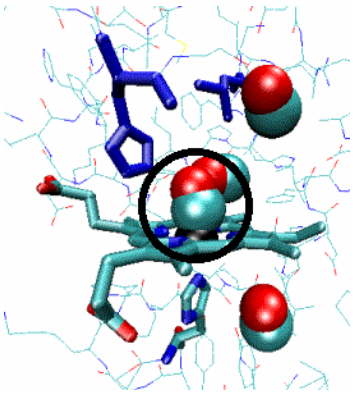

Mutations at Residue 64

In Fig. 3.1, we compare the CO stretch bands of WT (pH 7 and pH 5.4), H64L and H64V. For WT at pH 7, we observe a dominant peak for substate A_1 (1945 cm^{-1}), a second smaller peak for A_3 (1930 cm^{-1}) and an additional tiny band at ~1970 cm^{-1} in the spectral region of heme-bound CO. Two bands at 2119 cm^{-1} and 2131 cm^{-1} are resolved for the photoproducts, which we assign to B_2 and B_1 (55). Close inspection shows a third small peak, B_0, at 2149 cm^{-1}.

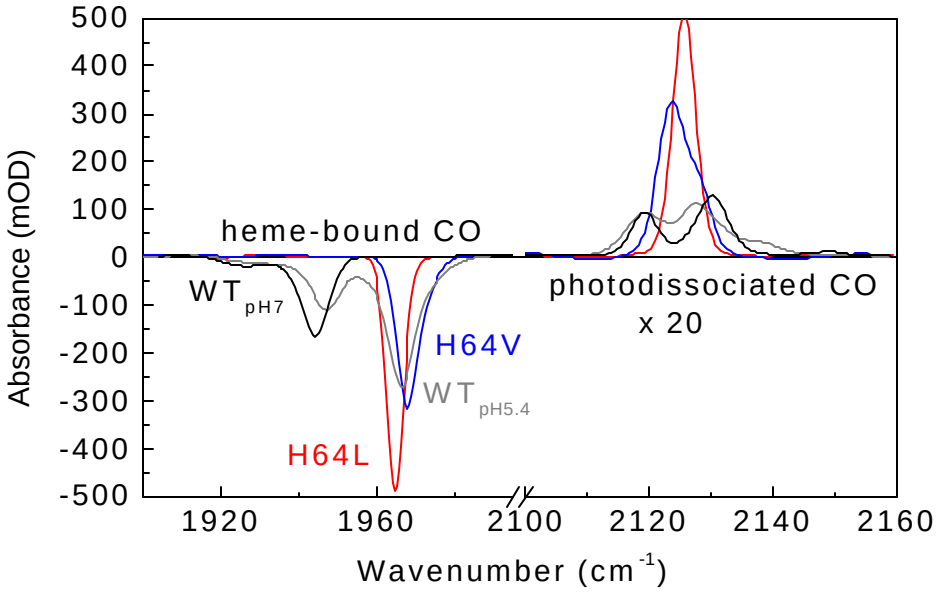

Fig. 3.1: FTIR absorbance difference spectra of WT MbCO (pH 7 and pH 5.4) and mutants H64L and H64V recorded at 3 K after illumination for 1 s.

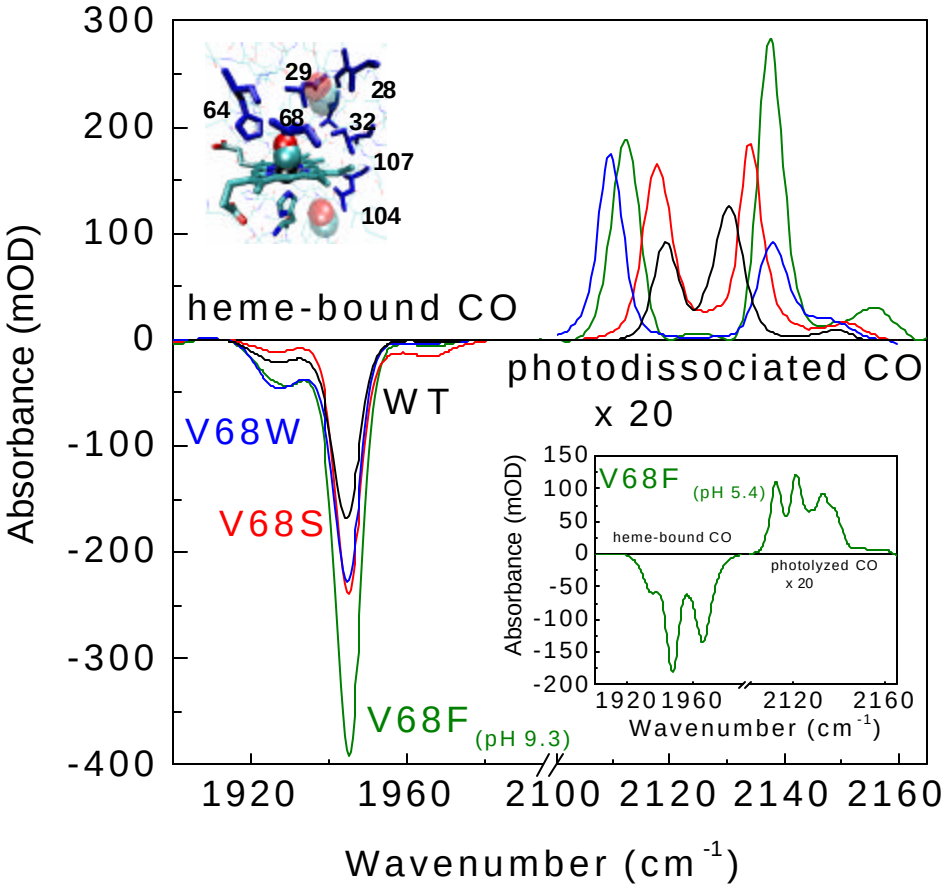

Fig. 3.2: FTIR spectra of WT MbCO and mutants V68S, V68F and V68W recorded at 3 K after illumination for 1 s; insets: (upper left) structure near the active site, (lower right) V68F at pH 5.4.

At pH 5.4, the composition of the WT sample has shifted towards substate A_0 at 1966 cm^{-1}. A significant fraction of the molecules, however, still have remained in substates A_1 and A_3. Two additional peaks have emerged in the photoproduct bands, they are associated with CO photolyzed from Mb molecules in the A_0 substate. Replacing the distal histidine with an aliphatic, apolar sidechain in H64V and H64L yields a single taxonomic substate characterized by a stretch band at ~1966 cm^{-1}. For simplicity, we call this substate A_0, because is has a similar stretch frequency as A_0 in WT (52, 83). With these mutants, it is easier to study photoproduct intermediates of A_0 than in WT because of the missing A_1 and A_3. The spectrum of heme-bound CO in H64L displays a single narrow A_0 peak. The corresponding band of H64V appears asymmetric, which indicates heterogeneity. In the photoproduct spectrum of H64L, a single CO stretch band is discernible, whereas H64V shows two partially overlapping bands.

Mutations at Residue 68

Like H64, V68 is another highly conserved residue in the vicinity of the active site (78, 96). Its sidechain points straight toward the docking site B. We have replaced the valine at position 68 by the polar serine and by phenylalanine and tryptophan, which have aromatic sidechains. For these mutants and WT for comparison, FTIR spectra at 3 K are plotted in Fig. 3.2. While the assignment of A_1 (1945 cm^{-1}) and A_3 (1930 cm^{-1}) fully agrees with the prevalent nomenclature, the nomenclature of the small peak at ~1970 cm^{-1} poses a difficulty. The high wavenumber would imply an A_0 type substate, characterized by a protonated H64 sidechain. However, the pK of H64 is known to be ~4.5, and therefore, a significant population can be excluded at pH values between 7.4 and 9.3. In accordance with earlier work by Müller *et al.* (69), we call the third substate A_x.

In the spectral region of photolyzed CO, IR bands associated with photoproducts B_0, B_1 and B_2 are visible. There is a systematic trend in the splitting between peaks B_2 at ~2120 cm^{-1} and B_1 at ~2130 cm^{-1}, it increases from WT < V68S < V68F < V68W. Simultaneously, B_0 at ~2150 cm^{-1} is shifted to increasingly higher stretch frequencies. In V68F at pH 5.4, part of the heme-bound population has adopted substate A_0, and consequently, two additional A_0 photoproduct bands can be discerned (Fig. 3.2, inset).

Double Mutant H64V/V68S

To examine the relative influence of residues 64 and 68 on the CO stretch bands, we employed double mutant H64V/V68S. Fig. 3.3 shows FTIR absorbance difference spectra of mutants H64V, H64V/V68S and V68S. The spectrum of WT is included for comparison. In the spectral region of heme-bound CO, we observe a dominant A_0 band for H64V and H64V/V68S. For the double mutant, additional small A substate bands at 1958 and 1945 cm^{-1} can be discerned.

The IR stretch bands of the photolyzed ligands all differ from those of WT. Insertion of a polar OH-group in V68S causes a larger splitting between the B_1 and B_2 bands. The splitting decreases when replacing histidine 64 by an apolar sidechain. For H64V/V68S, the B_1 and B_2 bands are clearly resolved at frequencies identical to those of H64V.

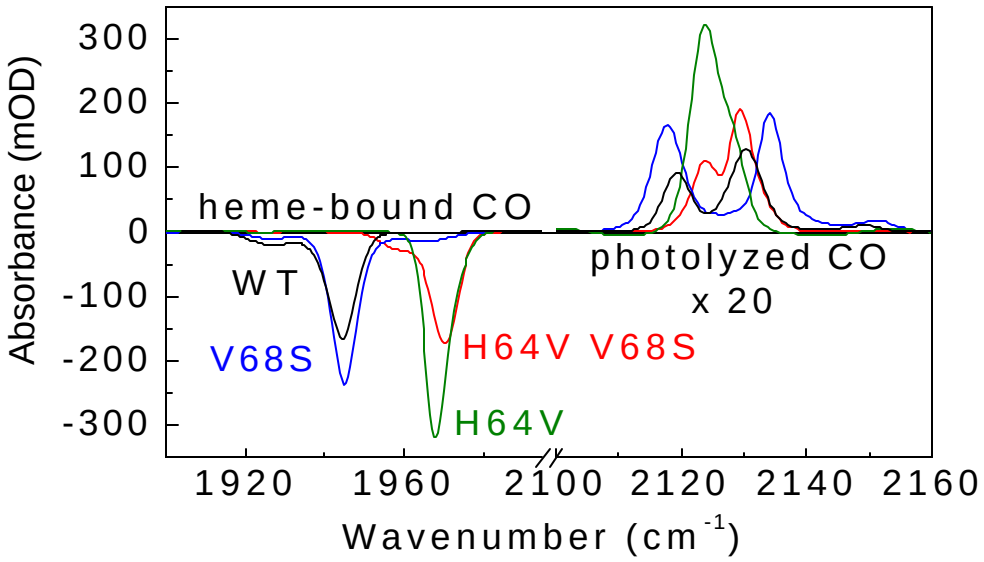

Fig. 3.3: FTIR absorbance difference spectra of WT MbCO and mutants V68S, H64V/V68S and H64V measured at 3 K after illumination for 1 s.

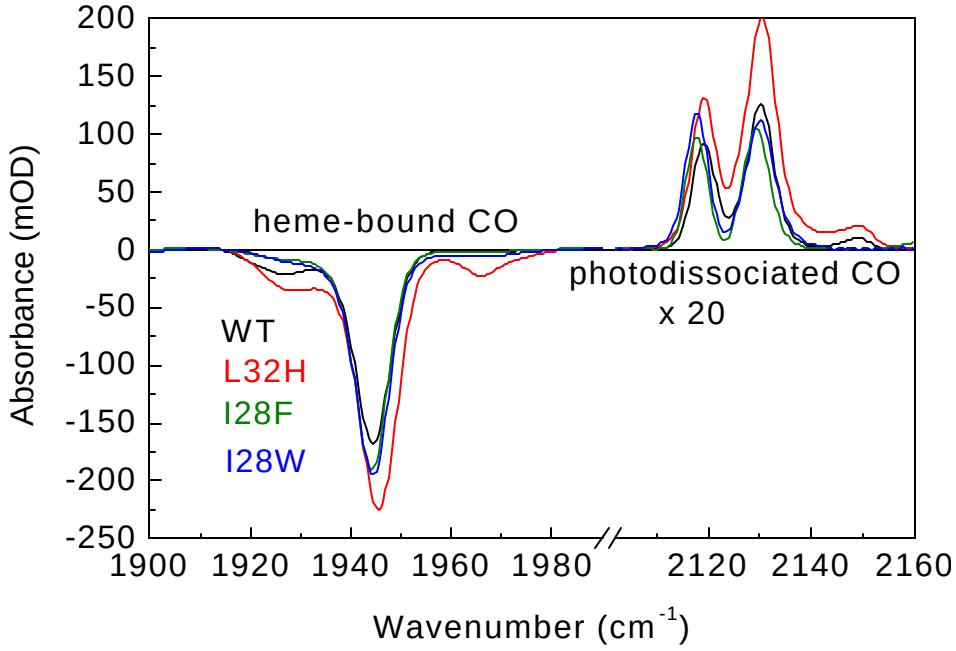

Fig. 3.4: FTIR absorbance spectra of MbCO samples WT, I28F, I28W and L32H at 3 K after illumination for 1 s.

Mutants I28F/W and L32H

Amino acids I28 and L32 line the back of the distal pocket. In Fig. 3.4, we display FTIR absorbance difference spectra of mutants I28F, I28W and L32H; the WT spectrum is again included as a reference. For L32H, the spectrum shows a dominant A_1 band (at ~1945 cm^{-1}), a smaller peak assigned to A_3 (at ~1930 cm^{-1}) and a third A_x band at ~1970 cm^{-1} in the spectral range of heme-bound CO. For the photoproducts, stretch bands B_2 at ~2120 cm^{-1} and B_1 at ~2130 cm^{-1} are visible, as well as a minor B_0 band at ~2150 cm^{-1}.

A_1 is the dominant substate in I28F and I28W, only a small fraction is in A_3. Photolysis gives rise to CO stretch bands B_1 and B_2. The minority species B_0 is not apparent, presumably due to the low fraction of A_3.

Mutant L29W

A third residue near the active site, L29, proved to have a major impact on ligand recombination. We will discuss these results separately and in great detail in section 3.2.

Mutants L104W and I107W

All mutants discussed so far have had structural modifications in the distal pocket. Whereas residue 107 is also situated on the distal side, residue 104 is located on the proximal side of the heme lining the Xe 1 cavity. In Fig. 3.5, we plot the CO spectra of I107W and L104W together with the spectrum of WT. Mutant I107W shows a markedly different spectrum over the entire spectral range, with substates A_1 and A_3 being populated about equally. The photodissociated ligands give rise to a broad, not well structured photoproduct spectrum with peaks at 2108 cm^{-1} (B_2), 2130 cm^{-1} (B_1) and 2150 cm^{-1} (B_0). In contrast, the spectrum of L104W is very similar to that of WT.

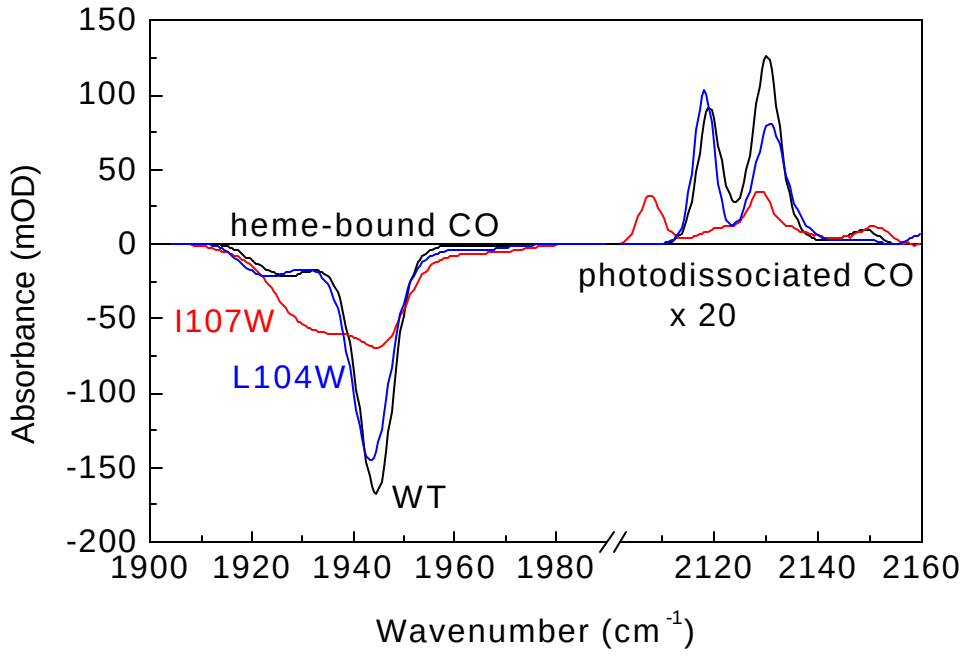

Fig. 3.5: FTIR absorbance difference spectra of WT MbCO and myoglobin mutants I107W and L104W at 3 K after illumination for 1 s.

3.1.1.2 TDS Contour Maps after Short Illumination

Brief illumination for 1 s at 3 K cleaves the bond between heme iron and CO ligand. The prevalent appearance of two distinct bands, B_1 and B_2, in the photoproduct spectra suggests that the photolyzed ligands are trapped mainly at the initial docking site B within the distal pocket. TDS experiments were performed on WT MbCO and the mutants already mentioned to study migration among cavities and recombination of CO ligands in the various substates.

Mutations at Position 64

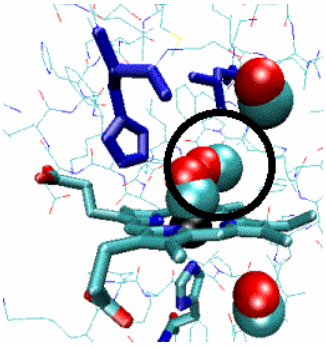

In Fig. 3.6, we have compiled contour plots of WT MbCO and mutants H64L and H64V. For WT (pH 7), recombination to A_1 peaks at 50 K and to A_3 at 78 K (Fig. 3.6 a, b). Black arrows indicate rebinding from B_1 to A_1 and B_0 to A_3. The dotted arrow marks an exchange from B_2 at 2119 cm^{-1} to B_1 at 2131 cm^{-1}. An additional solid contour at 2149 cm^{-1} and 18 K (Fig. 3.6 b) indicates an increase in population of intermediate B_0. The recombination signals at 78 K associate this particular photoproduct B_0 with A_3. Thus, the increase of this particular photoproduct is not related to the decrease of the A_1 photoproduct B_2.

At pH 5.4, the contour map of heme-bound CO (Fig. 3.6 c) is governed by recombination to A_0. The recombination feature from B_1 to A_1 is still visible, however. Return from B_0 to A_3 cannot be detected anymore because of the small population of A_3 at low pH. The photoproduct map (Fig. 3.6 d) appears rather complicated, and it is not immediately obvious which bands arise from intermediates of substate A_0.

To examine ligand recombination in an A_0 like substate, we have investigated mutants H64L and H64V. For H64L, the TDS map of heme-bound CO contains a single conformational substate A_0 with a FTIR stretch band at 1964 cm^{-1} (Fig. 3.6 e). Note that the feature at 1920 cm^{-1} is an isotope band. At first glance, there is also only one peak in the photoproduct map of H64L (Fig. 3.6 f). However, we observe an exchange between photoproducts below 10 K, indicative of two bands with not too different positions. Ligand recombination in H64L MbCO is complete at 70 K.

H64V shows an asymmetric contour in the A state map (Fig. 3.6 g). Two spectrally not well resolved photoproducts populations (Fig. 3.6 h) recombine at 30 K and 40 K. A total of three exchange processes are marked by dotted arrows. In contrast to H64L, recombination to H64V stretches out up to 100 K.

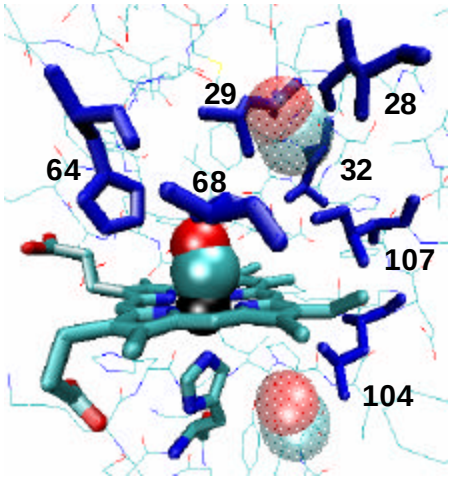

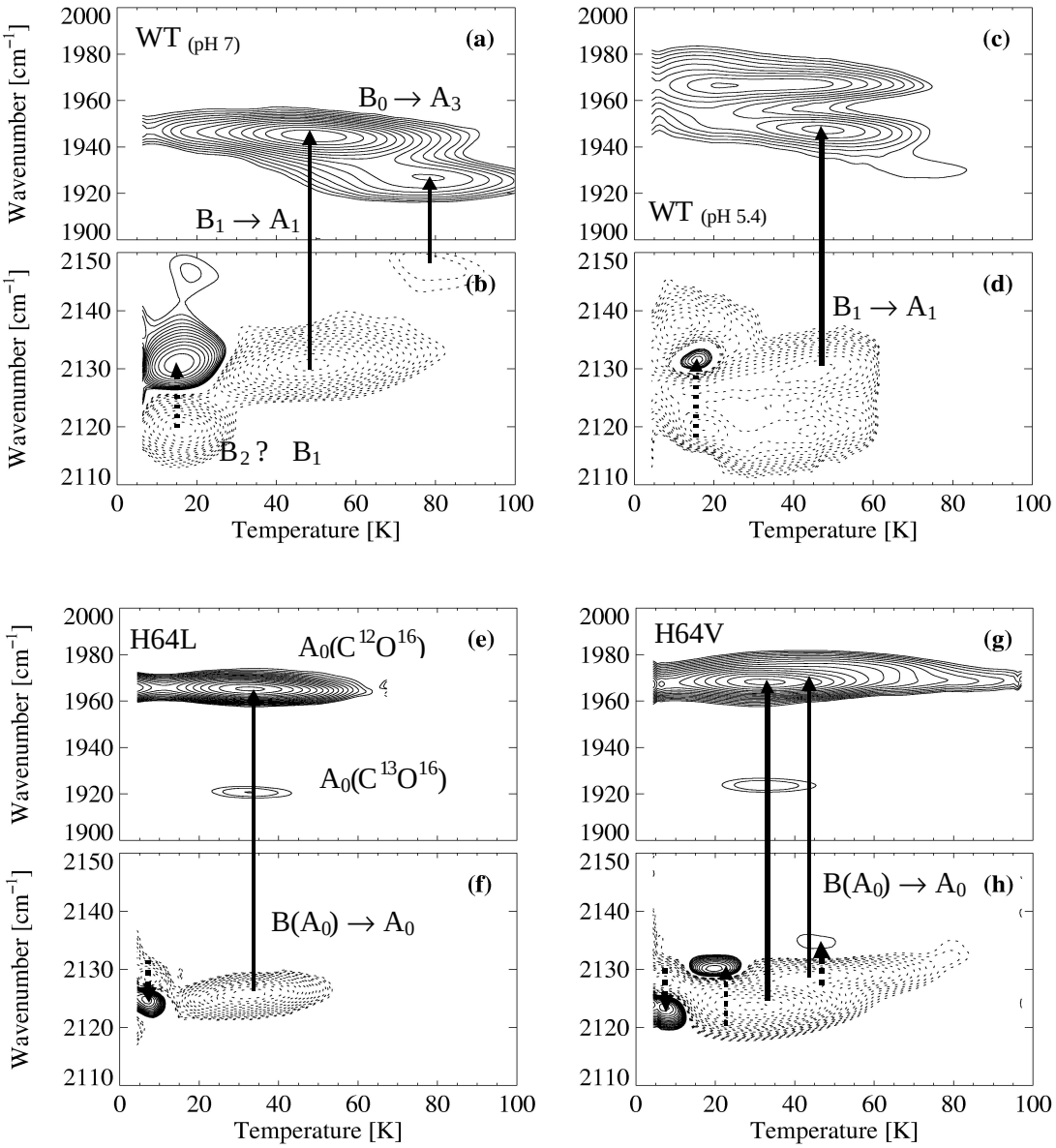

Fig. 3.6: TDS contour maps of (a, b) WT MbCO (pH 7), (c, d) WT MbCO (pH 5.4) as well as mutants (e, f) H64L and (g, h) H64V after illumination for 1 s at 3 K.

Mutations at Residue 68

To examine the effects of the crucial amino acid valine 68 on CO rebinding, it was replaced by the polar serine and the bulky phenylalanine and tryptophan. The TDS maps of heme-bound CO (left column in Fig. 3.7) show CO recombination from only one intermediate state (except for V68S) to each taxonomic substate, presumably from the initial docking site B. Substate A_1 at ~1945 cm^{-1}, which dominates all the contour plots, peaks at ~ 40 K (and 15 K for V68S). A_3 generally rebinds at higher temperatures (~70 K). The temperature of maximum recombination to both A_1 and A_3 systematically drops from WT > V68S > V68F > V68W. All samples display a third taxonomic substate, A_x, which is most pronounced in V68S and rebinds at temperatures similar to A_1. In WT MbCO, A_x has been known to exist before (69), but its population is so small that it does not appear in the TDS map in Fig. 3.7 a at the chosen contour levels.

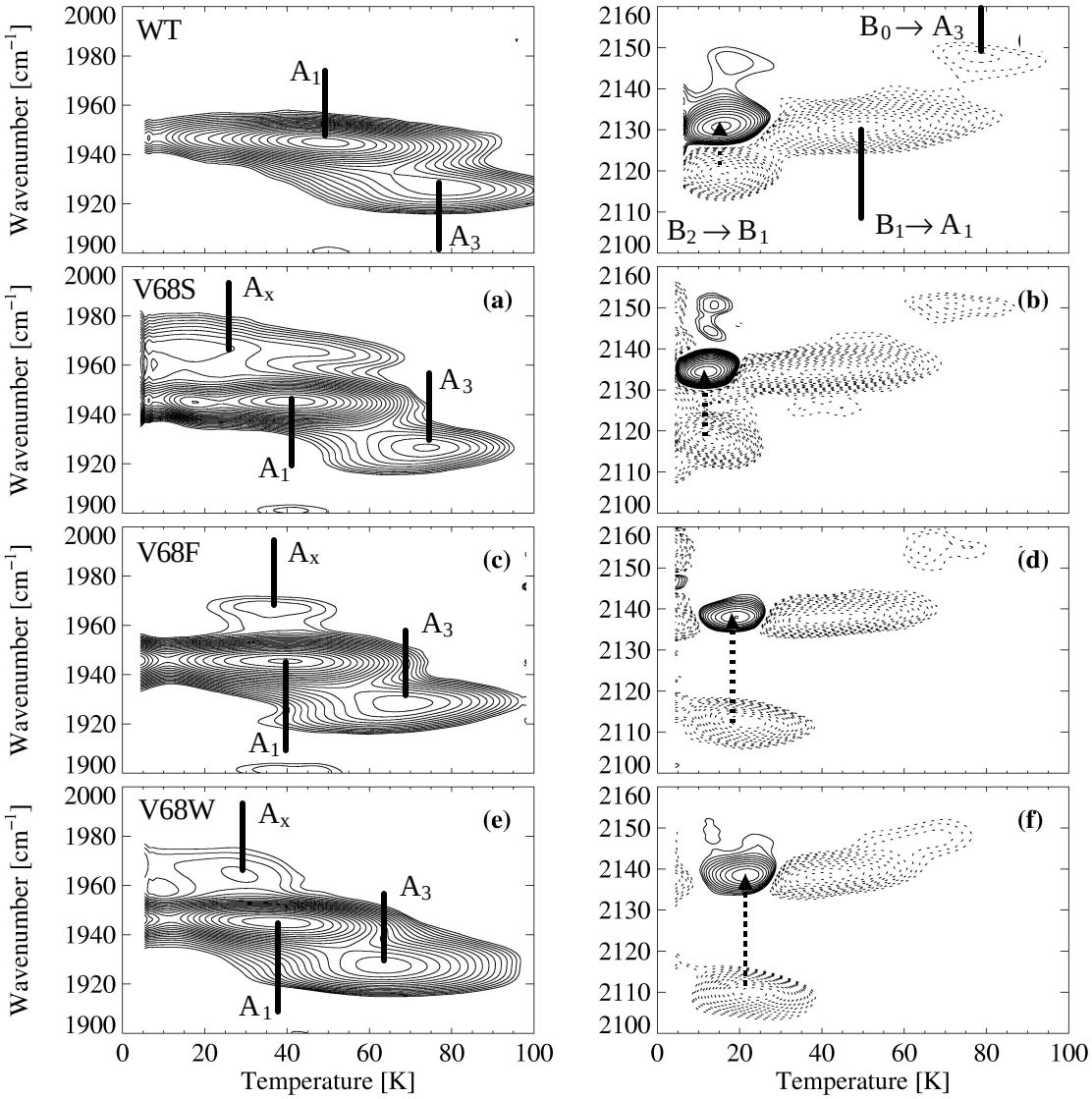

Fig. 3.7: TDS contour maps of WT MbCO (high pH) and mutants V68S, V86F and V68W after illumination for 1 s at 3 K.

In the maps of photodissociated CO (Fig. 3.7, right column), the V68 mutants show a large separation between the $B_1(A_1)$ and $B_2(A_1)$ bands, corresponding to CO ligands in opposite orientations at the initial docking site (see dotted arrows). The splitting increases from WT < V68S < V68F < V68W. Furthermore, the temperature of the transition from B_2 to B_1 increases from V68S < V68F < V68W.

In Fig. 3.8, we compare the TDS maps of V68F at pH 9.3 (panels a, c) and 5.4 (panels b, d). As for WT MbCO, the assignment of photoproduct bands to taxonomic substates becomes more difficult at low pH because of the appearance of the A_0 substate and its associated photoproduct bands. Nevertheless, it is obvious that the recombination features of the maps at pH 9.3 are still visible in the TDS maps of the pH 5.4 sample.

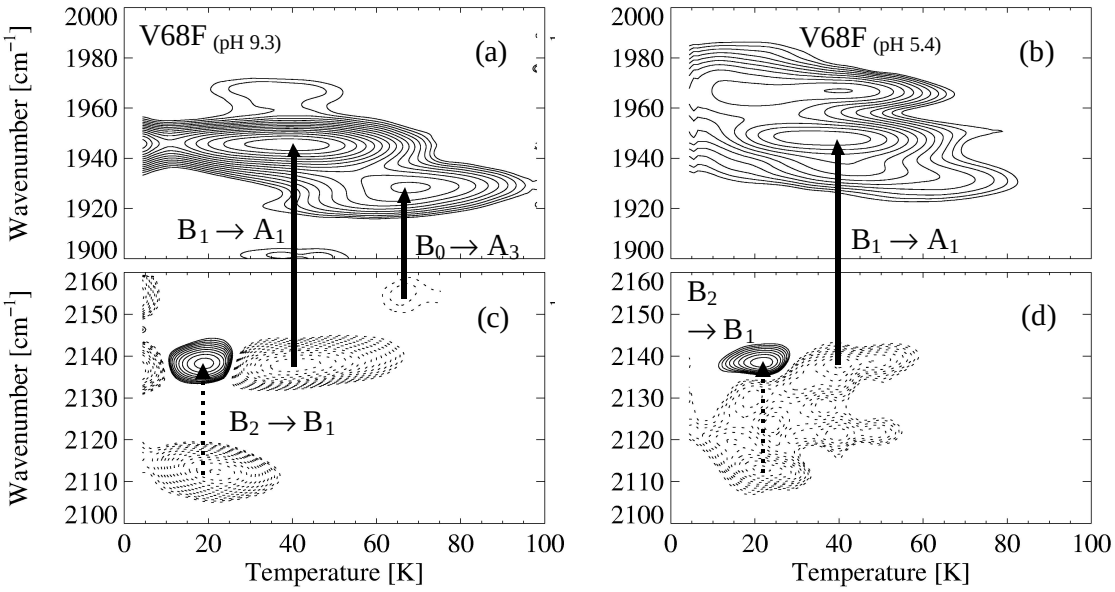

Fig. 3.8: TDS contour maps of MbCO mutant V68F at (a, c) high and (b, d) low pH after illumination for 1 s at 3 K.

Double Mutant H64V/V68S

The effects of mutations at positions 64 and 68 relative to each other become apparent in the TDS contour maps of double mutant H64V/V68S in Fig. 3.9. The strong A_0 peak appears at 1970 cm^{-1}, which is blue-shifted by 4 cm^{-1} from its position in H64V. This shift and the appearance of minor features at 1945 and 1960 cm^{-1} indicate changes in the local environment of the bound CO caused by the serine sidechain. Note that the signal at 1925 cm^{-1} is caused by $C^{13}O^{16}$ ligands in substate A_0, however.

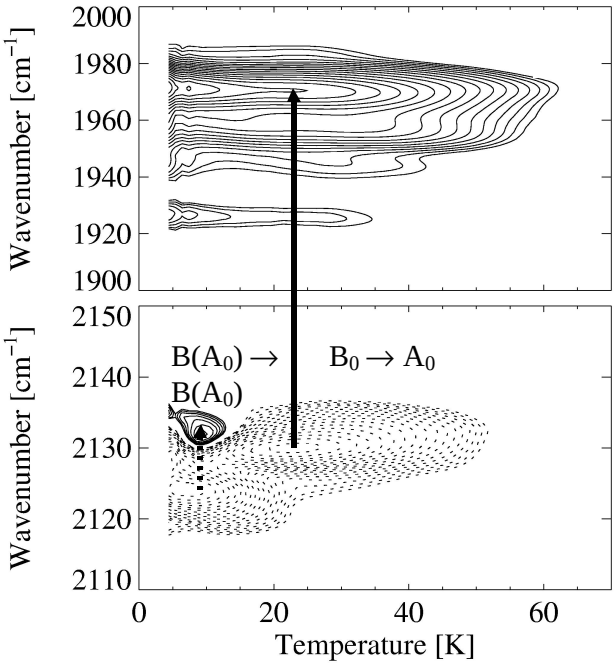

Fig. 3.9: TDS contour maps of MbCO mutant H64V/V68S after illumination for 1 s at 3 K.

The TDS maps in the photoproduct region of H64V (Fig. 3.6 h) and H64V/V68S show identical band positions 2125 and 2130 cm^{-1}, whereas those of V68S are different (2118 and 2134 cm^{-1}, see Fig. 3.7 b). Recombination temperatures are lowest in H64V/V68S as compared with all other mutants studied.

Mutants I28W, L32H, L104W and I107W

Based on the FTIR spectra at 3 K, mutations at positions 28, 32 and 104 do not seem to influence the immediate vicinity of the binding site (A) and initial docking site (B), whereas mutant I107W does. In Fig. 3.10, we have compiled the TDS maps of these mutants and WT for comparison. A first glance reveals already that every CO-bound substate recombines its ligands from only one photoproduct state.

Mutant L32H (Fig. 3.10 c, d) displays recombination from A_1 at 50 K and A_3 at 75 K. Moreover, intense contours associated with A_x catch the eye. The contour map of photodissociated CO in panel d, however, is almost identical to the one of WT in panel b. We also notice population transfer from $B_2(A_1)$ to $B_1(A_1)$, transfer into $B_0(A_3)$, although we cannot tell from the TDS map where this population comes from. Recombination occurs from B_1 to A_1 and from B_0 to A_3. A_x cannot be associated with its own photoproduct feature.

Mutant L104W (Fig. 3.10 e, f) reveals lower recombination temperatures for taxonomic substates A_1 and A_3. The general features in the map of photodissociated CO are conserved (Fig. 3.10 f). The same holds true for I28W (Fig. 3.10 i, j). For both mutants, a recombination signal from B_0 to A_3 cannot be discerned because of the low occupancy of A_3.

Although the 3 K spectrum of I107W was different from the other mutants in this set, its TDS maps, however, display the same overall features (Fig. 3.10 g, h). Recombination occurs from B_1 (~2130 cm^{-1}) to substate A_1 at ~40 K and from B_0 (2150 cm^{-1}) to A_3 at 60 K. Furthermore, the photoproduct map exhibits an exchange at ~20 K.

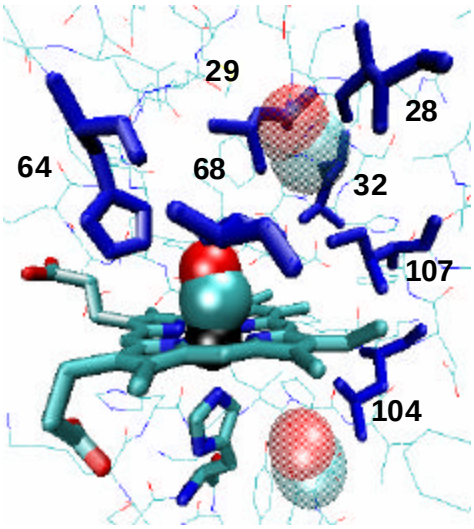

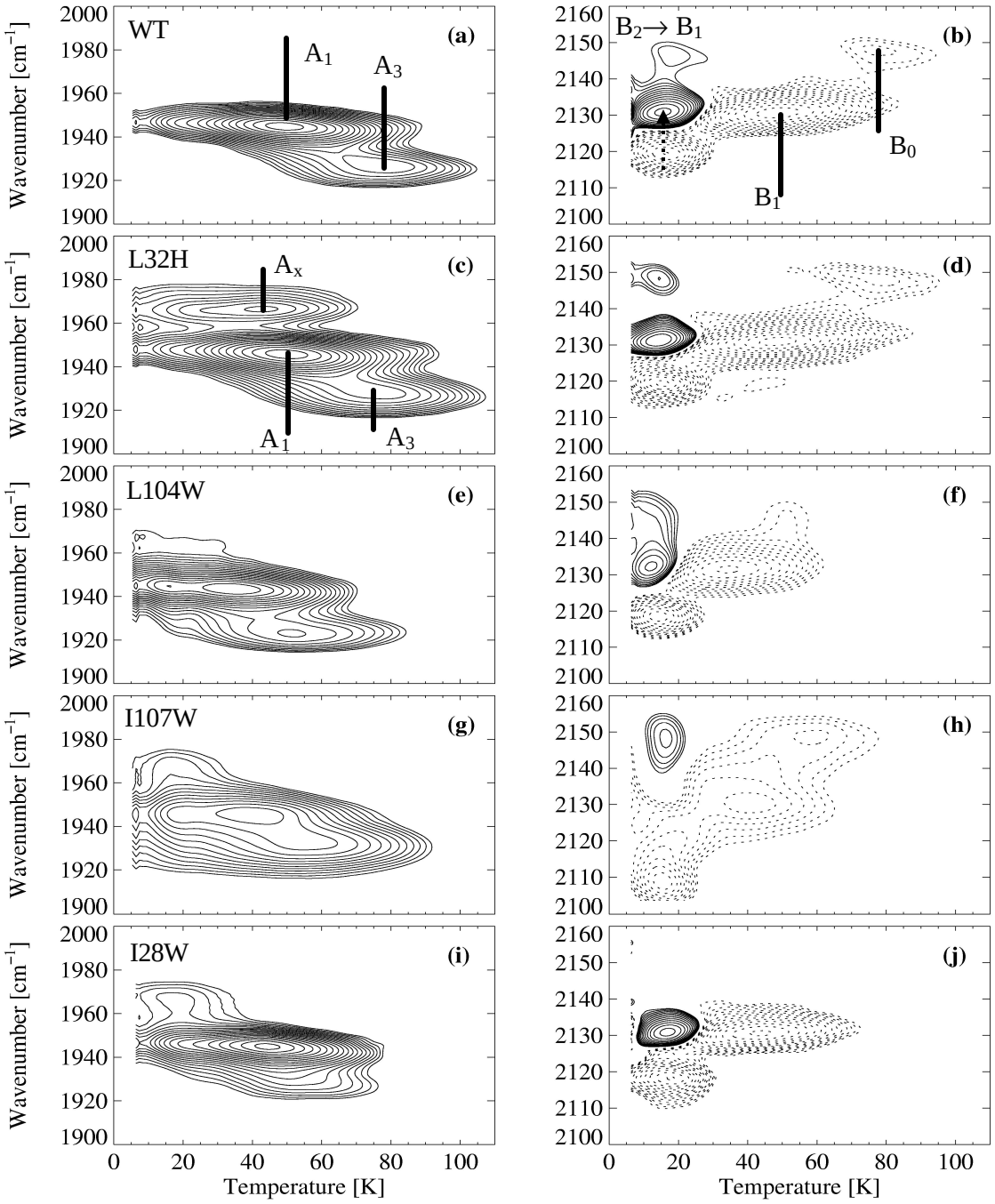

Fig. 3.10: TDS contour maps of WT MbCO (pH 7) and mutants L32H, L104W, I107W and I28W after illumination for 1 s at 3 K.

3.1.1.3. Discussion: Bound State A and Initial Docking Site B

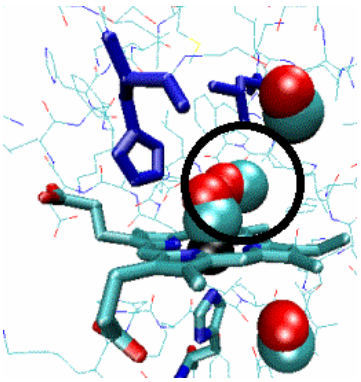

From the 3 K FTIR difference spectra of WT MbCO and related mutants, the impact of particular residues on the CO stretch bands of heme-bound and photodissociated CO can be assessed. TDS experiments performed after photolysis revealed the different recombination temperatures of photolyzed ligands at docking site B to taxonomic substates A_1, A_3 and A_0 (and A_x).

The crucial role of the distal histidine (H64) in the appearance of the substates has been known from IR studies of Mb mutants (52, 83, 97). X-ray diffraction experiments have provided direct structural evidence about the different H64 conformers that give rise to taxonomic substates A_1, A_3 and A_0. A_0 was identified as a substate with a doubly protonated imidazole sidechain, which has swung out of the distal pocket towards the solvent (72). In 1999, Vojtechovsky *et al.* determined the x-ray structure of MbCO to a resolution better than 1.2 A (73). They refined their structure with multiple occupancies of H64 and obtained – besides a 20% occupancy of A_0 – two positions of the imidazole sidechain inside the pocket, occupied to 60 and 20%. In both cases, only $N_{\varepsilon 2}$ was protonated, with the proton pointing towards the bound ligand. The distance from the ligand oxygen to $N_{\varepsilon 2}$ was calculated as 3.2 and 2.7 Å for the 60% and 20% populations, respectively. They suggested assigning these two conformations to A_1 and A_3. Detailed studies of the IR spectra of heme-bound CO in the pH range from 4.2 to 9.5 by Müller *et al.* (69) showed that the equilibrium distribution between taxonomic substates A_0 and A_1/A_3 is governed by pH, as seen in Fig. 3.1. The relative populations of A_1 and A_3, however, are not affected by pH. Johnson *et al.* (68) have studied the kinetic properties of the taxonomic substates by flash photolysis with monitoring in the A state bands. Below 160 K, no interchange between substates was observed; rebinding to each substate was found to be non-exponential and described by a different temperature-independent distribution of enthalpy barriers with different pre-exponentials. The TDS maps in Fig. 3.6 clearly show that pH changes only the relative populations of A substates; their TDS features, however, appear at identical temperature and wavenumber in WT at pH 7 and 5.4 (65). The same behavior is also observed in mutant V68F (Fig. 3.8).

Maximum recombination occurs to substate A_1 at ~45 K and to A_3 at ~70 K. Rebinding to substate A_0 is seen at temperatures of 30 K or even below. H64 is located in the vicinity of the active site and interacts strongly with the bound ligand (52, 83, 97). Therefore, it is expected to sterically hinder geminate rebinding. According to the diffraction data of Vojtechovsky *et al.*, this steric hindrance should be even larger in substate A_3 as compared to A_1 (73), which results in higher rebinding enthalpy barriers and thus explains the higher recombination temperatures observed in the TDS experiment. In A_0, however, the distal histidine has swung out of the distal pocket and, consequently, we observe lower rebinding temperatures. At higher temperatures, where protein motions are activated, the H64 imidazole even plays a dynamic role: After ligand escape from the distal pocket, the H64 sidechain rotates deeper into the distal pocket and may further occlude the active site. Indeed, time-resolved x-ray structures of photolyzed MbCO crystals with ns resolution showed that at ambient temperature, H64 rotates toward the heme iron within about 4 nanosecond after photolysis (51).

Instead of removing the H64 imidazole from the distal pocket by protonation in WT MbCO, we can mutate H64 to a small, essentially non-interacting aliphatic residue, which generates MbCO samples with a single taxonomic substate that resembles A_0. H64L is known to have one of the fastest recombination kinetics at room temperature of all mutants studied up to now (83). The apolar leucine sidechain prevents water molecules from entering the

distal pocket; and consequently, the distal pocket remains easily accessible to diatomic ligands (98). H64V has a less voluminous sidechain and is thus less effective in displacing water. Indeed, the x-ray structure of deoxy Mb H64V has a water molecule inside the distal pocket which needs to be removed before CO or O_2 can bind (75, 98).

Our studies with mutants H64L and H64V also revealed marked differences. H64L showed recombination to substate A_0 from two photoproducts with similar CO stretch frequencies. In the case of H64V, the asymmetric peak in the spectral region of heme-bound CO gives clear evidence of inhomogeneity. A possible explanation invokes a partial occupancy of the distal pocket with water even in the CO bound state. For photolyzed CO, at least two not well-separated IR bands rebinding at 30 and 40 K are discernible. They may again be related to opposite orientations of the ligand at docking site B. A detailed interpretation of the exchange features in the maps of photodissociated CO (Fig. 3.6 h) is not yet possible.

While the role of the distal histidine has been investigated in great detail, the impact of the highly conserved distal pocket residue V68 on the binding characteristics is less well understood (76, 77, 99). Egeberg *et al.* (100) measured association and dissociation rate coefficients of V68 mutants at room temperature by stopped flow rapid mixing and flash photolysis techniques. Their results indicated that V68 is part of the overall kinetic barrier to ligand binding. A monotonic decrease of the ligand association rate with increasing size of the V68 sidechain suggested that residue 68 regulates ligand approach to the heme iron. Moreover, the large benzyl sidechain of phenylalanine was found to trap the ligands adjacent to the iron and thus enhance the geminate rebinding process. In 1995, Quillin *et al.* (96) tried to relate functional properties in several V68 mutants to structure. In their x-ray structure of V68F Mb, the benzyl side-chain points away from the ligand-binding site and occupies a region in the back of the distal pocket. Carlson *et al.* (101) employed molecular dynamics simulations to investigate the structural influence of residue 68. They came to the conclusion that trimming V68 makes remote sites more accessible. Here we have investigated three different V68 mutants. Our results show that the IR stretch bands of heme-bound CO are not greatly affected by mutation at position 68 (Fig. 3.2). Apparently, the distance between the heme-bound CO and the V68 sidechain is too large to influence the stretch frequency. However, we have observed a continuous shift of the recombination temperatures from the initial docking site B to both A_1 and A_3 from V68S > V68F > V68W, implying that a factor common to both substates is responsible for this systematic behavior. In agreement with Egeberg *et al.* we may argue that voluminous residues at position 68 trap the ligands closer to the binding site. Unlike the A state bands, the photoproduct bands are clearly altered by the mutations (Fig 3.2). The polar sidechain of residue S68 leads to a slight increase of the separation between the B_1/B_2 bands related to opposite CO orientations at site B. Aromatic residues at position 68, with their extended π-electron systems, increase the splitting ever further. Apparently, the introduction of charges into the intrinsically hydrophobic distal cavity alters the local electric field significantly. Another interesting observation concerns the temperature of ligand rotation from B_2 to B_1, which increases from V68S < V68F < V68W (Fig. 3.7). It appears that the presence of bulky sidechains close to the docking site hinders the CO rotation.

Residues 64 and 68 have been suggested as important determinants of the local electric field at docking site B. To judge the relative influence of both residues, we engineered the double mutant H64V/V68S (Figs. 3.3, 3.9). Sugimoto *et al.* (102) measured the CO rebinding kinetics at 5° C to this mutant and found an extremely large geminate yield (70-80%) at ambient temperature, in contrast to 15% for V68S and 0% for H64V. In WT, 7% of geminate rebinding was observed. In this work, the interaction of the non-bonding electron pair at the serine oxygen with the CO ligand was made responsible for the large geminate yield in V68S. In the TDS maps of H64V/V68S (Fig. 3.9), we have seen extremely low recombination temperatures, which may have two structural reasons. (i) Replacement of H64 by the smaller

valine reduces the steric hindrance at the binding site, and (ii) the non-bonding electron pair at the serine oxygen traps the ligands close to the active site and allows for very fast recombination at the lowest temperatures. As a lone-pair interaction with the CO should be visible in the photoproduct spectra, we have to exclude the second argument. The FTIR/TDS data show an A_0 substate connected to two photoproduct bands at 2125 and 2130 cm^{-1}, as for the mutant H64V. We conclude that amino acid 64 has a more pronounced impact on the CO ligands at docking site B. The additional small peaks in the A substate TDS maps of H64V/V68S may originate from interactions of the bound CO with the serine, but unambiguous assignments cannot be made at this time.

Apart from the distal histidine mutants, only I107W produced significant changes to the IR bands of heme-bound CO. It displayed a very large fraction of A_3. A slight increase in the relative population of A_3 has also been observed in other mutants with an aromatic sidechain close to the binding site, e.g. V68F and V68W. The positions of photoproduct bands B_1 (2108 cm^{-1}) and B_2 (2130 cm^{-1}) related to A_1 differ by 22 cm^{-1}, whereas they are separated by only 12 cm^{-1} in WT. We observe B_0 at 2150 cm^{-1} in I107W. It is obvious that the large π-electron density of the indole side chain significantly influences the local electric field at the docking site B. This observation has been made earlier for mutant V68F, which also places an aromatic sidechain near the docking site (103), and was reconfirmed by the results on V68W. Straub and Karplus performed *ab initio* vibrational frequency calculations to relate the observed band shifts of photolyzed CO relative to free CO (2143 cm^{-1}) to interactions of the CO with the protein environment (104). They have already proposed that a 'nonpolar' phenyl sidechain appears highly polar to a CO molecule and thus might have a significant impact on the stretch frequency.

Mutant L32H caught our eye because of the relatively large population of substate A_x. The V68 mutants also displayed such a substate, most pronounced V68S. Müller *et al.* (69) had introduced substate A_x when discussing protonation equilibria of H97 and H64. They showed that this substate should not be identified with A_0, characterized by a protonated H64 imidazole, because of three differences: (i) it is slightly blue-shifted (by 2 cm^{-1} in WT), (ii) the A_0 population is governed by pK = 4.5 of H64, and therefore negligible above pH 7, and (iii) the TDS temperature dependence is different from that of A_0. Following a suggestion by Kushkuley and Stavrov (105), A_x was characterized as a substate with a neutral histidine that is expected to reside inside the heme pocket, with $N_{\varepsilon 2}$ protonated but pointing away from the bound ligand. In this conformation, the electrical field contribution of H64 is oriented perpendicular to the CO dipole, thus minimizing the interaction. Oldfield and coworkers (86) had earlier assigned this conformation erroneously to A_0. Mutants L32H and V68S both introduce sidechains that would allow for hydrogen bonds to the bound ligand. These may favor the A_x conformation of the distal histidine.

It is somewhat surprising that mutant L104W displays the lowest temperatures for rebinding to A_1 and A_3 among those discussed here, because the structural modification is situated on the proximal side of the heme, opposite to the distal heme-pocket. Liong *et al.* (106) as well as Scott *et al.* (107) have shown that residue 104 is important for defining the position of the porphyrin within the protein, which in turn influences the reactivity of the heme group towards the ligands. Immediately after photodissociation, there is a rapid initial displacement of the iron out of the heme plane and a relaxation of the protein towards the equilibrium deoxy conformation. The large tryptophan inside the proximal cavity may hinder the iron movement out of the heme plane in the photodissociated intermediate state Mb*CO. Since recombination reverses the protein conformational change, rebinding to a conformation that is closer to that of the ligated molecule is faster than ligand rebinding to the relaxed deoxy conformation (108). The mutation at position 104 on the proximal side of the heme does not have a significant influence on the peak positions for the IR stretch bands of CO ligands residing within the distal pocket.

3.1.2 Probing Intermediates within the Xenon Cavities

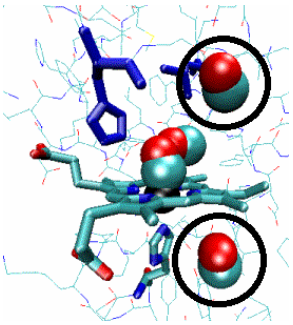

In the previous section, we have presented FTIR/TDS data collected after 1-s illumination at 3 K. It is well known that exposure to prolonged illumination, also performed at higher temperatures, enables ligands to sample intermediates with higher barriers opposing recombination (47, 57, 103). As a convenient survey of these effects, we cooled all our MbCO samples slowly from 160 to 3 K under steady illumination. Subsequently, FTIR transmission spectra were collected and referenced against a 3-K transmission spectrum taken without prior illumination.

Below 160 K, it is generally assumed that protein dynamics is arrested, and therefore, taxonomic substates cannot interchange (46). Indeed, we did not observe any changes in the A state bands. A slight increase in the intensity of those bands as compared with those after short illumination is explained by incomplete photolysis after short exposure. Thus, in the following two-panel-plots we will concentrate on the IR stretch bands of the photolyzed ligands, the upper and lower panels displaying the stretch bands of the photolyzed CO after brief (1 s at 3 K) and extended (slow cooling from 160 to 3 K) illumination, respectively. For better comparison, we plot all spectra normalized to equal area of 1 ODcm^{-1}.

3.1.2.1 FTIR Absorbance Difference Spectra after Slow Cooling from 160 to 3 K

Mutations at Residue 64

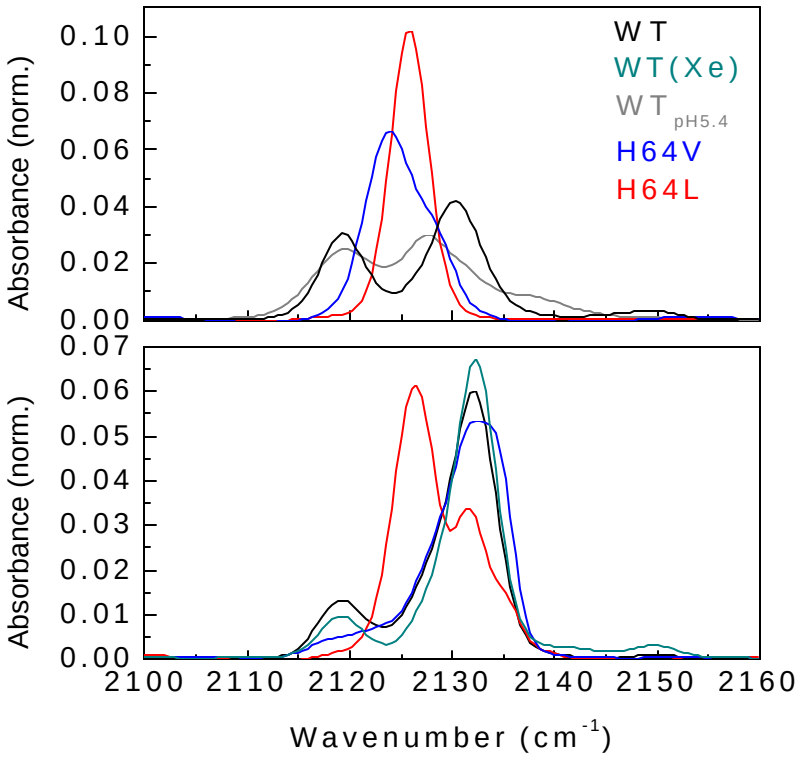

Fig. 3.11: FTIR spectra of WT MbCO and mutants H64L and H64V in the spectral region of photodissociated CO; top: after short illumination for 1 s at 3 K; bottom: after slow cooling from 160 to 3 K under illumination.

In Fig. 3.11, light-induced changes in the spectra of WT, H64L and H64V are apparent. After extended illumination, WT (pH 7) displays a dominant photoproduct peak around 2133 cm^{-1}, shifted by about two wavenumbers compared to B_1 at 2131 cm^{-1} after short illumination (top panel). B_1 is still discernible as a shoulder. Furthermore, B_2 at 2119 cm^{-1} has decreased in intensity; and B_0 at 2149 cm^{-1} is hardly visible. The presence of xenon induces minimal changes. After extended illumination, the photoproduct spectra of H64V and WT are similar. Mutant H64L responds markedly different to extended exposure to light. The dominant peak of photolyzed CO remains at 2126 cm^{-1}; only a small fraction of ligands contributes to the band at 2133 cm^{-1}.

Mutations at Residue 68

In Fig. 3.12, we present the FTIR photoproduct spectra of V68S, V68F, V68W and WT for comparison. After extended illumination, V68S, like WT, displays a pronounced peak at ~2133 cm^{-1} that was not present after short illumination. For V68F and V68W, however, we note the typical peaks assigned to B_0, B_1 and B_2. However, the peak for B_1 at ~2138 cm^{-1} has lost intensity. Instead, a new band of low intensity at 2130 cm^{-1} has emerged that is slightly more pronounced in V68F than in V68W.

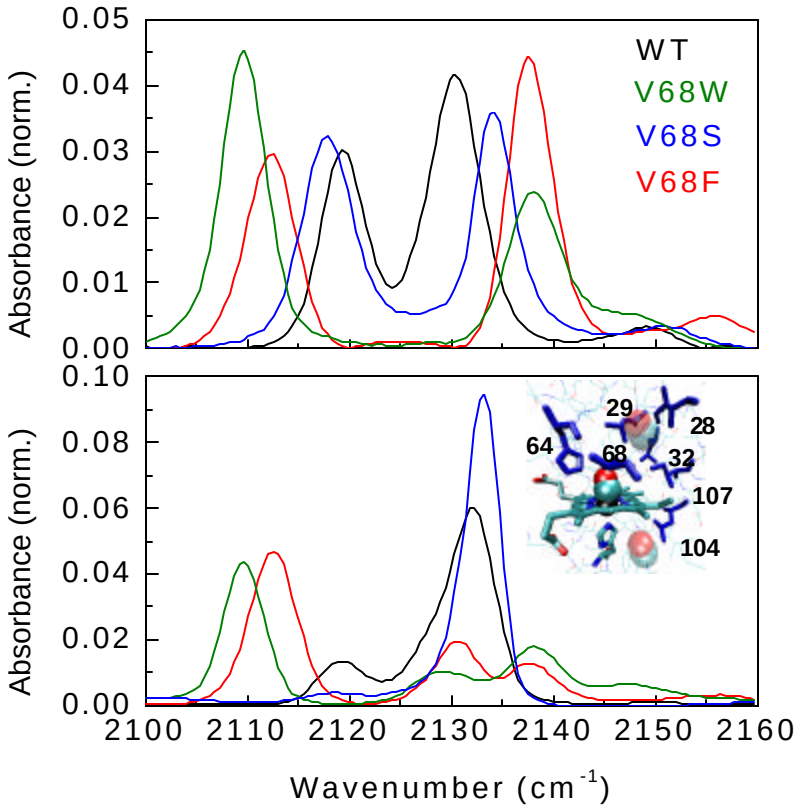

Fig. 3.12: FTIR spectra of WT MbCO and mutants V68S, V68F and V68W in the spectral region of photodissociated CO; upper panel: after illumination for 1 s at 3 K; lower panel: after slow-cool from 160 to 3 K under illumination; inset: sketch of the active site.

Double Mutant H64V/V68S

We compare the photoproduct spectra of mutants H64V, H64V/V68S and V68S to WT in Fig. 3.13. Whereas the CO stretch frequencies of the photoproduct bands after 1 s illumination differ markedly, all mutants display a similar photoproduct spectrum with a dominant band at ~ 2133 cm^{-1} subsequent to extended illumination.

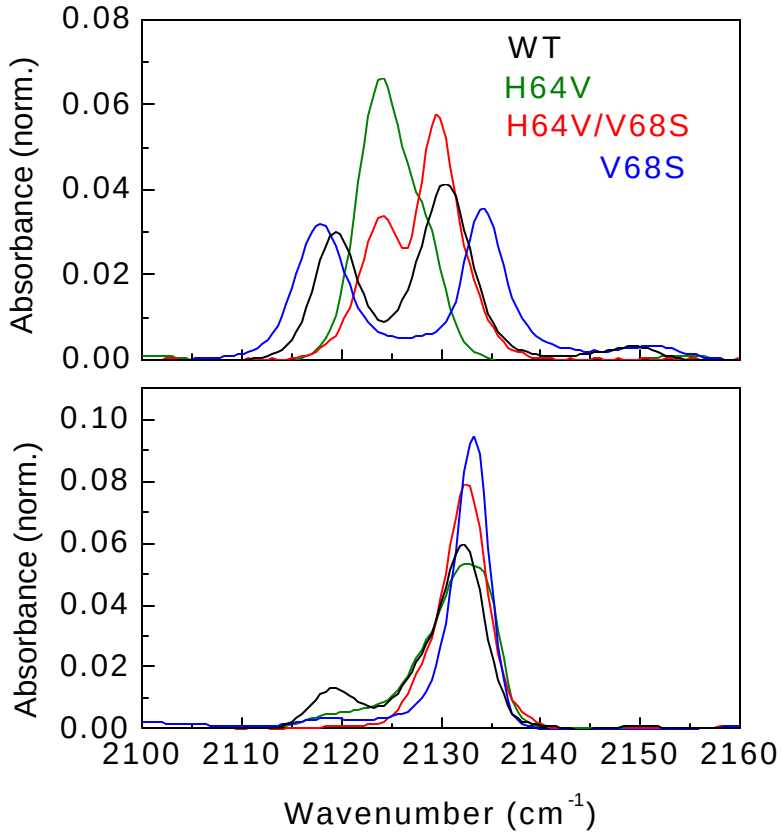

Fig. 3.13: FTIR spectra of WT MbCO and mutants H64V, H64V/V68S and V68S in the spectral region of photodissociated CO; top panel: after illumination for 1 s at 3 K; lower panel: after slow cooling from 160 to 3 K under illumination.

Mutants I28F, I28W and L32H

The photoproducts of mutants I28F, I28W and L32H after 1 s illumination have CO stretch bands almost identical to WT (Fig. 3.14). After extended exposure to light, the FTIR absorbance difference spectrum of L32H resembles the one of WT. Mutant myoglobins I28F and I28W, both having a bulky aromatic sidechain at position 28, respond differently, however. While the bands B_2 at ~2119 cm^{-1} and B_1 at ~2130 cm^{-1} are still pronounced, a shoulder has emerged on B_1 at ~2133 cm^{-1}.

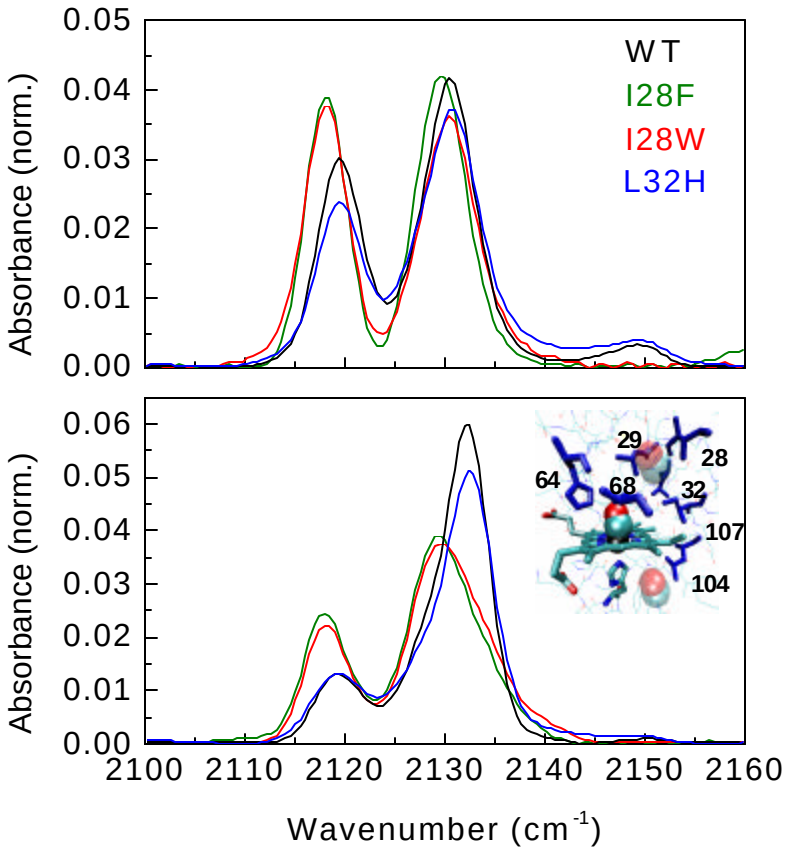

Fig. 3.14: FTIR absorbance spectra of WT MbCO and mutants I28F, I28W and L32H in the spectral region of photodissociated CO; top panel: after illumination for 1 s at 3 K; lower panel: after slow-cool from 160 to 3 K under illumination; inset: sketch of the active site.

Mutants L104W and I017W

Fig. 3.15 presents the photoproduct spectra of I107W, L104W and WT. The three proteins show rather similar photoproduct spectra after extended illumination, all having the dominant band at ~2133 cm^{-1}. For WT and L104W, there is a residual population of B_2 at 2119 cm^{-1}. The spectrum of I107W is very broad and, except for the band at ~2133 cm^{-1}, rather featureless.

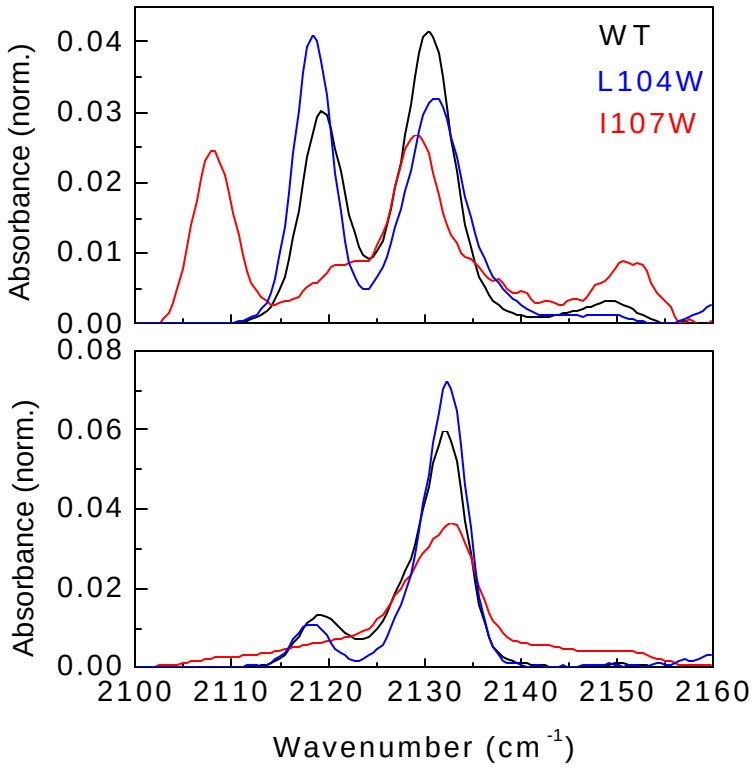

Fig. 3.15: FTIR spectra of the photoproducts of WT MbCO and mutants I107W and L104W; top panel: after illumination for 1 s at 3 K; lower panel: after slow-cool from 160 to 3 K under illumination.

3.1.2.2 TDS after Slow Cooling from 160 to 3 K

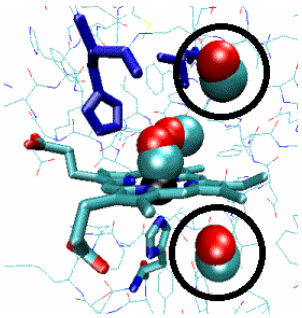

The FTIR absorbance difference spectra measured after extended illumination differ markedly from those after 1-s exposure at 3 K. This suggests that photolyzed ligands get trapped at intermediate sites different from the initial docking site B. FTIR/TDS experiments were performed subsequent to slow cooling under illumination to observe ligand recombination as a function of temperature. The results will be presented below.

WT and Mutants I28W, L32H, L104W and I017W

Fig. 3.16 compiles the FTIR/TDS contour plots of six different mutant samples. For WT (Fig. 3.16 a), the map of heme-bound CO shows three subpopulations rebinding to A_1 around 50, 80 and 115 K. For A_3, two subpopulations with recombination maxima at 70 and 160 K can be discerned. The corresponding map of the photoproducts (Fig. 3.16 b) displays positive as well as negative contours. Below 25 K, an exchange from B_{2119}[2] to a doublet at 2131 and 2136 cm^{-1} occurs (dotted arrow). Rebinding from the dominant photoproduct band B_{2133} to A_1 extends from 30 to 140 K, with no distinct change in peak position up to 100 K. Afterwards,

[2] In combination with the wavenumber as index, the letter B indicates a photoproduct band in general and is not confined to the initial docking site B.

the position shifts to slightly lower wavenumbers. An absorbance change in the stretch band B_{2119} can be observed over almost the entire temperature range. Return to A_3 from B_{2149} is visible around 80 K. No photoproduct bands can be resolved for rebinding to substate A_3 at 160 K.

Fig. 3.16 c, d displays the TDS maps of WT equilibrated with 1 atmosphere of xenon at 0°C, denoted WT(Xe). The equilibration with xenon was intended to at least partially prevent access to one or more of the four xenon cavities by the CO ligands. In the A state map, we observe almost identical features as with WT, except for a significant decrease of the subpopulation rebinding to substate A_1 at 115 K and a marked decrease of the population rebinding to A_3 at 160 K (Fig. 3.16 c). The map of the photoproducts (Fig. 3.16 d) is almost identical to that of WT; the extensive recombination features in B_{2119}, however, are not discernible.

In L104W, two subpopulations rebind to A_1, peaking at 40 K and 70 K (Fig. 3.16 e). Rebinding to A_3 occurs around 65 K. The photoproduct map (Fig. 3.16 f) looks very similar to the one for WT. Exchange at low temperatures occurs from B_{2119} to B_{2131} and B_{2136}. We notice extended recombination from B_{2133} to A_1 over a large temperature range and a small population of B_{2149} recombining to A_3. The stretched feature in B_{2119} mentioned earlier for WT (panel b) is missing.

The contour plots of mutant I107W (Fig. 3.16 g, h) exhibit major differences. The TDS map of heme-bound CO shows only a single well-resolved population rebinding to A_1 around 40 K. At higher temperatures, the contours display a featureless tail. The fraction of A_3, which is much larger than for the other proteins, rebinds around 60 and 160 K. The photoproduct map (Fig. 3.16 h) displays a minor exchange from B_{2108} to B_{2144} at 15 K. Recombination is seen from B_{2131} between 30 and 60 K. Moreover, at 70 K, we observe a clear shift of the photoproduct bands to 2134 cm^{-1}. A second change is noticeable at 120 K. The band at 2134 cm^{-1} narrows considerably, and the shoulder at 2131 cm^{-1} disappears.

In the TDS maps of mutant I28W (Fig. 3.16 i, j), two subpopulations recombine to A_1 at 40 and 120 K. Rebinding to A_3 occurs at 60 and, although not visible in the TDS map (panel i), also at 160 K. The contour plot of photolyzed CO (panel j) resembles that of WT. The contour plots of L32H (panel k, l) are very similar those of WT, except for the additional A_x band at 1970 cm^{-1}.

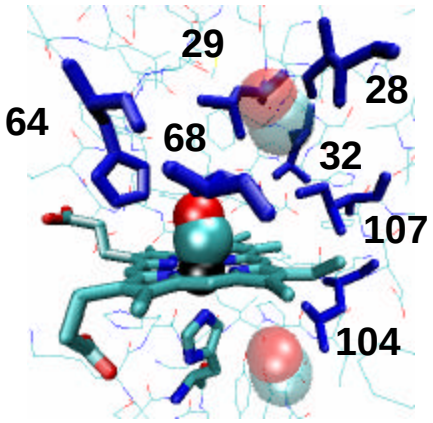

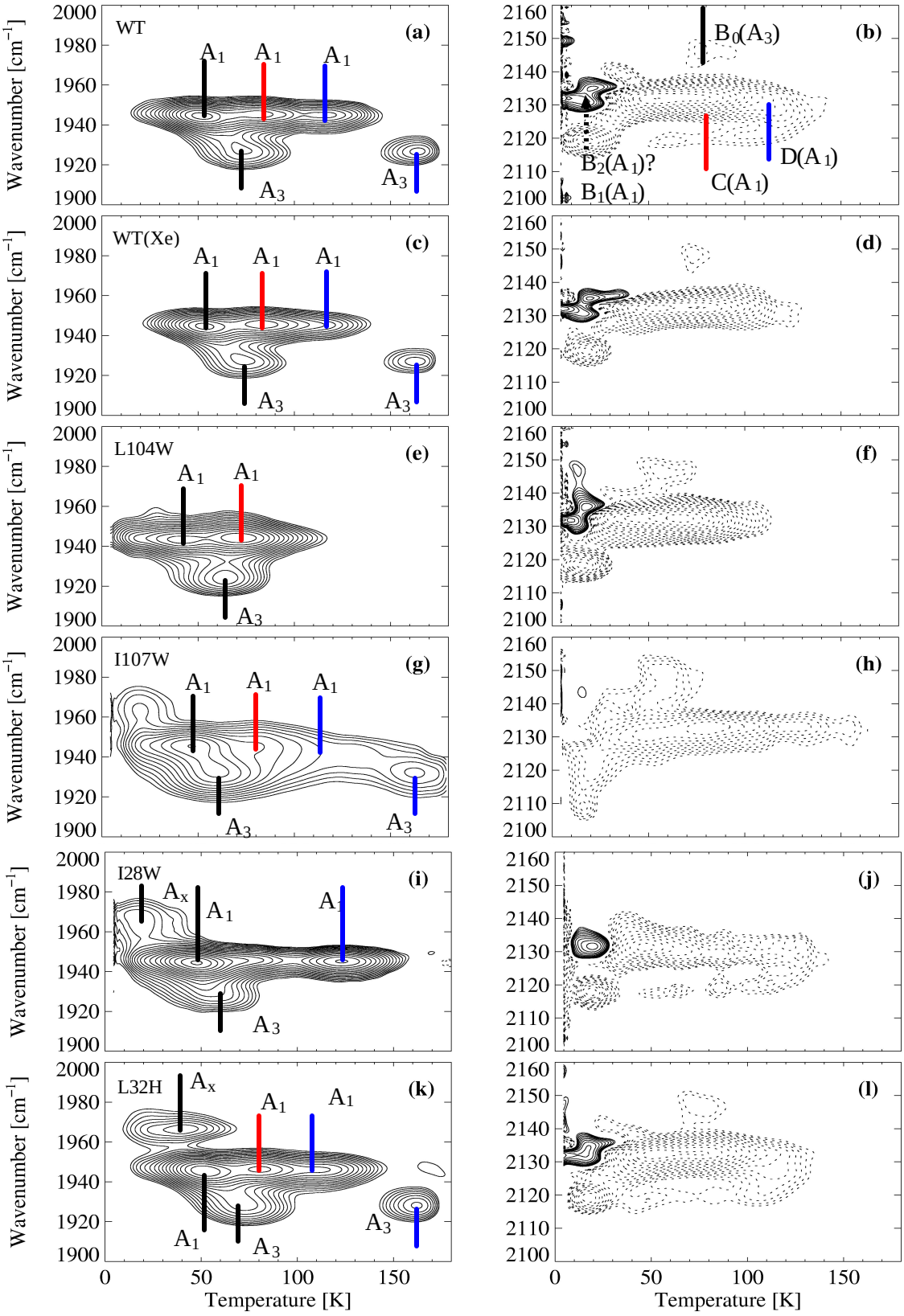

Fig. 3.16: TDS contour maps of WT MbCO (pH 7), WT(Xe) and related mutants L104W, I107W, I28W and L32H after slow cooling from 160 to 3 K.

Mutations at Residue 64

To investigate the effects of extended illumination on taxonomic substate A_0, samples H64L and H64V were cooled from 160 to 3 K under constant illumination. For H64L, the TDS maps (Fig. 3.17 a, c) show recombination to A_0 from photoproducts bands at 2125 cm^{-1} and 2133 cm^{-1} at 40 and 70 K. In contrast, the extended tail in the A state map of H64V (Fig. 3.17 b) suggests a third photodissociated subpopulation. We observe recombination from B_{2126} at 30 K, B_{2133} at 80 K and B_{2130} at 120 K. Note that the contour plot of the photoproducts is very similar to the one of WT above 30 K (Fig. 3.16 b). The photoproduct maps of H64L and H64V both depict a multiplicity of similar exchange signals below 25 K.

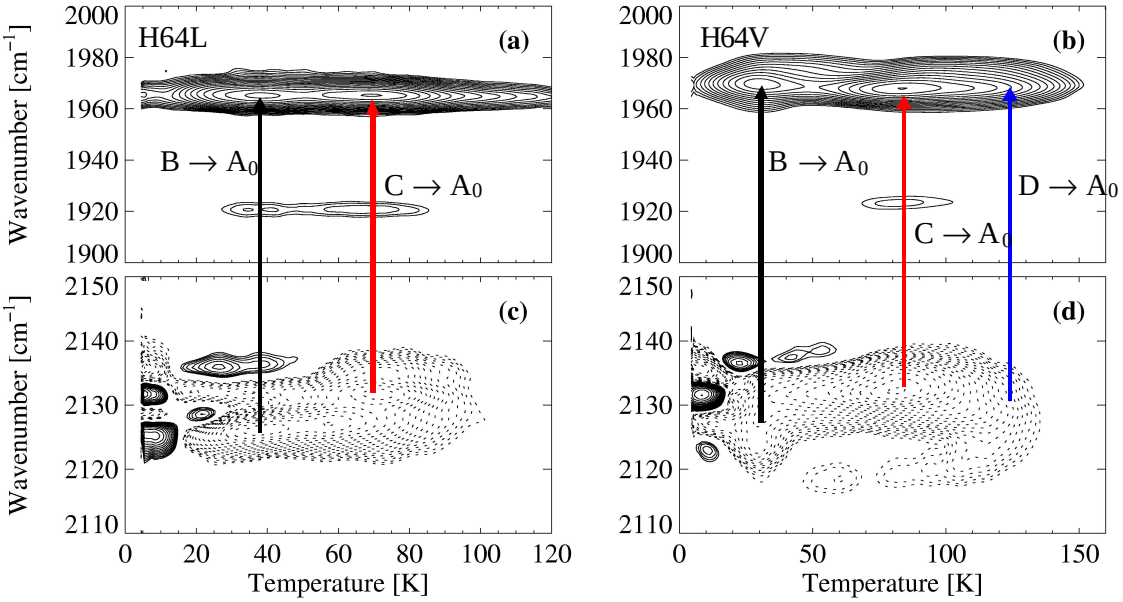

Fig. 3.17: TDS contour maps of mutants H64L and H64V after slow cooling from 160 to 3 K.

Mutations at Residue 68

TDS contour maps of all V68 mutants in Fig. 3.18 depict recombination to substates A_1 and A_3 at ~40 K and ~60 K. Additional, much less pronounced recombination to A_1 is apparent as a long tail up to 130 K. For V68S, this tail does not exhibit any structure, whereas a shoulder at ~80 K is apparent for V68F. In V68W, a second population rebinding at 90 K is clearly separated from the peak at 40 K (panel e). Furthermore, ligands in V68S and, less distinctly, in V68F recombine to substate A_3 at 160 K. In V68W, this subpopulation is missing. The contour maps of the photoproducts (panels in the right column) emphasize the different response to extended illumination. V68S displays a markedly different TDS map (panel b) compared to the one after short illumination (Fig. 3.7). For instance, the extensive exchange feature at 15 K has almost disappeared, and recombination from the band at 2133 cm^{-1} is stretched up to 100 K. In contrast, V68F/W exhibit identical contours compared to short illumination with an additional peak at ~2130 cm^{-1} (panels d, f) related to photoproducts at more remote sites (compare Fig. 3.7).

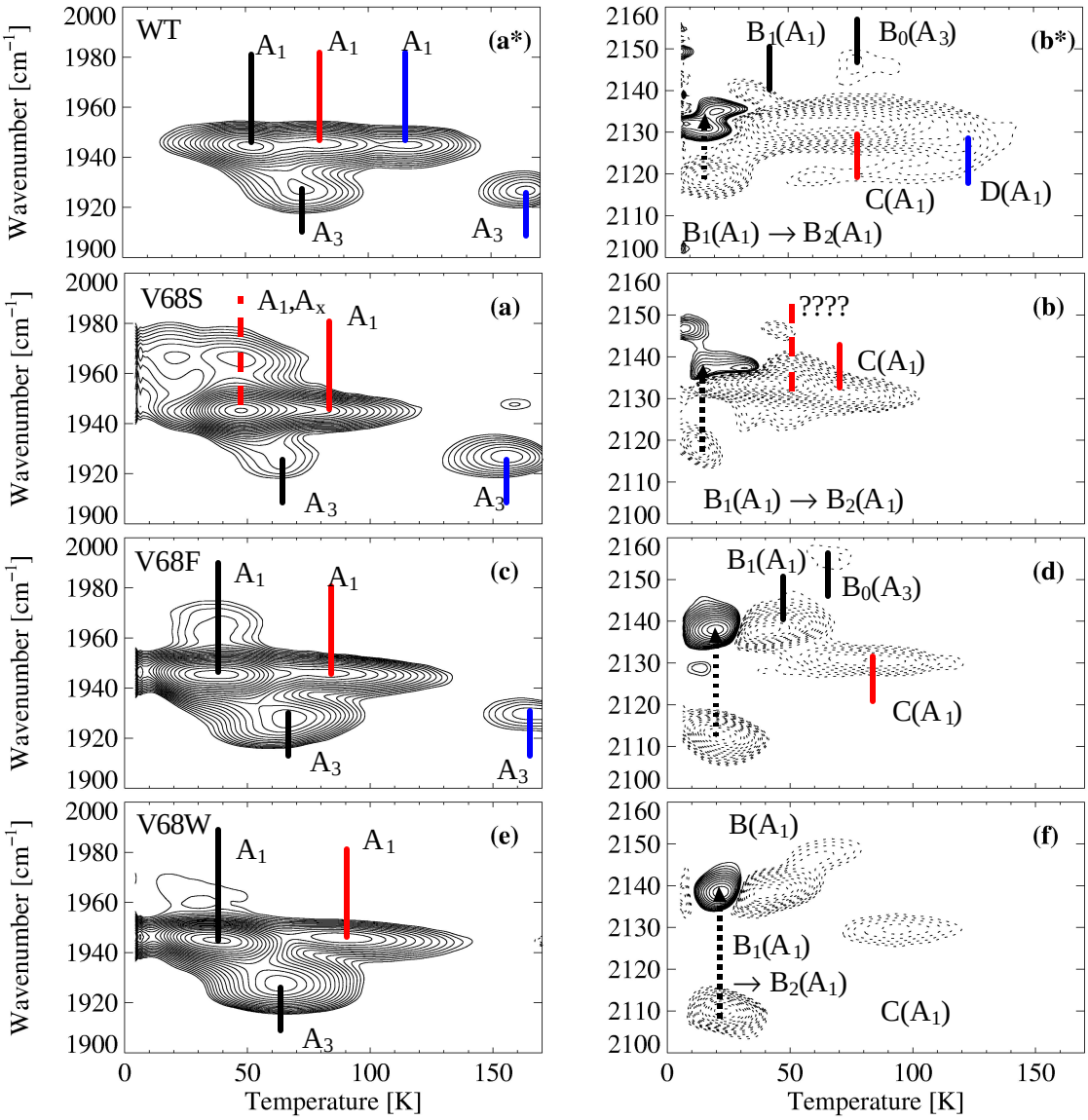

Fig. 3.18: TDS contour maps for WT (pH 7) MbCO and mutants V68S, V68F and V68W after slow-cooling from 160 to 3 K.

Double Mutant H64V/V68S

In Fig. 3.19, we compare the TDS maps of H64V/V68S, V68S and H64V. Subsequent to extended illumination, the A state map of H64V/V68S depicts recombination to substate A_0 at ~40 K extending up to 140 K, a feature similar to recombination to A_1 in V68S (panels a, c). The photoproduct map of the double mutant (panel d) appears as a combination of the maps of V68S and H64V. Below 20 K, the exchange features are comparable to those of H64V. Above ~40 K, V68S and double mutant H64V/V68S both show recombination from a band at ~ 2133 cm^{-1}.

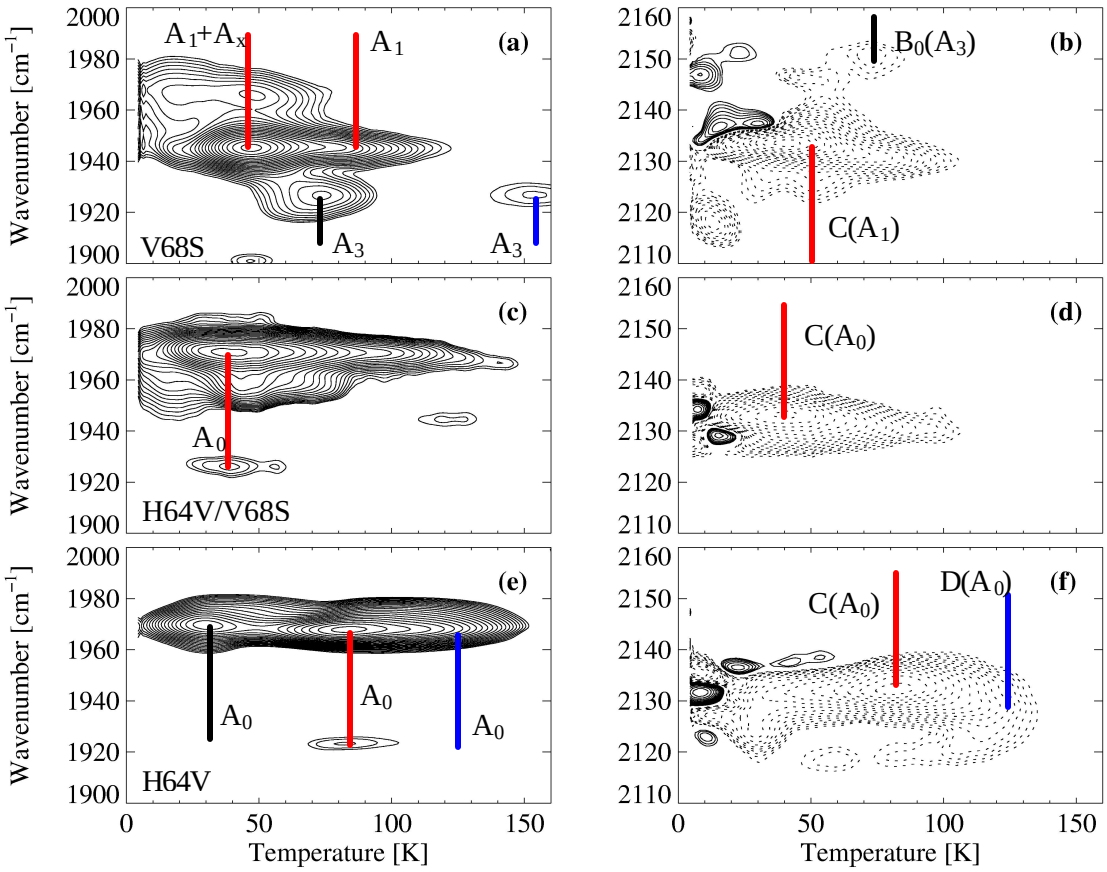

Fig. 3.19: TDS contour maps of MbCO mutants V68S, H64V/V68S and H64V after slow cooling from 160 to 3 K.

3.1.2.3. Interpretation and Discussion: TDS after Slow Cooling from 160 to 3 K

Assignment of Spectral Features to Structural Properties

The phenomenon that extended illumination enables ligands to sample longer-lived states at cryogenic temperatures was observed by Powers *et al.* (109) in 1987 and carefully investigated by Nienhaus *et al.* in 1994 (47). At that time, the effect was explained by relaxation of the protein to a conformation with a higher barrier for rebinding, with the photolyzed ligand residing at site B. Whereas the initial experiments were done in glycerol/buffer cryo-solvents, discrete populations with higher rebinding temperatures were also reported for MbCO crystals in 1998 (57). In this work, clear shifts of the stretch bands of photodissociated CO between 100 and 130 K were noticed and explained by movements of the ligand in the heme pocket between discrete sites. Our results on WT and related mutants provide clear evidence that the CO ligands after photodissociation are not confined near the active site, but migrate to more remote cavities.

While conformation A_1 displays up to three recombining subpopulations, depending on the mutant, A_3 shows at most two. We propose that rebinding to A_1 occurs at 40 K from docking site B, at 70 K from the Xe 4 (site C) and at 110 K from the Xe 1 cavity (site D). Most likely, our assignment of the slow populations to rebinding from the Xe 4 and Xe 1 cavities is also valid for A_0 (47). Recombination to A_3 is suggested to occur from B (70 K) and from D/Xe 1

(160 K). To justify these assignments, we discuss the integrated absorbances of the FTIR/TDS derivative spectra of A_1, A_3 and A_0 as a function of temperature from 3 to 180 K.

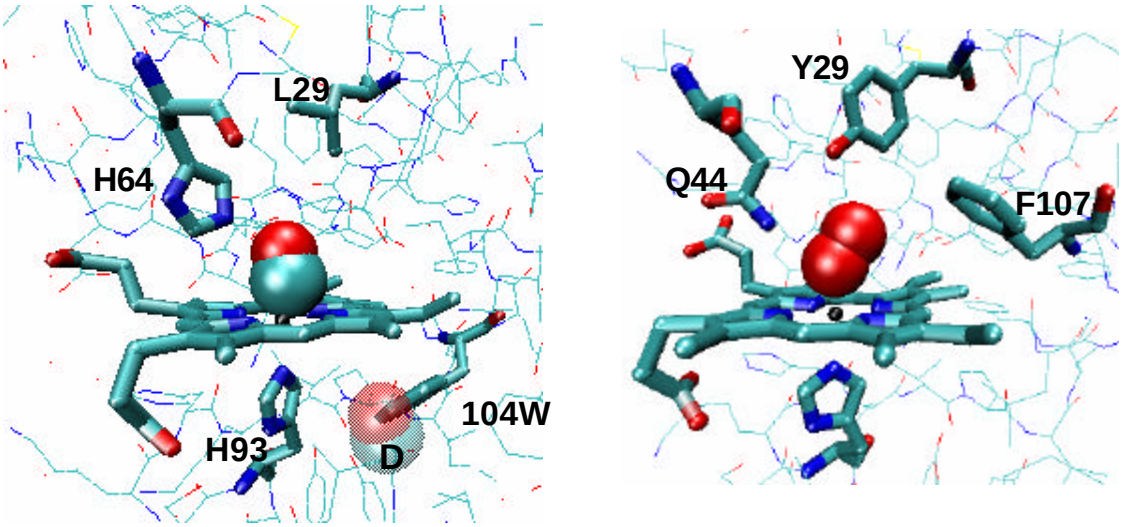

Fig. 3.20: Left: active site of mutant L104W MbCO (pdb code 1CPW); right: active site of mutant YQRF MbO_2.

In WT, four internal cavities are spacious enough to accommodate a photolyzed ligand. In the presence of xenon, however, photodissociated ligands and xenon atoms will compete for these volumes, and fewer CO ligands can migrate to the secondary docking sites. The effect should be especially pronounced for the Xe 1 cavity because it has the highest affinity for xenon atoms (27). Fig. 3.20 (left) shows that, in mutant L104W, the Xe 1 cavity is blocked by the W104 indole sidechain in all three A substates (106). Consequently, we expect not to find any ligands at site D in this mutant.

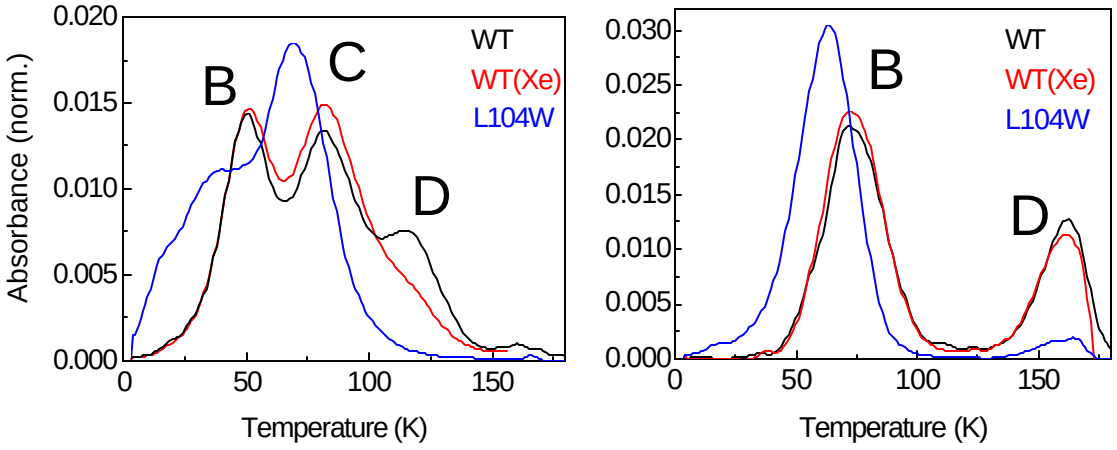

Fig. 3.21: Integrated absorbance differences $\int \Delta A\,d\nu$ calculated from the TDS experiments in Fig. 3.16 of WT, WT(Xe) and L104W as a function of temperature; left panel: A_1; right panel A_3.

In Fig. 3.21, we compare the absorbance changes with temperature, integrated along the wavenumber axis, for WT, WT(Xe) and L104 calculated from the TDS maps in Fig. 3.16. WT shows three subpopulations along the temperature axis, with their relative populations decreasing with temperature. In WT(Xe), the populations rebinding to A_1 at 120 K and A_3 at 160 K are markedly suppressed. In L104W, the populations at 120 K (for A_1) and at 160 K

(for A_3) have disappeared. These observations give clear evidence that these two populations should be assigned to CO ligands recombining from the Xe 1 site.

In Fig. 3.22, we have plotted the integrated absorbance changes of mutants L32H, I107W, I28F, I28W and WT as a function of temperature. For mutant I107W, the populations recombining from C and D to the A_1 substate are much smaller than in WT. Especially rebinding from D is more broadly distributed along the temperature axis. For substate A_3, the population recombining from site D has dropped. The TDS data indicate that the large W107 indole sidechain hinders a fraction of CO ligands from migrating towards the more remote sites. It is interesting to relate these observations to data on quadruple mutant YQRF (L29Y/H64Q/T67R/I107F), which possesses a phenylalanine at position 107. The structure of YQRF MbO_2 is also shown in Fig. 3.20 (right). FTIR-TDS experiments were performed on YQRF and YQR MbCO, and the comparison revealed that ligand escape to Xe 4 is markedly hindered by the voluminous sidechain of residue 107 (110). Furthermore, molecular dynamics simulations by Elber and Karplus suggested that residue 107 is situated along the passageway to site Xe 2 and, among other residues, gates the access (79).

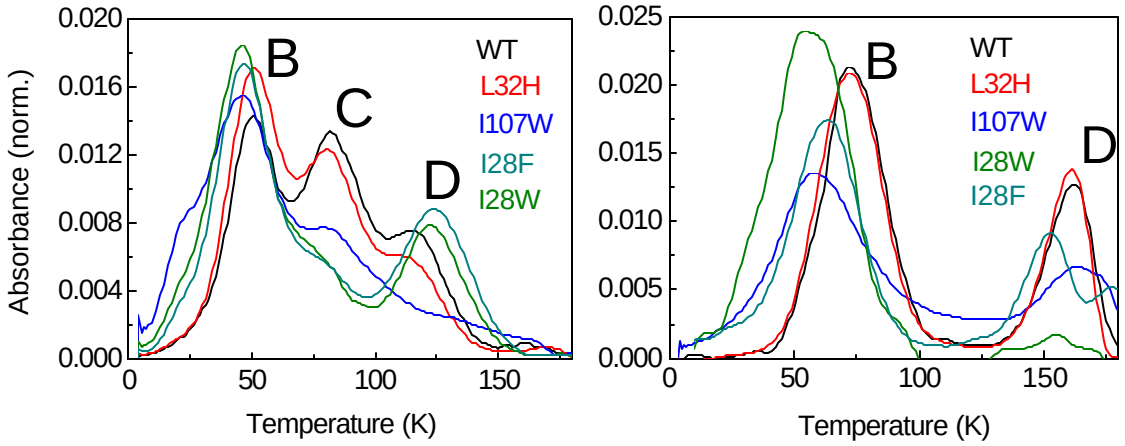

Fig. 3.22: Integrated absorbance differences $\int \Delta A\,dv$ calculated from the TDS experiments in Fig. 3.16 of WT, L32H, I107W, I28F and I28W as a function of temperature; left panel: A_1; right panel A_3. The TDS plots of I28F are not shown.

Mutant L32H exhibits a similar occupancy of internal sites after extended illumination as WT. It seems somewhat surprising that the replacement of the apolar leucine by the bulky, more polar histidine does not affect the affinity of the Xe 4 pocket for photodissociated ligands. Perhaps, this mutation is not the local modification that we aim for, but rather a larger structural adjustment, which will be studied by x-ray structure analysis in the future. This hypothesis is supported by the marked change of the isoelectric point after the point mutation. The effect of extended illumination is quite different when we place large aromatic residues into the back of the distal pocket. Mutants I28F and I28W both display a drastically lower occupancy of site C, further supporting the assignment of site C to Xe 4. However, a rather large fraction of CO ligands is recovered at site D in these mutants, from where recombination occurs at slightly higher temperatures than in WT. Apparently, a high yield of CO in the proximal cavity D is not correlated with a high yield of CO in site C. While it is tempting to suggest from this observation that ligand migration away from B to the proximal cavity does not necessarily occur sequentially via site C, such a statement should be carefully examined by quantitative modelling.

The FTIR spectra in Fig. 3.12 show a markedly different effect of extended illumination for V68S and V68F/W. We superimpose the structures of the active sites of WT and V68F in the left panel of Fig. 3.23, including the CO ligand at sites B and C. In WT, residue V68 points directly toward the initial docking site. By contrast, the aromatic sidechain of V68F lines the wall of the distal pocket and thus, despite of its large size, allows for unhindered migration to site B. In the right panel, we compare the structures of V68F MbCO (gray) and deoxy V68F (red). Upon photolysis at room temperature, the benzyl sidechain rotates toward docking site C, and H64 swings deeper into the distal pocket. Thus, the Xe 4 cavity becomes effectively smaller. Moreover, residue 68 is supposed to gate ligand access to more remote sites Xe 2 and Xe 1 (79). Consequently, we expect a low occupancy of intermediates C and D for V68F and V68W. As serine 68 is even smaller than valine, all internal cavities should be more easily accessible.

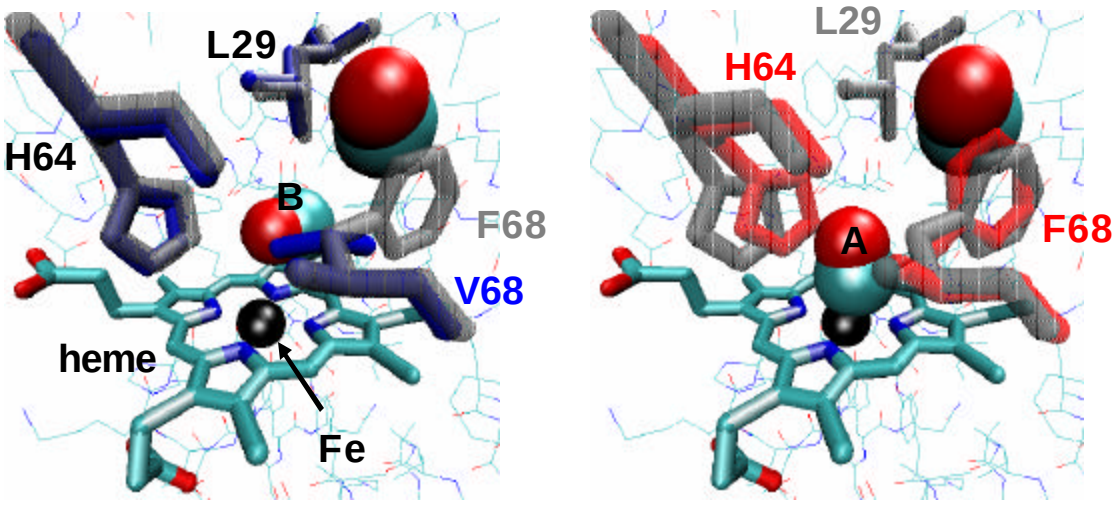

Fig. 3.23: Left Panel: superposition of WT (pdb code 1ABS) depicted in blue and V68F MbCO (pdb code 1MJL) depicted in gray; right panel: superposition of V68F deoxy (pdb code 1MKL) depicted in red and V68F MbCO (pdb code 1MJL) depicted in gray.

We compare the integrated absorbances of mutants V68S, V68F and V68W in Fig. 3.24. V68F and V68W rebind most of their ligands from site B at ~40 K. The very large subpopulation recombining at ~50 K to V68S comes as a surprise. It appears as if most ligands still reside at the initial docking site B. The subpopulation in D(A_3), however, is even larger than the one in B(A_3), indicative of unhindered migration away from site B. We have included the integrated absorbance after 1-s illumination at 3 K to demonstrate that the subpopulation rebinding at ~50 K does not originate from site B, but rather from site C. The concomitant shift of the IR bands of photolyzed CO supports this model. The minor subpopulation recombining in V68F and V68W at ~70 K shows an IR band at ~2130 cm^{-1}. In these two mutants, only few ligands escape from the initial docking site B. Based on the TDS maps in Fig. 3.18, we expect most of the CO in the back of the distal pocket, and a minor fraction on the proximal side of the heme plane.

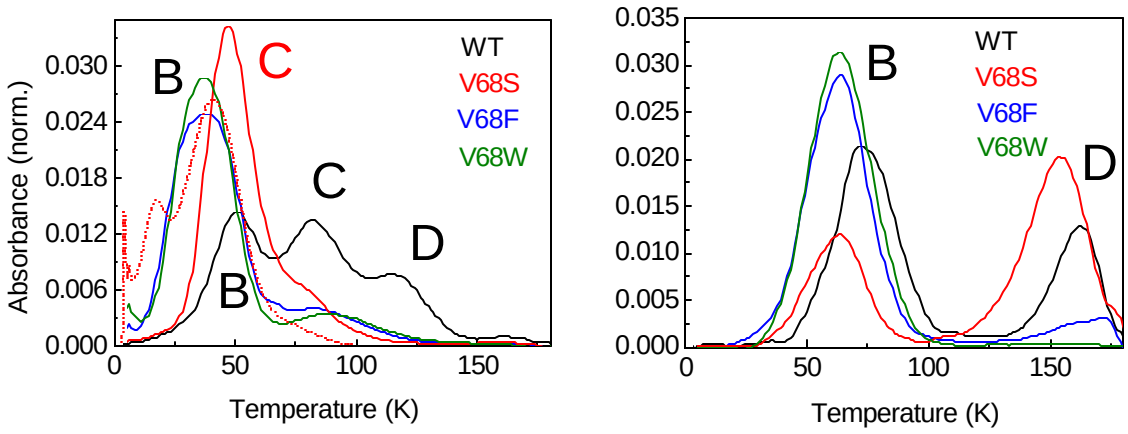

Fig. 3.24: Integrated absorbance differences $\int \Delta A\,d\nu$ calculated from the TDS experiments in Figs. 3.16, 3.18 of WT, V68S, V68F and V68W as a function of temperature; left panel: A_1; right panel A_3.

FTIR spectra at 3 K as well as TDS maps of H64L and H64V have indicated several intermediate sites. Although both mutants have an aliphatic residue at position 64, they exhibit markedly different ligand recombination, with H64L displaying two intermediate populations that recombine at 40 and 70 K, and H64V three populations rebinding at 30, 90 and 110 K (Fig. 3.25). We again can assign these features to recombination from intermediates B, C and D. The temperature of maximal recombination from site B increases in the order H64V < H64L < WT. This is explained by an increase in steric hindrance at the binding site from the sidechains of valine over leucine to histidine. Moreover, we emphasize that WT and H64V have similar temperatures of rebinding from C and D, implying that it is not the enthalpy barrier at the active site that governs recombination from these more remote sites, but barriers along the migration pathway towards the heme iron. In H64L, the population returning from site D at ~120 K is missing; ligands cannot be trapped in the Xe 1 cavity. In support of this finding, a recent study by Dantsker *et al.* (111) also showed less photodissociated CO in the Xe sites in H64L than in WT. Lambright *et al.* performed flash photolysis on H64 mutants and observed two geminate recombination steps in H64L which

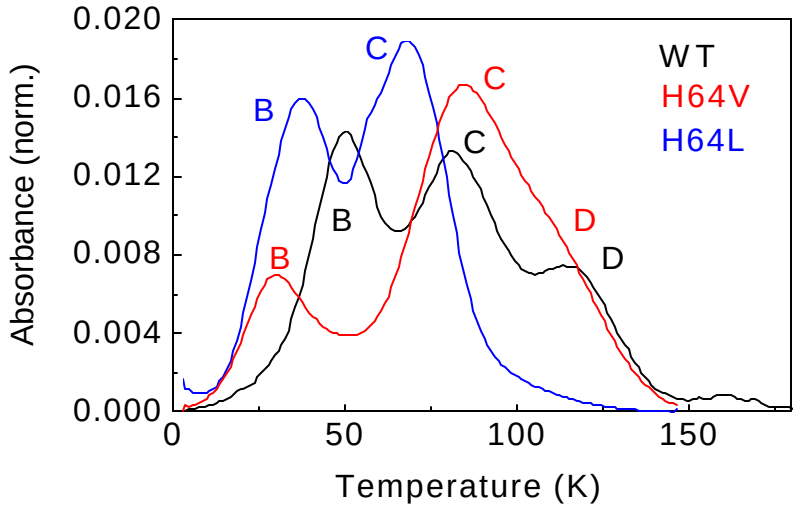

Fig. 3.25: Integrated absorbance differences $\int \Delta A\,d\nu$ calculated from the TDS experiments in Figs. 3.17 of WT MbCO and mutants H64L and H64V as a function of temperature.

they interpreted in terms of discrete kinetic intermediates (112). We associate these steps to recombination from B and C. Subsequent to photolysis at temperatures above 100 K, CO ligands are initially trapped at site B, from where they can migrate to site C by thermal activation. The low temperature of peak C in H64L as compared with H64V and WT gives evidence of smaller barriers to rebinding. Return to the active site is much more probable than escape to site D, and therefore, migration to site D is strongly suppressed in H64L.

In Fig. 3.26, the integrated absorbances of H64V, H64V/V68S, V68S and WT are compared. We have already argued that the dominant population recombines from site C in V68S despite the low recombination temperature of ~50 K. By analogy, we suggest that rebinding to H64V/V68S at ~40 K also occurs from the Xe 4 cavity. For comparison, we have added the integrated absorbance of H64V/V68S after illumination for 1 s at 3 K. We note that rebinding starts at the lowest temperatures and is complete at ~60 K. Only a minor fraction of photodissociated ligands contributes to recombination from docking site B. It occurs at the same temperature (~30 K) as in H64V, evidencing the strong influence of residue 64 on the initial docking site B.

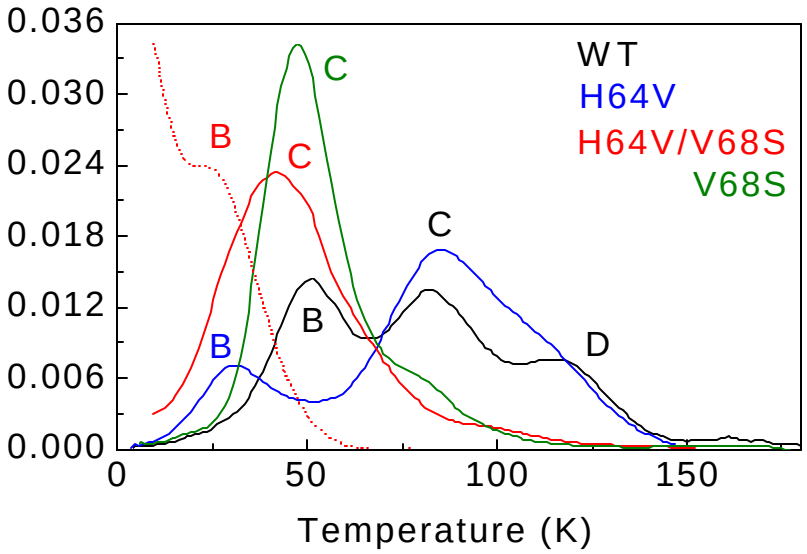

Fig. 3.26: Solid lines: integrated absorbance differences $\int \Delta A\,d\nu$ calculated from the TDS experiments in Figs. 3.19 of WT, H64V, H64V/V68S and V68S; dotted line: data after 1-s illumination of H64V/V68S.

Assignment of IR Bands to CO Ligands in Intermediates B, C and D

A detailed comparison of the A state maps of WT and related mutants has allowed us to relate individual photolyzed subpopulations observed in the FTIR/TDS experiments to intermediate states which have been associated with CO ligands sampling the hydrophobic cavities Xe 4 and Xe 1.

The CO stretch frequency is influenced by the local environment of the CO molecule, predominantly by the electric field (Stark effect). Therefore, each photoproduct is characterized by its individual FTIR spectrum. IR band positions of the individual photoproducts are, however, not easily extracted from the contour plots of the photoproducts. Fig. 3.16 b demonstrates this difficult task. The contours at ~2133 cm^{-1}, extending from ~30 to ~140 K, are assigned to absorbance changes arising from photolyzed CO ligands at three

different sites (B, C and D), which constitute chemically different environments. However, they apparently experience very similar local electric fields. They are surrounded by mainly aliphatic and apolar residues, histidines being the exception. Based on our results with V68W, V68F and I107W, we have experienced that aromatic sidechains, with their extended π-electron system, affect the CO stretch frequencies of the photoproducts markedly, whereas aliphatic sidechains do not have a significant effect. On the basis of these observations, it comes as no surprise that in earlier studies, Nienhaus *et al.* (47) interpreted their results on the influence of light on ligand recombination with relaxation of the protein, changing the barriers at the heme iron instead of movement of the CO among different intermediate docking sites. In Fig. 3.27, we have plotted the IR bands of the individual photoproducts, B, C, and D of WT MbCO. Substates A_1 and A_3 have two peaks for intermediate B, representing opposite orientations of the CO at the initial docking site. State C(A_1) displays only one band at 2130 cm^{-1} that is slightly shifted to lower wavenumbers as compared with B_{2131}. A small band at 2120 cm^{-1} may represent the opposite orientation. Since taxonomic substates A_1 and A_3 differ

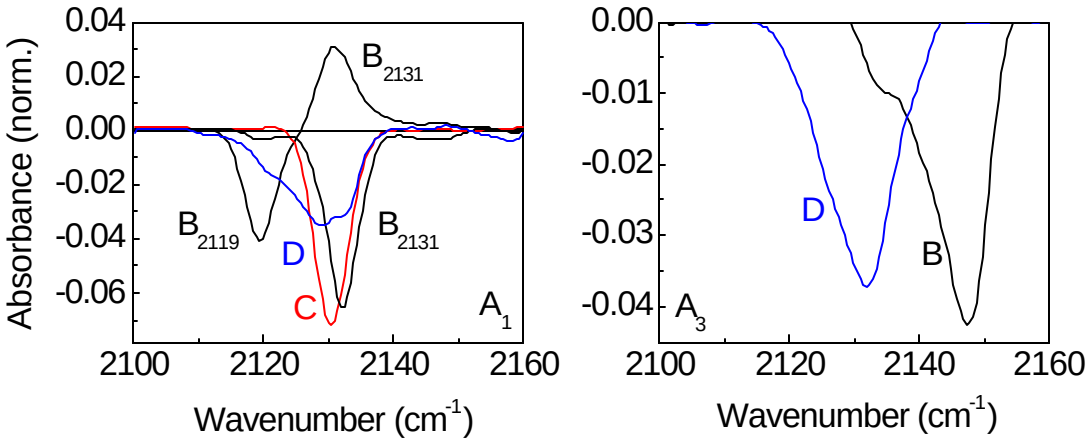

Fig. 3.27: FTIR absorbance bands for intermediates B, C and D of A_1 (left) and A_3 (right).

only in the exact position of the distal histidine, their spectra of D are expected to be identical. Ligands at site D give rise to a wide and not well-featured band centered around 2130 cm^{-1}. Only the doublet of peaks of site B can always be clearly defined. In their studies on myoglobin crystals in two space groups ($P2_1$ and P6), Nienhaus *et al.* (57) also reported very minor shifts of the photoproduct bands, occurring between 100 and 130 K, which is the temperature range of the transition from C to D. We note that an unambiguous assignment of specific bands to specific intermediate docking sites is a daring endeavor.

For WT MbCO and the mutants discussed so far, we have found very similar CO stretch bands for the remote cavities, instead of identifying each intermediate docking site by an individual spectral fingerprint. The situation is much more fortunate for mutants that carry an aromatic sidechain at residue 29, which produces substantial band shifts. In section 3.2, we will present data on mutant L29W. For that mutant, FTIR/TDS experiments have enabled us to isolate distinct photoproduct spectra characteristic of CO ligands at particular sites. As a matter of fact, many of the results discussed here became only clear after the analogous experiment with L29W MbCO.

FTIR Spectra of Photolyzed CO: Intrinsic Band Changes

A peculiar feature in the TDS maps of photodissociated CO attracted our attention. Contours of B_{2119} span a large temperature range, from ~50 to ~130 K in the photoproduct TDS maps of WT, I28W, L32H and H64V (Figs. 3.16 b, j, l, 3.17 d). We also noticed that the corresponding contours are missing in the TDS plots of L104W and WT(Xe). These observations suggest that B_{2119} is a CO band of intermediate $D(A_1)$. Consequently, we expect to monitor true recombination features only at temperatures around 120 K. TDS experiments with especially designed illumination protocols have proven that these contours between 50 and 120 K within the TDS maps do not reflect rebinding, but intrinsic, temperature-induced changes of an individual photoproduct band arising from the dynamics of the CO ligand in the cavity. A detailed examination of these effects is beyond the scope of this thesis. We will, however, present these experimental data in the appendix A.

3.1.3 Probing Intermediate States above the Dynamic Transition Temperature

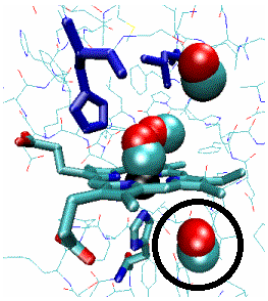

In the previous sections, we have investigated recombination within a frozen protein sample. We have observed CO ligands migrating to and rebinding from two of the four internal xenon cavities of Mb. The physiological binding process however, occurs in a fluctuating protein. Above ~180 K, large-scale protein motions are activated, and taxonomic substates can interconvert (68, 113). To gain insight into ligand migration and recombination in a fluctuating protein, MbCO samples were illuminated at 185 K for 2 hours and then slowly cooled to 160 K. For these experiments, we chose WT and preferentially those mutants where the original residue was replaced by tryptophan. Whereas we do not expect single tryptophan point mutations to influence the overall three-dimensional structure significantly, the bulky indole sidechain should markedly modify the ligand migration pathways within the protein.

3.1.3.1 FTIR Absorbance Difference Spectra at 160 K

Subsequent to illumination, a FTIR transmission spectrum was recorded at 160 K and referenced against a transmission spectrum taken at 160 K without prior illumination to obtain the FTIR absorbance difference spectrum.

WT and Mutants L104W and I107W

In Fig. 3.28, we have plotted the CO stretch spectra of WT, WT(Xe), L104W and I107W. WT shows the typical FTIR stretch bands of A_1 and A_3. The broad FTIR spectrum of the photoproducts can be fitted as a doublet with components peaking at 2128 and 2133 cm^{-1}. Although the overall photoproduct yield is low (~30%), we note that molecules of substate A_3 are over-represented in the photoproduct fraction as compared to after 1-s illumination at 3 K (Fig. 3.1). At 160 K, the ratio of the integrated absorbances of bound-state bands and photoproduct bands is about 30. At higher temperatures, this ratio increases to up to 50, indicative of CO ligands escaping into the solvent, where their spectrum is so broad that it cannot be detected. The presence of xenon does not change the spectral characteristics significantly. Mutant I107W exhibits photolysis mainly of A_3, and the corresponding photoproduct band is asymmetric with a maximum at ~2128 cm^{-1}. Mutant L104W shows hardly any signal, indicating that it is not possible to populate long-lived states at these temperatures.

FTIR Absorbance Difference Spectra at 160 K: WT versus I28W, L32H and V68W

We have displayed the FTIR absorbance difference spectra for I28W, L32H, V68W and WT in Fig. 3.29. For heme-bound CO, we observe a dominant peak for A_1 and a relatively large photolyzed fraction of A_3 for all mutants. The photoproduct spectra of WT and L32H are almost identical and consist of a doublet at 2128 and 2133 cm^{-1}. The spectra of I28W and I107W are very similar. For V68W, the two individual photoproduct peaks are explicitly resolved.

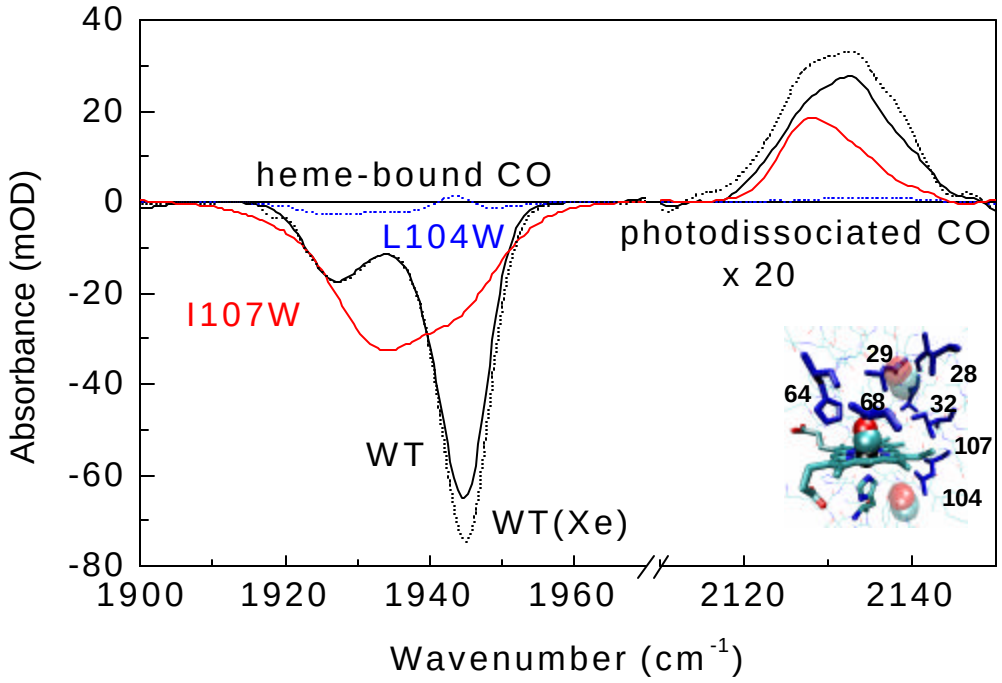

Fig. 3.28: FTIR spectra of WT MbCO, WT(Xe), L104W and I107W recorded at 160 K after illumination at 185 K for two hours and slow cooling to 160 K under light. Inset: active site structure showing important residues.

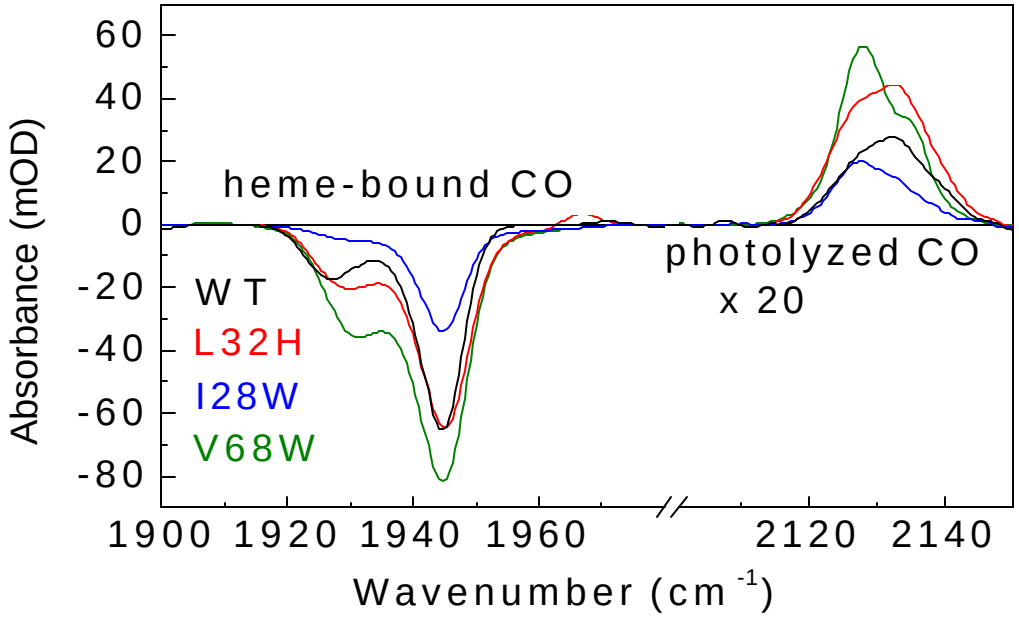

Fig. 3.29: FTIR spectra of WT MbCO and mutants L32H, I28W and V68W recorded at 160 K after illumination at 185 K for two hours and slow cooling to 160 K under light.

3.1.3.2. TDS after Illumination at 185 K and Slow Cooling to 160 K

To monitor recombination in a fluctuating protein, a TDS experiment was performed after the described illumination protocol.

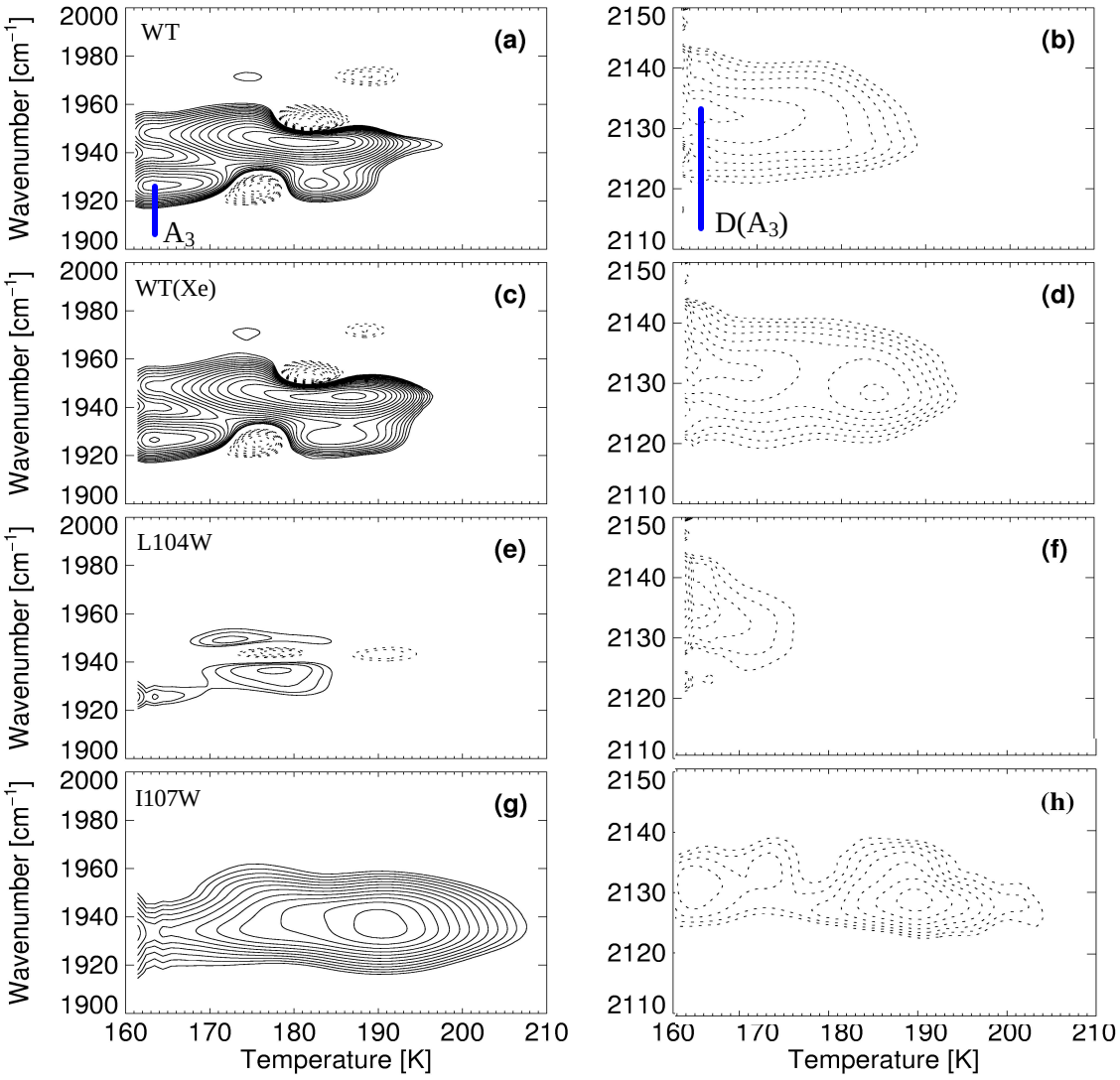

Fig. 3.30: TDS contour maps for WT MbCO, WT(Xe), L104W and I107W after illumination at 185 K for two hours and slow-cool to 160 K.

We have compiled the TDS contour maps of WT, WT(Xe), L104W and I107W in Fig. 3.30, and those of L32H, V68W and I28W in Fig 3.31. WT exhibits a rather peculiar behavior at high temperatures. The bound state contour map (Fig. 3.30 a) shows solid as well as dashed contours. At temperatures of 175 K, solid contours in A_1 and dashed contours in A_3 indicate an exchange between taxonomic substates. The second exchange feature is depicted at 185 K. The map of the photoproducts (panel b) shows a large and undefined contour of low intensity. The frequency of the broad band shifts from ~2132 cm^{-1} at 160 K to 2128 cm^{-1} at ~190 K.

The presence of xenon does not induce significant alterations (Fig. 3.30 c, d). The main difference is the less pronounced tail from A_1 rebinding at temperatures above 190 K. The very weak contours of L104W are considered as insignificant, they may arise from baseline and referencing errors. The A state contour map of I28W in Fig. 3.31 a shows a strong resemblance to the one of WT. The map of photolyzed CO (Fig. 3.31 b), however, depicts a distinct recombination signal at 190 K from bands at 2128 and 2133 cm^{-1}. The TDS contour plots of mutant L32H (Fig. 3.31 c, d) are interchangeable with the ones of WT. V68W resembles I107W (Fig. 3.30 g, h and Fig. 3.31 e, f), with distinct recombination features at temperatures of ~190 K not only in the bound state region, but also in the bands of photodissociated CO, with a dominant band at 2128 cm^{-1} and a minor band at 2135 cm^{-1}.

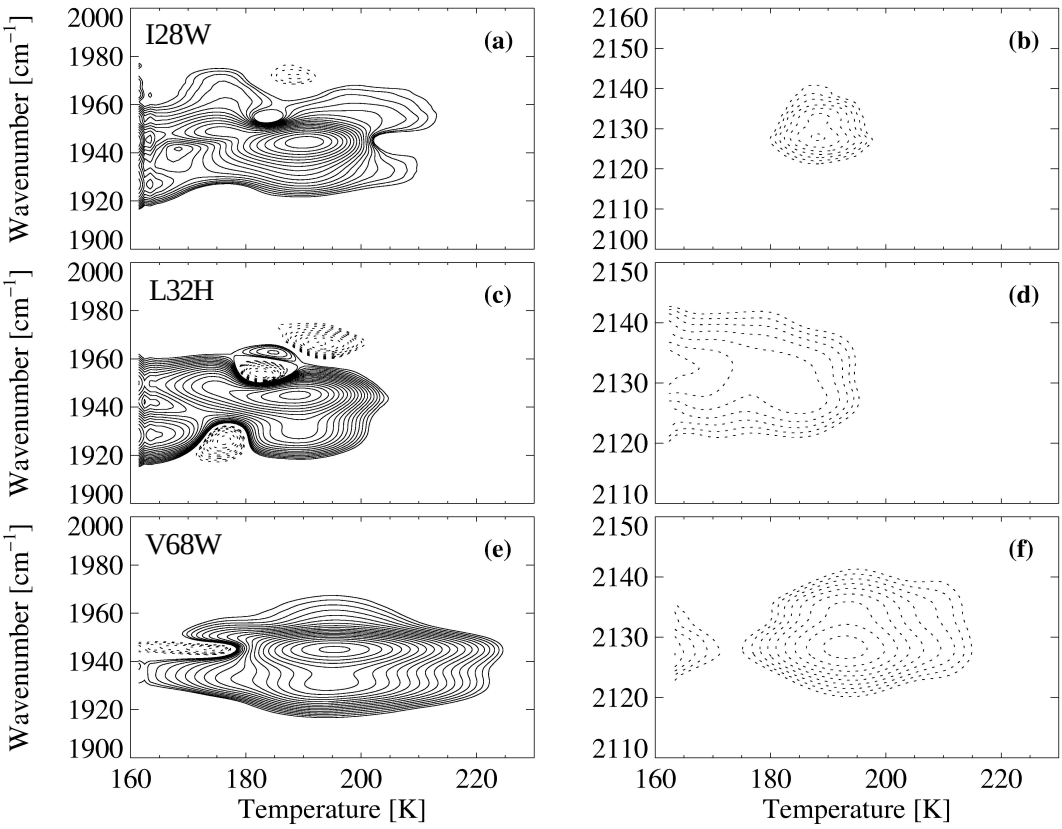

Fig. 3.31: TDS contour maps of MbCO mutants I28W, L32H and V68W after illumination at 185 K for two hours and slow cooling to 160 K.

3.1.3.3 Interpretation and Discussion: Intermediate States above the Dynamic Transition Temperature

FTIR Absorbance Difference Spectra at160 K

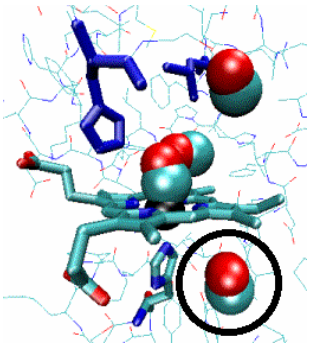

Around 160 K, less than 50% of all ligands are photolyzed from both taxonomic substates A_1 and A_3 by the described illumination protocol. To explain the large subfraction of A_3 within the photolyzed population, we refer to the TDS contour maps after slow cooling from 160 to 3 K (Fig. 3.16). They showed that recombination from intermediate D occurs at ~120 K to A_1 and at ~160 K to A_3. Thus, the illumination protocol employed here allows for efficient trapping of CO ligands at site D(A_3). In contrast, thermally activated recombination from site D(A_1) is much faster than the photolysis rate k_L.

The photoproduct bands of the various samples all show a set of two bands at 2128 and 2133 cm^{-1}. The intensity of these bands is low, as judged from the ratio of the integrated absorbances of heme-bound CO and photolyzed CO. This ratio, which is ~22 at 3 K, grows to 30 - 70 above 160 K for two reasons, which are both associated with line broadening effects: (i) the narrow CO bands lose area because of CO rattling around in the cavity, and (ii) only a fraction of the photodissociated ligands may remain within the protein, while significant part can escape into the polar solvent, which also leads to drastic line broadening, so that the CO signal can no longer be detected.

In mutant L104W, CO ligands can only sample the distal side of the protein, and recombination occurs at temperatures below 100 K in the TDS experiment. Consequently, we do not expect any absorbance signal from photolyzed CO ligands trapped within the protein at 160 K. The absence of absorbance signals in the spectral range of heme-bound CO indicates that ligands have not escaped into the solvent. This observation suggests that the long-lived state D assists ligand escape into the solvent, at least around 160 K.

TDS after Illumination at 185 K and Slow Cooling to 160 K

The A substate TDS map of WT MbCO in Fig. 3.30 a shows solid as well as dashed contours. Solid contours for A_3 located at ~165 K can be assigned to recombination of ligands from D(A_3), in agreement with the contour maps after slow-cooling from 160 to 3 K. From 175 to 185 K, we observe solid contours for A_1, while A_3 simultaneously displays dashed contours. This combination indicates an exchange of *bound* population from A_3 to A_1. At 175 K, molecules of the A_3 conformation are over-represented in the bound population because photodissociated ligands have recombined almost exclusively to A_3. Upon warming, as soon as large-scale protein motions become activated, the ensemble adjusts to the equilibrium composition. The top panel of Fig. 3.32 displays IR spectra before and after the exchange at 172 and 180 K. FTIR/TDS transmission data were referenced versus a transmission spectrum of a 'met' sample to obtain the true absorbance band of the heme-bound population.

The second exchange feature is located at 185 K. In the lower panel of Fig. 3.32, we compare the bound populations at 180 K and 187 K. We notice the development towards a narrower and more intense A_1-band, which is shifted to lower wavenumbers. In the temperature interval from 180 to 200 K, we still observe recombination contours. Rebinding to A_1 and A_3 is kinetically identical, indicative of a fast equilibrium between substates.

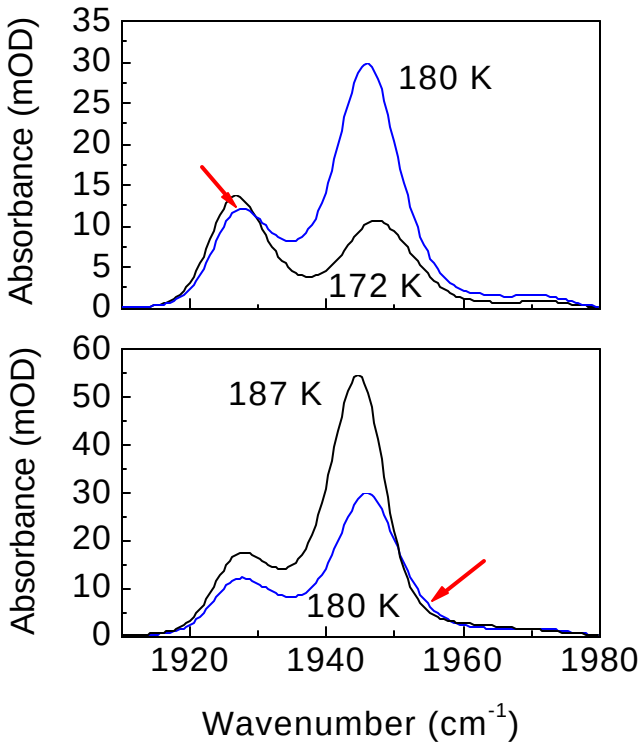

Fig. 3.32: FTIR absorbance difference spectra $-\log(I_{light}/I_{met})$ of WT at selected temperatures; spectra display the bound population at a given temperature.

In 1991, Srajer *et al.* (44) performed resonance Raman and absorption measurements to investigate laser-induced long-lived states of photolyzed WT MbCO in great detail. A multiple-state scenario was suggested to explain the generation of long-lived states below 180 K. Although structural evidence had been lacking, it was already proposed that the CO ligands became trapped in different cavities. After cooling the sample under laser light, an additional ultra-slow rebinding population was observed, which was assigned to CO molecules rebinding from the solvent. Around 185 K, it was impossible to discriminate between geminate recombination and recombination from the solvent. We encounter the same problem here. Recombination occurs at ~185 K from the solvent and from site D. This raises the interesting question why we observe rebinding from D at 120 K in the frozen protein and above 160 K in the fluctuating protein. Apparently, the lifetime of the photoproduct and thus the effective free energy for rebinding must have increased with the onset of protein motions. There are a number of reasons that explain this effect: As the protein fluctuates and relaxes towards the equilibrium deligated structure, (i) the iron may move slightly further out of the heme plane and (ii) the H64 rotates deeper into the heme pocket and occludes the active site, (iii) a water molecule may enter the distal pocket (73, 76, 99, 114), (iv) the heme group shifts with respect to the protein, and (v) fluctuations themselves can change the energetics of the passageways between the cavities.

Whereas the contour maps of WT(Xe) and mutants L32H and I28W display very similar contours, mutants V68W and I107W differ. Both show distinct recombination features at 190 K in A state and photoproduct bands. Based on molecular dynamics simulations, Elber and Karplus suggested residues 107 and 68 as gatekeepers for entering Xe 2 and subsequently moving on to Xe 1 (79). Large bulky sidechains at these two locations trap CO ligands more efficiently at site Xe 1. FTIR stretch bands at 2128 and 2135 cm^{-1} represent two distinct orientations within the docking site D.

3.2 Mutant L29W and Related Double Mutants

Compared with other Mb mutants, L29W stands out because of its extremely slow recombination kinetics at ambient temperatures (83). In recent years, we have employed flash photolysis of L29W MbCO in the IR bands of substates A_I and A_{II} over a wide temperature range (20 – 300 K) to investigate ligand binding in this mutant (115). It was found that the kinetic traces displayed a few temporally well separated steps. To understand the nature of these kinetic intermediates, the kinetic studies were complemented by X-ray crystallographic investigations of L29W crystals illuminated at temperatures where the populations of intermediates could be accumulated (15).

Fig. 3.33 compares the structures of WT MbCO (A_1) and L29W (A_I and A_{II}) at the active site. The structures of A_I and A_{II} of L29W MbCO can easily be determined, because A_I and A_{II} are majority populations at low (110 K) and high (300K) temperature. Except for the bulky indole sidechain, the structure of L29W substate A_I is in good agreement with WT in conformation A_1. In A_{II}, H64 has rotated deeper into the distal pocket, the tryptophan sidechain has rotated by 45° with respect to the A_I position and shifted closer towards the heme plane (90, 116). Upon photodissociation below 30 K, ligands migrate to site B (48). For L29W MbCO, it was shown that photolysis in the temperature range 110 - 180 K leads to CO migration to the Xe 4 cavity (site C) of an essentially immobilized, frozen protein. Upon photodissociation above 180 K, ligands escape from the distal pocket, aided by protein fluctuations that transiently open exit channels in the protein matrix. The majority of the ligands were recovered in the Xe 1 cavity (site D on the opposite side of the heme group).

Because of the excellent structural data available for L29W, we have performed detailed FTIR/TDS experiments on L29W and related double mutants to further study the dynamics of both protein and ligand. It became evident that L29W has a clear advantage in these experiments: The strong interaction between the W29 indole side chain and the CO produces large spectral changes which have aided us enormously in relating these changes to ligand migration and protein dynamics. As a matter of fact, the results with L29W were pivotal for the correct interpretation of the rather subtle effects observed with the WT protein.

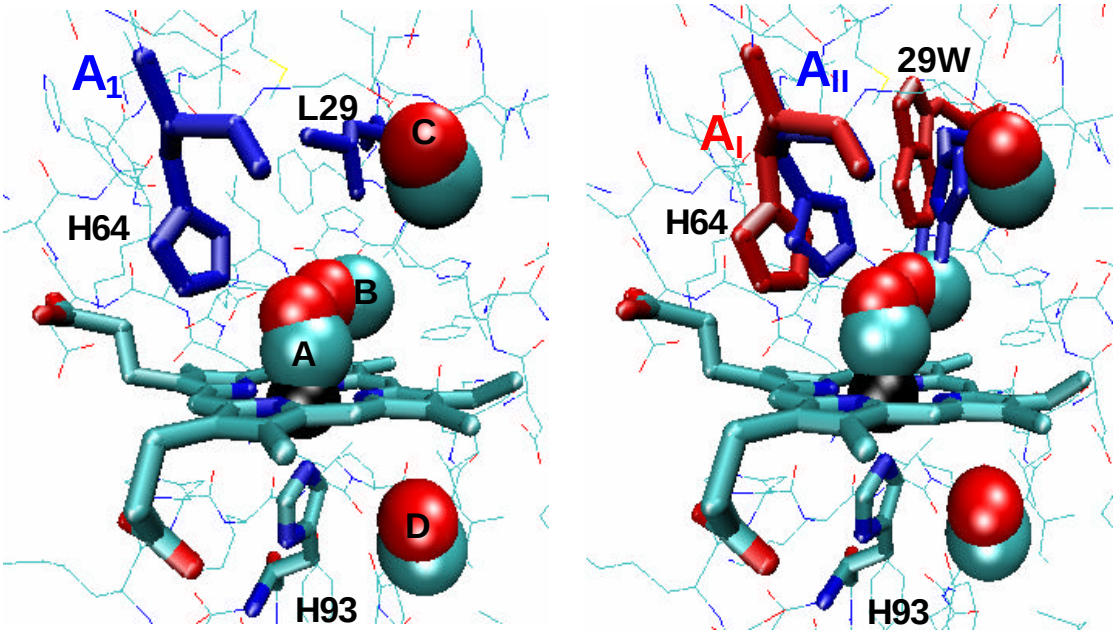

Fig. 3.33: Active site of sperm whale MbCO substate A_1 (left) and mutant L29W (right) substates A_I (red) and A_{II} (blue); the CO ligand is depicted in the bound state A and at intermediate locations B, C and D.

3.2.1 Probing Taxonomic Substates A_I and A_{II}

3.2.1.1. FTIR Absorbance Difference Spectra at 3 K

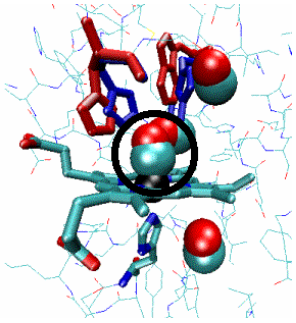

For L29W MbCO and a selection of double mutants, FTIR transmission spectra were collected at 3 K in the dark and referenced against a second FTIR transmission spectrum of a 'met' sample to obtain the CO stretch spectra of the overall population (Fig. 3.34). Two FTIR stretch bands of the bound CO, A_I at ~1945 cm^{-1} and A_{II} at ~1960 cm^{-1} are typical for these mutants. L29W/L72F, L29W/L104W and L29W display more or less equal amounts of both substates, whereas L29W/S108L and L29W/L32T clearly favor substate A_I; A_{II} appears only as a shoulder. L29W/L72F has an additional, weak CO stretch band at 1915 cm^{-1}. In mutant L29W/I107W, A_I and A_{II} are spectrally not well separated, and therefore, the CO spectrum displays a broad asymmetric band peaking at 1940 cm^{-1}. All peak positions are compiled in Table 3.2 (Appendix B).

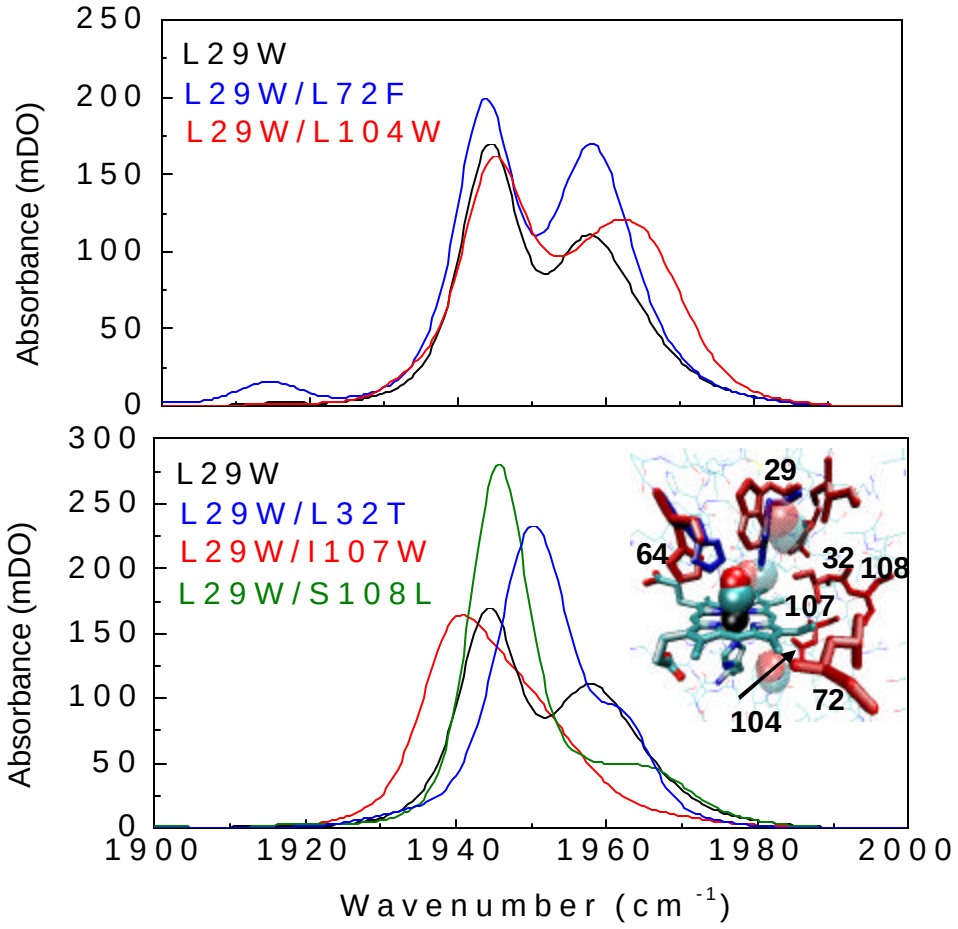

Fig. 3.34: FTIR spectra of L29W MbCO and related double mutants at 3 K. Transmission spectra were referenced against 'met' spectra to determine the IR bands of the overall bound population; inset: sketch of the active site.

In Fig. 3.35, we plot the FTIR spectra of L29W as a function of temperature for three different sample preparations, (a) L29W MbCO in glycerol/buffer, (b) L29W(Xe) in the same buffer equilibrated with 1 atm of Xe, (c) L29W in buffer solution saturated with trehalose. It is immediately obvious that the equilibrium distribution between substates A_I and A_{II} depends strongly on temperature and solvent conditions. The relative populations of A_I and A_{II} are constant at lower temperatures, implying that the molecules are frozen in their respective A substates. Above the dynamic transition temperature, these substates can interconvert, and Fig. 3.35 shows that the population shifts towards A_{II} at ambient temperature.

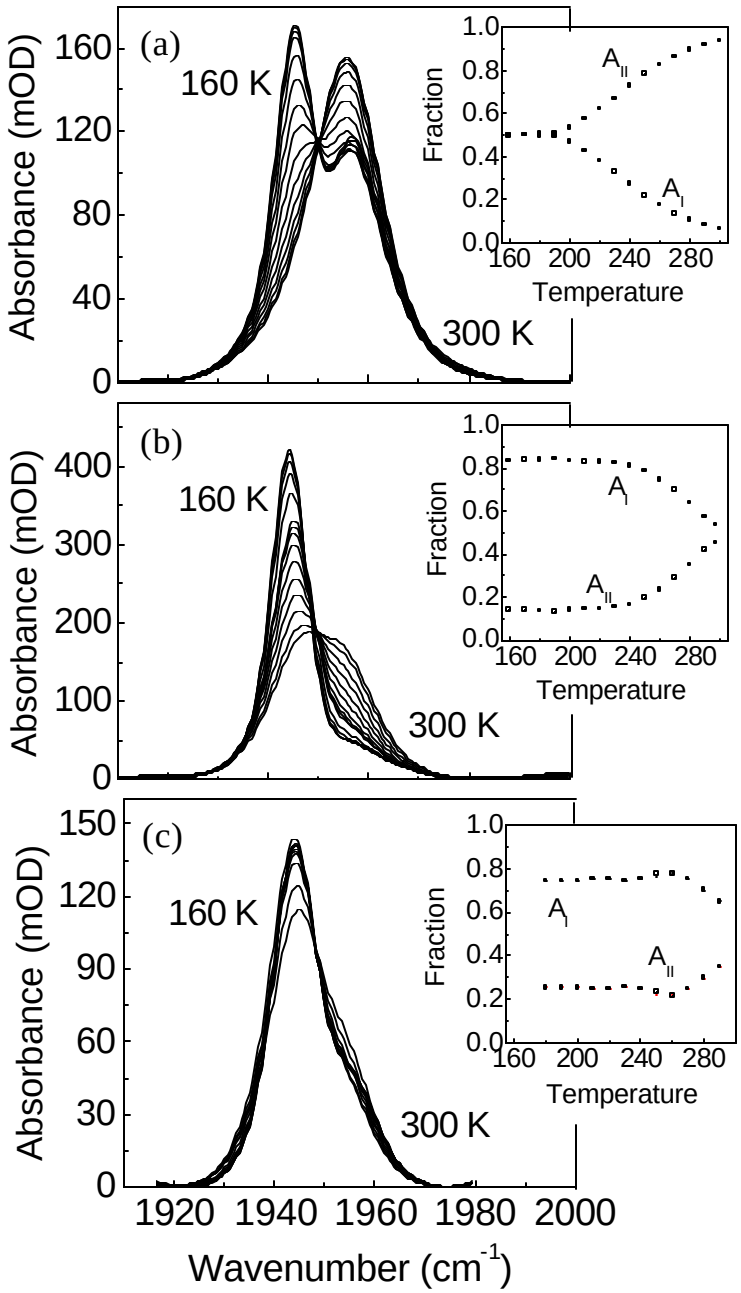

Fig. 3.35: Temperature dependence of IR spectra of samples (a) L29W in glycerol/buffer, (b) L29W(Xe) in glycerol/buffer and (c) L29W in buffer saturated with trehalose. Transmission spectra were referenced against a 'met' transmission spectrum; insets: temperature dependence of fractions n_I of A_I and n_{II} of A_{II}.

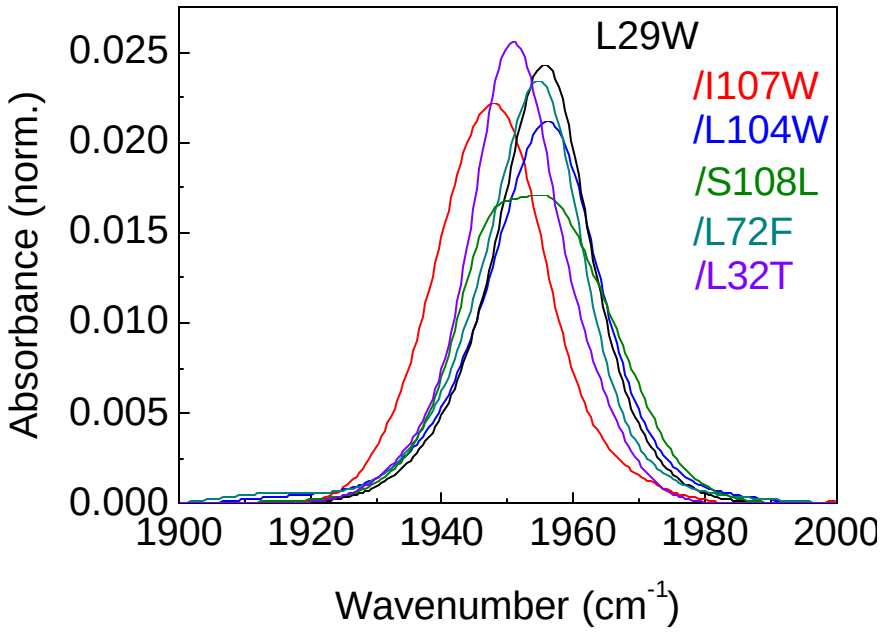

Fig. 3.36: FTIR spectra of L29W MbCO and related double mutants in 75%/25% glycerol/buffer at 300 K; the FTIR transmission spectra were referenced against a 'met' transmission spectrum; the area was normalized for comparison.

In Fig. 3.36, we plot the FTIR absorbance difference spectra at 300 K for all double mutants of L29W. Comparison with the 3-K spectra in Fig. 3.34 shows that all spectra shift towards the high frequency substate A_{II} with temperature, except for L29W/L32T, where the dominant peak at 1950 cm^{-1} remains unchanged, while the shoulder at ~1963 cm^{-1} disappears. The frequency shift is less pronounced in L29W/I107W, and in L29W/S108L, only 50% of the molecules adopt substate A_{II} at 300 K.

Not only temperature, but also xenon strongly affects the equilibrium ratio A_I/A_{II} in L29W MbCO (Fig. 3.35 a, b). In the presence of xenon, the equilibrium is shifted towards A_I, with ~90% instead of ~50% in A_I at 3 K, and ~50% instead of 5% at room temperature. In Fig. 3.37, we compare the effect of xenon on the CO stretch spectra of three mutants at 3 K. It is apparent that xenon changes the A substate ratio in L29W MbCO very effectively. The effect is less dramatic for L29W/L104W, and mutant L29W/I107W does not show a significant change at all.

A third factor that governs the equilibrium ratio between taxonomic substates A_I/A_{II} is the solvent composition. In Fig. 3.38, we display A substate spectra of L29W MbCO in four different solvent environments at 3 and 290 K. It is apparent that an increase in water content shifts the equilibrium towards A_I. At lower water activity (high concentration of glycerol or trehalose) substate A_{II} is favored.

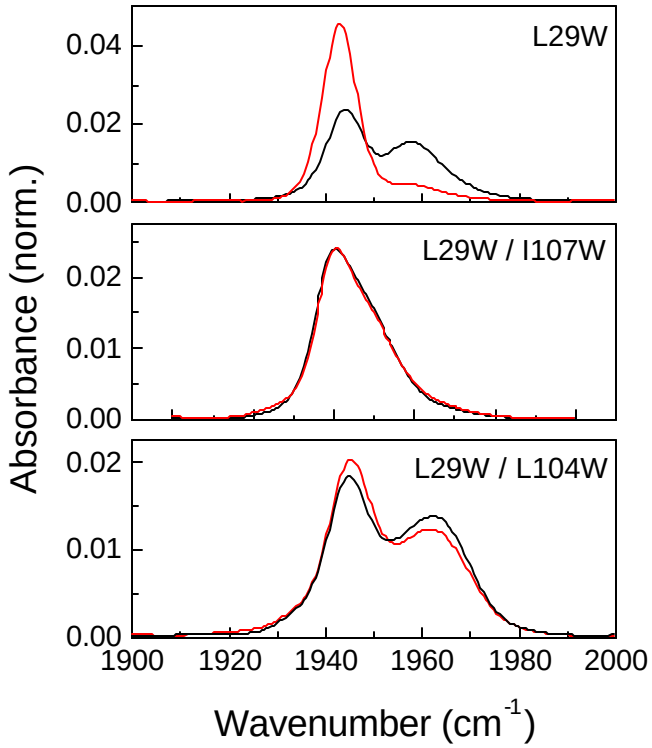

Fig. 3.37: Effect of xenon on the relative populations of A_I/A_{II} in IR spectra of three mutants of MbCO at 3 K; black lines: samples without xenon; red lines: samples equilibrated with 1 atm of xenon at 0°C.

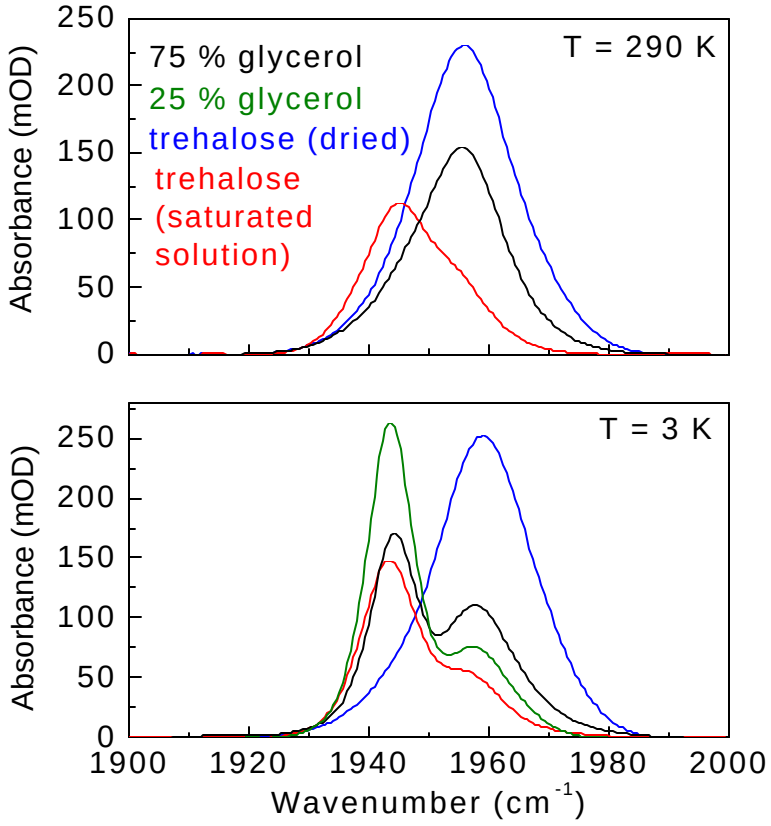

Fig. 3.38: FTIR spectra of L29W MbCO at 3 K (bottom) and 290 K (top) in different solvents.

3.2.1.2. Interpretation and Discussion: Interconversion between Substates A_I and A_{II}

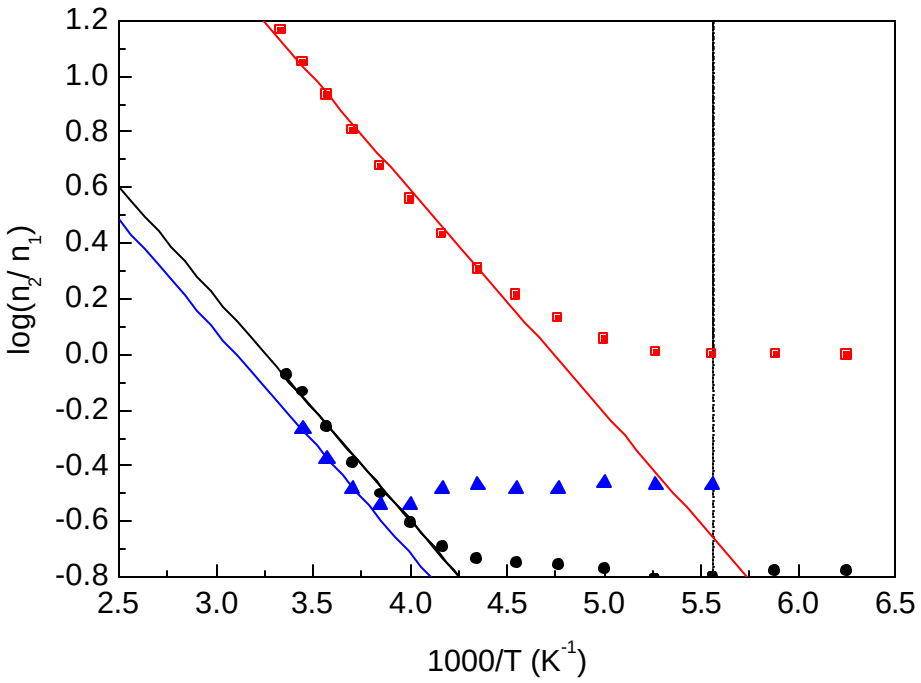

Fig. 3.39: Van't Hoff plots of the A_I/A_{II} equilibrium population ratios of three different L29W MbCO samples; red symbols: L29W in 75%/25% glycerol/buffer; black symbols: L29W(Xe) in 75%/25% glycerol/buffer; blue symbols: L29W in buffer saturated with trehalose; lines represent linear fits to the population changes; the dotted line marks the temperature of 180 K.

The temperature-dependent FTIR spectra in Figs. 3.35 a-c were fitted using two Gaussian lines. The areas of the bands were taken to compute fractional populations n_I and n_{II} of substates A_I and A_{II}. They are related to the free energy difference, ΔG:

$$\Delta G = -RT \ln K = -RT \ln\left(\frac{n_{II}}{n_I}\right) = \Delta H - T\Delta S \qquad (3.1)$$

with equilibrium constant K, temperature T and gas constant R. For all three samples, the slopes in the van't Hoff plot (Fig. 3.39) are equal, yielding an average enthalpy difference $\Delta H = 15.3$ kJ/mol between the two bound states. The curves are shifted with respect to each other, implying that the solvent rather affects the entropy change DS between taxonomic substates A_I and A_{II}.

From Eq. 3.1, the entropy difference DS represents the relative number of available microstates associated with substates A_I and A_{II} in the limit $T ? 8$,

$$\Delta S = R \ln \frac{n_{II}}{n_I}\Big|_{T\to\infty} . \qquad (3.2)$$

In the van't Hoff plot, this ratio of microstates is given by the offset of the line. From the fit, we obtain $n_{II}/n_I = 10^{3.8} = 6400$ for L29W, $10^{2.6} = 400$ for L29W(Xe) and $10^{2.5} = 316$ for the trehalose sample.

From this two-state analysis, it is clear that the presence of xenon shifts the equilibrium towards the A_I substate by a factor of $10^{1.2} \sim 16$. However, this thermodynamic scheme is too simplistic, since not all molecules may have bound xenon (at 1 atm partial pressure). To model the population shift towards A_I, we define four subpopulations A_I, $A_I(Xe)$, A_{II} and $A_{II}(Xe)$ within the L29W(Xe) sample that are connected by equilibrium constants $K(A_I)$, $K(A_{II})$, K and $K(Xe)$ as depicted in Fig. 3.40. Note that $A_I(Xe)$ represents molecules in the A_I conformation that have incorporated a xenon atom.

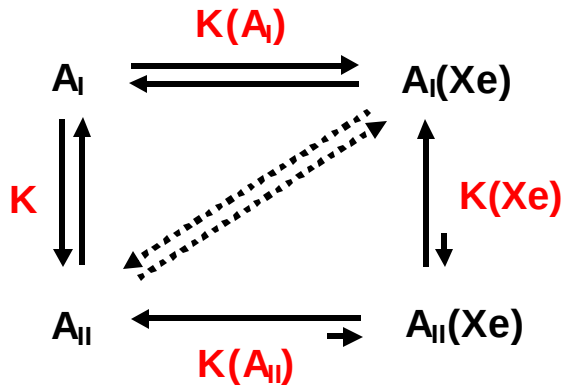

Fig. 3.40: Four-state-model to explain the influence of xenon on the equilibrium ratio A_I/A_{II} in MbCO mutant L29W.

The four equilibrium coefficients K in this scheme are defined by

$$K(A_I) = \frac{A_I(Xe)}{A_I}; \quad K(A_{II}) = \frac{A_{II}(Xe)}{A_{II}}; \quad K = \frac{A_{II}}{A_I}; \quad K(Xe) = \frac{A_{II}(Xe)}{A_I(Xe)} \tag{3.4}$$

In the presence of xenon, the IR spectra yield the overall populations of conformations A_I and A_{II}, whether they have bound CO or not. The apparent equilibrium ratio, K_{app}, is thus the overall ratio of molecules in conformations A_{II} and A_I,

$$K_{app} = \frac{A_{II} + A_{II}(Xe)}{A_I + A_I(Xe)} = \frac{A_{II} + (K(A_{II}) \cdot A_{II})}{A_I + (K(A_I) \cdot A_I)}$$

$$= \frac{A_{II} \cdot (1 + K(A_{II}))}{A_I \cdot (1 + K(A_I))} \tag{3.5}$$

$$= K \cdot \left(\frac{1 + K(A_{II})}{1 + K(A_I)} \right)$$

Note that without xenon, $K(A_I)$ and $K(A_{II})$ are zero and the expression yields $K_{app} = K$. If $K(A_I)$ and $K(A_{II})$ were equal, there would again be no effect on the measured ratios. From the experimental results, however, the shift towards A_I is evident, which implies that $K(A_I) > K(A_{II})$. For simplicity, we assume that $K(A_{II})$ and, therefore, also $K(Xe)$ are approximately zero, which reduces our thermodynamic scheme to three states. From Eq. 3.5, we then obtain

$$\frac{K_{app}}{K} = \frac{1}{1+K(A_I)} = 10^{-1.2} = \frac{1}{16}, \tag{3.6}$$

and thus

$$K(A_I) = 15. \tag{3.7}$$

Consequently, A_I has a pronounced preference for xenon binding, or in other words, the A_I conformation is stabilized by xenon. Concomitantly, the overall equilibrium K_{app} shifts towards A_I.

Clearly, the present analysis cannot give quantitative information about the equilibrium coefficients of A_{II}. The question is also still open which of the xenon-binding cavities is responsible for the stabilization of A_I. Xe 1, the highest affinity cavity in WT Mb, is an unlikely candidate, as it is located on the proximal side. From the observation in Fig. 3.37 that the A_I/A_{II} ratio of L29W/I107W, a mutant specifically designed to block the Xe 4 cavity, is not affected by xenon, we suggest that the observed shifts in the equilibrium arise from binding xenon in this cavity.

3.2.2 Probing the Initial Docking Site B

3.2.2.1 FTIR Absorbance Difference Spectra after Short Illumination for 1 s at 3 K

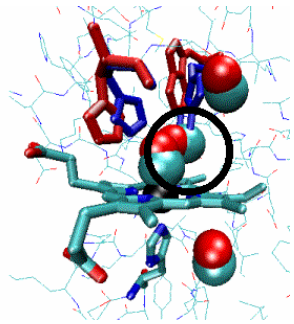

Brief illumination at 3 K cleaves the Fe-CO bond, and we expect the ligand to migrate to docking site B. FTIR transmission spectra were measured before and after photolysis to calculate the photoinduced absorbance differences at 3 K. The spectra of L29W and L29W(Xe) MbCO in Fig. 3.41 show the A_I and A_{II} bands, which indicates that ligands in both substates are photolyzable. The photodissociated CO ligands give rise to a dominant peak at 2122 cm^{-1} and a minor peak at 2131 cm^{-1}. Note that this spectrum is a superposition of FTIR stretch bands of photoproducts from A_I and A_{II}.

The FTIR absorbance difference spectra of L29W, L29W/L72F and L29W/L104W in Fig. 3.42 are very similar over the whole spectral region. The photoproduct spectra have essentially identical peak frequencies. The relative populations of the two bands at 2122 cm^{-1} and 2131 cm^{-1}, however, vary slightly. In Fig. 3.43, we compare a second set of mutants, L29W, L29W/L32T, L29W/S108L and L29W/I107W. Except for L29W/I107W, we observe again an impressive similarity in the photoproduct spectra. For this mutant, the FTIR bands of heme-bound and photodissociated CO differ markedly from L29W (compare Table 3.2, Appendix B).

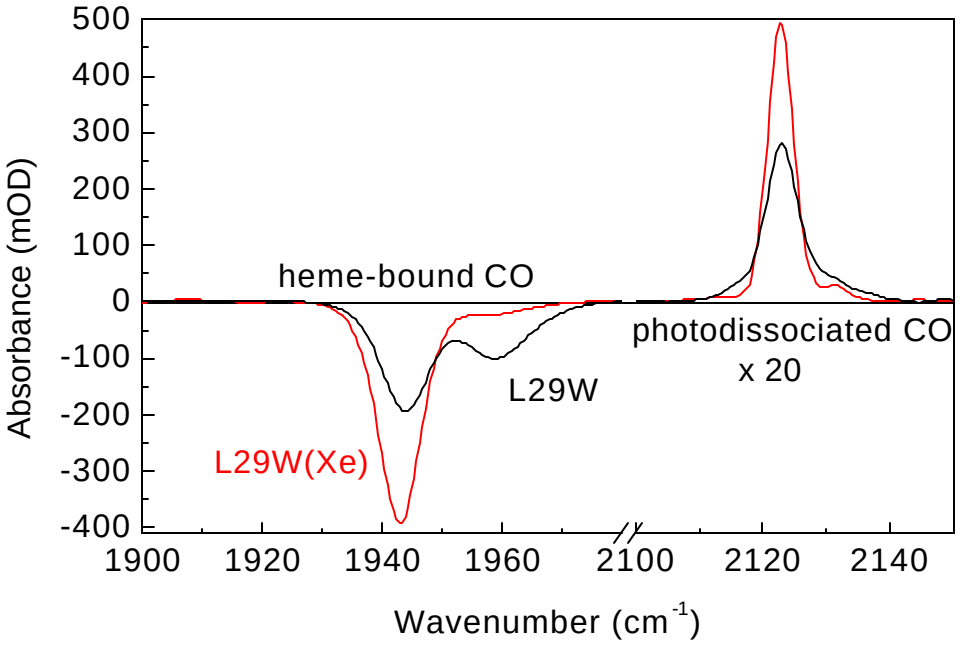

Fig. 3.41: FTIR absorbance difference spectra of MbCO samples L29W and L29W(Xe) after illumination for 1 s at 3 K.

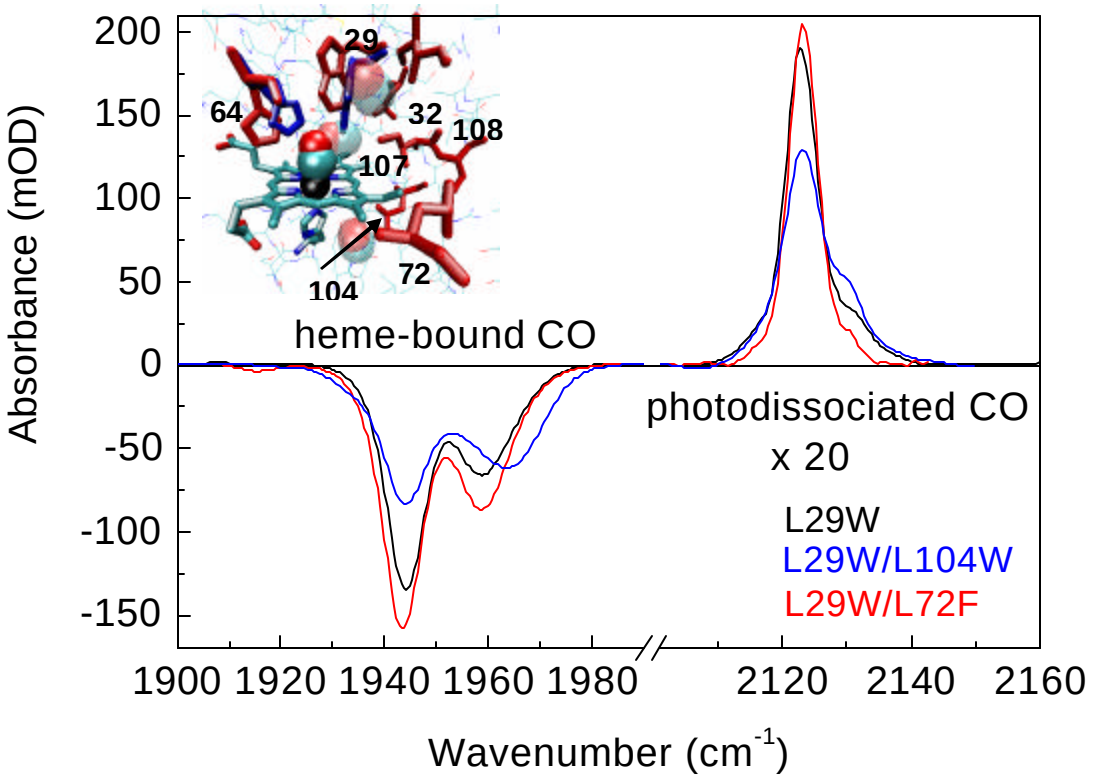

Fig. 3.42: FTIR spectra of MbCO mutants L29W, L29W/L72F and L29W/L104W after illumination for 1 s at 3 K; inset: sketch of the active site.

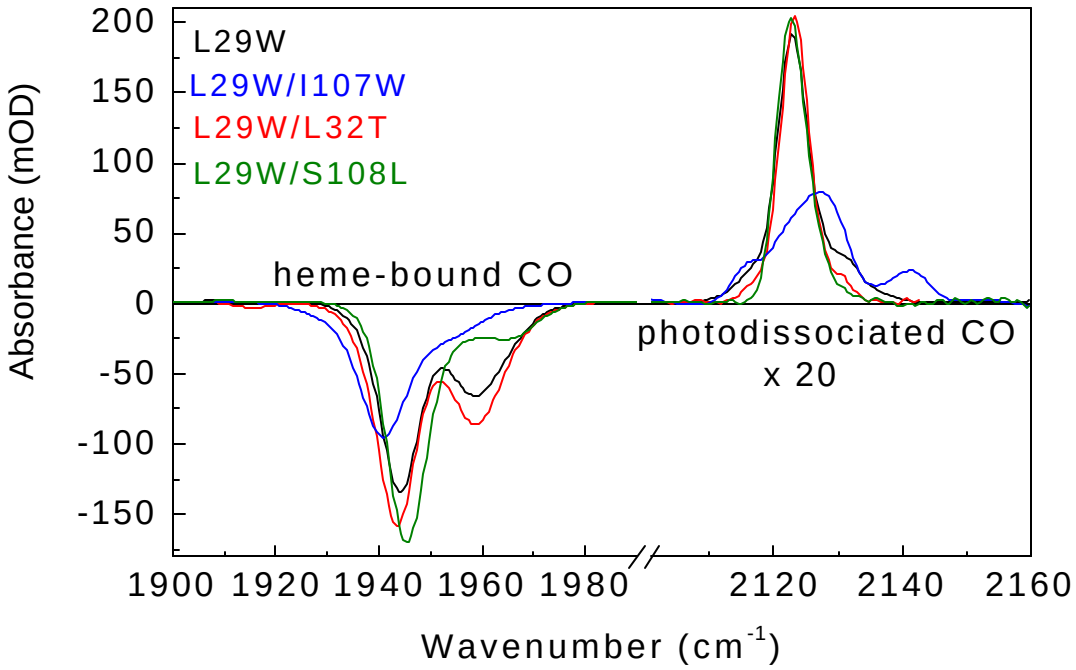

Fig. 3.43: FTIR spectra of MbCO mutants L29W, L29W/L32T, L29W/I107W and L29W/S108L after illumination for 1 s at 3 K.

3.2.2.2 TDS after Short Illumination at 3 K

To separate the photoproducts created at 3 K according to their recombination temperature, we have collected the TDS data of L29W and L29W(Xe) that are shown in Fig. 3.44. For L29W, we notice pronounced rebinding from two bands at 2122 and 2131 cm^{-1} to A_I at ~35 K. Additional recombination to A_I occurs at 120 K (Fig. 3.44 a, c). The related photoproduct signals are not resolved in the map. Recombination to substate A_{II} occurs over a widely distributed temperature range (3 - 110 K), indicating a very broad barrier distribution. To obtain the CO stretch bands of the A_{II} photoproduct, we have calculated the FTIR absorbance difference from 70 to 90 K, where only rebinding to A_{II} occurs. This procedure yields two broad bands at 2118 and 2125 cm^{-1} (Fig. 3.45).

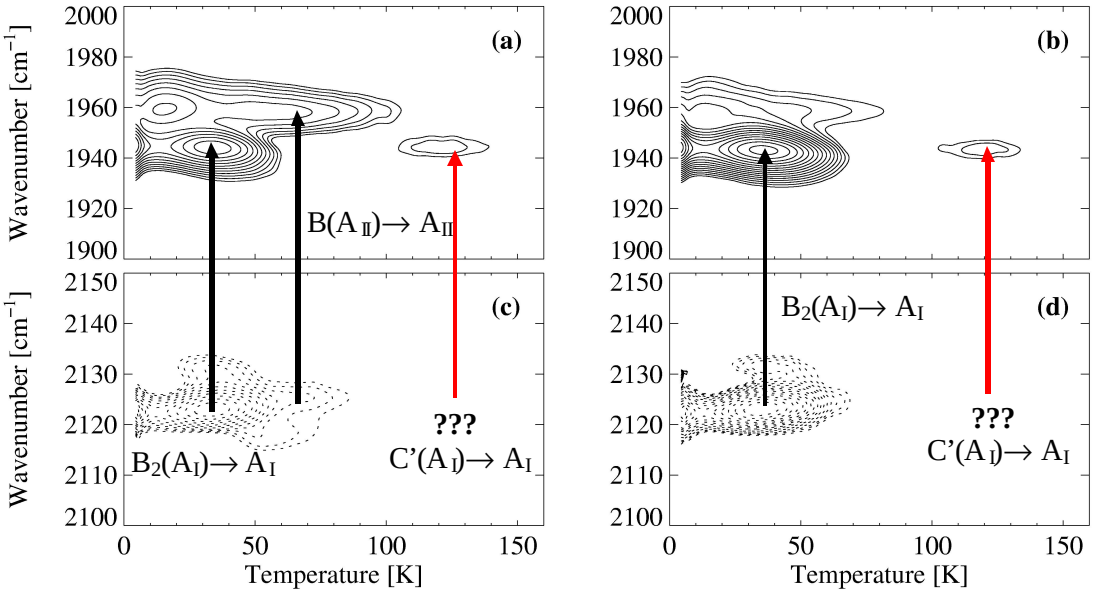

Fig. 3.44: TDS contour maps of (a, c) L29W and (b, d) L29W(Xe) after illumination for 1 s at 3 K.

The contour maps of L29W(Xe) in Fig. 3.44 b, d appear less complicated because the A_{II} population is suppressed. Due to the low occupancy and the contour spacing, recombination to A_{II} appears to be confined to lower temperatures. For A_I, we again observe two different rebinding populations at 35 and 120 K. Between 30 and 40 K, A_I rebinds most strongly so that contributions by A_{II} are negligible. Therefore, calculation of the difference spectrum between these two temperatures yields the FTIR stretch spectrum of the $B_{1,2}(A_I)$ bands. It is plotted in Fig. 3.45.

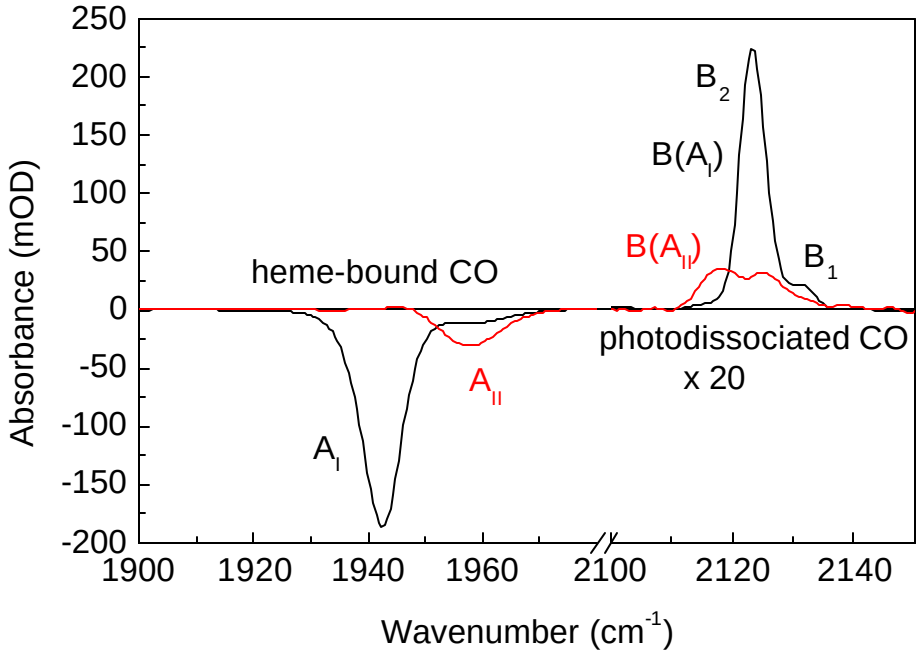

Fig. 3.45: FTIR/TDS absorbance differences calculated across the recombination features in the TDS maps after illumination for 1 s at 3 K in Fig. 3.44.

In Fig. 3.46, we display the TDS contour maps of L29W double mutants after short illumination at 3 K. All A state maps (left column) show recombination around 40 K. Additional rebinding above ~100 K occurs in all double mutants except for L29W/L104W. The fraction of CO ligands that is trapped in the new intermediate site with markedly higher recombination temperatures is most pronounced for those mutants - L29W/I107W and L29W/L32T – with a modified the structure around the Xe 4 cavity (Fig. 3.46 g, i). Moreover, distinctly different features appear in the corresponding photoproduct maps (Fig. 3.46 h, j), which contain broad distributions of absorbance changes stretched over the whole temperature range covered.

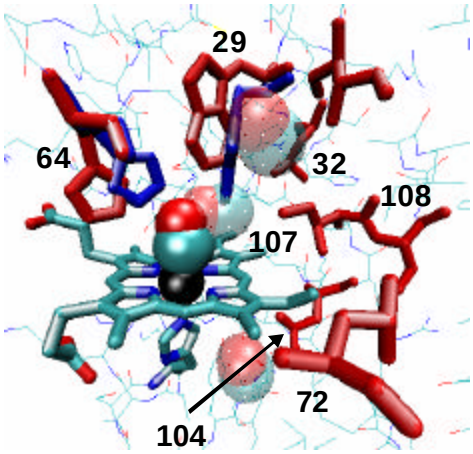

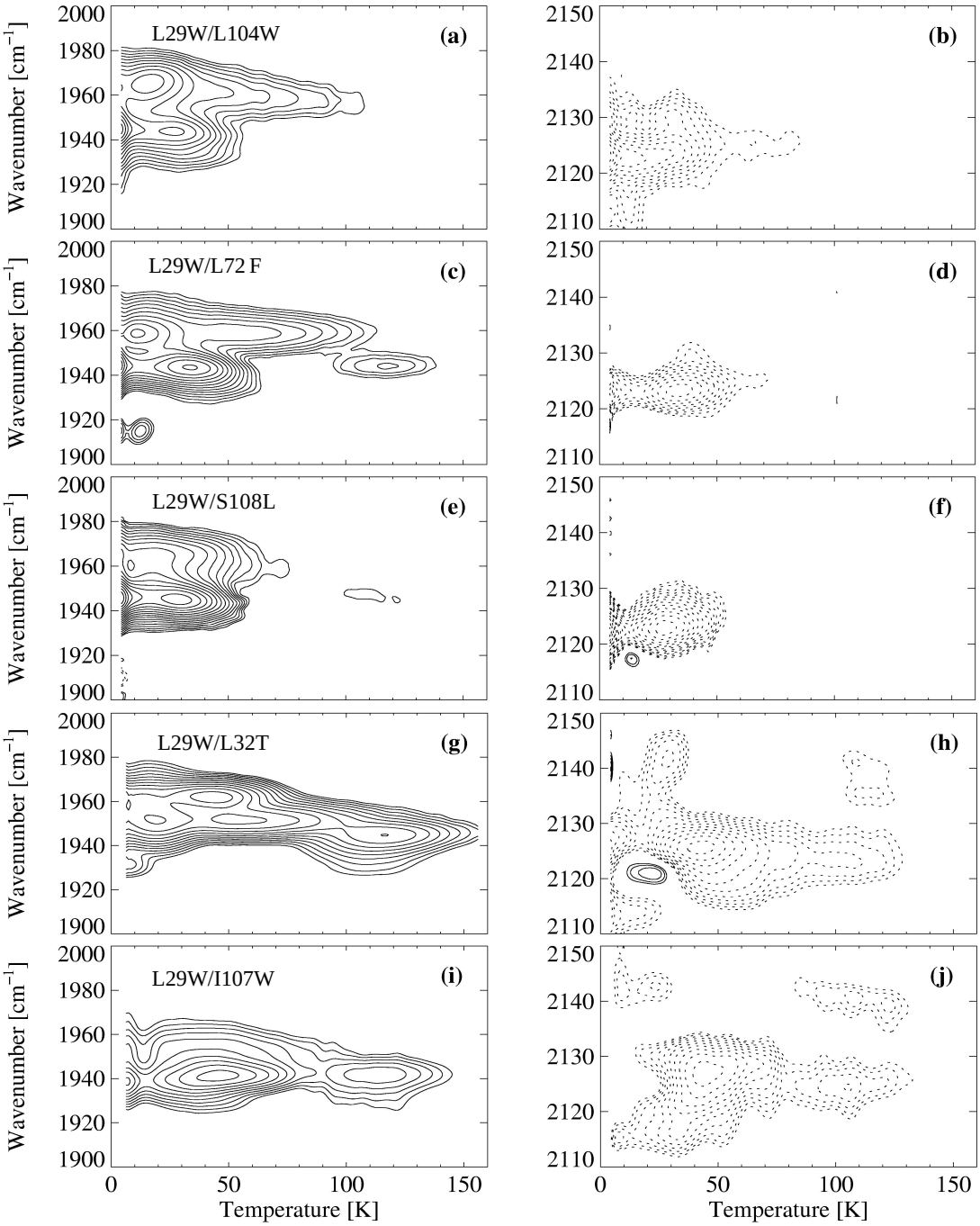

Fig. 3.46: TDS contour maps of MbCO mutants L29W/L104W, L29W/L72F, L29W/S108L, L29W/L32T and L29W/I107W after illumination for 1 s at 3 K.

3.2.2.3 Interpretation and Discussion: Probing the Initial Docking Site B

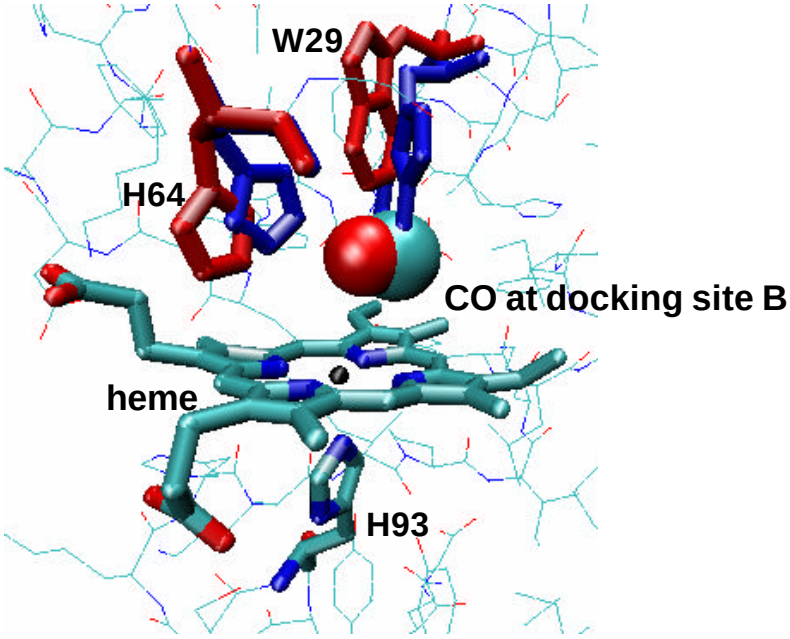

Fig. 3.47: The active site of MbCO mutant L29W; the CO ligand is depicted at the initial docking site B (pdb code 1ABS); red: A_I, blue: A_{II}.

In this subsection, we have presented IR difference spectra and TDS maps of L29W MbCO and related double mutants after illumination for 1 s at 3 K. We have seen that most photolyzed ligands migrate to docking site B. A minor population, however, becomes trapped at a new intermediate site C', from where they rebind at markedly higher temperatures. In Fig. 3.47, we display the structures of substates A_I and A_{II} near the binding site (A) and initial docking site (B). The CO ligand is included at site B as determined by Schlichting *et al.* (50). The figure gives a structural explanation as to why substates A_I and A_{II} show such a markedly different temperature dependence of recombination. In molecules of substate A_I, the initial docking site B can be occupied by the ligands. In A_{II}, however, the indole sidechain of W29 interferes sterically with this position. The complete blockage of the initial docking site eventually guides the photodissociated CO into the space between W29 and H64. The broad distribution of recombination temperatures indicates that site B(A_{II}) is structurally not well-defined.

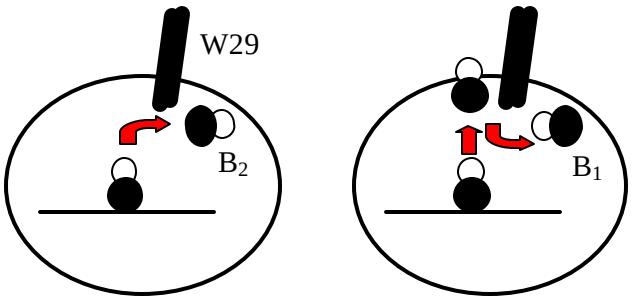

Fig. 3.48: Schematic explaining how of CO populates the $B_{1,2}$ photoproduct sites after photodissociation (adapted from Lim *et al.* (54)).

The FTIR stretch frequencies of the photoproducts B(A_1), 2122 cm^{-1}, and 2131 cm^{-1}, are similar to those of WT (2119 cm^{-1} and 2131 cm^{-1}) and thus, we assign them to B_2 and B_1 (55, 117, 118). Lim *et al.* investigated the nature of ligand motion within Mb by measuring femtosecond time-resolved infrared spectra of photolyzed CO (54). They observed two trajectories for the CO ligands, distinguished spectroscopically and kinetically, into the docking site B (Fig. 3.48). The faster trajectory was assigned to those ligands that settle directly into the docking site. They point the ligand carbon towards the heme iron. Spectroscopically, they are represented by B_2. Ligands that occupy site B in the opposite orientation give rise to the stretch band B_1.

In L29W, photoproduct B_2 is clearly favored energetically. As the bulky tryptophan sidechain occupies a significant fraction of the distal pocket, the CO ligand might not be able to rotate into the orientation B_1 according to the scheme in Fig. 3.48. Moreover, electrostatic interactions between the aromatic indole sidechain and the photolyzed ligand might support this particular orientation.

3.2.3 Remote Intermediates: Site C'

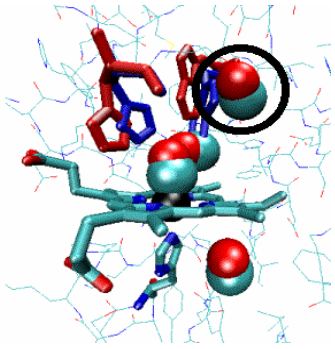

3.2.3.1 Isothermal Illumination at 3 K

After illuminating L29W MbCO for 1 s at 3 K, only a tiny fraction of ligands was trapped at the more remote intermediate site C'. To investigate the effect of extended exposure to light, we recorded FTIR transmission spectra continuously for 15,000 s at 3 K while illuminating the sample. FTIR absorbance difference spectra were calculated by referencing these transmission data against the 'dark' transmission spectrum at time $t = 0$. The temporal development of the spectra is shown in Fig. 3.49.

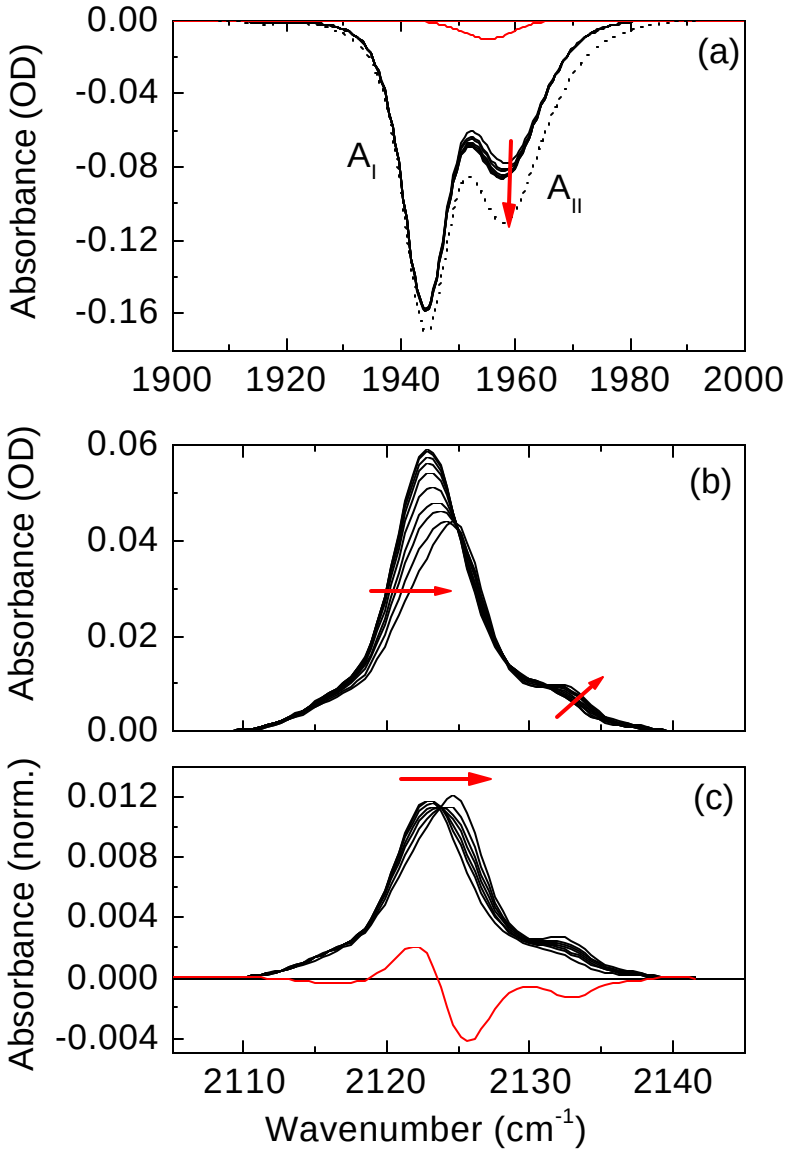

Fig. 3.49: Temporal development of FTIR spectra of L29W MbCO during illumination for 15,000 s at 3 K; (a) heme-bound CO, dotted line: total population (b) photodissociated CO, (c) photodissociated CO, normalized to equal areas; spectra in red: overall change within each data set; arrows indicate time progression.

In panel a, we see the development of the photolyzed fraction in the bands of heme-bound CO. The dotted line represents the total population within our sample. Apparently, photolysis of A_I is not complete, a few ligands rebind very quickly. The photolyzed fraction of substate A_I, however, does not change over time, implying that recombination and photolysis is in equilibrium, and conversion of fast-rebinding molecules to slowly rebinding ones does not take place. In contrast, the photodissociated fraction of A_{II} increases with time. The total change is given by the red line in Fig. 3.49 a. We conclude that for this substate pumping is possible; extended illumination leads to slower rebinding, at least in a fraction of proteins.

Due to the overall increase in A state band area, a corresponding increase is expected for the photoproduct bands in Fig. 3.49 b, as ligands cannot leave the protein at 3 K. Instead, we observe that the dominant peak at 2122 cm^{-1} shifts towards 2125 cm^{-1}, and a minor peak at 2132 cm^{-1} increases in intensity. To interpret these findings, we plot the normalized spectra in Fig. 3.49 c. The red line represents the overall change induced by illumination. Positive as well as negative features denote an exchange within the photolyzed population. The sharp isosbestic point at 2124 cm^{-1} indicates a two-state-interconversion.

3.2.3.2 TDS Experiment after Isothermal Illumination at 3 K

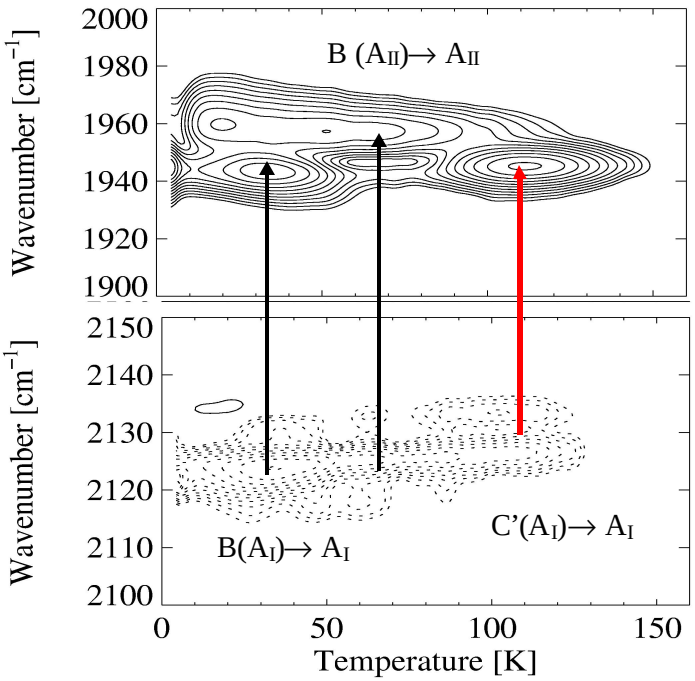

Fig. 3.50: TDS contour maps of mutant L29W MbCO after illumination for 15,000 s at 3 K.

To obtain insight into the changes within the photolyzed population caused by extended illumination, a TDS experiment was performed subsequent to illumination at 3 K. In Fig. 3.50, we plot the TDS contour maps of heme-bound CO (top) and photolyzed CO (bottom). In comparison to the maps after short illumination (Fig. 3.44), pronounced changes are visible. Substate A_I shows recombination from two about equally populated intermediates B and C' at temperatures centered around 35 and 110 K. For A_{II}, an additional peak at higher temperature

is lacking, which suggests that the channel to site C' is blocked. Compared with short illumination (Fig. 3.44), there is only a clearly visible change at the lowest temperature, where population has been removed. Together with the data taken under illumination, this observation indicates that low-barrier (temperature) and hence fast rebinders have shifted to higher barriers (temperature). The photoproduct map has become even more complicated. The features of two intermediates recombining to A_I and at least one population rebinding to A_{II} are superimposed. Nevertheless, it is clear that both the IR spectra of the photoproducts at 35 and 120 K consist of two bands. Furthermore, we notice weak positive contours at 2135 cm^{-1} at ~20 K, indicating an exchange within the photolyzed population.

3.2.3.3 Isothermal Illumination at 80 K

To unravel the features in the somewhat crowded photoproduct map, we performed an isothermal illumination experiment on MbCO sample L29W at 80 K for 15,000 s (Fig. 3.51). At 80 K, the photodissociated fraction of A_I increases significantly during illumination, whereas no change occurs in A_{II}, as seen from the overall absorbance change depicted in red in panel a. Therefore, the corresponding changes in the difference spectra of the photoproducts (red line in Fig. 3.51 b) can be assigned exclusively to photoproducts of A_I. A subsequent TDS experiment confirmed that extended illumination had no effect on the photoproducts of A_{II}.

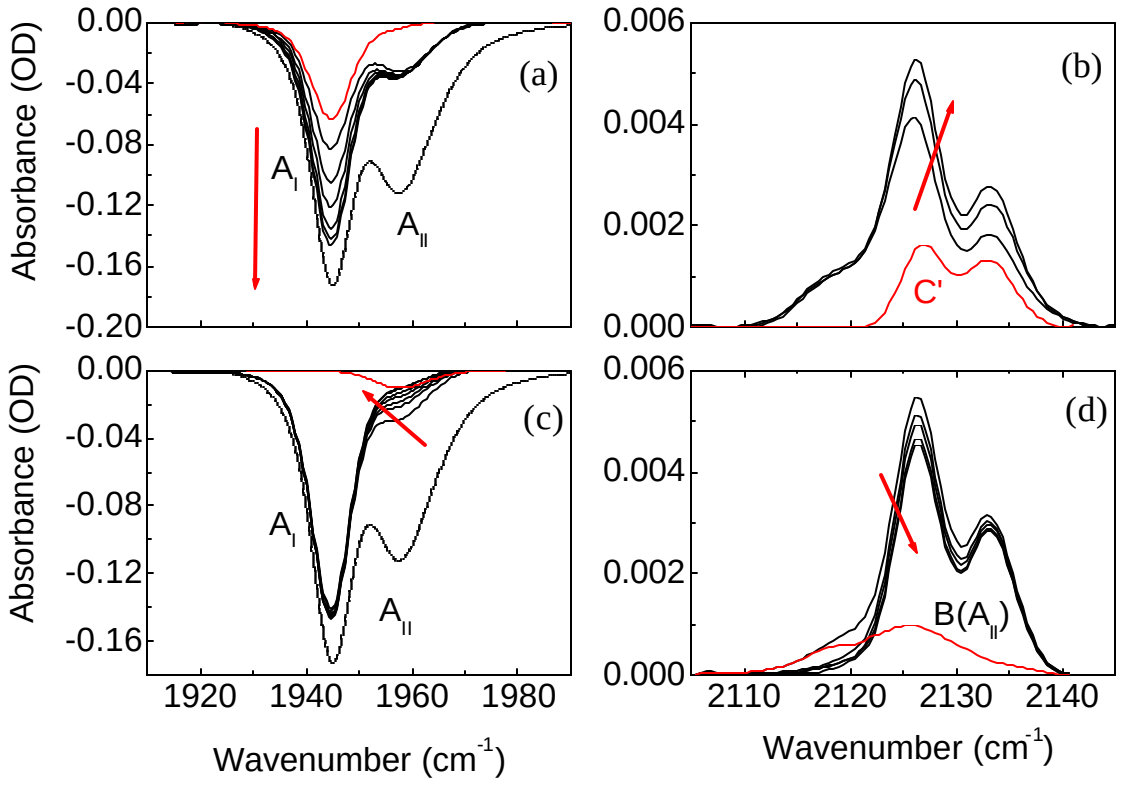

Fig. 3.51: Temporal development of the CO stretch bands of MbCO mutant L29W at 80 K; (a) heme-bound and (b) photolyzed ligands during illumination for 15,000 s; (c) heme-bound and (d) photolyzed ligands after termination of the illumination for 50,000 s; spectra in red: overall change within each data set; arrows indicate time progression; dotted lines: total A state population.

After 15,000 s under illumination, we subsequently probed the evolution of the spectra in the dark for 50,000 s (Fig. 3.51 c, d). Apparently, changes in the bands of heme-bound CO occurred only for the A_{II} conformation, as seen from the red line in panel c which represents the overall rebinding. The corresponding change in the stretch bands of photolyzed CO yields the very broad and not well-structured spectrum of $B(A_{II})$ in Fig. 3.51 d, which suggests that $B(A_{II})$ comprises a collection of different docking sites. We remark that the nomenclature $B(A_{II})$ is merely intended to describe the primary A_{II} photoproduct; it is clearly *not* equivalent to the primary docking site determined by x-ray diffraction.

3.2.3.4 Interpretation and Discussion: Structural Interpretation of Intermediate Site C'

In L29W molecules in substate A_I, extended illumination at 3 K or other temperatures up to 80 K (Figs. 3.49, 3.50, 3.51) enables a large fraction of CO ligands to escape to intermediate C'. At 80 K, thermally activated recombination from site C' is slow on the time scale of the TDS experiment, and ligands return to the heme iron at ~110 K. In Fig. 3.52, we plot the CO spectrum calculated from the TDS data (Fig. 3.50) across the rebinding feature of C' (110 - 120 K). Two bands at 2126 and 2133 cm^{-1} correspond to opposite orientations of the ligand at site C'. As seen from the different populations, they are energetically not equivalent. The positive contours below 30 K in the TDS map in Fig. 3.50 can be assigned to reorientation of CO ligands at site C'.

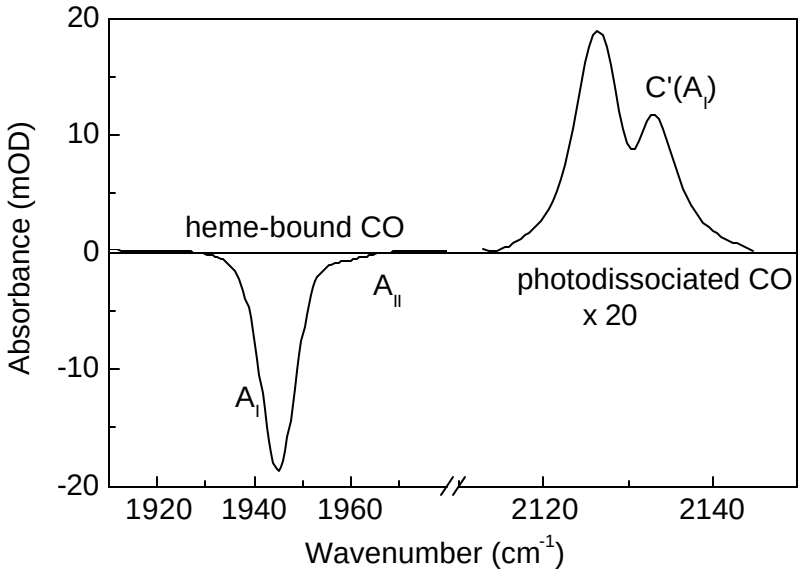

Fig. 3.52: CO stretch bands of the A states and photoproduct C' of L29W MbCO.

Photolysis of crystals of L29W MbCO at 105 K yielded essentially all of the CO ligands in the Xe 4 cavity (15, 119), while the protein moiety had adopted the A_I conformation. Consequently, we conclude that intermediate C' can be assigned to a photoproduct having CO in the Xe 4 cavity. In the A_{II} substate, the W29 indole sidechain is shifted closer to the heme group, blocking site B and the pathway to C'. Thus, we propose that the Xe 4 cavity is no intermediate docking site in A_{II} molecules. Fig. 3.53 compares the Xe 4 cavities of substates A_I and A_{II}.

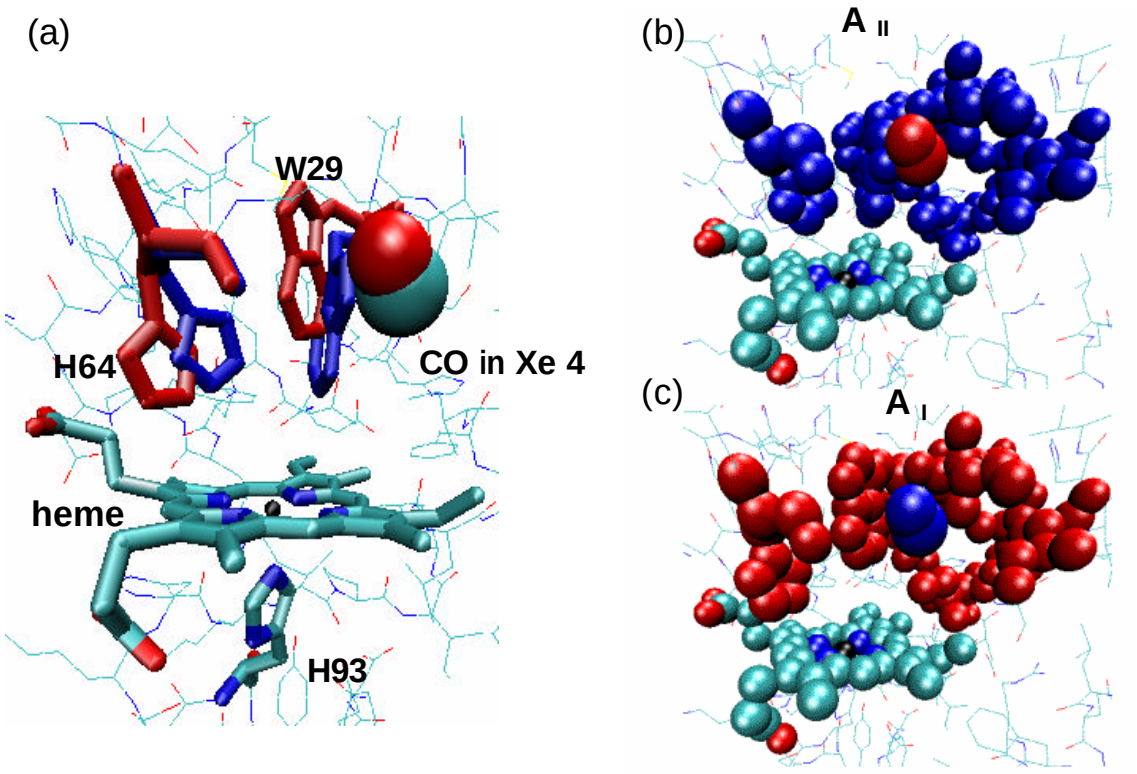

Fig. 3.53: (a) Active site of L29W; the CO ligand is located in the Xe 4 cavity. (b-c) residues lining the Xe 4 cavity are depicted as van der Waals spheres (70 % of actual size); (b) A_{II} conformation; (c) A_{I} conformation.

The CO Stretch Spectrum of B(A_{II})

The contour maps of L29W MbCO after extended illumination at 3 K (Fig. 3.50) contain contributions from different photoproducts. To isolate the CO stretch spectra characteristic of a specific intermediate, we have calculated absorbance differences not for a temperature interval of 1 K, as in the usual TDS evaluation, but over a temperature interval covering the recombination feature. We chose these intervals based on the recombination contours in the TDS maps of heme-bound CO. Note that this approach assumes that the spectral changes within the particular temperature interval are exclusively caused by recombination. For B(A_I), we integrated the FTIR derivative spectra from 30 to 40 K, for B(A_{II}) we chose 60 to 70 K. The spectra are plotted in Fig. 3.54. We have also added the spectrum of B(A_{II}) calculated across the TDS data in Fig. 3.44 after short illumination (red dashed line) and from the isothermal data in Fig. 3.51 (red dotted line). For comparison, we have included B(A_1) from WT (35 - 45 K). For all spectra, the integrated absorbance was normalized to 1.

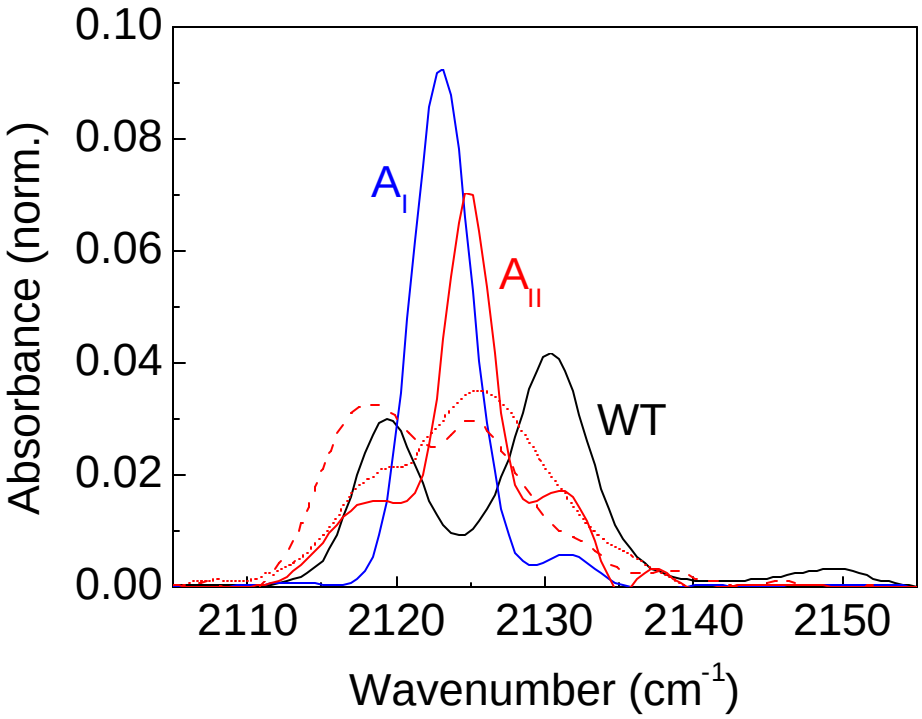

Fig. 3.54: Normalized FTIR spectra of CO at site B in L29W and WT MbCO, as determined from experiments with different sample preparation history. For details, see the text.

Whereas we were able to isolate photoproduct spectra of B(A_I) and C', the B(A_{II}) spectra vary markedly with the preparation history of the sample. In the Appendix A, we will present evidence that the absorbance spectra of B(A_{II}), calculated across recombination features in the TDS maps, are strongly affected by temperature-induced changes of the CO stretch bands for photoproduct C', which are superimposed on the spectrum for B(A_{II}) in a chosen temperature interval. Consequently, only the isothermal protocol yields the true spectrum B(A_{II}).

Mechanism of Light-induced Ligand Migration

In the A_I conformation, the majority of photodissociated CO settles into docking site B after brief photolysis at 3 K (Fig. 3.44), but a tiny fraction of ~1% is able to escape to the Xe 4 cavity even at 3 K. This observation was initially very surprising for us because this was the first experiment in which light-induced ligand migration had been observed at low temperatures. In WT MbCO, pumping into alternative sites was always observed at temperatures that were only a bit lower than the rebinding temperatures from these photoproduct states. This suggests that the free energy barrier for migration from B → C is much smaller in L29W than in WT MbCO.

To examine if the barrier for ligand migration between B and C was even small enough for thermally activated or tunneling transitions at 3 K, we monitored the IR bands following a short flash for 7,000 s in the dark. During this time, ~30% of the photolyzed ligands were seen to recombine from site B(A_I) at 3 K, as depicted in Fig. 3.55. From the CO bands of the photodissociated CO, we could see that recombination in A_I occurred from B(A_I); no thermally activated migration to the secondary docking site C' was observed (inset).

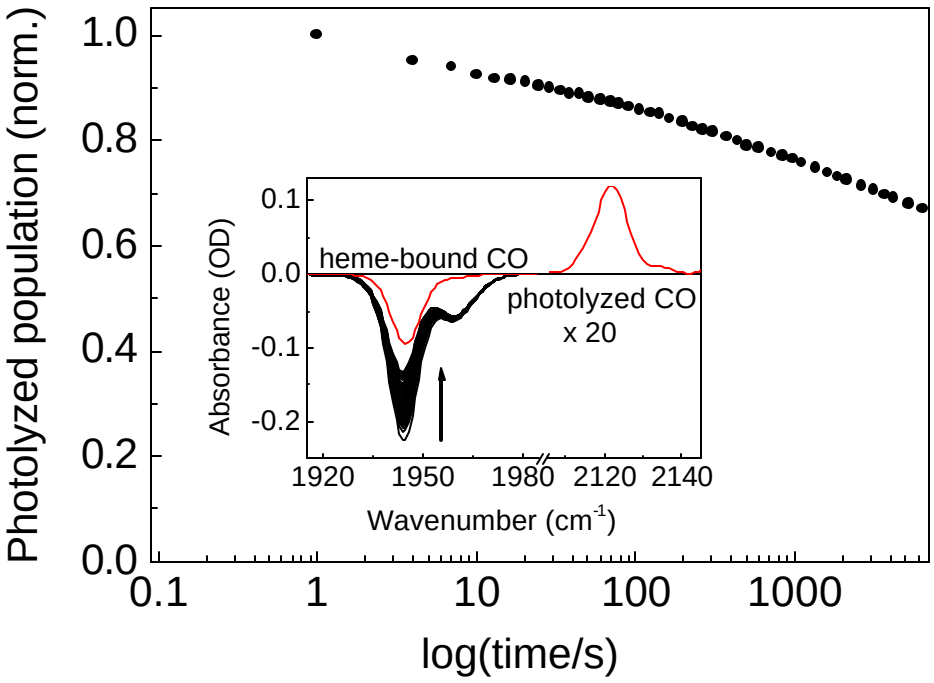

Fig. 3.55: Temporal development of the integrated absorbance of L29W MbCO at 3 K, monitored in the A state bands after 1-s illumination at 3 K; inset: FTIR absorbance spectra; arrow: time progression; red: overall change during rebinding for 7,000 s.

By contrast, extended illumination for 15,000 s at 3 K enables ~50% of ligands in A_1 molecules to migrate to the back of the distal pocket. In Fig. 3.56, we plot the temporal development of the ligand occupancies at sites B and C' during extended exposure to light. The trace of the A states is included to point out that photolysis is complete within seconds. We note that the CO population in C' gains significantly at the expense of CO population in B; the transition can be described by a power law.

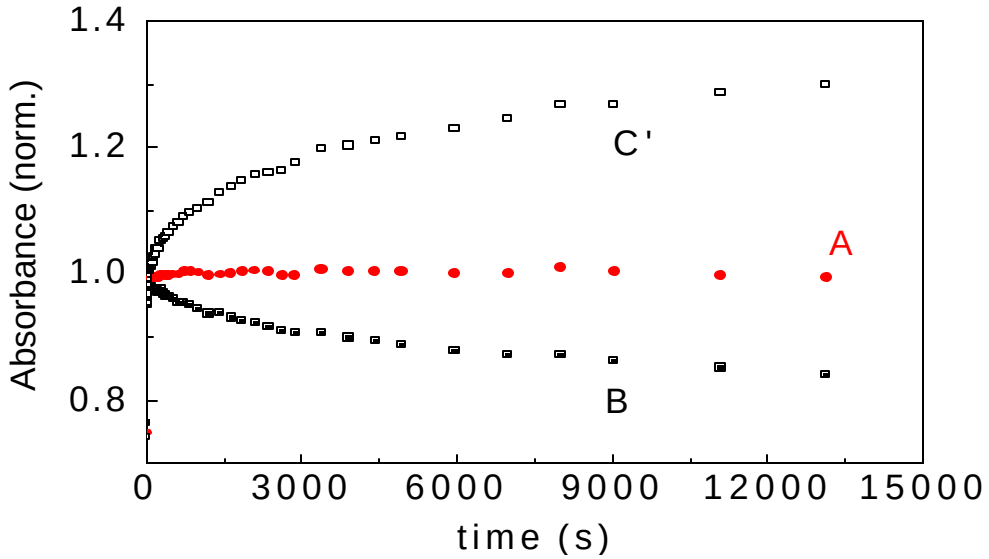

Fig. 3.56: Temporal development of the photoproduct populations at sites B and C' in L29W MbCO; red: integrated absorbance in A state bands with respect to time.

It is interesting to inquire about the physical mechanism of how light absorption in the heme group induces migration of the CO over barriers that, at 3 K, are far too high to be overcome by thermal activation. Two scenarios appear: (i) A considerable fraction of the light energy deposited in the heme group ends up as kinetic energy of the CO ligand, which may enable it to surmount the barrier and migrate from A to C'. (ii) Photodissociated ligands will initially become trapped in site B, which is in contact with the heme group. Energy from photoexcitation of the heme can be transferred to the CO, thus enabling it to migrate to site C'. Figs. 3.55 and 3.56 prove that the light-induced CO migration follows the second mechanism. If ligand migration to C' occurred only upon photolysis of bound CO, we could only expect an additional 0.3% of photodissociated ligands in C' after illumination for 7,000s, because only ~30% of photolyzed ligands recombine within 7,000 s so that they can experience a second photolysis event and migrate to C'. As we observe much larger CO population increases in site C' (Fig. 3.50), we conclude that, at 3 K, photodissociated ligands residing in the primary docking site B pick up energy from photoexcitation of the heme group to migrate to C'.

3.2.4 Detailed Investigations of Photoproduct State C' reveal an Additional Photoproduct State C''

3.2.4.1 Isothermal Illumination at 120 K

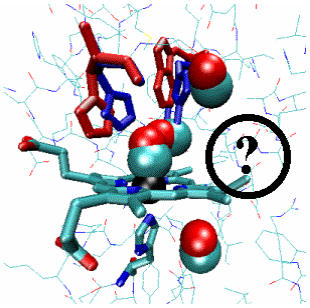

At ~120 K, recombination from C' reaches its maximum. To examine if CO ligands can migrate to further sites with even higher effective rebinding barriers, MbCO sample L29W was illuminated at 120 K for 15,000 s. In Fig. 3.57 a, we present the temporal development of the FTIR absorbance difference spectra in this experiment. The black, dotted line represents the total bound CO spectrum.

In the spectral region of heme-bound CO, we observe that the photolyzed fraction increases over time. Closer inspection shows that, in the first spectra of the series, the population of photodissociated A_I molecules increases, and concomitantly, the spectral signature of C' appears in the bands of photolyzed

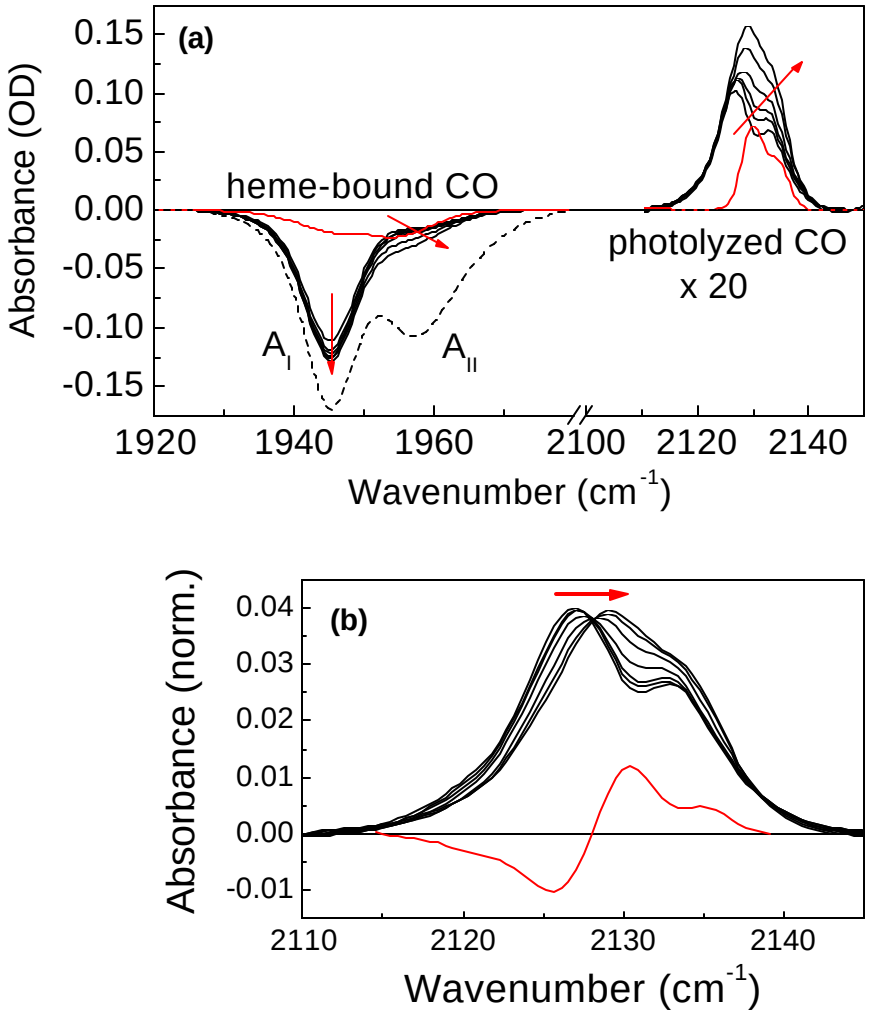

Fig. 3.57: (a) Temporal development of the FTIR absorbance bands of MbCO mutant L29W at 120 K during illumination for 15,000 s; (b) photoproduct spectra normalized to equal area; spectra in red: overall change within each data set; arrows indicate time progression; dotted line: overall population.

CO. At longer times, the fraction of photodissociated A_{II} molecules increases, and the FTIR absorbance spectra of the photoproducts shift distinctly. The overall absorbance differences between times $t_{initial}$ = 1 s and t_{final} = 15,000 s are represented by red lines. For the photoproducts, two peaks at 2130 and 2135 cm^{-1} emerge over time, which we tentatively associate with a new intermediate state, C''. The normalized photoproduct spectra in Fig. 3.57 b show an isosbestic point. Moreover, the difference spectrum (red line) reveals that CO stretch bands below 2127 cm^{-1} lose intensity ($B(A_{II})$?, C'?) under extended illumination, while the two peaks at 2130 and 2135 cm^{-1} increase.

3.2.4.2 FTIR Absorbance Difference Spectra after Slow Cooling from 160 to 3 K

We have seen that, depending on the illumination protocol, photolyzed ligands explore different intermediate sites. Spectroscopically, we have identified sites $B(A_I)$, $B(A_{II})$, C' and C''. To populate all these intermediates in one experiment, we have used the slow-cool protocol, in which we cool the MbCO samples from 160 to 3 K under illumination. FTIR transmission spectra were recorded at 3 K and referenced against transmission spectra collected at 3 K after cooling in the dark. In the region of the photodissociated CO, we thus obtain a superposition of all photoproducts that were populated during the cooling.

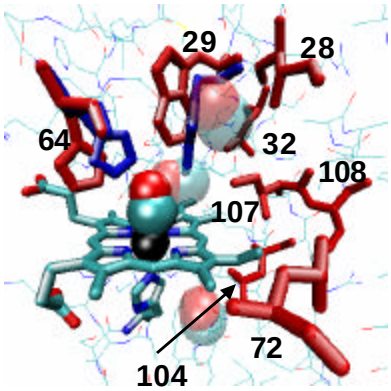

In Fig. 3.58, we compare the FTIR spectra of L29W, L29W/L72F (modified Xe 2 cavity) and L29W/L104W (blocked Xe 1 cavity). For L29W, we have added the IR spectrum (dotted line) at 3 K after illumination for 1 s. In the spectral range of heme-bound CO, we clearly notice a pronounced increase in the photoproduct yield under slow-cool illumination instead of 1 s photolysis at 3 K. Comparison with the total bound CO spectrum reveals complete photolysis upon slow cooling under illumination. Moreover, we observe a significantly changed spectrum for the photodissociated CO. Whereas a strong peak at 2122 cm^{-1} is characteristic of the photoproduct after 1 s illumination at 3 K, the spectrum after slow-cool illumination shows a dominant peak at 2126 cm^{-1} and a weaker one at ~2133 cm^{-1} for all three samples. L29W and L29W/L72F both show a small shoulder at 2118 cm^{-1} which is missing for L29W/L104W.

In Fig. 3.59, spectra of mutants L29W/L32T, L29W/I107W and L29W/S108L are shown. Residues 32 and 107 line the Xe 4 cavity, residue 108 forms the borderline between Xe 2 and solvent. Again we have included the spectra of L29W after short (dotted black line) and extended illumination (solid black line). Samples L29W and L29W/S108L display discrete A_I and A_{II} bands, with L29W/S108L greatly favoring substate A_I. In the photoproduct region, both mutants display the new dominant peak at 2126 cm^{-1}. For L29W/S108L, an additional and rather strong band appears at 2138 cm^{-1}; the one at 2133 cm^{-1} is only visible as a shoulder.

Double mutants L29W/L32T and L29W/I107W show markedly different IR spectra. In the bands of heme-bound CO, we realize significant deviations from the typical A_I and A_{II} bands of L29W, and the same holds true for the photoproducts. Both of these mutants reveal a similar and not well-structured absorbance spectrum in the photoproduct region.

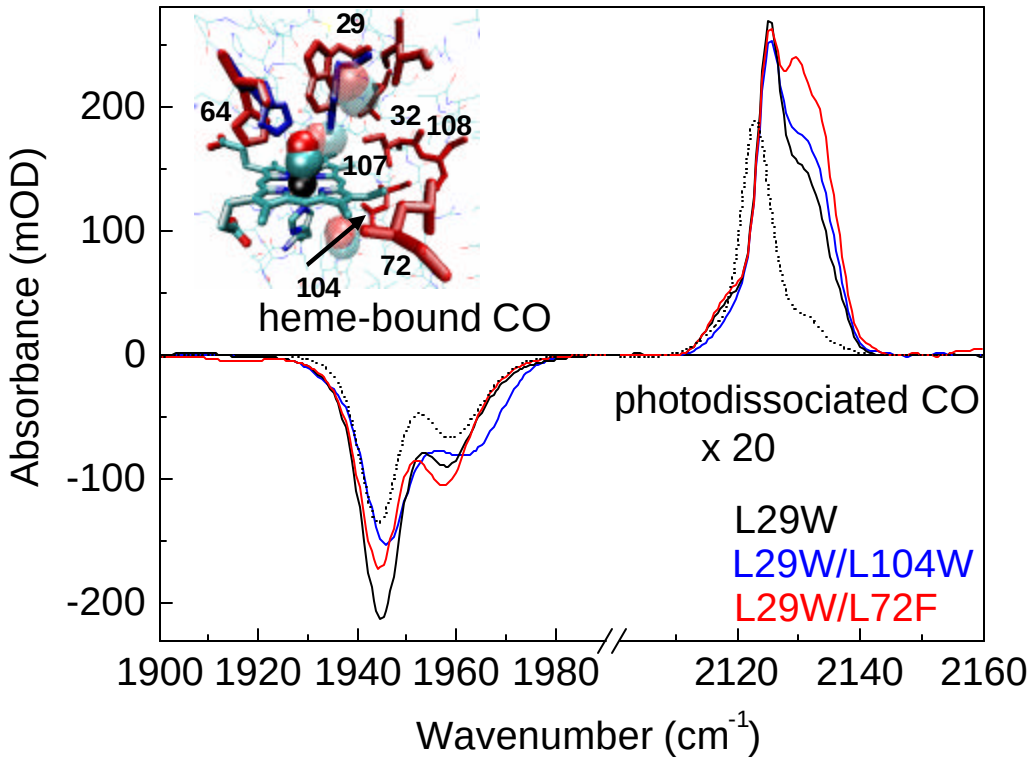

Fig. 3.58: FTIR spectra of heme-bound and photodissociated CO of L29W, L29W/L72F and L29W/L104W after slow cooling under illumination from 160 to 3 K (solid lines) and of L29W after 1-s illumination at 3 K (dotted line); inset: sketch of the active site.

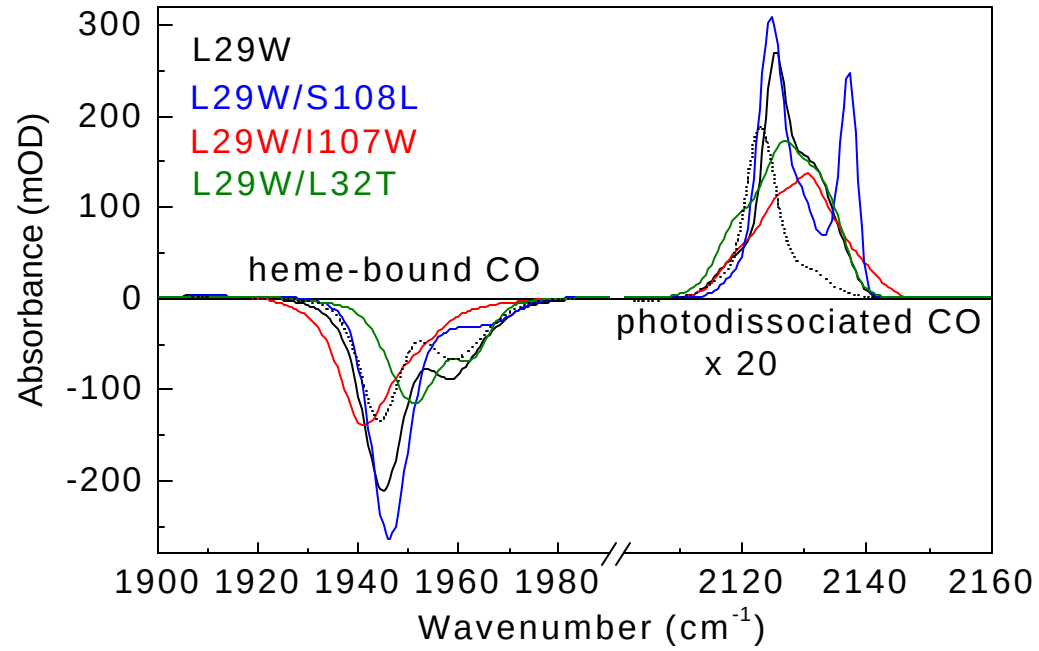

Fig. 3.59: FTIR spectra of heme-bound and photodissociated CO of MbCO mutants L29W, L29W/L32T, L29W/I107W and L29W/S108L after slow cooling from 160 to 3 K (solid lines) and of L29W after 1-s illumination at 3 K (dotted line).

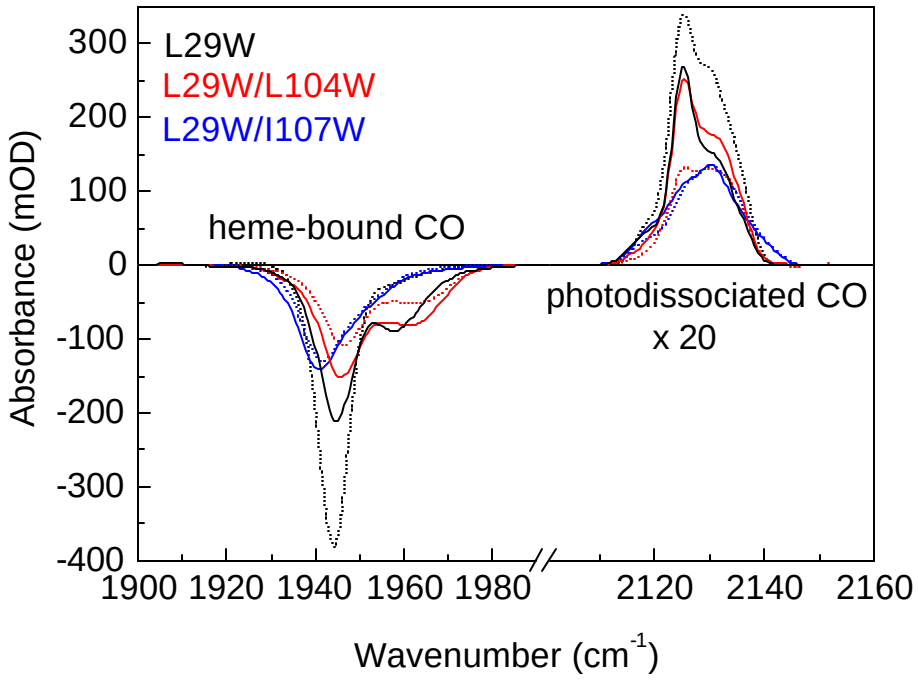

Fig. 3.60: CO stretch bands of MbCO mutants L29W, L29W/I107W and L29W/L104W after slow cooling under illumination from 160 to 3 K; solid lines: samples without xenon; dotted lines: the identical samples after equilibration with 1 atm of xenon.

To examine the effect of blocking internal cavities by xenon, Fig. 3.60 shows the spectra of samples L29W, L29W/I107W and L29W/L104W before and after equilibration with 1 atm of xenon. The spectral changes in the bands of heme-bound CO have already been discussed in section 3.2.1.1. The photoproduct spectra of L29W differ mainly in the intensity. Hardly any change is observed for L29W/I107W. L29W/L104W displays a decreased photoproduct yield in both spectral regions. Whereas the photolyzed populations of A_I and A_{II} decrease by about the same amount, the photoproduct at ~2126 cm^{-1} shows a much more pronounced loss than the band at 2133 cm^{-1}.

3.2.4.3 TDS after Slow Cooling from 160 to 3 K

To disperse the different intermediates generated by slow cooling according to their rebinding temperature, we performed a TDS experiment subsequent to slow cooling. In Fig. 3.61, the TDS contour plots of L29W and related double mutants are compiled.

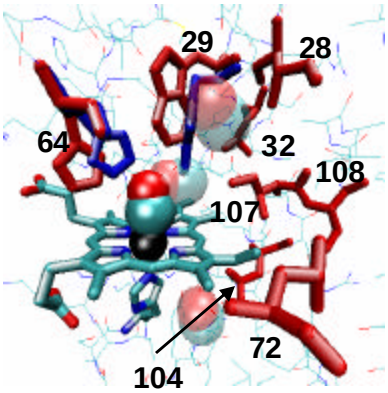

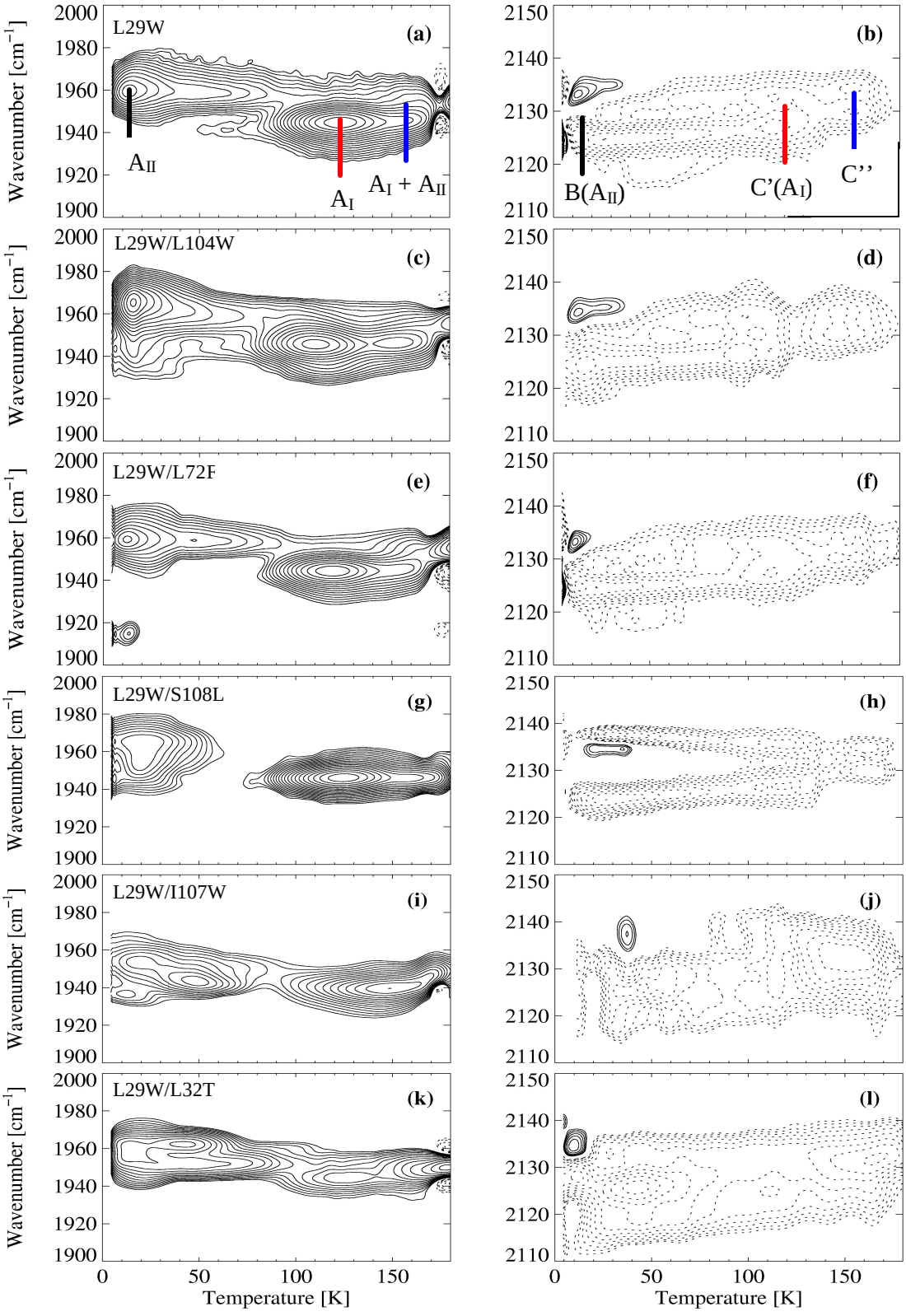

Fig. 3.61: TDS contour maps of L29W MbCO and related double mutants after slow cooling from 160 to 3 K under illumination.

Below 70 K, the A state map (Fig. 3.61 a) of L29W shows only rebinding to A_{II}. Consequently, all CO ligands in Mb molecules of substate A_I have migrated away from the initial docking site B to remote locations. Rebinding in A_I occurs in the temperature range from 90 to 170 K from apparently two subpopulations, as suggested by the maximum at 120 K and the shoulder at 150 K. The corresponding map of the photoproducts (Fig. 3. 61 b) reveals an exchange within the photolyzed population below 30 K. Up to 80 K, recombination predominantly occurs from a band at 2125 cm^{-1}. At 120 K, the map depicts rebinding from two bands associated with C' at 2126 and 2133 cm^{-1}. Around 140 K, the contours clearly display a shift in band positions and thus indicate recombination from a spectroscopically different intermediate state. The corresponding CO stretch bands at 2130 and 2135 cm^{-1} represent intermediate C''.

The TDS maps of the double mutants related to L29W (Fig. 3. 61 c-l) reveal certain similarities. In the A substate maps on the left, we observe recombination to A_{II} with broadly distributed recombination barriers, as evidenced from the stretched contours from the lowest temperatures up to ~100 K. In contrast, recombination to A_I occurs from two subpopulations peaking at 120 and 150 K. The shoulders on the blue side of the A_I contours at ~160 K indicate additional recombination to A_{II}.

Mutants L29W/L104W (Fig. 3. 61 c, d), L29W/L72F (panels e, f) and L29W/S108L (panels g, h) have additional structural modifications that are not in the direct vicinity of the active site. They were chosen to influence sites Xe 2 (positions 72 and 108) and Xe 1 (position 104 on the proximal side). Thus, all three mutants are expected to show a recombination pattern similar to L29W as long as the CO ligands remain in the distal pocket. The contour maps of heme-bound CO indeed show similar features. All corresponding photoproduct maps exhibit recombination from the band at 2125 cm^{-1} up to 80 K, the rebinding from C' at ~120 K and from C'' above 140 K. An additional feature is seen for L29W/S108L. The photoproduct map reveals changes in a band at 2138 cm^{-1} that span the temperature range from 3 to 100 K.

Mutants L29W/I107W (Fig. 3. 61 i, j) and L29W/L32T (panels k, l) were both designed to modify the local structure of the Xe 4 cavity. Mutant L29W/I107W is expected not only to decrease the volume of the Xe 4 pocket, but also to at least partially block the pathways to Xe 2 and Xe 1. L29W/L32T introduces a polar hydroxyl group into the Xe 4 cavity. For L29W/I107W, recombination below 70 K shows contributions from both A substates. At 150 K, recombination occurs mainly to A_I. The map of the photodissociated population appears perplexing. Individual photoproduct bands can hardly be discerned. In mutant L29W/L32T, three A state bands are discernible. In addition to A_I at 1945 cm^{-1}, we observe two bands at 1955 and 1963 cm^{-1} which develop from a single band at 20 K and recombine ligands at ~40 K. A_I exhibits rebinding at 120 K, typical of CO ligands returning from C'. At temperatures above 150 K, recombination to A_{II} dominates.

To shift the population of A substates towards A_I by binding of xenon, the slow-cool TDS experiments were repeated on L29W(Xe), L29W/L104W(Xe) and L29W/I107W(Xe). These contour plots are displayed in Fig. 3.62. Panels a and b show maps of L29W(Xe). The fraction of A_{II} has decreased drastically, and we observe rebinding to both A_I *and* A_{II} below 80 K, indicating that a significant fraction of the CO ligands in Mb molecules in substate A_I cannot migrate away from the initial docking site B. The relative population of CO ligands in intermediate C'' as compared to C' has also increased. While mutant L29W/L104W displays similar changes, the presence of xenon has no obvious influence on L29W/I107W. In the maps of the photoproducts, we observe qualitatively similar features as in the plots without xenon.

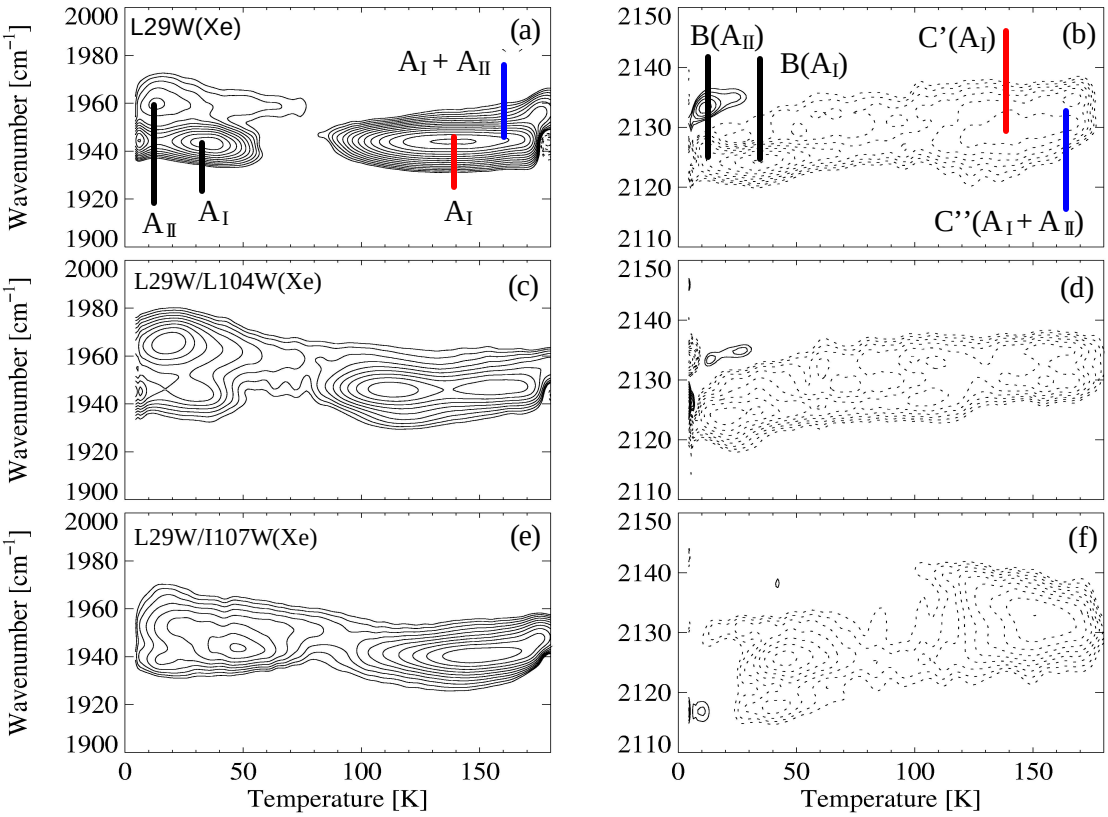

Fig. 3.62: TDS contour maps after slow cooling from 160 K to 3 K under illumination for MbCO mutants L29W, L29W/L104W and L29W/I107W, equilibrated with 1 atm of Xe at 0° C.

Fig. 3.63 displays the CO stretch spectra of the C' (peaks at 2127 and 2133 cm^{-1}) and C'' (peaks at 2130 and 2135 cm^{-1}) intermediates for all L29W mutants. To obtain these spectra, absorbance differences were calculated from the TDS data, choosing temperature intervals between which the desired photoproduct predominantly rebound, i.e. 110 to 120 K for C' (red lines), and 150 to 160 K for C'' (blue lines). Spectra were normalized to equal area. Black lines depict the absorbance change from 80 to 160 K. The similarities between most mutants are obvious. For L29W/I107W and L29W/L32T, the spectra assigned to C' and C'' differ considerably from those of L29W, indicating that these two mutations have altered the local environment of the CO ligand in both intermediate states, C' *and* C''.

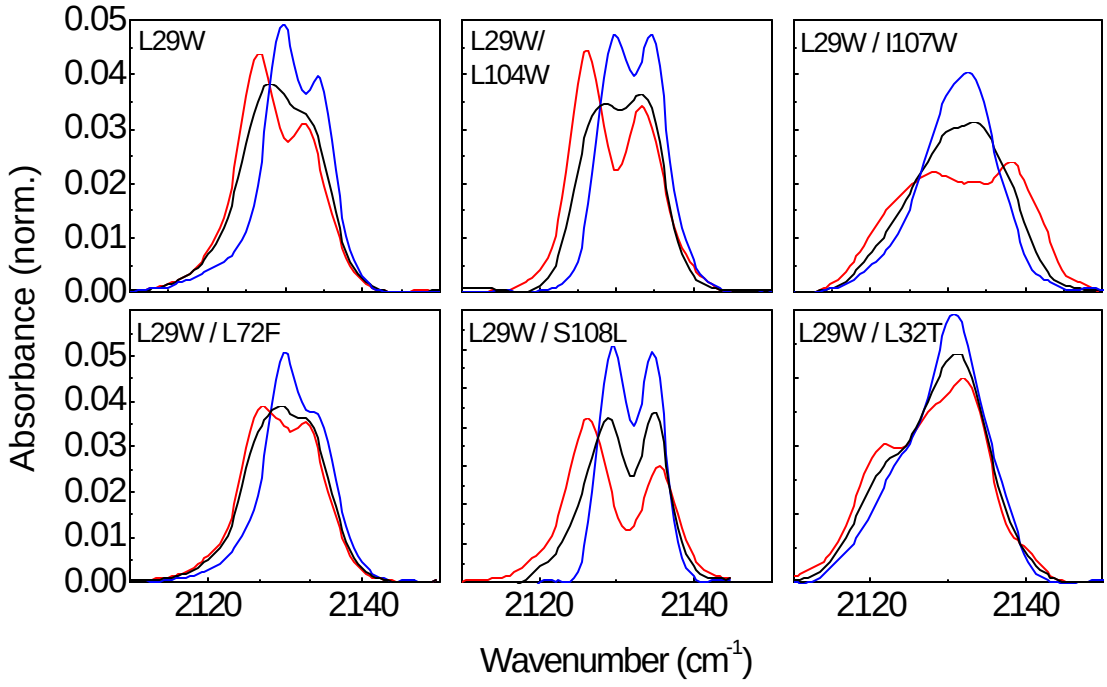

Fig. 3.63: CO stretch bands associated with intermediates C' and C'' of L29W MbCO and related double mutants, calculated from the TDS data in Fig. 3.59; red lines: C'; blue lines: C''; black lines: combined contributions of C' and C''.

3.2.4.4 Isothermal Illumination at 160 K

The TDS data after slow cooling under illumination from 160 to 3 K showed a temperature of ~160 K for ligands rebinding from site C''. To explore possible pathways to further intermediate states, we illuminated L29W for 15,000 s at 160 K. Fig. 3.64 displays the temporal development of the CO spectra during illumination (Fig. 3.64 a, b) and in the dark afterwards (Fig. 3.64 c, d). They were obtained by referencing FTIR transmission spectra recorded at time t against a single transmission spectrum taken in the dark at $t = 0$. The dotted lines in panels a and c represent the absorbance difference upon complete photolysis.

Extended illumination results in an increased photoproduct yield in both A_I and A_{II} (red line in Fig. 3.64 a). The concomitant absorbance change in the bands of photodissociated CO is depicted by the blue line in panel b, indicative of C''. The subsequent relaxation in the dark, Fig. 3.64 c, reveals that ligands recombine exclusively to A_I. A significant fraction rebinds very quickly (within 1s). The absorbance difference between the first two spectra of the photoproducts (Fig. 3.64 d, red line) is caused by these fast rebinders; they originate from C'. The slowly rebinding fraction displays the spectrum of C'' (blue line, Fig. 3.64 d). In contrast, the photodissociated population of protein molecules in the A_{II} conformation does not change. The population that does not rebind at 160 K within 50,000 s (green line, Fig. 3.64 d) displays a broad band peaking at ~2130 cm^{-1}.

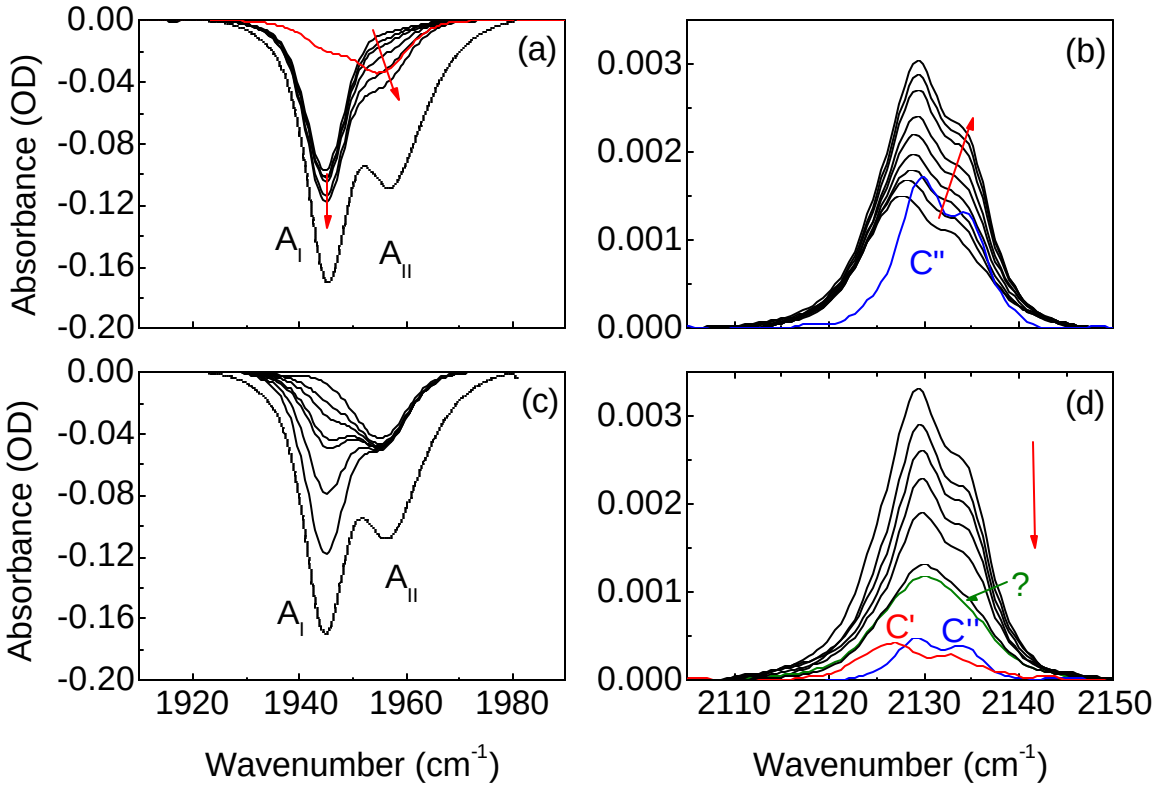

Fig. 3.64: Temporal development of the CO stretch bands of MbCO mutant L29W at 160 K; (a) heme-bound and (b) photolyzed ligands during illumination for 15,000 s; (c) heme-bound and (d) photolyzed ligands after termination of the illumination for 50,000 s; colored spectra: absorbance changes within each data set (for details see text); arrows indicate time progression; dotted lines: overall A band spectra.

3.2.4.5 TDS after Isothermal Illumination at 160 K

Monitoring the relaxation of the L29W MbCO sample at 160 K revealed that CO ligands rebound from intermediate C'', but only those in protein molecules in the A_I conformation. Molecules in A_{II} remained photodissociated even after 50,000 s, suggesting that access to the heme iron is completely blocked. To obtain information on the recombination temperatures of these residual ligands, we performed a FTIR/TDS experiment directly after 15,000 s illumination at 160 K. In Fig. 365 a, three different features can be distinguished in the A substate map. From 160 to 180 K, recombination occurs from intermediate C''. Between 180 and 195 K, the A substate map shows both positive and negative features, indicative of an exchange between A_I and A_{II}. Above 190 K, a pronounced peak represents recombination from a new intermediate. This process happens at markedly higher recombination temperatures as compared with ~160 K for C''. The spectrum of this intermediate is rather broad and peaks at ~2128 cm^{-1}. We call this intermediate state D.

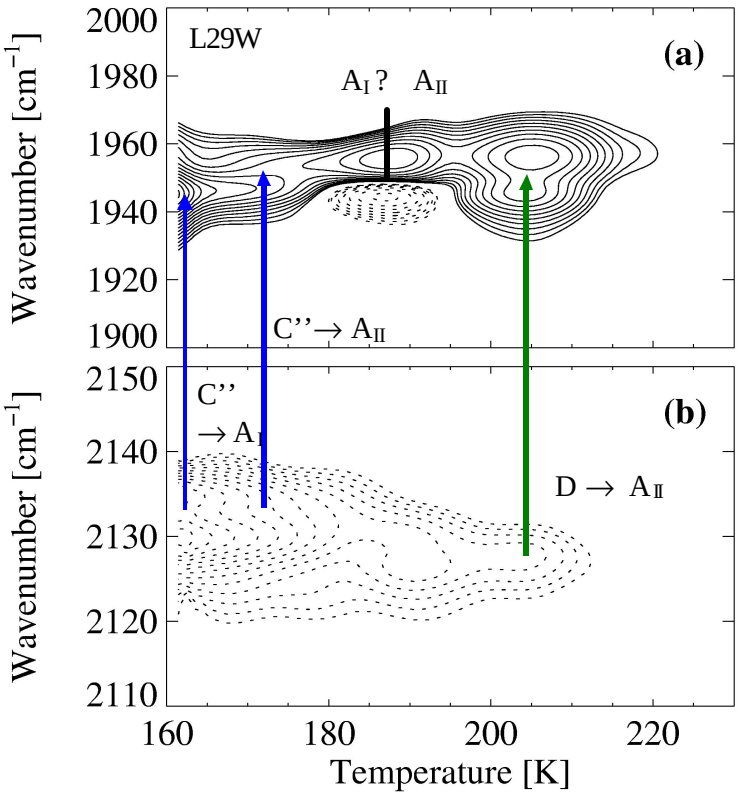

Fig. 3.65: TDS contour maps of MbCO mutant L29W after illumination for 15,000 s at 160 K.

3.2.4.6 TDS after Slow Cooling from 160 to 100 K

We have thus gathered evidence of two additional intermediate states C'' and D. In glycerol/buffer solvent, recombination from site C'' occurs below and recombination from site D above the dynamic transition temperature. We used different cryo-solvents with markedly different glass transition temperatures, glycerol/buffer, trehalose/buffer and dried trehalose/buffer to examine if these processes are coupled to the dynamics of the solvent. The L29W MbCO samples were slowly cooled under light from 160 K to 100 K. Subsequently, TDS experiments were performed. Fig. 3.66 shows the contour maps.

For L29W in glycerol/buffer, recombination occurs at 120 K from C' to A_I and at 160 K from C'' (Fig. 3.66 a, b). A substate interconversion occurs around 180 K. In a saturated trehalose solution (Fig. 3.66 c, d), A_I is the dominant substate; it exchanges with A_{II} at ~220 K, as indicated by positive and, hardly visible, negative contours in panel c. CO ligands return to A_I from C' at ~120 K. Around 160 K, the photoproduct bands shift from C' to C''. Concomitantly, the A state map signals a transition from recombination in A_I to recombination in A_{II}. The dried trehalose sample consists mainly of MbCO in substate A_{II} (Fig. 3.66 e, f); recombination from C' to A_I is not discernible. Instead, recombination from a band at 2130 cm^{-1} to A_{II} is most pronounced around 180 K. This band reminds one of the broad and rather featureless photoproduct spectrum assigned to the A_{II} conformation, which does not show rebinding at 160 K (Fig. 3.64 d).

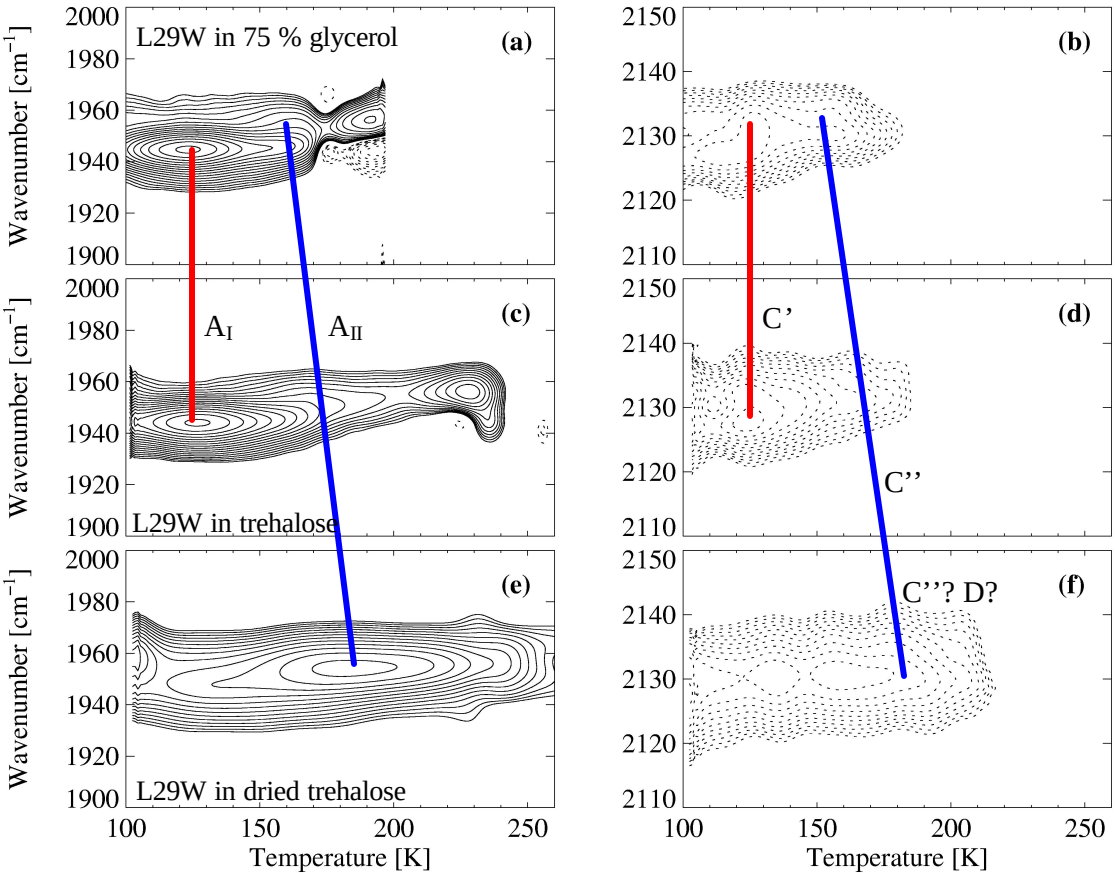

Fig. 3.66: TDS contour maps of L29W MbCO in different cryo-solvents after slow cooling from 160 to 100 K under illumination.

Red and blue lines (Fig. 3.66) connect the corresponding populations within the different maps. Choosing a different cryo-solvent does not change the temperature for recombination from C' to A_I, implying that this process is completely decoupled from the solvent dynamics. Rebinding from C'', by contrast, appears to be coupled to the solvent dynamics.

3.2.4.7 Interpretation and Discussion: Structural Interpretation of Intermediate Site C''

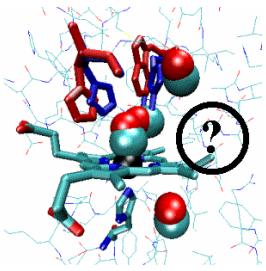

The FTIR/TDS characterization of photoproduct intermediates C' and C'' in L29W and related double mutants (Fig. 3.61) enables us to make conclusions as to where the CO resides in these intermediates. In mutant L29W/L104W, the voluminous tryptophan occludes the proximal cavity Xe 1. Yet, this mutant displays CO stretch bands typical of C''. Consequently, we can exclude the proximal cavity Xe 1 as a potential location of ligands in C''. Furthermore, cavity Xe 2 can be ruled out because the CO bands associated with C'' of mutants L29W/S108L and L29W/L72F are identical to those of L29W, implying an identical environment of the ligand. Especially for L29W/L72F, we would expect a strong effect on the stretch frequency if the CO ligands were in Xe 2, since the small sidechain of serine 108 has been replaced by a voluminous aromatic

sidechain. Only for L29W/I107W and L29W/L32T, the CO spectra assigned to C' and C'' differ considerably from those of L29W, implying that residues 32 and 107 are both in close contact with the CO not only in C', but also in C''. Residues 32 and 107 line the back of the distal pocket at the Xe 4 site. Therefore, we conclude that the CO resides in the Xe 4 cavity in both C' and C''. We remind you that the Xe 4 cavity is *not* populated at all in A_{II} molecules (compare section 3.2.3.4).

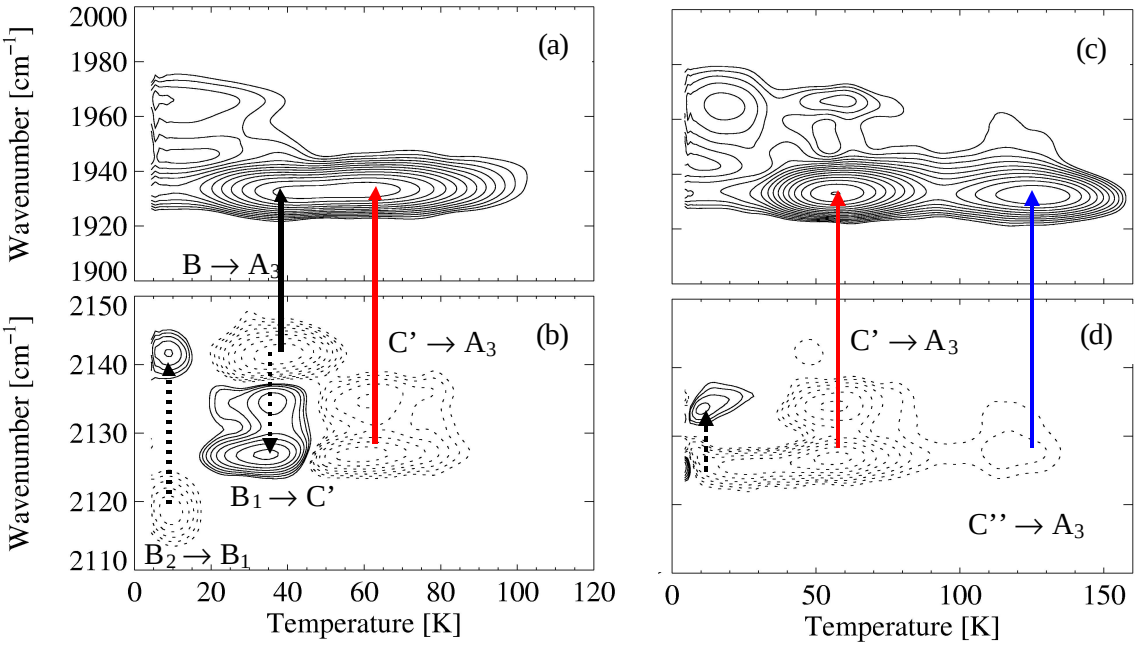

Fig. 3.67: TDS maps of YQR MbCO after illumination for 1 s at 3 K (a, b) and slow cooling under illumination from 140 to 3 K (c, d).

To change the spectral fingerprint from C' to C'', the protein has to rearrange around the CO ligand and/or the ligand has to reorient within the cavity. Due to the lack of structural data on C'' in mutant L29W, we refer to myoglobin mutant YQR (L29Y/H64Q/T67R), which also has an aromatic amino acid at position 29. FTIR/TDS experiments have revealed significant similarities to L29W (110). In Fig. 3.67, we plot the TDS maps after illumination for 1 s at 3 K and slow cooling under light from 140 to 3 K. Recombination from the primary docking site B to taxonomic substate A_3 at 1933 cm^{-1} peaks at ~30 K. Furthermore, ligands migrate by thermal activation to intermediate site C', as depicted by the dotted arrow pointing downwards in Fig. 3.67 b. At ~60 K, ligand rebinding occurs predominantly from the secondary docking site C', in which the CO ligand is trapped in the Xe 4 cavity, as shown by cryo-crystallography of photolyzed YQR MbCO crystals at 40 K (18). Rebinding from kinetic state C'' occurs around 130 K. Clearly, recombination from intermediates C' and C'' is much more separated in temperature in YQR (60 and 130 K) than in L29W MbCO (120 and 160 K), which makes it much easier to isolate the two intermediates. To study the structure of C'', we photolyzed YQR MbCO crystals while slow cooling from 180 to 105 K to trap CO ligands exclusively in intermediate C'' (120). At 105 K, x-ray diffraction data were collected in the dark. In Fig. 3.68, we superimpose the structures of photoproducts C' taken from (18) in blue and C'' obtained from (120) in red. We see that the transition from C' to C'' involves movements of residues 29 and 64 deeper into the distal pocket. Whereas the movement of Y29 is minor, Q64 approaches the heme iron and sterically hinders recombination. To allow for this rearrangement, the whole E helix has to shift slightly, as depicted in Fig. 3.69.

Consequently, this protein motion is coupled to the solvent dynamics. Only when the solvent allows for the helix to rearrange, can site C'' be generated.

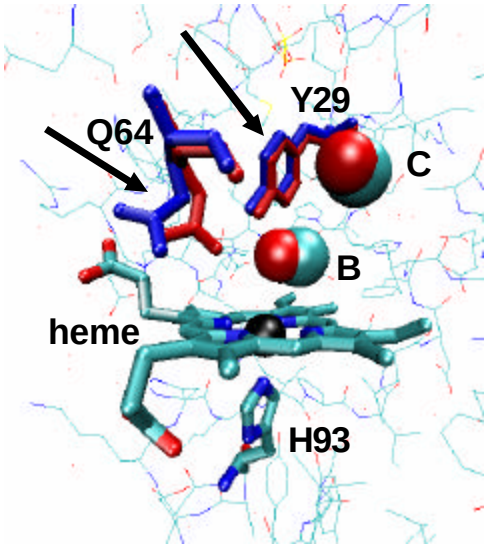

Fig. 3.68 : Superposition of the three-dimensional structures of C' (blue) and C'' (red) intermediates of YQR mutant MbCO.

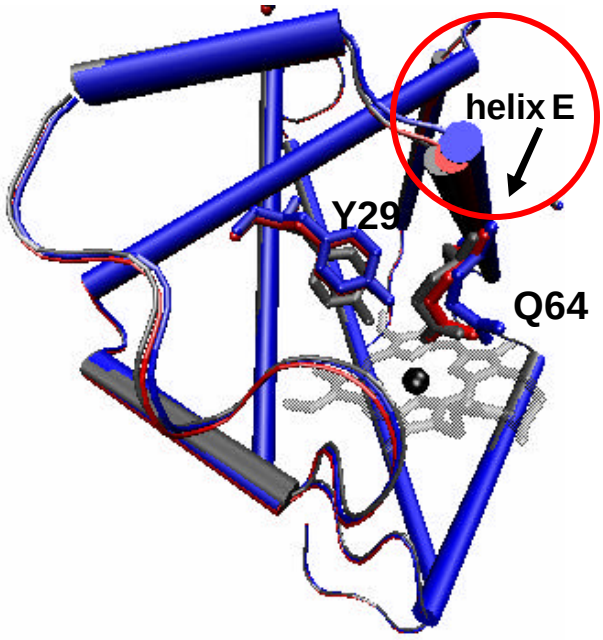

Fig. 3.69: Superposition of cartoons of YQR MbCO structures: C' (blue) ,C'' (red) and deoxy YQR (dark gray).

In analogy to YQR, we propose that intermediate C'' in mutant L29W is characterized by CO ligands located within the Xe 4 cavity, surrounded by a protein in conformation A_I that has partially relaxed toward the A_{II} conformation. This model is supported by the observation that recombination from site C'' is dependent on the solvent composition. In trehalose/buffer, the dynamic transition temperature is shifted to higher temperatures compared to glycerol/buffer. Consequently, the repositioning of residues 29 and 64 asks for higher temperatures in trehalose as was observed in the TDS experiment displayed in Fig. 3.66. We emphasize that photoproducts B and C' are generated by ligand migration, whereas protein motions are responsible for intermediate state C''.

For L29W in dried trehalose, we do not see the characteristic spectrum of C''. As we find only A_{II} molecules within this sample, this comes as no surprise. Thus, we suggest that recombination to A_{II} at ~180 K occurs from a different ligand location, most likely from the site we have called D (Fig. 3.65).

3.2.5 Photoproducts in a Fluctuating Protein

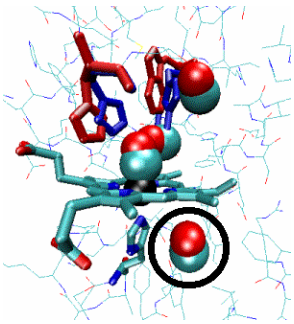

As of yet, we have described photoproducts B, C' and C'' which exist in a protein essentially arrested by the surrounding solvent glass. Only for the transition from C' to C'' there is evidence of small conformational rearrangements of the protein chain. TDS experiments after extended illumination gave first indications of an additional intermediate D, from which recombination occurs at ~190 K in glycerol/buffer solvent, above the glass transition of the solvent (Fig. 3.65). Consequently, conformational transitions leading to this intermediate are expected to involve large-scale protein motions.

3.2.5.1 TDS under Illumination

To induce ligand migration and protein motions, the temperature was ramped under illumination from 100 to 220 K. Thus, the ratio of ligand-bound and photolyzed protein molecules was defined by the temperature-dependent competition between photolysis and recombination. Samples L29W, L29W/L104W and L29W/S108L were investigated in detail. The contour maps in Fig. 3.70 display a multiplicity in positive and negative contours.

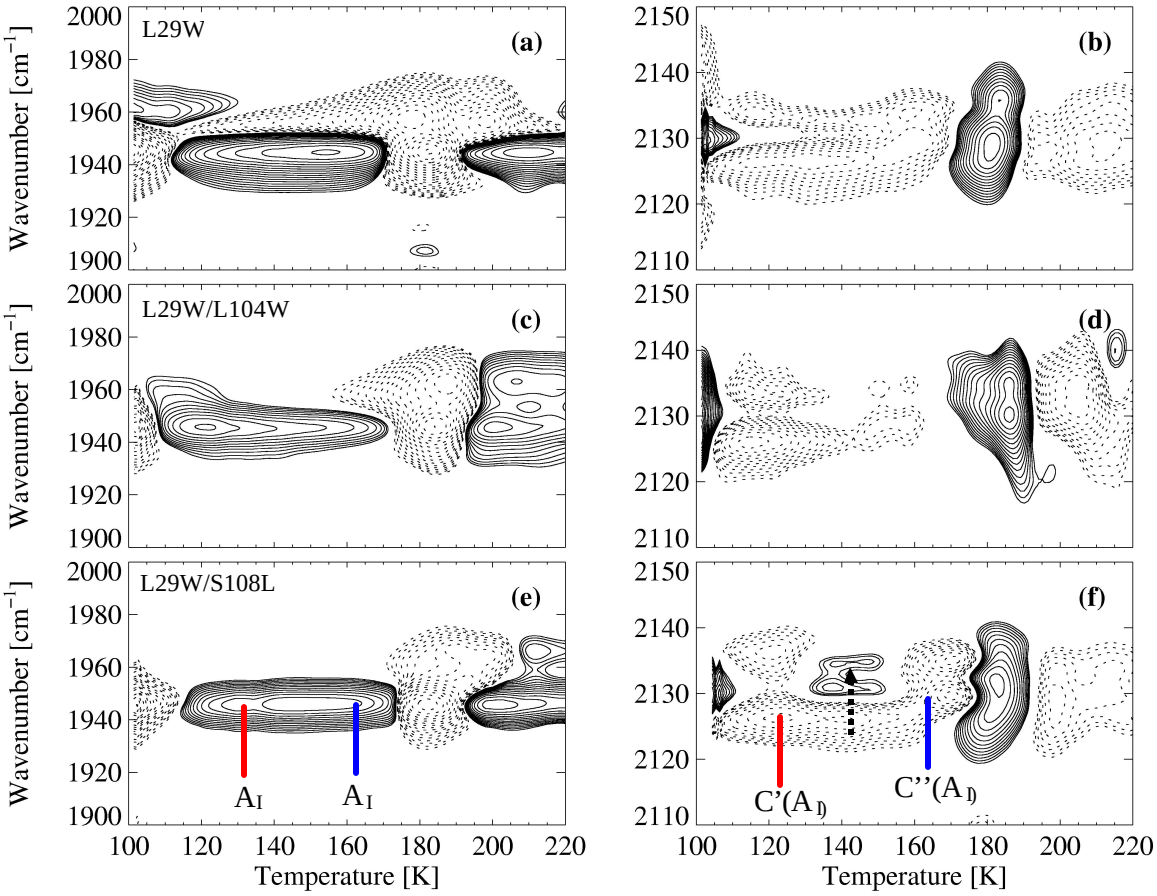

Fig. 3.70: TDS maps of L29W MbCO and related double mutants collected while ramping the temperature from 100 to 220 K under illumination.

For L29W, the map of the heme-bound CO (panel a) shows an increased photolysis of A_I (dotted contours) and recombination to A_{II} (solid contours) up to 110 K. Between 120 and 170 K, recombination occurs to A_I, whereas the photodissociated fraction of A_{II} increases. At 180 K, both substates show increasing photolysis. At 200 K, the photodissociated fraction of A_{II} further increases, while we observe recombination in A_I. Double mutants L29W/L104W and L29W/S108L exhibit a similar behavior (panels c and e).

The photoproduct TDS map of L29W (panel b) helps to explain this puzzling behavior: In A_I, CO ligands populate state C' around 100 K (solid contours). CO ligands recombine to A_{II} from site B(A_{II}). Between 120 and 170 K, recombination to A_I occurs from C' (below 150 K) and C'' (above 150 K). Moreover, CO ligands in A_{II} molecules are photodissociated and some of them get trapped in D. Positive signals around 180 K signal net photolysis into site D for both substates. Recombination from intermediate D is observed at 200 K.

The TDS maps of mutant L29W/L104W in Fig. 3.70 d again shows very similar behavior at temperatures up to 180 K. A closer look, however, reveals that the FTIR absorbance bands of the photoproducts D of L29W/L104W peak at 2130 and 2135 cm^{-1}, whereas the bands of L29W show a maximum at ~2128 cm^{-1}. In mutant L29W/S108L, recombination in A_I occurs from C' at around 120 K (compare the slow-cool experiment in Fig. 3.61). At temperatures between 130 and 150 K, an exchange within the photolyzed fraction is apparent, showing that photolyzed protein molecules in the A_I substate (partially) relax towards A_{II} and thus generate photoproduct C''. We emphasize that the C' to C'' transition arises from protein (and possibly ligand) motions and not ligand migration alone. At temperatures around 160 K, recombination occurs from C'' only. At ~190 K, we notice photolysis to D and subsequent recombination.

3.2.5.2 Isothermal Kinetics at 180 K

The previous TDS experiments indicated that site D is efficiently populated at ~180 K. To obtain further insight, MbCO samples L29W and L29W(Xe) were studied by FTIR spectroscopy at 180 K. In the first part of the experiment, samples were illuminated for 15,000 s, and subsequently they were allowed to recombine in the dark for another 50,000 s. FTIR transmission spectra were taken continuously and referenced to a single transmission spectrum taken at 180 K without prior illumination.

Selected data are compiled in Fig. 3.71. Illumination of L29W (Fig. 3. 71 a) results in an increasing photolyzed fraction of both substates. The overall change is depicted in red in panel a. The spectrum of the corresponding photoproduct (Fig. 3. 71 b, red line) is rather broad and featureless. Recombination occurs mainly to A_I, although most ligands do *not* recombine within 50,000 s (Fig. 3. 71 c). The photoproduct spectrum of those ligands that rebind (Fig. 3. 71 d, red line) is very similar to that representing the total photolyzed fraction. In sample L29W(Xe), ligands from substate A_I are photodissociated (Fig. 3. 71 e) and give rise to a photoproduct spectrum with two distinct bands at 2130/2135 cm^{-1}, which we have earlier assigned to C'' (compare Fig. 3.61). When illumination is terminated (Fig. 3. 71 g), *most* of these CO ligands recombine (red line in Fig. 3. 71 g) from intermediate C'', as evidenced by the FTIR stretch bands at 2130/2135 cm^{-1} (red line in Fig. 3. 71 h). The CO ligands that do not rebind (blue line, Fig. 3. 71 h) exhibit a broad band similar to the one of the photoproduct of L29W without xenon.

The distinctly different photoproduct spectra of L29W and L29W(Xe) indicate different local environments of the CO molecules. Whereas in L29W(Xe) the CO ligands appear to be trapped in Xe 4, at the present stage of our investigations we can only speculate about the actual location of photodissociated ligands in L29W.

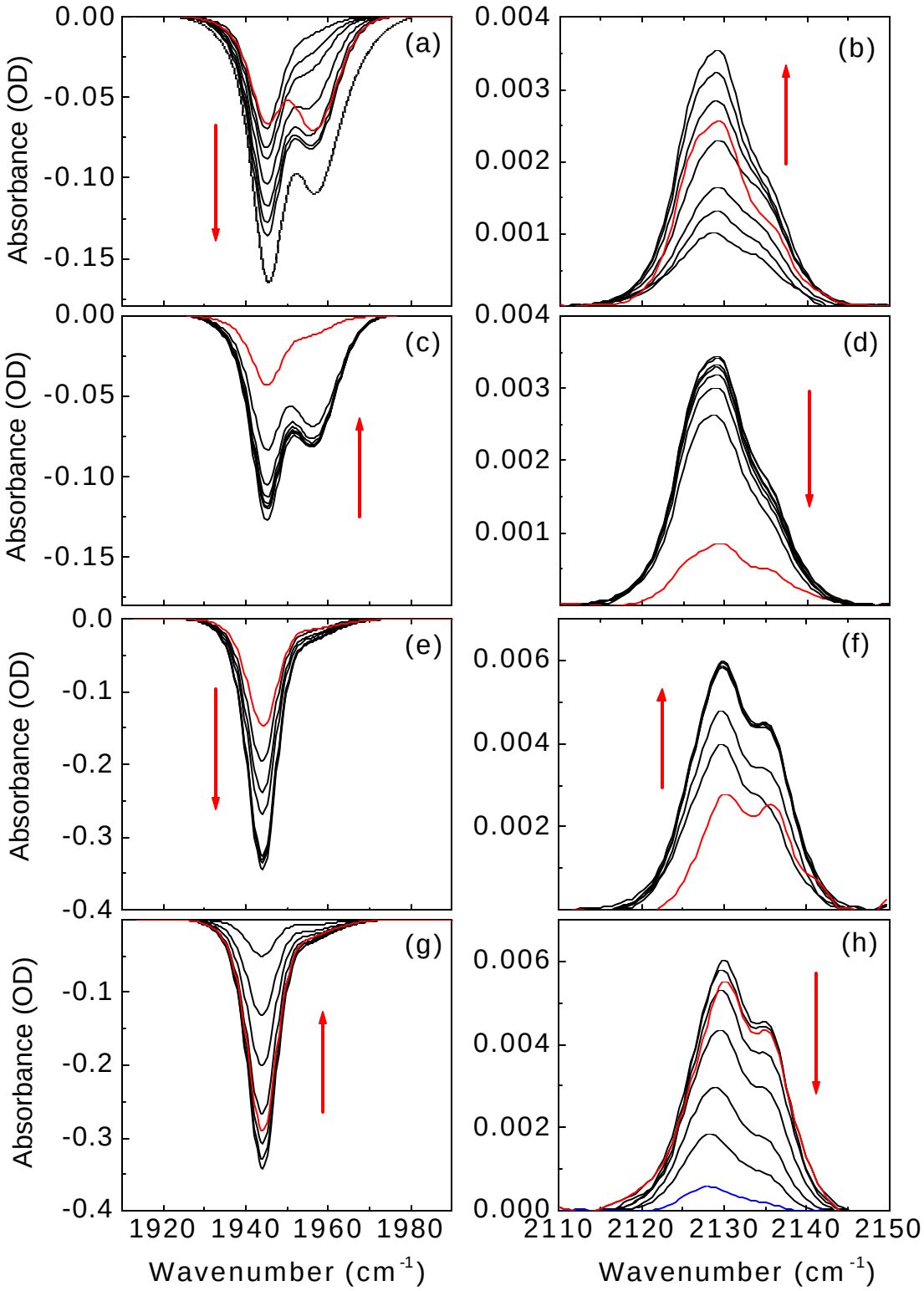

Fig. 3. 71: Temporal development of the IR stretch bands of (left column) heme-bound and (right column) photodissociated CO in samples L29W and L29W(Xe) at 180 K during 15,000 s of illumination and subsequent 50,000 s in the dark; (a, b) L29W during illumination and (c, d) in the dark; (e, f) L29W(Xe) during illumination and (g, h) in the dark; spectra in red: overall change within each data set; arrows indicate time progression.

To demonstrate the different responses of the two samples to light, the integrated absorbances of the A state bands during illumination and recombination in the dark are plotted as a function of time in Fig. 3.72.

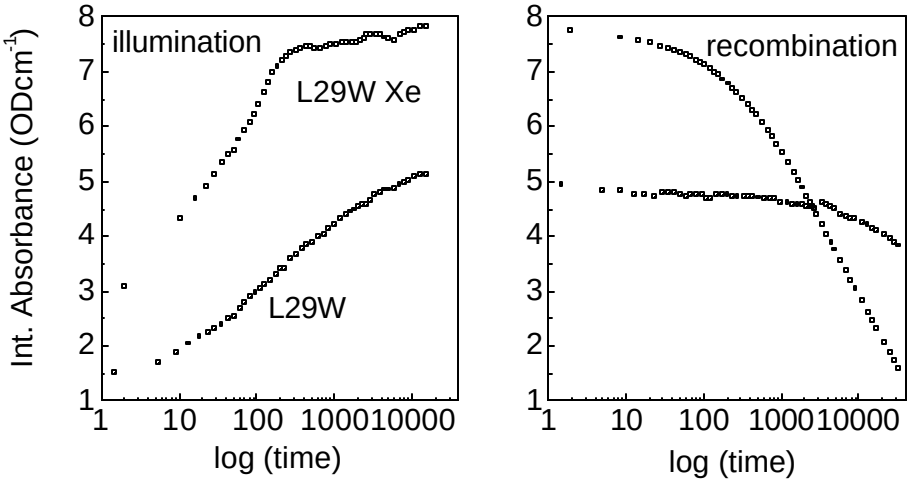

Fig. 3.72: Temporal evolution of the integrated absorbances of the FTIR bands of heme-bound CO under illumination and during subsequent rebinding in the dark.

3.2.5.3 FTIR Spectra after Illumination at 185 K and Slow Cooling under Light to 160 K

The isothermal kinetics experiments on L29W and L29W(Xe) have shown that both samples respond differently to prolonged illumination at 180 K. To examine these effects also in the related double mutants, these were illuminated at 185 K for 2 hours. Subsequently, the temperature was ramped to 160 K under light, and transmission spectra were collected and referenced against a transmission spectrum measured at 160 K without prior illumination to obtain absorbance difference spectra. We have plotted the spectra of L29W/L72F, L29W/L104W and L29W/I107W in Fig. 3.73. Also included is the spectrum of L29W obtained by the identical protocol. In the bands of heme-bound CO, we observe absorbance signals of 150 mOD and more, reflecting a high photoproduct yield. For the photodissociated CO in L29W, we notice a broad band peaking at 2130 cm^{-1} with a distinct shoulder at 2135 cm^{-1} and an additional broadening at 2128 cm^{-1}. Mutants L29W/L107W and L29W/L72F display similar spectra. L29W/L104W however, exhibits two distinct components.

We repeated the slow-cool experiment on L29W(Xe), L29W/I107(Xe) and L29W/L104W(Xe). The spectra with and without xenon are compared in Fig. 3.74. While the spectra of L29W/L104W and L29W/I107W with and without xenon differ only by a scaling factor, the spectrum of L29W is altered over the whole spectral range. In the region of heme-bound CO, xenon shifts the A_I/A_{II} equilibrium almost completely to A_I. The FTIR stretch bands of the photoproducts of L29W(Xe) display two bands at 2130 and 2135 cm^{-1}, characteristic of the C'' intermediate.

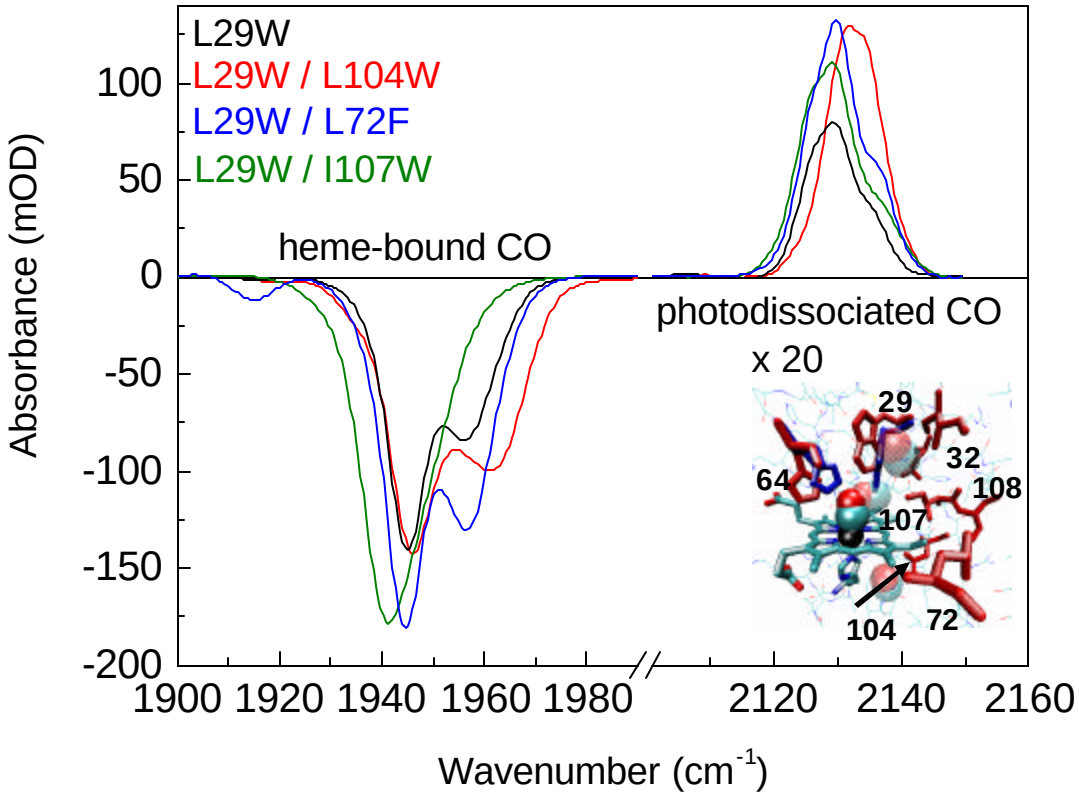

Fig. 3.73: FTIR spectra of MbCO mutants L29W, L29W/L72F, L29W/I107W and L29W/L104W after illumination at 185 K for 2 h and slow cooling under light to 160 K; inset: sketch of the active site.

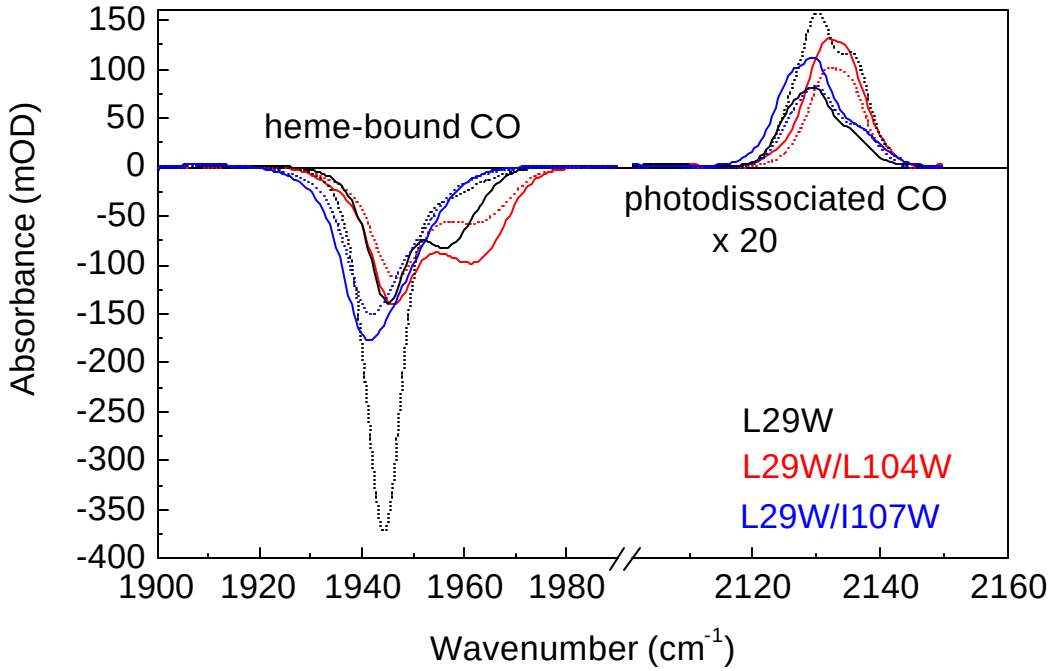

Fig. 3.74: FTIR absorbance difference spectra of MbCO mutants L29W, L29W/I107W and L29W/L104W after illumination at 185 K for 2 h and slow cooling under light to 160 K; solid lines: without xenon; dotted lines: samples equilibrated with 1 atm of xenon.

3.2.5.4 TDS after Illumination at 185 K and Slow Cooling to 160 K

To monitor ligand recombination in a fluctuating protein, TDS experiments were performed subsequent to illumination. TDS contour maps of L29W and several double mutants are compiled in Fig. 3.75. For all samples, recombination to A_I and A_{II} occurs at ~190 and ~200 K, respectively (left column). For L29W/I107W, discrete bands for A_I and A_{II} cannot be resolved (Fig. 3.75 e). Rather intense contours of a peak at 1915 cm^{-1} in L29W/L72F are remarkable. The TDS maps of the photoproducts (right column) reveal recombination from a broad band at ~2128 cm^{-1} with a shoulder on the blue side. In L29W/L104W, this band is shifted to ~2132 cm^{-1}.

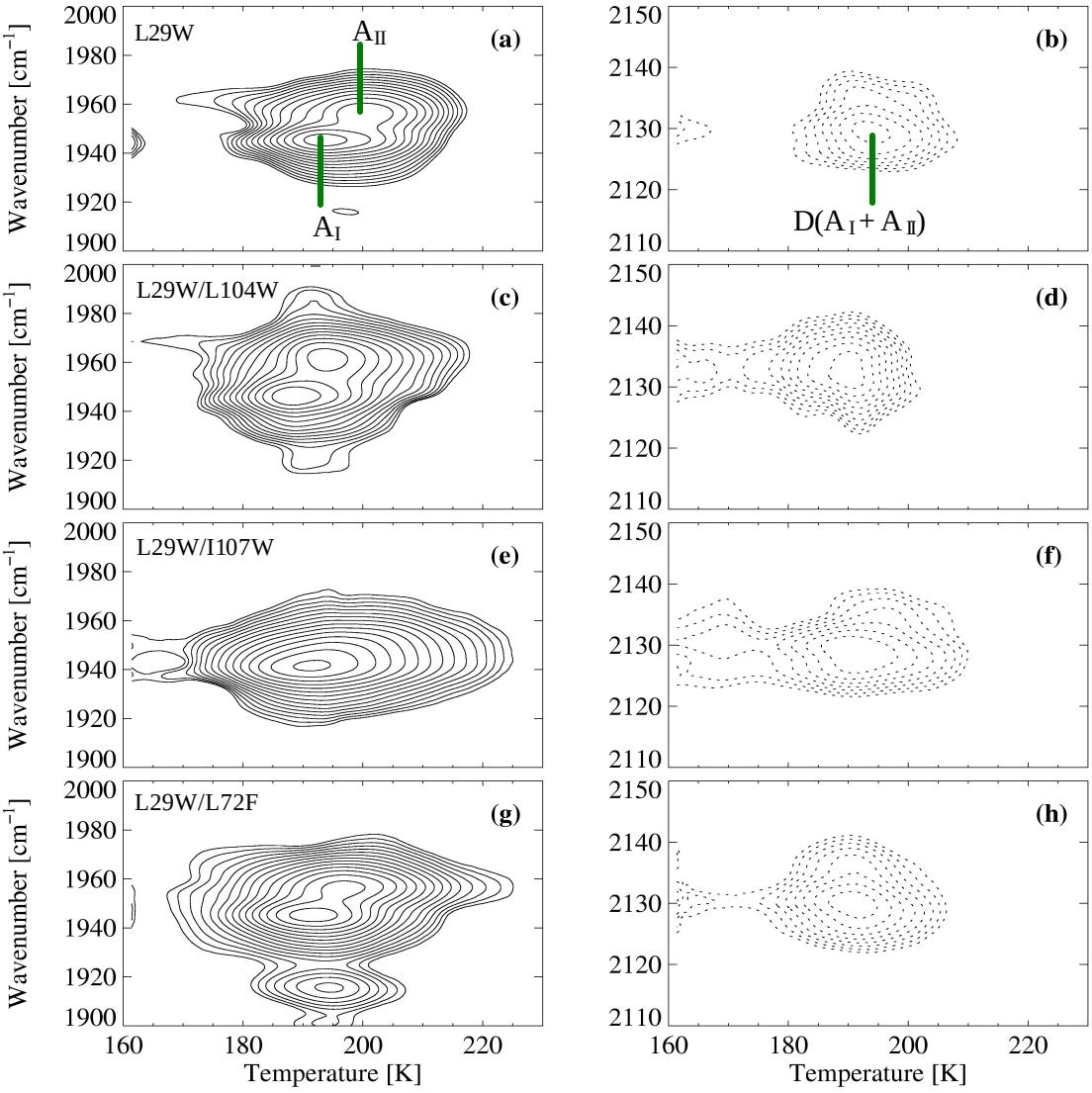

Fig. 3.75: TDS maps of L29W MbCO and related double mutants after illumination for 2 h at 185 K and slow cooling to 160 K while illuminating the sample.

In the presence of xenon, recombination occurs at lower temperatures (Fig. 3.76). This effect is most pronounced for L29W, where the temperature of maximal recombination drops from 195 to 185 K (in A_I). Furthermore, rebinding is complete at 210 K instead of 220 K. The photoproduct maps on the right hand side appear slightly more featured.

Since individual bands are difficult to discern from the TDS maps, we plot the absorbance differences calculated across the recombination features at ~190 K (Figs. 3.75 and 3.76) of MbCO samples L29W, L29W(Xe) and L29W/L104W in Fig. 3.77. The spectrum of C'' of L29W is also included, and all spectra are scaled to 1 OD cm^{-1}. The spectra of L29W, L29W(Xe) and C'' appear to show a smooth development among three bands; the absorbance spectrum of L29W/L104W, however, seems to consist of only two bands.

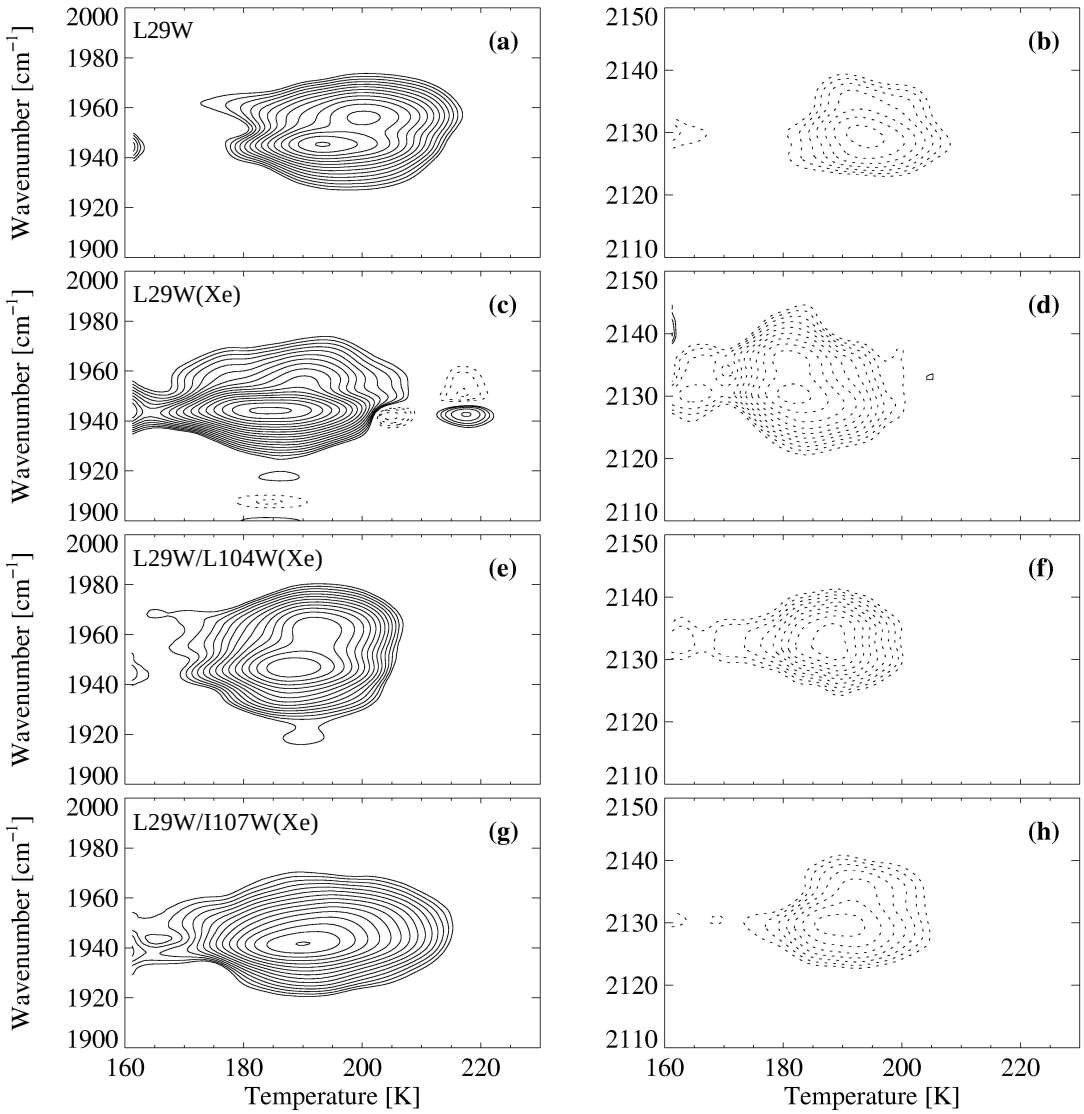

Fig. 3.76: TDS maps of L29W MbCO and related double mutants equilibrated with xenon after illumination for 2 h at 185 K and slow cooling to 160 K.

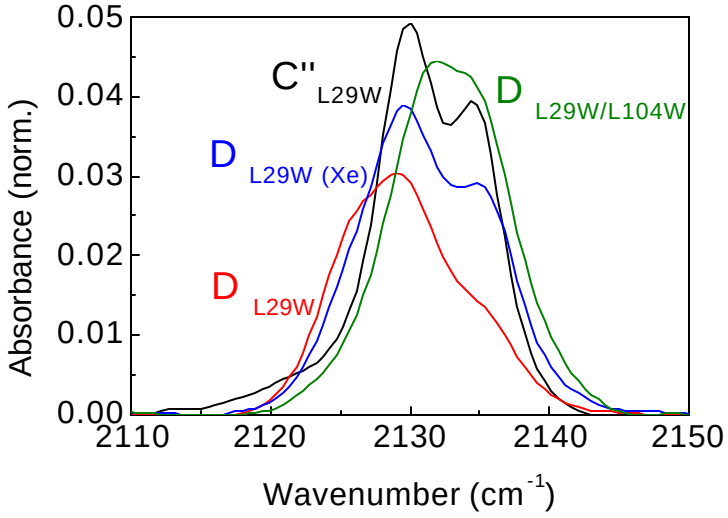

Fig. 3.77: FTIR spectra normalized to 1 ODcm $^{-1}$ of intermediates C'' (L29W) and D of MbCO samples L29W, L29W(Xe) and L29W/L104W.

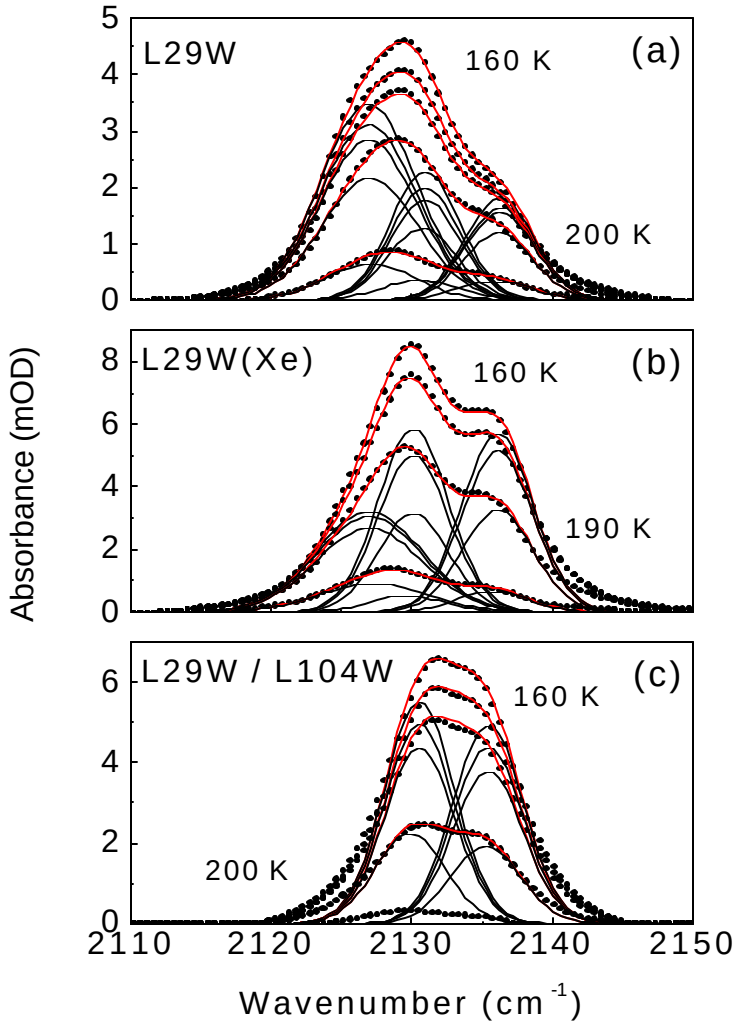

Fig. 3.78: FTIR spectra of photoproduct D in L29W, L29W(Xe) and L29W/L104W; symbols: data from the TDS experiments after illumination at 185 K and slow cooling to 160 K under light; black lines: Gaussians to fit the data; red lines: sum of the individual Gaussians.

In Fig. 3.78 a and b, we plot selected photoproduct spectra of the TDS experiments in the temperature range 160 - 200 K on L29W and L29W(Xe) that were modeled by a set of three Gaussians. While the stretch band at 2128 cm^{-1} dominates the spectra of L29W, the absorbance bands for L29W(Xe) show a major contribution of two bands at 2130 and 2135 cm^{-1}, which remind one of the spectrum of C''. We have observed the CO stretch band at 2128 cm^{-1} before in the TDS experiment after illumination for 15,000 s at 160 K (Fig. 3.65). The FTIR spectra of L29W/L104W (Fig. 3.78 c) can indeed be fitted with only two lines similar to C''.

3.2.5.5 Interpretation and Discussion: Photoproducts in a Fluctuating Protein

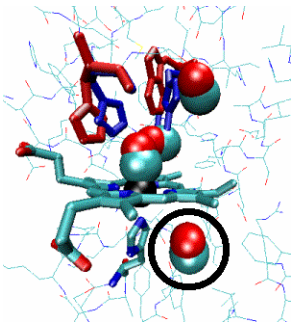

FTIR spectroscopy at 180 K and TDS experiments after illumination at 185 K and subsequent slow cooling under light to 160 K gave evidence for a long-lived intermediate population. A detailed look at the absorbance spectra (Figs. 3.77, 3.78), however, revealed contributions of three components to the CO stretch bands. As opposite CO orientations at one particular site can only account for two stretch bands, recombination at ~190 K must occur from two different locations inside the protein, one of them being C'' (Xe 4). Consequently, we associate the remaining band at 2128 cm^{-1} with a new site, D.

X-ray crystallography on L29W crystals photolyzed at temperatures above 180 K reported up to ~60% of the CO ligands in the Xe 1 cavity on the proximal side of the heme plane (15, 90). The missing fraction of ligands was either never photodissociated (less than 10%) or had escaped into the solvent. The protein moiety had adopted the A_{II} conformation. Consequently, we propose that the photoproduct D is structurally defined by a CO molecule in the Xe 1 cavity of the A_{II} conformation.

To account for recombination at ~190 K from both C'' and D in a fluctuating protein, we propose the following model: After photolysis, ligands in A_I molecules of L29W become trapped initially in intermediate state C' in the Xe 4 cavity, and subsequently, a minor protein relaxation towards the A_{II} conformation generates intermediate state C''. Because the CO has disappeared from the active site, the imidazole sidechain of H64 moves deeper into the heme-pocket, which is expected to slow recombination from intermediate C'' as compared with C'. This relaxation progresses with increasing temperature. As a consequence, recombination from C'' slows even more. The rearrangement of the W29 indole sidechain into the A_{II} conformation may still be hindered as long as the ligand is in the Xe 4 cavity. Above the dynamic transition temperature, ligand migration to the proximal side is aided by protein fluctuations. After ligand exit from the distal cavity, the protein relaxes completely to the A_{II} conformation. The W29 indole sidechain in A_{II} molecules sequesters the CO ligands in the proximal cavity and strongly hinders access to the distal cavity. Conformational fluctuations between the A substates are necessary to transiently open exit channels for the ligands to rebind. This recombination scheme explains ligand rebinding at ~190 K in L29W(Xe) and L29W/L104W. Although these samples show a (partially) blocked proximal cavity, protein relaxation toward the A_{II} conformation hinders recombination from C'' at temperatures of 160 K.

Based on this model, we now can explain the TDS maps after extended illumination at 160 K (Fig. 3.65) in detail. The contours above ~190 K differ considerably from those in Fig. 3.75 a, b, although both monitor recombination above the dynamic transition temperature; A_I and A_{II} show the same peak temperature of maximum rebinding, the photoproduct contours are narrower and confined to a band at ~2128 cm^{-1}. In Fig. 3.79 (left column), we plot the FTIR/TDS absorbance difference spectra, $-log(I_{light}/I_{met})$, representing heme-bound CO

ligands. In the right column, absorbance difference spectra, $-log(I_{light}/I_{dark})$, are shown that represent the population that has their ligands photolyzed (compare Fig. 2.5).

We follow the temperature-dependent development of both subpopulations with monitoring in the spectral region of heme-bound CO in parallel. Up to 180 K, recombination occurs exclusively to A_I, as seen from the absorbance increase in the bands of the heme-bound CO (Fig. 3.79 a) and the concomitant absorbance loss of photolyzed species (Fig. 3.79 b). As we see no residual absorbance in A_I in Fig. 3.79 b, rebinding in this substate is complete at 180 K. Between 180 and 195 K, an exchange is visible in Fig. 3.79 c, d. Since A_I has rebound all ligands and A_{II} none at all, the ratio A_I/A_{II} of the bound part of the sample differs from the equilibrium ratio. To approach equilibrium, ligand-bound molecules in A_I alter their conformation and become ligand-bound A_{II} molecules. Above 195 K, A_{II} recombines (Fig. 3.79 e), as seen from the expected loss in the absorbance band of the photolyzed fraction in substate A_{II} (Fig. 3.79 f). Moreover, we also observe spectral changes that would suggest recombination in A_I. This signal, however, is not due to rebinding but arises from temperature-dependent changes of the A_I/A_{II} equilibrium in the 'dark' transmission data set $I_{dark}(n,T)$ that we have used to calculate the absorbance difference spectra (see Section 2).

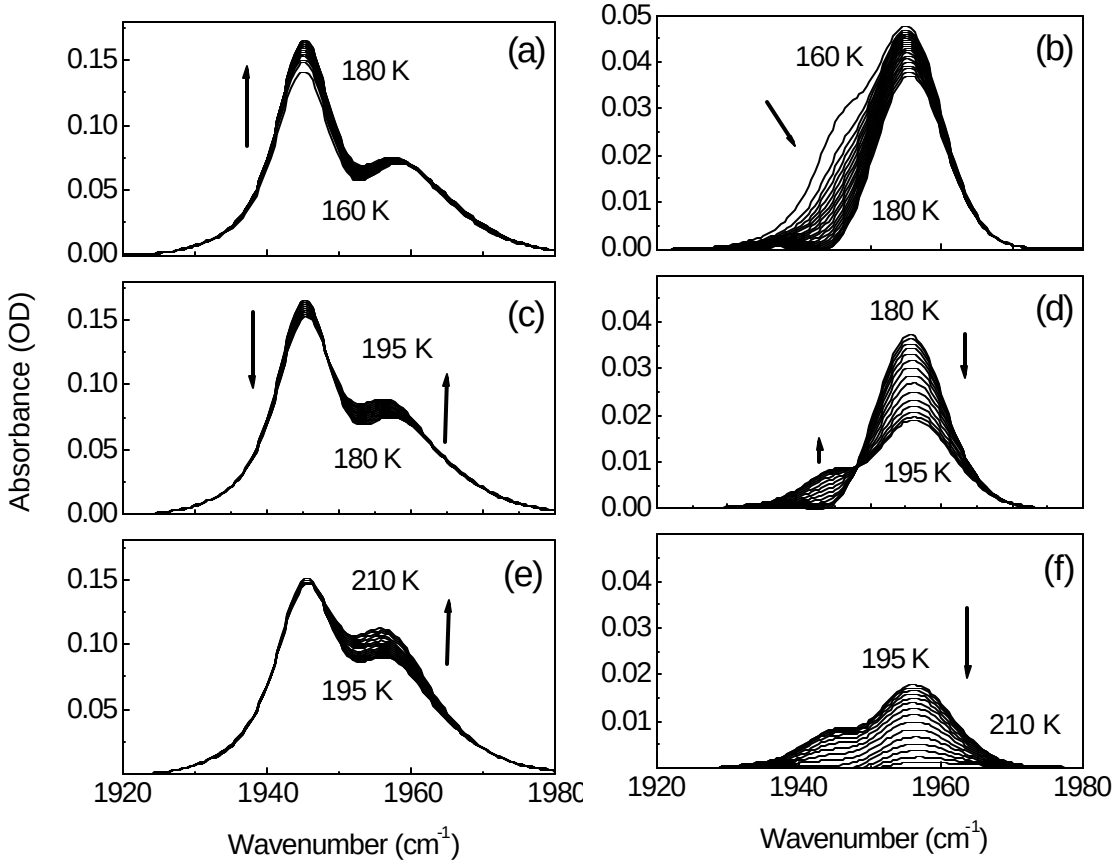

Fig. 3.79: FTIR/TDS absorbance difference spectra of (left column) heme-bound and (right column) photolyzed CO monitored in the spectral range of heme-bound CO in L29W MbCO after 15,000 s of illumination at 160 K.

As a consequence, A_{II} and A_I show identical kinetics in the contour map in Fig. 3.65 a. We emphasize that a transient substate interconversion also in the deoxy species is a prerequisite for any recombination, as A_{II} rebinds ligands only from site B. At 210 K, recombination to A_{II} is complete. Recombination can only occur from site D as the Xe 4 cavity is not available in A_{II} molecules. Thus, we observe a photoproduct spectrum only of state D that is not obscured by the spectrum of C'' (Fig. 3.65 b).

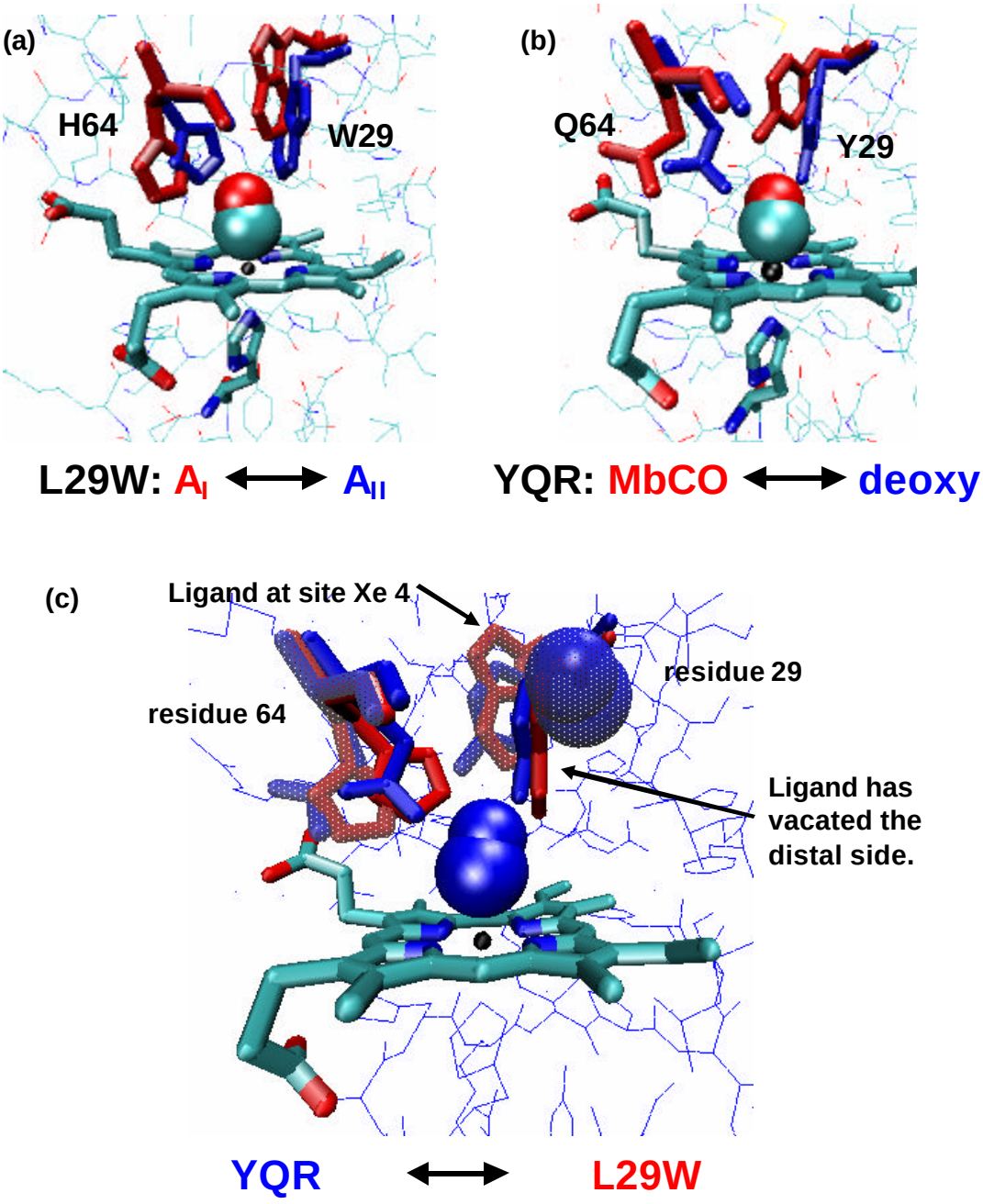

Fig. 3.80: L29W versus YQR: (a) Superposition of taxonomic substates A_I and A_{II} in L29W; (b) superposition of YQR MbCO and deoxy YQR ; (c) comparison of L29W and YQR.

The A_I/A_{II} interconversion is *not* an intrinsic property of this particular mutant. Recently, Brunori *et al.* (18, 121) have made extensive studies of Mb mutant YQR. The structural and dynamical similarities between YQR and L29W are impressive (Fig. 3.80). Both mutants have an aromatic sidechain at position 29. We have observed that this voluminous sidechain markedly enhances the ability of the Xe 4 cavity to trap photodissociated ligands. In YQR, thermally activated ligand migration from site B to site C' occurs already at ~30 K. In L29W, photon-induced migration occurs at 3 K and thermally activated migration at 80 K. Furthermore, both proteins show *four* characteristic photoproduct spectra, B, C', C'' and D. Minor protein relaxations are activated at ~130 K, during which the aromatic sidechains of residues 64 and 29 of both mutants perform a very similar, concerted motion and generate a new intermediate state C''. We do not know whether this relaxation also occurs in WT, because the CO stretch bands of the WT photoproducts are rather unspecific (compare section 3.1.2.3). Above 180 K, protein fluctuations on a larger scale open transient migration pathways. The CO ligands can vacate the distal side in YQR and L29W, and subsequently both proteins adopt an A_{II}-like conformation, where the sidechains of residues 29 and 64 are fully relaxed.

4. The Role of Internal Cavities in Physiological Ligand Binding

To understand the role of internal cavities and packing defects in controlling ligand migration to the heme iron in Mb, we have created a variety of mutants using protein engineering. The effects of local structural modifications on the occupation of the internal docking sites and migration pathways to these sites were examined by IR spectroscopy of the CO stretch bands, combined with kinetic experiments, including temperature ramp techniques such as TDS and sophisticated illumination procedures that allowed us to specifically enhance particular photoproduct intermediates.

The CO stretch bands of heme-bound and more importantly, of photodissociated CO have served as powerful tools to probe the immediate vicinity of the CO molecule inside the protein matrix. An important experience gained from these studies is that pronounced band shifts accompanying CO migration are more the exception than the rule. Aliphatic amino acids like leucine or valine that line the Xe cavities in the native protein give rise to a very similar hydrophobic, apolar environment and thus small changes in the stretch frequencies of the photolyzed ligands that are hard to detect. Aromatic groups, like heme or the aromatic amino acids F, Y, and W in close vicinity to the photodissociated ligand were found to have a strong effect on the CO stretch frequencies. In V68F and V68W, for instance, the presence of F or W near the CO leads to a larger wavenumber separation of the doublets of CO bands associated with opposite ligand orientations at site B. Moreover, the W29 indole sidechain in L29W significantly affects the stretch frequency of CO in the Xe 4 cavity. In mutants YQR and YQRF, the aromatic sidechain from Y29 yields the same effect as the W29 in the L29W mutant. Thus, in this work and ongoing research on other globins we have adopted the strategy of preferentially introducng bulky aromatic sidechains to enhance the environmental sensitivity of our molecular probe CO.

4.1 Migration and Recombination in WT MbCO

4.1.1 The Primary Docking Site B

The sharp IR lines emerging in the photolysis difference spectra of heme proteins at cryogenic temperatures suggested the existence of structurally well defined ligand docking sites in the protein matrix (55). The primary docking site B was subsequently characterized by diffraction experiments on MbCO crystals under illumination at cryogenic temperatures (48-50). Lim *et al.* (54) performed femtosecond IR spectroscopy of the photoproduct bands at room temperature and proposed that site B mediates ligand recombination even under physiological conditions. This was recently confirmed by nanosecond time-resolved crystallography by the Moffat group (19).

In this work, we have measured the photoproduct bands of many different mutants at cryogenic temperatures. At 3 K, CO ligands are observed to universally settle into the primary docking site B as long as this site remains available upon modification of the structure. This observation underscores the role of site B as the most easily accessible state after photodissociation. In the physiological process, ligand dissociation is driven by thermal energy and not by light. Docking site B likewise serves as the first transient CO storage site after bond rupture.

The IR studies reveal a complexity that is completely hidden from the x-ray data. After 1-s illumination at 3 K (Figs. 3.6, 3.7, 3.10), CO reorients in docking site B at ~15 K in the TDS experiments, as evidenced from a pairwise gain and loss of absorbance in two photoproduct bands. Photolyzed ligands initially occupy site B in an orientation that is governed by the relative accessibility of the two sites after the CO leaves the bound-state position with high

kinetic energy. The exchange between the two orientations occurs at a temperature where sufficient thermal energy is available so that the free energy barrier can be surmounted (on the experimental time scale). This barrier is finely tuned by steric determinants in the immediate vicinity of the docking site B, as shown from the TDS experiments with V68 mutants, in which an inverse correlation between reorientation temperature and volume of the residue 68 sidechain became apparent (Fig. 3.7). Furthermore, contour maps of H64L and H64V show the exchange at lower temperature (T < 10 K), which reflects a decreased barrier for rotation as compared to WT because of less steric hindrance from a smaller residue 64 (Fig. 3.6).

For WT MbCO, the exchange between opposite orientations is easily observed in the dominant A_1 substate from the increase in photoproduct B_1 at 2131 cm^{-1} that is accompanied by a loss in B_2 at 2118 cm^{-1}. Our excellent experimental data also show a clear increase in the A_3-photoproduct B_0 for the first time. This raises the question from which photoproduct the population transfer occurs. Naïvely, one could interpret the contour plots such that B_2 feeds into B_1 *and* B_0. However, B_2 is a photoproduct band of A_1 and, therefore, can only be associated with B_1. Because of the small population in A_3, the missing $B(A_3)$ partner of B_0 may either be hidden underneath the spectral changes in B_2 or B_1. The exact assignment is also obscured by the fact that we observe rebinding in A_3 exclusively from the photoproduct band B_0 in our maps, meaning that the $B(A_3)$ state with opposite orientation has a much higher free energy and exchanges completely. In 1993, Mourant *et al.* (65) studied the IR bands of a photolyzed orthorhombic MbCO crystal where ~90% of all molecules had adopted substate A_3. They observed rebinding from B substates at 2131 and 2149 cm^{-1} to A_3. Assuming that protein crystals behave similarly, this observation would suggest that the missing partner is hidden beneath B_1. Another scenario that deserves mentioning is that, given that A_3 has significantly higher barriers than A_0 and A_1, rebinding to A_3 could also happen from state C instead of B, so that the increase in B_0 absorbance at ~15 K would be interpreted as thermally activated ligand migration of CO in A_3 molecules from site B to site C. However, in mutants V68F and V68W we have also noted pronounced recombination in A_3 at ~70 K, although the TDS plots (Fig. 3.18) revealed that photodissociated ligands are essentially confined to the vicinity of the active site. Thus, the FTIR data do not support the theory that migration of the ligands to state C is responsible for the slow rebinding in the A_3 substate.

4.1.2 Ligand Migration Across a One-dimensional Energy Landscape

Our results on a large amount of myoglobin mutants give an unprecedented wealth of experimental evidence of the involvement of the Xe cavities in ligand migration through the protein matrix. For WT MbCO, a number of photoproduct states, characterized by ligands trapped in the different cavities of the protein, have been identified on the basis of both their CO stretch spectra and their recombination temperature in the TDS data sets (compare section 3.1.2.2). The slow-cool protocol described in section 2.6.4 has been a valuable tool to populate intermediate docking sites. In substate A_1, most photolyzed CO ligands were found at the initial docking site B (Figs. 3.16, 3.21). A fraction of ligands, however, could also be trapped in the back of the distal pocket (Xe 4), while an even smaller subpopulation of CO ligands was found on the proximal side of the heme (Xe 1). Not the slightest piece of evidence has emerged for occupation of cavities Xe 2 and Xe 3 by CO. This result was already anticipated by Scott *et al.* (107) who proposed that this portion of the Mb structure may be too rigid to allow rapid penetration by ligand molecules, as it remains intact even in the molten globule intermediate that is observed during either acid, urea, or guanidinium chloride-induced denaturation of apomyoglobin (122, 123).

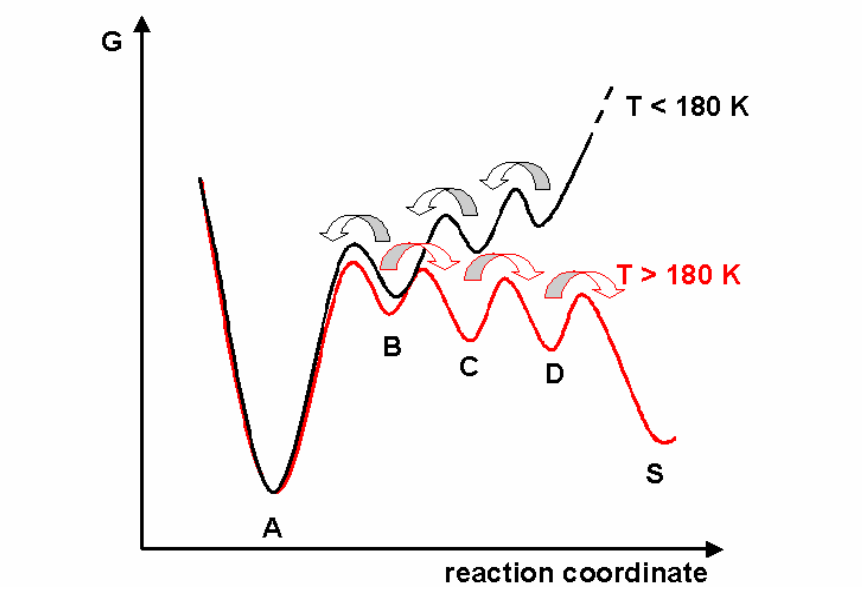

Fig. 4.1: Sequential multi-well model of WT (substate A_1).

To describe a chemical reaction such as ligand binding, one defines an enthalpy or free energy surface as a function of a reaction coordinate, upon which the various metastable species appear as local minima (Fig. 4.1), as introduced for ligand binding to myoglobin by Austin *et al.* in 1975 (14). Of course, such a one-dimensional (or in general lower-dimensional) description is an utterly simplistic model for a protein with several thousand degrees of freedom and a CO ligand that can take different migration pathways (and thus can have multiple reaction coordinates). For example, the scheme in Fig. 4.1 is strictly sequential, but from the Mb structure or the experimental data we cannot exclude that the CO migrates from D directly to B. Another complication arises from the fact that the energy surfaces are strongly temperature-dependent. This is not only for the trivial reason that, in the free energy expression, $G = H - TS$, the entropy term scales with temperature. Rather, entropy and enthalpy of a protein are intrinsic functions of temperature. This complication is particularly evident from the ligand binding behavior above and below the glass transition.

Below the glass transition, fluctuations of the protein are arrested, and the barrier against ligand escape is so high that ligands cannot penetrate it on any reasonable timescale. Above the glass transition, the protein fluctuates and opens transient low-energy pathways for the ligands to enter or exit the protein. Therefore, in the energy landscape in Fig. 4.1, the barrier between site D and S (solvent) is strongly dependent on temperature. This treatment follows the work of Beece *et al.* (124), who studied the dependence of ligand rebinding on solvent viscosity by flash photolysis of MbCO and MbO_2. They introduced a dynamic model in which ligand migration into (and inside) myoglobin is governed by fluctuations between conformational substates. The internal barriers were modeled by gates that open and close. For a ligand to pass, a gate had to open just far enough to lower the barrier to the point where the ligand can pass. Other models have also been suggested for this process, for example the one by Robert Zwanzig, who described ligand exit into the solvent as a passage through a fluctuating bottleneck that changes its geometrical dimensions (125, 126). Thus, his barrier was exclusively entropic.

At temperatures below the glass transition, the description of the energy surface is simpler because protein dynamics is essentially arrested. Note, however, that local motions (like C' → C'' in L29W MbCO) can still happen and cause significant changes in the energy landscape.

Another complication exists, though, and that is the presence of multiple A substates having their individual reaction surfaces.

After these words of caution, we now discuss our results with the simple sequential arrangement of enthalpy barriers (Fig. 4.1). In WT MbCO below the glass transition, the consecutive barriers are arranged such that migration towards the binding site A is favored over migration towards the solvent.[3] At ~80 K, we observe recombination from intermediate state C in A_1 molecules of WT sperm whale MbCO. There is no evidence, whatsoever, for CO in the Xe 4 cavity in protein molecules of conformation A_3. The yields of occupying metastable intermediates apparently depends on the different A states, and also on the type of species. For example, Nienhaus *et al.* (47) have shown that only a very small fraction of ligands become trapped at site C in A_1 molecules of horse heart myoglobin.

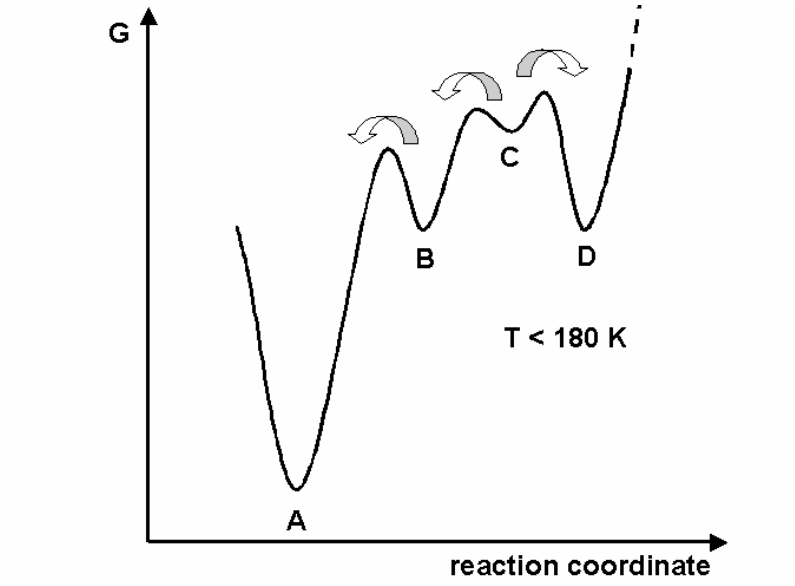

Fig. 4.2: Sequential multi-well model of WT (substate A_3) and mutants I28F and I28W.

In this work, we have designed mutants I28F and I28W to fill the Xe 4 cavity with a bulky sidechain and thus to prevent occupancy by ligands. The TDS experiments clearly showed a reduced occupancy of the Xe 4 pocket (Fig. 3.22), but we were unable to block access to the cavity completely. From this observation, we have to conclude that either (i) a subpopulation exists where the aromatic sidechain has adopted a conformation in which it does not block the Xe 4 cavity or (ii) secondary site C remains available for ligands in all protein molecules, but they are not trapped efficiently. In the absence of an x-ray structure, which could help to decide between the two possibilities, we argue that in the heterogeneous scenario (i), photodissociated ligands would migrate to site C in protein molecules with an open Xe 4 cavity, where they would be in close contact with the aromatic sidechain of residue 28. We would expect distinctly shifted photoproduct bands, in analogy to our results on L29W. As we do not observe any band shift from state C, we favor the homogeneous model (ii), which we explain with the energy surface given in Fig. 4.2. In this model, introduction of a bulky sidechain at residue 28 causes structural changes in the Xe 4 cavity so that it cannot trap incoming ligands effectively. The well representing state C is proposed to be shallow with similar and rather low escape barriers to B and D, so that ligands sampling site C may either return to the initial docking site B or will migrate to site D. In fact, subsequent to the slow-

[3] Note that this behavior is the opposite of that observed at room temperature. There, 96% of the ligands escape from the protein after bond dissociation. Consequently, the free energy barriers are lower towards the outside.

cool protocol, a significant fraction of ligands was indeed trapped in site D and recombined at a higher temperature compared to WT (Fig. 3.16).

For horse heart MbCO, we can presently only speculate about the structural differences to sperm whale MbCO that cause the much lower population of the Xe 4 cavity under illumination. We point out that the G-helix has a very different orientation, which might lead to a decreased ability of the Xe 4 cavity to trap ligands (Fig. 4.3). Additional information may possibly be obtained from molecular dynamics simulations of CO in this cavity.

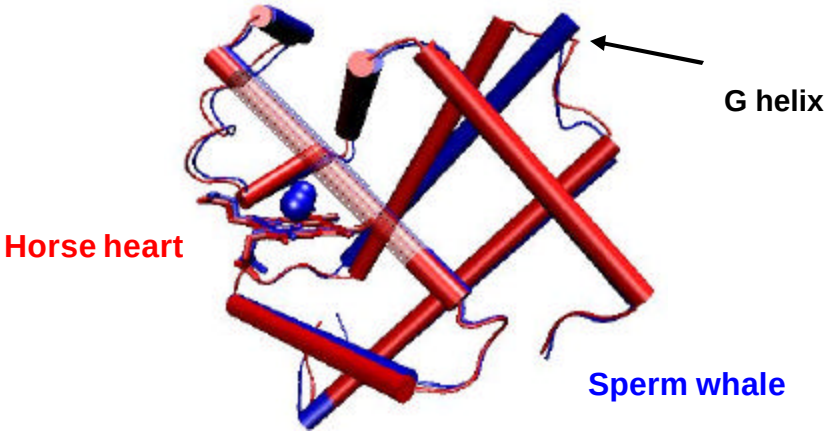

Fig. 4.3: Superposition of structural cartoons of sperm whale myoglobin (pdb code 1VFX) in blue and horse heart myoglobin (pdb code 1DWR) in red.

To examine the relevance of our low-temperature study of photoproduct states, a comparison with the results of a time-resolved Laue X-ray diffraction experiment with nanosecond time resolution by Srajer *et al.* (19) is of particular importance. Using a variable time delay between a pulsed (synchrotron) x-ray source and a pulsed photolysis laser, Moffat and coworkers were able to measure x-ray structures of MbCO as a function of time after photolysis. In these data, the photodissociated CO molecules were detected in two locations, at the distal pocket docking site B and at the Xe 1 binding site in the proximal pocket. The population by CO of the primary site decayed from the earliest times (1 ns delay time) to half its peak value within 70 ns. The proximal docking site was found to reach its highest occupancy (20%) ~100 ns after photodissociation. At this time, all CO molecules were still accounted for within the protein; in one of either two docking sites or bound to the heme. Interestingly, at earlier times, a fraction of photodissociated CO molecules was reported as missing, which suggests that other locations with low occupancies may exist in the distal pocket. At longer times, the population in Xe 1 decayed and reached half of its peak value at ~10 µs, and CO molecules disappeared into non-observable sites (e.g. solvent) with the time constant of 3 µs and subsequently rebound to deoxy Mb in a bimolecular process with a second-order rate coefficient of 4.5×10^5 M^{-1} s^{-1} (the solvent population decayed to half of its peak value at ~150 µs). The additional intermediate C studied here was not observed in the x-ray data, however. Note that this observation cannot be explained with differences between crystal and solution preparations, since Nienhaus *et al.* (57) have shown earlier that photoproduct C (and even further photoproduct intermediates) exists in WT MbCO crystals in $P2_1$ and P6 space groups (below 200 K).

It is important to realize that the room temperature time-resolved crystallography results do *not* prove that site C is absent at room temperature and, thus, that is not relevant for physiological ligand binding. In the x-ray structure analysis, intermediates can only be observed if they accumulate to an extent that produces appreciable electron density. However, this is only the case if the rate coefficients for depletion of the intermediate are not faster than the ones that feed population into it. By performing the experiment at cryogenic temperatures with the protocols employed here, we can lengthen the lifetimes, which allows us simpler steady-state spectroscopy techniques. Using sophisticated illumination protocols, as we have shown in this thesis, we are also able to selectively enhance intermediates and study them individually. A disadvantage of our temperature ramp protocols, however, arises from the fact that they are rate-window methods and not real kinetic experiments. With kinetic data, detailed models can be introduced, and enthalpy and entropy contributions in the free energy can be distinguished. In practice, however, this is very difficult, as frequently intermediates are only populated appreciably in a too narrow temperature interval for a meaningful analysis (Arrhenius plot). Moreover, it can be exceedingly difficult or impossible to unambiguously distinguish between sequential models and other connectivities among several transient states. In the following, we will continue this discussion with a few interesting observations of the

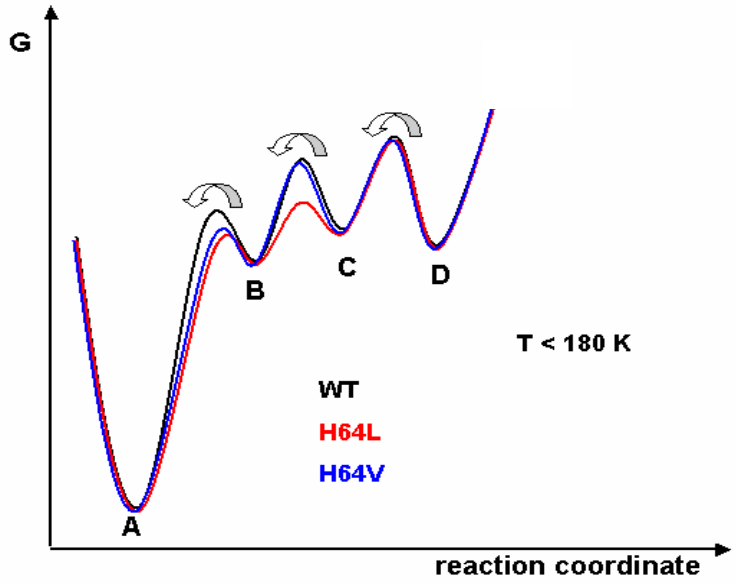

Fig. 4.4: Sequential multi-well model of WT (substate A_1) depicted in black and mutants H64L (red) and H64V (blue).

generation of photoproducts by extended illumination in distal pocket mutants. In H64L, state D was not occupied after the slow-cool protocol (Fig. 3.25). Even extended illumination at 180 K (data not shown) did not result in any significant photolysis. Furthermore, recombination from site C occurred at ~70 K as compared to ~80 K in WT. By contrast, H64V shows rebinding from intermediates C and D at 80 and 120 K, similar to WT. In 1994, Nienhaus *et al.* (47) studied WT MbCO at lower pH (pH 6) and gave evidence that photoproduct states C and D can also be populated in molecules of substate A_0, although to a lesser extent than in A_1. A possible explanation of these observations can be given with the energy surfaces depicted in Fig. 4.4. For WT A_0 molecules and the H64 mutants, the barriers for recombination from B to A are lower than in WT A_1, which is a direct consequence of the decreased steric hindrance of the ligand by residue 64 at the binding site. Furthermore, for H64L, the barrier from C to B is assumed to be lower than in WT and H64V, as indicated by the lower temperature at which rebinding from C occurs in H64L MbCO. Thus, the

probability of occupying site D is essentially zero, as ligands in state C will much more likely migrate back towards site B. The conformational determinants responsible for the different barriers between B and C in H64L and H64V are presently unclear. A possible explanation could be the presence of a water molecule in the larger pocket of H64V that hinders approach of the CO ligand to the primary docking site.

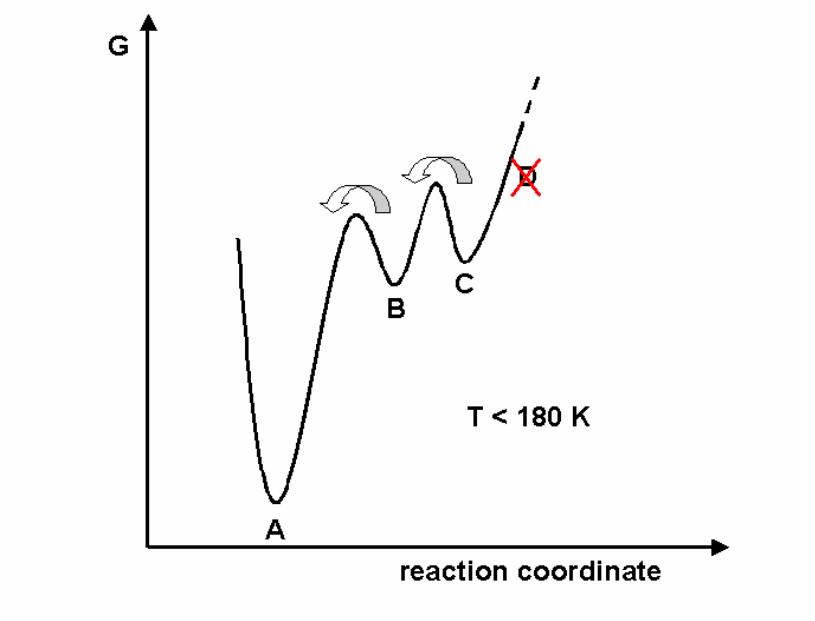

Fig. 4.5: Sequential multi-well model of MbCO mutant L104W.

In the x-ray structure of mutant L104W, the W104 indole sidechain completely blocks the proximal cavity (106). This observation was indeed confirmed by our TDS data. Intermediate sites B and C, however, are efficiently sampled by the photodissociated ligands in this mutant. It was somewhat surprising that the TDS experiment performed on L104W after illumination at 185 K showed no ligand escape into the solvent (Fig. 3.30). Obviously, site D is needed to store the CO for a sufficiently long time so that it can wait for a (rather slow) protein fluctuation that allows escape below 200 K. Without this state, the ligand has no choice but to rebind. Note that H64L shows the same effect, but the explanation is entirely different. In this mutant, the Xe 1 cavity is available, but cannot be accessed because intermediate C reflects essentially all the ligands back to B, at least below 200 K.

The simplistic energy landscapes we have used to describe the occupancy of intermediate sites assume sequential ligand migration. An extended model, as depicted in Fig. 4.6, allows for direct migration from B to D or from B to S. Based on our data, we cannot distinguish between these pathways.

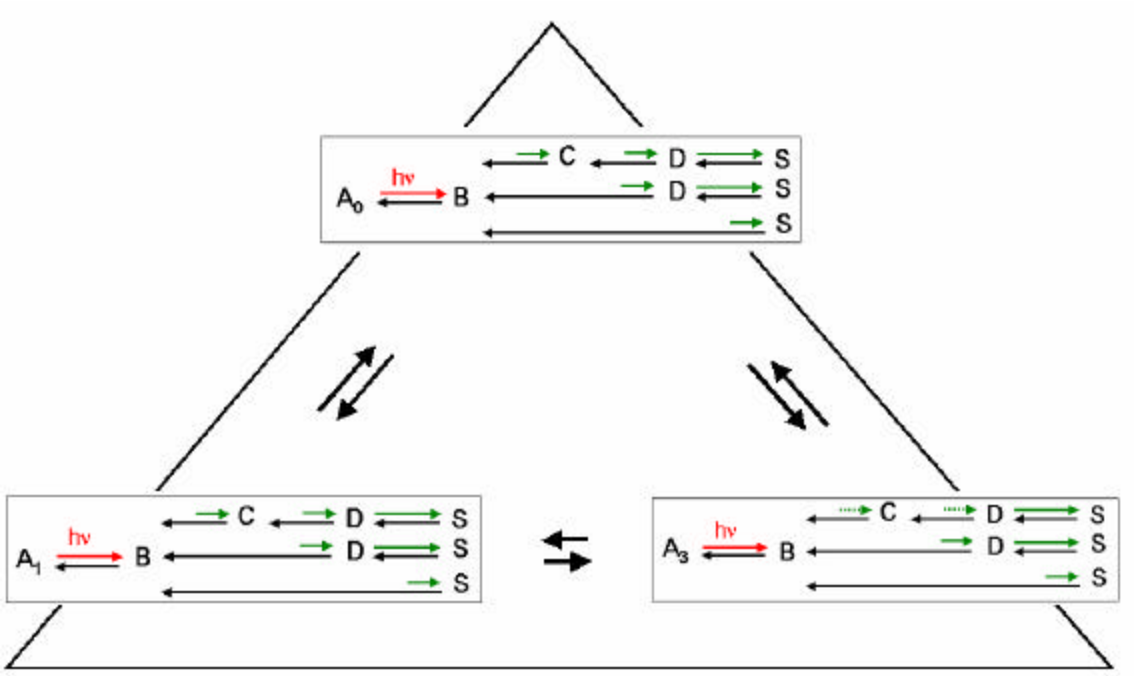

Fig. 4.6: Two-dimensional scheme of ligand migration and recombination in WT MbCO.

4.1.3 Physiological Ligand Binding in WT MbCO

In a flash photolysis study of MbO_2 on a large number of mutant Mbs, Scott and Gibson presented kinetic evidence that dissociated ligands can access the Xe 4 and Xe 1 cavities at ambient temperature (56). Non-exponential geminate rebinding was observed from a few nanoseconds to a few microseconds after photolysis in the presence and absence of 12 atm of xenon. In all cases, two kinetic phases were observed: an initial fast phase (half-time 20 ns) and a slower, smaller phase (half-time 0.5-2 µs). The fast phase was assigned to recombination from the initial docking site B, whereas the slower phase was interpreted as ligand recombination from secondary sites C and D.

We have also measured room temperature flash photolysis data on our MbCO mutant samples (1 atm CO) to establish connections between FTIR/TDS data and physiological binding (Fig. 4.7). From these data, we can extract two important parameters, which are compiled in Table 4.1: (i) the amplitude N_S, which represents the fraction of Mb molecules from which ligands escape after photodissociation. They subsequently rebind CO in a bimolecular reaction. (ii) The (pseudo-first order) apparent rate coefficient l_S for bimolecular rebinding, which quantifies the temporal decay of the kinetics.

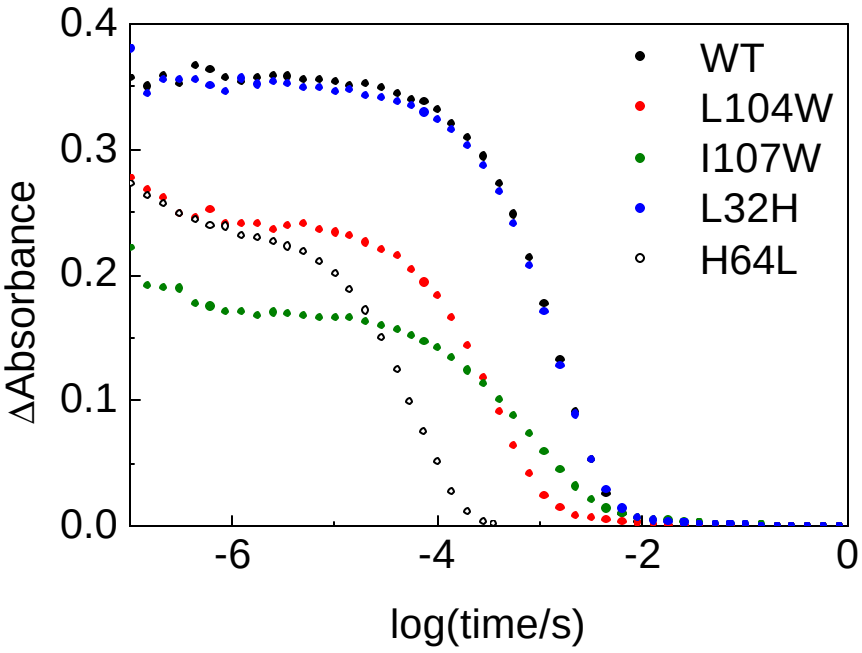

Fig. 4.7: Kinetic traces of WT MbCO and related mutants in 100 mM potassium phosphate buffer, pH 8 monitored at 436 nm after flash photolysis at room temperature.

In WT and L32H, essentially all photodissociated ligands escape from the protein after photodissociation (N_S > 95%). In the other proteins, a significant fraction of CO rebinds geminately on time scales below ~1 µs, and we can only see the tail of this nonexponential phase in our data. Rebinding in WT and L32H MbCO is kinetically identical and exponential. L104W also rebinds exponentially, about four-fold faster than WT, whereas I107W is markedly non-exponential. It appears as if it contains a mixture of the fast recombination of L104W and the slower recombination of WT. Indeed, a fit with two exponentials, using the rate coefficients of WT and L104W, matches the data very well. H64L rebinds again exponentially and much faster than all the other mutants. Apparently, the two proteins with the largest bimolecular fraction, WT and L32H, have the slowest bimolecular rebinding, and mutants with restricted access to the internal cavities have a significant geminate phase and rebind faster.

Table 4.1: Fraction of ligands escaping into the solvent, N_{out}, and apparent rate coefficient l_S of WT and related mutants.

Mutant	**N_{out} (%)**	**l_{on} (s^{-1})**
WT	96	$1.6 \cdot 10^{-3}$
L104W	64	$4.3 \cdot 10^{-4}$
L32H	96	$1.6 \cdot 10^{-3}$
H64L	64	$6.5 \cdot 10^{-5}$
I107W (fixed λ_{on})	45 (27 / 18)	$1.6 \cdot 10^{-3}$ / $4.3 \cdot 10^{-4}$
I107W (free fit)	45 (27 / 18)	$2.0 \cdot 10^{-3}$ / $2.8 \cdot 10^{-4}$

The observed kinetics can be explained with the free energy surface drawn in Fig. 4.8, where the inner barrier (bond formation) and the outer barrier (entry/exit) are proposed to be much larger than the internal barriers between geminate sites. After photodissociation, the ligand sits in state B in all the mutants. The typical barrier height for rebinding to the heme iron, H_{BA}, of all the mutants except H64L is ~10 kJ/mol, and with an Arrhenius prefactor, A_{BA},

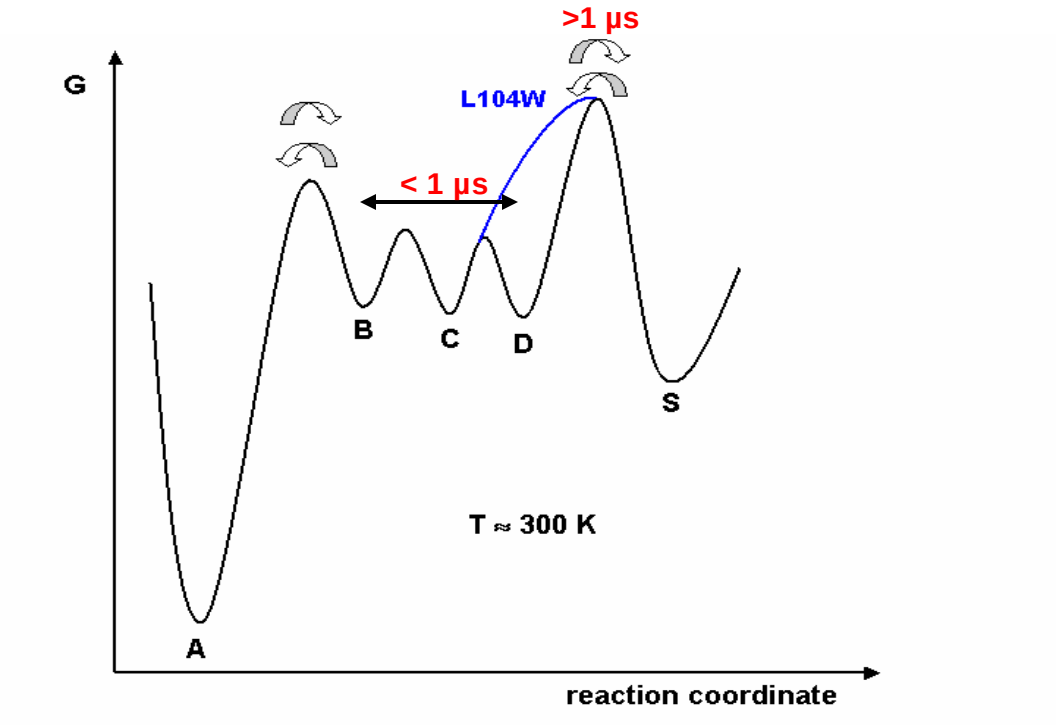

Fig. 4.8: Energy landscape to describe physiological ligand binding.

of ~10^9 s^{-1}, the barrier crossing time in B is ~200 ns. Considering that the barrier is distributed, we can expect deviations from this estimate by an order of magnitude to faster and slower times, depending on the particular substate. The Arrhenius prefactor is exceptionally small due to the fact that CO, the heme iron, and the distal histidine have to move in concert to enable the CO to form the bond with the heme iron (38). In the kinetic data, geminate rebinding extends out to ~1µs, which implies that ligand exit from the protein is a comparatively slow process. However, in WT and L32H, ligands are able to efficiently sample secondary sites C and D (compare the TDS maps in Fig. 3.16). Transitions of CO among the internal cavities are much faster than escape from the protein, as shown by time-resolved crystallography at room temperature (19). The intermediate locations B, C, and D will be similar in binding enthalpy (van-der-Waals). C and or D may be a little lower in free energy, so that the CO ligands spend only a small fraction of time in B, the only site through which bond formation can occur (54). By fluctuating among states B, C, and D, the photolyzed ligands have a much lower probability of geminate rebinding, so that more of them can take advantage of (slow) protein fluctuations to escape. Ligands will shuttle back and forth many times among the geminate sites before exiting, and thus the exact escape route itself remains obscure. In L104W, however, the Xe 1 site is blocked, state D is thus missing, and photodissociated ligands are confined to the distal side. Consequently, they are more likely to rebind geminately. In mutant I107W, access to the Xe 4 cavity is strongly hindered. The TDS map in Fig. 3.16 g does not show a distinct contour associated with recombination from C. The majority of ligands rebind geminately, and only a minor fraction can escape into the solvent and rebind in a bimolecular process.

Further support for this binding scheme comes also from a comparison of the bimolecular rate coefficients l_S. This quantity is given by a complicated expression that – in general – depends on all the relevant rate coefficients. For a model with multiple photoproduct intermediates, a strict mathematical analysis becomes intractable. For the simple three-well-model with bound state A, photoproduct state B inside the protein and solvent S, we have earlier introduced a simple approximation, which is valid whenever the internal and solvent rebinding are clearly separated in time (section 1.2.3, Eqs. 1.3 - 1.8). In this approximation, the bimolecular rate coefficient l_S is given by the product of three factors, k_{BA}, the rate coefficient for recombination from B to A, the pocket occupation factor P_B, which represents the equilibrium coefficient for binding CO at the geminate (B) site (if there were no recombination at the heme iron), and N_{out}, the probability for ligands to escape from the

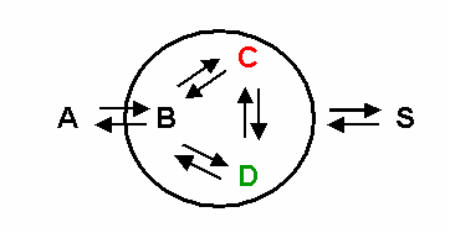

Fig. 4.9: Our scheme to explain ligand migration and recombination.

protein after dissociation. We can actually extend this simple model to describe the case of multiple internal CO binding sites. We assume that, within the first few hundred nanoseconds after dissociation and, therefore, on time scales faster than bond formation and entry/exit of ligands, the photolyzed CO molecules quasi-equilibrate among states B, C, and D, as depicted by the circle in Fig. 4.9. This 'geminate' equilibrium modulates the rate coefficient k_{BA}; it decreases the probability of CO to be at the B site, which is considered the only site through which bond formation can take place. To account for this effect, we introduce an 'internal' pocket occupation factor $P_{B/CD}$, defined as an equilibrium coefficient between states B and states C, D if no recombination would occur.

$$\begin{aligned} k'_{BA} &= k_{BA} \cdot P_{B/CD} \\ &= k_{BA} \cdot \frac{k_{CB} + k_{DB}}{k_{BC} + k_{BD}}, \end{aligned} \tag{4.1}$$

The bimolecular process is presumed to be well separated in time from this initial equilibration process, which implies $k_{BA}, k_{BS}, k_{CS}, k_{DS} << k_{BC}, k_{BD}, k_{CB}, k_{DB}$. As a consequence, we may treat states B, C and D formally as one geminate state and are left with a system that consists of bound state A, geminate state (B,C,D) and solvent state S. Ligand binding from the solvent can be approximated by a three-well model. According to Eq. 1.6, the rate coefficient l_S that determines bimolecular recombination is given by

$$l_S = k'_{BA} \cdot P_{BCD/S} \cdot N_{out}$$

$$= k'_{BA} \cdot \frac{k_{SB} + k_{SC} + k_{SD}}{k_{BS} + k_{CS} + k_{DS}} \cdot \frac{k_{BS} + k_{CS} + k_{DS}}{k'_{BA} + k_{BS} + k_{CS} + k_{DS}}. \tag{4.2}$$

The 'external' pocket occupation factor $P_{BCD/S}$ determines the overall equilibrium population at internal sites B, C and D with respect to the solvent S (if no recombination would occur at the heme iron). N_{out} denotes the probability that ligands at geminate site (B, C, D) exit the protein. Eq. 4.2 transforms into the simple description of the three-well model (Eq. 1.6), if sites C and D were not taken into account (as indicated by the red boxes in Eq. 4.2).

The ligand dissociation rate coefficient l_{off} can be written accordingly:

$$l_{off} = k_{AB} \cdot N_{out}$$

$$= k_{AB} \cdot \frac{k_{BS} + k_{CS} + k_{DS}}{k'_{BA} + k_{BS} + k_{CS} + k_{DS}}. \tag{4.3}$$

We assume that subsequent to photolysis, all ligands are found at site B. From l_S and l_{off}, the association coefficient K_a can be calculated:

$$K_a = \frac{l_S}{l_{off}} = \frac{k'_{BA} \cdot P_{BCD/S} \cdot N_{out}}{k_{AB} \cdot N_{out}}$$

$$= \frac{k'_{BA}}{k_{AB}} \cdot \frac{\frac{k_{SB} + k_{SC} + k_{SD}}{k_{BS} + k_{CS} + k_{DS}} \cdot \frac{k_{BS} + k_{CS} + k_{DS}}{k'_{BA} + k_{BS} + k_{CS} + k_{DS}}}{\frac{k_{BS} + k_{CS} + k_{DS}}{k'_{BA} + k_{BS} + k_{CS} + k_{DS}}}$$

$$= \frac{k'_{BA}}{k_{AB}} \cdot \frac{\frac{k_{SB} + k_{SC} + k_{SD}}{k'_{BA} + k_{BS} + k_{CS} + k_{DS}}}{\frac{k_{BS} + k_{CS} + k_{DS}}{k'_{BA} + k_{BS} + k_{CS} + k_{DS}}}$$

$$= \frac{k'_{BA}}{k_{AB}} \cdot \frac{k_{SB} + k_{SC} + k_{SD}}{k_{BS} + k_{CS} + k_{DS}}$$

$$= \frac{k_{BA}}{k_{AB}} \cdot P_{B/CD} \cdot P_{BCD/S}$$

$$= \exp(-\Delta G_{SA}). \tag{4.4}$$

with free energy difference between bound state and solvent, ΔG_{SA}, temperature T and universal gas constant R. In WT MbCO and mutants L32H, L104W and I107W, the inner barriers at the heme iron will all be similar because the mutations are not in the immediate vicinity of the active site. The fact that all mutants show the same temperatures of maximal rebinding in the TDS data (Fig. 3.16) reconfirms this assertion. Therefore, we expect essentially identical rate coefficients at the active site, k_{BA}. N_{out} also does not vary much (0.45 – 0.96, see Fig. 4.7 and Table 4.1). Note that the decrease in N_{out} would lead to a smaller l_S; the rate coefficients of the mutants with the lower bimolecular yields are larger, however. Consequently, the differences in l_S in these mutants arise from different pocket occupation factors.

To explain the by a factor of ~4 larger l_S in L104W than in WT MbCO, we have to assume that the probability of CO to reside in site B must be increased by a factor of ~8 We attribute this increase to the fact that the Xe 1 site is not available, and thus the CO is forced to be in the 'dangerous' site B much longer. We also remark that, f site D would be a crucial waystation on the exit/entry pathway, blocking this site would prevent ligand exit, and $k_{BS} = 0$.

The interesting non-exponential bimolecular reaction in I107W that can be modeled by two populations, one binding CO with l_S of WT, and the other one with l_S of L104W, suggests that two conformations with markedly different ligand binding and, therefore, structural properties exist in the deligated (deoxy) state. Note that two discrete components can only be observed if interconversion between these conformations is slower than the reaction. We have already explained the large amplitude of geminate rebinding in I107W by partial blockage of the Xe 4 cavity. From the behaviour of l_S, we would argue that the two conformations of deoxy Mb I107W differ in particular by two alternative positions of the W107 sidechain, one with a small and one with a large effect on the accessibility of internal cavities. Crystallographic studies will be performed in the future to test this hypothesis. As of now, we can only refer to multiple mutant YQRF (Fig. 4.10), where indeed two different conformation of the F107 sidechain have been observed (127).

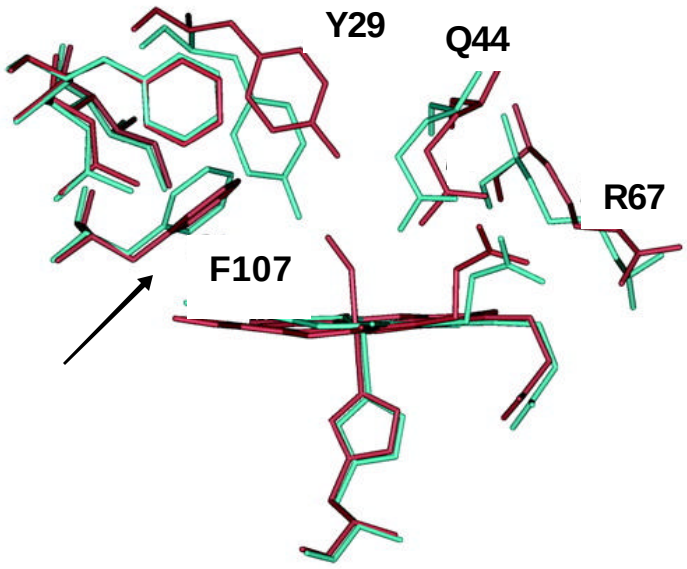

Fig. 4.10: Three-dimensional structure of the active site of YQRF MbO_2 (red) and deoxy YQRF (green), adapted from Draghi *et al.*(127); please note the distinctly different orientations of residue 107.

In 1990, Chatfield *et al.* (128) studied the temperature dependence of oxygen escape from Mb with flash photolysis. In an attempt to fit the multi-step and non-exponential kinetic traces, they proposed three different schemes for ligand migration and recombination (Fig. 4.11). The simple sequential model assumed that, after photolysis, ligands exit the protein matrix sequentially via sites B, C and D into the solvent. A slightly more intricate scheme suggested that ligands take parallel pathways away from B. Furthermore, the authors developed a so-called side path model. Whereas they could exclude the sequential model, their data could be fit to either of the remaining models.

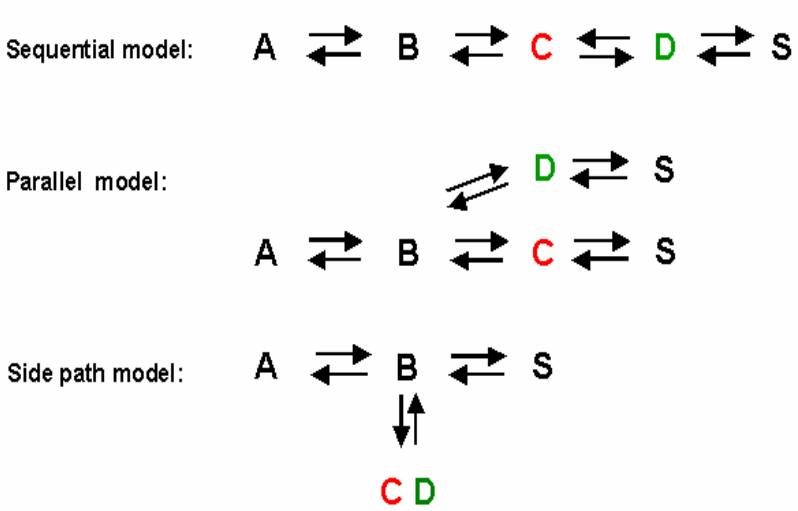

Fig. 4.11: Schemes for ligand migration and recombination in Mb (adapted from Chatfield *et al*. (128))

Scott *et al.* (107) have suggested that the globin acts like a baseball glove to 'catch' and then trap incoming ligands long enough to allow bond formation with the heme iron. They employed a slightly modified side path scheme to explain their kinetic traces of oxygen recombination to mutant myoglobin (Fig. 4.12), in which the initial docking site B is proposed to play a central role. After photolysis, ligands migrate to site B, which theyuse as a 'hub'. From there, they rebind directly, exit the protein through the histidine gate or migrate to secondary docking sites C and/or D, only to return to site B and then rebind (or escape).

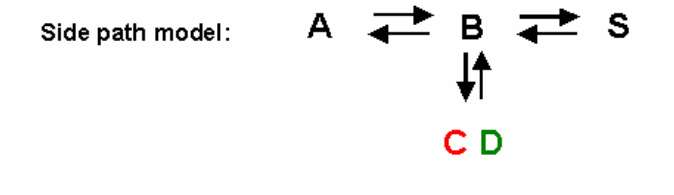

Fig. 4.12: Modified side path model adopted from Scott *et al.* (107).

To determine the fraction of ligands, F_{gem}, that rebind geminately from site B, the authors used a simple three-well model (compare Eq.1.6) with bound state A, unbound state B and solvent S,

$$F_{gem} = \frac{k_{BA}}{k_{BA} + k_{BS}}. \qquad (4.5)$$

The bimolecular recombination rate coefficient k'_{on} and the entry rate coefficient k'_{entry} were defined according to the same model,

$$k'_{on} = k'_{entry} \cdot F_{gem}$$

$$k'_{entry} = \frac{k'_{on}}{F_{gem}}. \tag{4.6}$$

This treatment excludes any ligand exchange within the internal states, but more importantly, it also neglects equilibration of ligand in secondary sites C and D with site B. Geminate recombination from secondary sites C and D was calculated from

$$F_{\text{sec}} = \frac{k_{B(C,D)}}{k_{BA} + k_{B(C,D)} + k_{BS}}. \tag{4.7}$$

It is only in this particular step of their calculations that the authors incorporate multiple internal docking sites.

The model that has been put forward in this thesis (Figs. 4.8, 4.9) acknowledges the fact that entry and exit are slow processes, and thus the globin is indeed a glove that confines the CO for a long time. However, in comparison to the one by Olson and coworkers described above, our model is far more specific. It emphasizes that state B is the gateway to bond formation, whereas the other cavities have been identified as transient storage sites that rather prevent ligand binding, so that the probability of ligand release is enhanced. We assume that CO equilibrates among the cavity states B, C, and D on nanosecond time scales. As a consequence, we are unable to make any definitive statements about the entry and exit pathways, except that we can exclude a sequential model B → C → D → S.

4.2 Ligand Migration and Recombination in L29W MbCO

4.2.1 Ligand Dynamics in a Frozen Protein

The replacement of leucine 29 by the aromatic amino acid tryptophan leads to a decrease of the CO association rate coefficient l_S at room temperature by a factor of 130 (83). L29W MbCO showed pronounced changes in the stretch bands of the photodissociated CO in our low temperature FTIR/TDS experiments, which facilitated the interpretation of the spectral changes in terms of ligand migration and recombination. We have seen pronounced differences to WT MbCO that are caused by the bulky indole sidechain sequestering the Xe 4 site from the rest of the distal pocket, as depicted in Fig. 4.13. In this subsection, we will discuss how the low temperature results provide insights into the exceptionally slow ligand binding properties of L29W Mb at physiological temperatures.

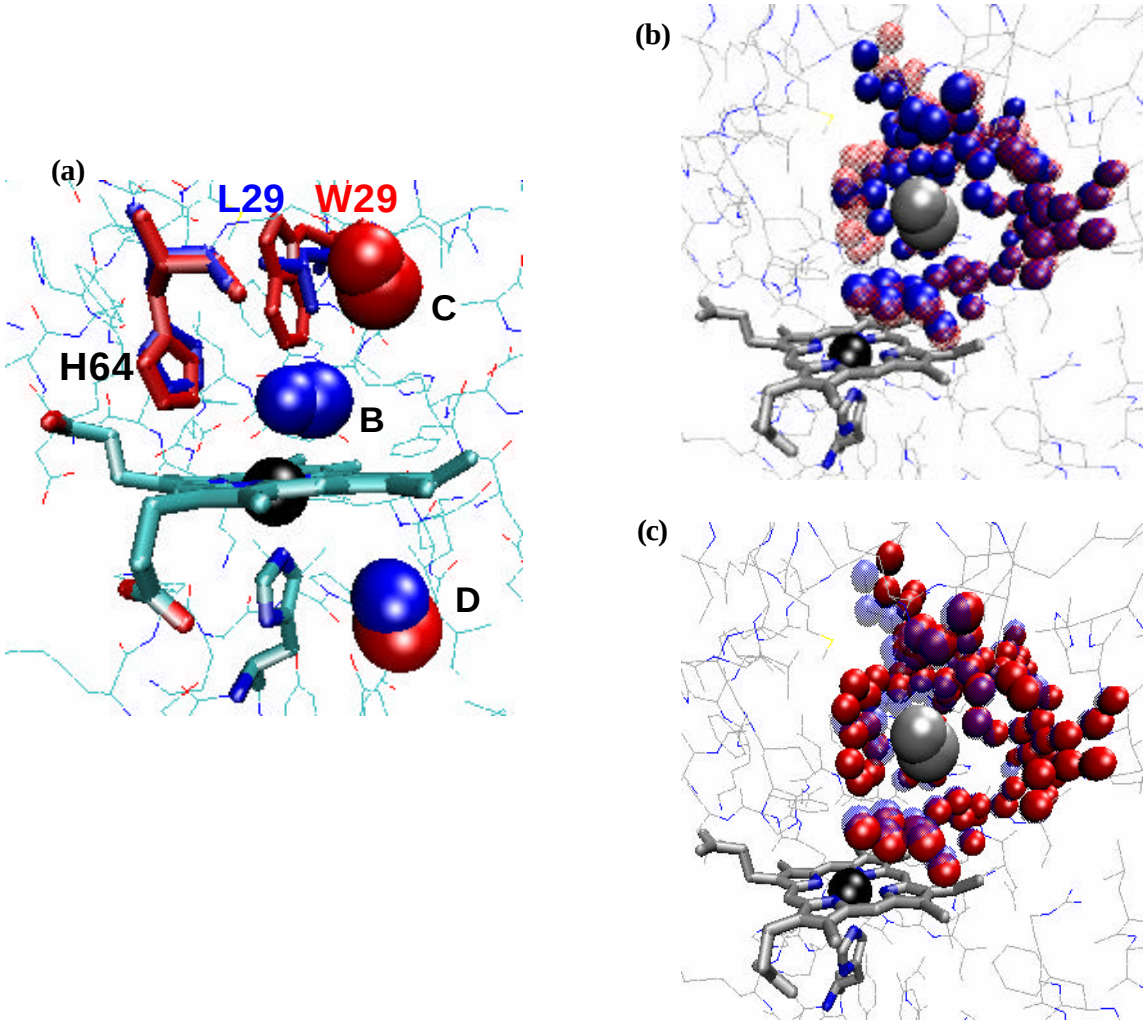

Fig. 4.13: (a) Superposition of the three-dimensional structures of taxonomic substates A_1 of WT MbCO (blue) and A_I of L29W MbCO (red) ; Xe 4 cavities in (b) WT and (c) L29W.

The FTIR/TDS experiments reveal two different conformations, A_I and A_{II} with markedly different geminate rebinding properties at low temperatures. In the frozen A_{II} conformation, CO is confined to the immediate vicinity of the active site at 3 K and rebinds very heterogeneously. There is evidence from the x-ray structure analysis that, in A_{II}, the 'normal'

primary docking site is inaccessible, and the very heterogeneous low temperature rebinding suggests that CO rebinds from less well defined distal pocket locations. In the A_I conformation, the majority of photodissociated CO settles into docking site B after brief photolysis at 3 K (Fig. 3.44), but a tiny fraction of ~1% is able to escape to the Xe 4 cavity even at 3 K. We have shown that the population in this photoproduct state C' can be greatly enhanced (to ~50% at 3 K) by extended illumination for 15,000 s. The physical mechanism was identified as transfer of energy from photoexcitation of the heme group to the CO molecules in photoproduct state B. At higher temperatures, CO migration to C' can also happen by thermal activation. At 80 K, for example, migration from B to C' is observed on the millisecond time scale in the flash photolysis data at 80 K (Fig. 4.14). They show that, after a single flash, 85% of the ligands rebind, but 15% escape to state C' (15). By extended illumination for 15,000 s at 80 K, the CO molecules get multiple chances to escape, so that eventually, all CO ligands in A_I molecules are transferred to the Xe 4 cavity (Fig. 3.51).

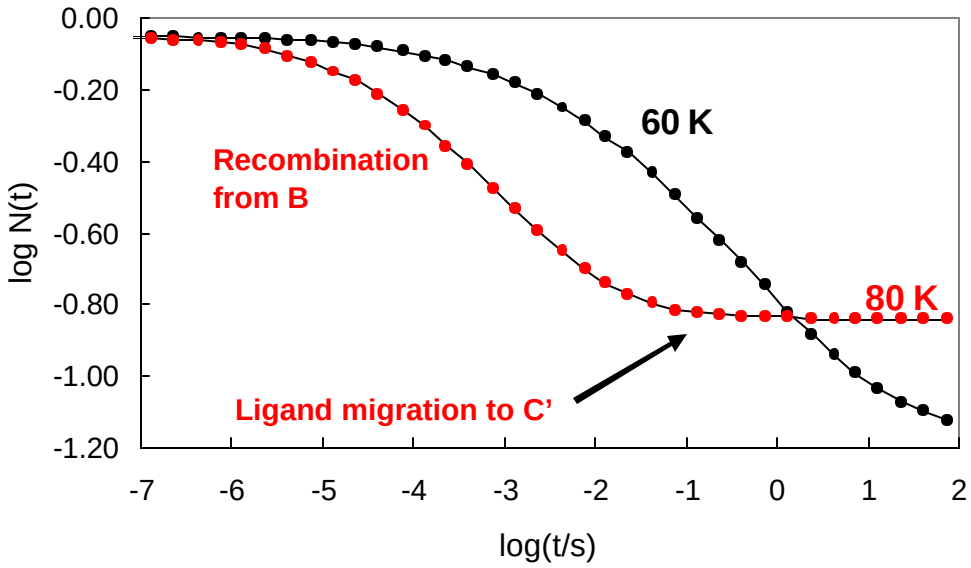

Fig. 4.14: Flash photolysis kinetics of L29W MbCO at 60 and 80 K, measured in the CO stretch band of the A_I conformation at 1,945 cm^{-1}.

While the CO is in the Xe 4 cavity, the characteristic spectral signature of photodissociated CO changes from C' to a new spectrum associated with photoproduct C'' at ~130 K. A comparison of different mutants has provided evidence that this change is not caused by migration of CO to a different location, but rather by a slight relaxation of the sidechains of residues 29 and 64 towards a more A_{II}-like conformation.

At ~180 K, large-scale protein motions are activated that can transiently open additional migration pathways. As Nienhaus and coworkers have shown (15), CO vacates the distal side and migrates to the proximal side, with concomitant relaxation of the protein to the A_{II} conformation. We cannot distinguish cause and effect here, i.e., if CO migration causes the protein relaxation, or if the relaxation 'squeezes' the CO out of the Xe 4 cavity. We do know, though, that A_{II} molecules cannot host a ligand in the Xe 4 cavity. Flash photolysis experiments with monitoring in the A_{II} stretch band near 200 K have shown that, after a fast geminate phase from ligands in the vicinity of the active site, recombination essentially stalls and only continues on time scales slower than transitions between the two A conformations (115). This suggests that CO can only rebind as long as it is still in the distal pocket. After exiting, relaxation of the distal pocket into the A_{II} conformation blocks the active site, and only through conformational transitions to A_I, rebinding can occur. Fig. 4.15 summarizes the different bound and intermediate states in L29W MbCO. We note that, although not

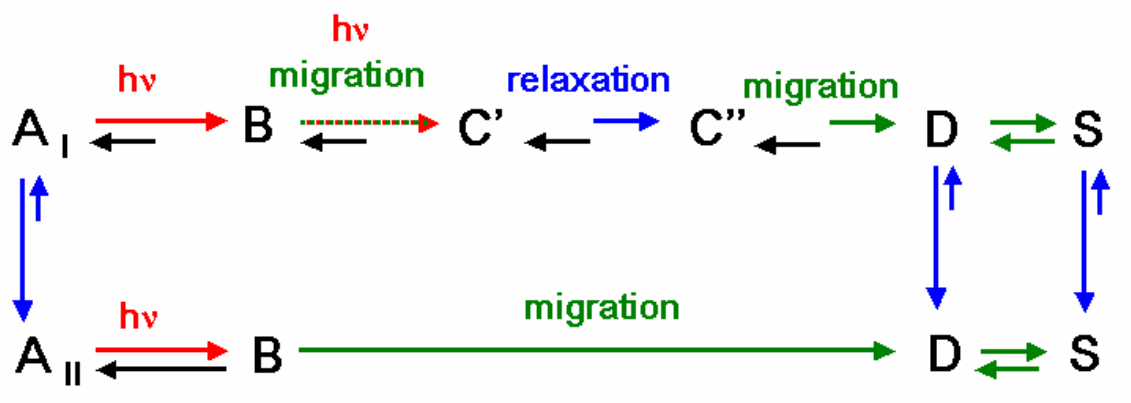

Fig. 4.15: Ligand migration and recombination in L29W MbCO.

explicitly included in the diagram, ligand escape in A_I molecules should also be possible from states B, C' and C''.

In WT, ligand migration to the proximal side occurs already at 120 and 160 K in A_1 and A_3, well below the solvent glass transition temperature. In L29W, however, only in A_{II} molecules we have observed a few CO ligands in site D below ~180 K. We can think of two explanations for the different behavior: (i) Either the structure of L29W at the heme plane differs from the one of WT and does not allow for the transition to the proximal side in a frozen protein, or (ii) site D is not populated in the frozen L29W MbCO because site C' is somewhat lower in free energy than in WT MbCO and thus preferentially occupied.

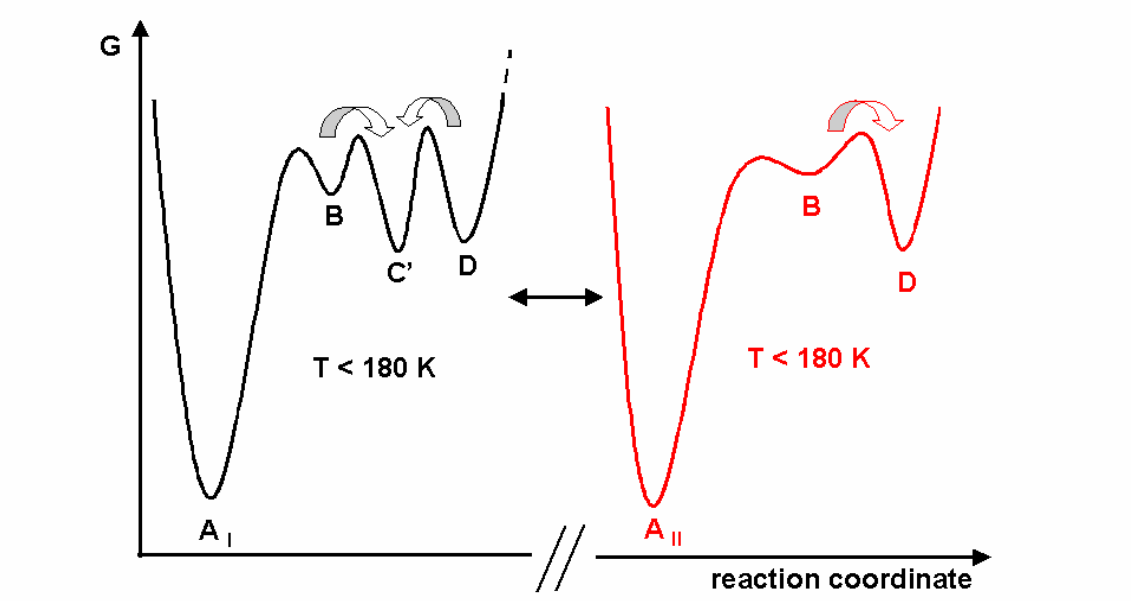

Fig. 4.16: Sequential multi-well model of L29W MbCO substates A_I and A_{II}.

Above 180 K, protein relaxation into the A_{II} conformation raises the free energy of the Xe 4 pocket, which shifts the equilibrium towards state D (Fig 4.16). The discussion of the physiological ligand binding in the following section will show that the CO migration process can be understood qualitatively with the reaction surfaces in Fig. 4.16, and that it is indeed the extremely high affinity of C' that governs the ligand dynamics in frozen L29W MbCO.

4.2.2 Physiological Ligand Binding in L29W MbCO

In Fig. 4.17, we plot the flash photolysis traces of L29W, some of its double mutants, and WT MbCO at room temperature (293 K). As in the case of WT MbCO, we observe nearly complete ligand escape into the solvent in L29W and *all* related double mutants. Bimolecular recombination from the solvent, however, is slowed substantially in all L29W mutants, by factors ranging from 25 – 130 as compared to WT.

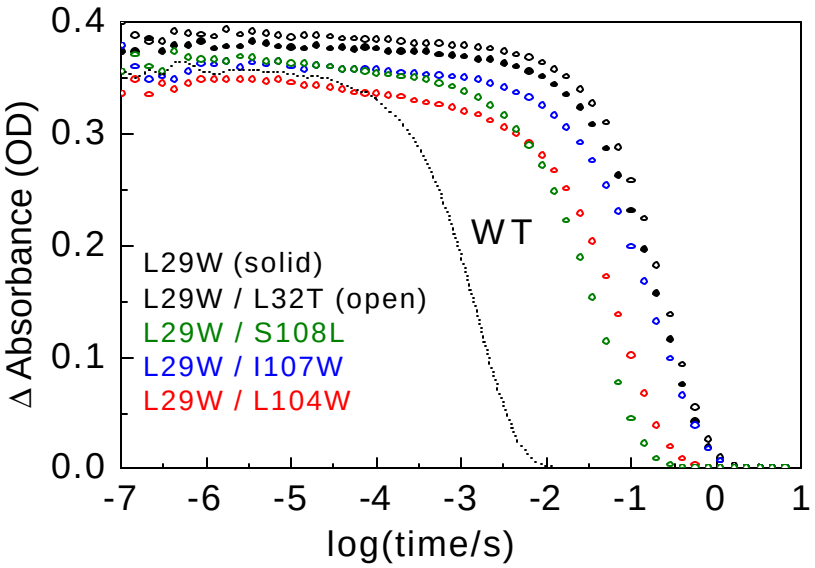

Fig. 4.17: Kinetic traces of MbCO mutant L29W and related double mutants in 100 mM potassium phosphate, pH 8, monitored at 436 nm after flash photolysis at room temperature; included: kinetic trace of WT.

To explain the room temperature kinetic data on the basis of our low temperature observation, we need to be aware of the temperature dependence of the A substate populations in L29W MbCO. Fig. 3.35 shows that the majority of molecules are in A_I at low 200 K but in A_{II} at 293 K. Fig. 4.18 displays the structure of deoxy L29W (black) at room temperature, which is – except for the CO ligand – in good agreement with the ligand-bound structure at ambient temperature (A_{II}) (116). On the deoxy structure, we have superimposed the structures of L29W MbCO in substate A_I (red) and photoproduct D (A_{II}-like distal pocket conformation) after photolysis of L29W MbCO above 180 K (blue). The two latter structures were determined at 105 K. A global comparison of the three structures reveals a marked reorientation of the G-helix in the deoxy protein as compared to the photoproduct and also to ligand-bound L29W at 105 K (Fig. 4.18, right). The W29 indole sidechain in the A_{II} conformation does not only occlude the initial docking site B, but also prevents occupancy of the Xe 4 cavity (compare section 3.2.4) and the Xe 1 cavity. Consequently, at room temperature, no long-lived metastable states exist in the predominantly A_{II}-type molecules, and thus, dissociated ligands will efficiently exit the protein, $N_S \tilde{} 1$.

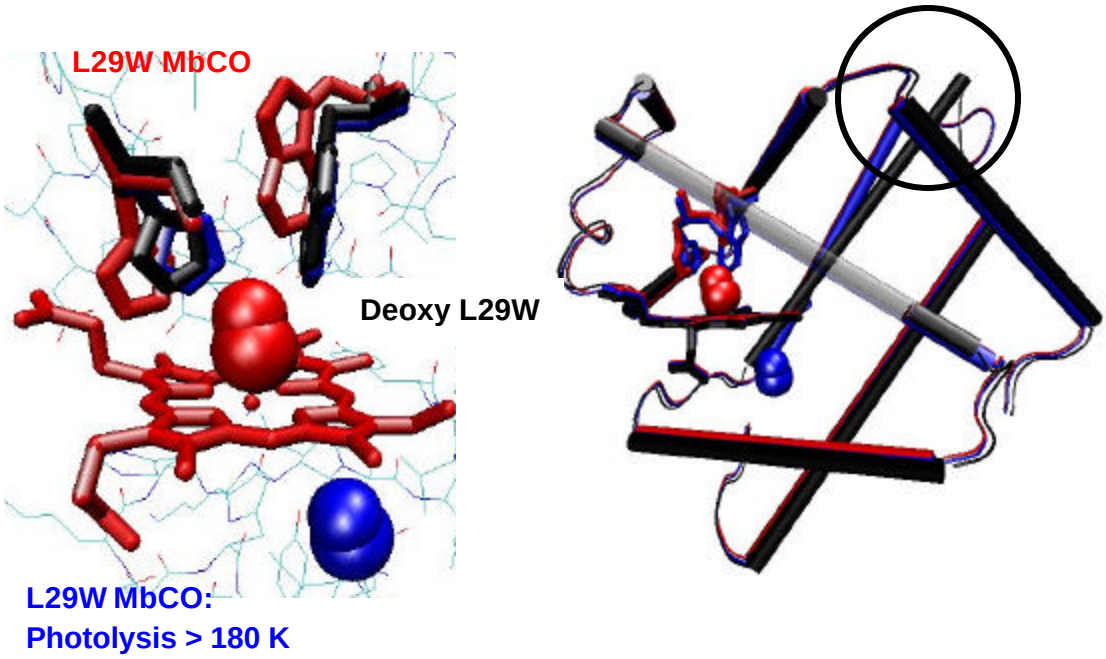

Fig. 4.18: Comparison of deoxy L29W (black) at room temperature, L29W MbCO (red) and L29W MbCO after photolysis above 180 K (blue); the photolyzed ligand is located in Xe 1; left: structure around the heme-plane; right: global view of the three-dimensional arrangement of the helices.

For the ligand association process, we could envision a scenario where the ligands enter the protein from the distal side, for instance through the often mentioned 'histidine gate' and bind to the heme iron (107). Fig. 4.18 shows that the central heme iron should be accessible. However, this model would not give an explanation as to why the kinetics are slowed with respect to WT. The key issue in ligand binding to heme proteins is that bond formation can only occur by a concerted adjustment of the active site, which is responsible for the low Arrhenius prefactors of ~10^9 s^{-1} and also leads to a lowered activation enthalpy barrier of ~10kJ/mol. Therefore, ligands have to stay around long enough at the active site to wait for this fluctuation to happen. The A_{II}-like deoxy conformation lacks a long-lived state that mediates recombination, as the primary docking site B is occluded by the W29 indole sidechain. CO that enters the distal pocket will not stay long enough for bond formation to occur and escape again. Only when it enters and finds the protein in the A_I-like deoxy conformation, it will settle in docking site B which enhances the probability of bond formation. Consequently, a transient conformational change from the A_{II}-like deoxy conformation to A_I is a prerequisite for docking at site B and subsequent binding. Bimolecular recombination will thus be slowed by the equilibrium deoxyA_{II}/deoxyA_I, which is shifted towards A_{II}. Likewise, if the CO should not directly access the distal pocket but enter through the Xe 1 cavity, a conformational transition $A_{II} \rightarrow A_I$ would be the only means to open the door to the distal pocket and make state B available. This latter mechanism, however, does not apply to double mutant L29W/L104W with its occluded Xe 1 cavity.

Among the L29W double mutants, slight differences in the rates of bimolecular rebinding are visible in Fig. 4.17 and Table 4.2. Our model is supported by the observation that mutant L29W/S108W shows the fastest recombination from the solvent. This mutant displays a pronounced fraction of the A_I conformation in the MbCO spectrum at room temperature (Fig. 3.36). Although we cannot directly determine the equilibrium between the two conformations

in the deoxy form (at least with IR spectroscopy), it is reasonable to assume that is also shifted towards A_I. Consequently, recombination is faster in this mutant because more B sites are accessible on average. We remark that, even in the A_I state, ligand binding should be slower than in WT because of the very efficient Xe 4 trap, which reduces the probability of CO to reside in B. A comparison of the ratios of the association rate coefficients of the pairs, WT : L104W ~ 4 and L29W : L29W/ L104W ~ 3, is also interesting. In both L104W mutants, blockage of the Xe 1 site should lead to a larger (and similar) fraction of time that the CO spends at the primary docking site.

Table 4.2: Fraction of ligands escaping into the solvent, N_{out}, and apparent rate coefficient l_S of L29W and related double mutants (fitted with a single exponential).

Mutant	**N_{out} (%)**	**l_{on} (s^{-1})**
L29W	100	0.23
L29W / L104W	85	0.09
L29W / L32T	100	0.28
L29W / I107W	93	0.21
L29W / S108L	96	0.04

In a three-state kinetic analysis of their flash photolysis data on many mutant MbO_2 samples at room temperature, Scott *et al.* (107) came to the conclusion that the inner barrier (bond formation) and the outer barrier (entry/exit) were both much larger in L29W than in WT. They explained the high inner barrier by interference from the W29 indole side chain hanging directly over the center of the heme group. The high outer barrier was assumed to arise from ligands escaping through the Xe 4 and Xe 1 cavities, which is expected to be more difficult than passing through the 'histidine gate' which they considered as blocked by W29 as well. In the simple three-state model by Scott *et al.*, taxonomic substates with vastly different structures and ligand binding properties were not included. Therefore, they came to entirely different conclusions than those presented here. In our model, bond formation can only occur in A_I. With the equilibrium favoring A_{II}, this effect leads to an apparent increase in the activation enthalpy barrier. In their analysis, Scott *et al.* noticed that ligand entry to the active site is difficult, and thus they suggested that the CO enters and exits through less efficient channels involving the Xe cavities. Our model shows that the real problem is not ligand migration in the protein, but ligand access to docking site B.

Our extensive studies of L29W MbCO have provided valuable insight into heme-protein engineering principles. No other mutation that we have performed as of yet has had such a drastic impact on ligand migration. By enhancing the pocket-like character of the Xe 4 site we have succeeded in shifting the preferred distal geminate site from B to C. Nevertheless, as in WT Mb, state B remained the crucial docking site that mediates ligand binding, and replacement of residue 29 with aromatic amino acids markedly slows ligand binding by sterically occluding the primary docking site B. Through a thorough investigation of the intricate interplay between taxonomic substates A_I and A_{II}, a dynamic ligand binding model of L29W was developed. Application of spectroscopic and diffraction techniques in parallel has proven essential to connect kinetic and structural aspects of the model.

4.3 Conclusion

Myoglobin has served as a model system for structure–function relationship studies for many years. The photosensitivity of the adducts of the reduced protein with CO, O_2 and NO allows events related to the migration of the ligand through the matrix to be followed. Using infrared spectroscopy over a wide temperature range, we have been able to draw a detailed picture of CO migration to and recombination from various sites within the protein matrix. These spectroscopic observations have been correlated with the structural data obtained by cryo-crystallography of photoproducts. They have proven extremely useful in the interpretation of room temperature kinetic and crystallographic data obtained after laser photolysis, supporting the significance of our results for the control of ligand binding and, therefore, for the biology of O_2 transport.

Our structural and kinetic investigations of protein relaxation and CO migration in myoglobin after photodissociation below and above the dynamic transition temperature emphasize the crucial interplay between protein dynamics and function and support the following picture of the physiologically important ligand escape process: within picoseconds after dissociation from the heme iron, ligands predominantly settle in a specific docking site B in the distal heme pocket, which plays a crucial role in iron-ligand bond formation. Ligands can reside in this site for nanoseconds without rebinding and also migrate to internal cavities C and D, which lowers the geminate rebinding probability. Thus they can reside long enough in the protein interior until large-scale protein fluctuations on nanosecond to microsecond timescales open exit channels through which ligands finally escape from the protein.

The internal protein cavities that are in the center of this thesis are clearly thermodynamically disadvantageous. Already Tilton *et al.* (27) observed an overall reduction in temperature factors upon xenon binding, which they interpreted as a ligand-induced restriction of the number of conformational substates. Although packing defects reduce the thermodynamic stability, internal cavities seem to play an important role in controlling protein function by providing hosting stations for photolyzed ligands (17). The emerging picture is that there may be a selective advantage in building a protein with ‘packing defects’.

Appendix A: Intrinsic Absorbance Changes of Photoproduct Bands

The individual IR bands of *heme-bound* CO are known to change shape and intensity at temperatures above the glass transition temperature of the cryo-solvent (Ansari 1987). The integrated absorbance, however, changes only by a few percent and hence, the A substate bands can serve as sensitive probes to determine the populations within the individual taxonomic substates in a given sample. In the photoproduct states, the CO acquires additional mobility, which can lead to a decrease of the band area (ref Anfinrud JPC). As of yet, no clear experimental manifestation of this effect has been given in the published literature.

We have been able to provide evidence of intrinsic, temperature-related absorbance changes of the photoproduct bands with a specially designed sequence of FTIR/TDS experiments (Fig. A1). In a first TDS experiment (TDS 1), the MbCO sample was cooled under light from an initial temperature T_i to 3 K. CO ligands were sequentially trapped at intermediate sites (compare with the slow-cool protocol described in section 2.6.4). At 3 K, illumination was terminated. A second TDS experiment (TDS 2) performed immediately afterwards, spanning the temperature range from 3 K to a final temperature T_f, was performed to monitor the extent of recombination. These two data sets were taken as controls to determine the combined effect of illumination *and* temperature. Subsequently, the sample was cooled under illumination once again, starting at the same initial temperature T_i (TDS 3). However, illumination was switched off at an intermediate temperature T_{dark}. The remainder of the FTIR data collection was performed in the dark. As a consequence, ligands in long-lived states remained trapped, and those in short-lived states were depleted quickly. Thus, the remaining photoproduct bands are exclusively associated with long-lived, secondary states. Any subsequent change in band shape and/or area can only arise from intrinsic, temperature-induced modifications. A final TDS experiment (TDS 4) in the dark (3 K to T_f) confirmed the reversibility of temperature-induced band modifications.

In the following TDS maps, arrows indicate the direction of the temperature ramp. Red arrows correspond to TDS measurements under illumination; black ones are associated with experiments in the dark. Whereas solid arrows refer to the actual TDS plot, dotted arrows mark the 'sample history'.

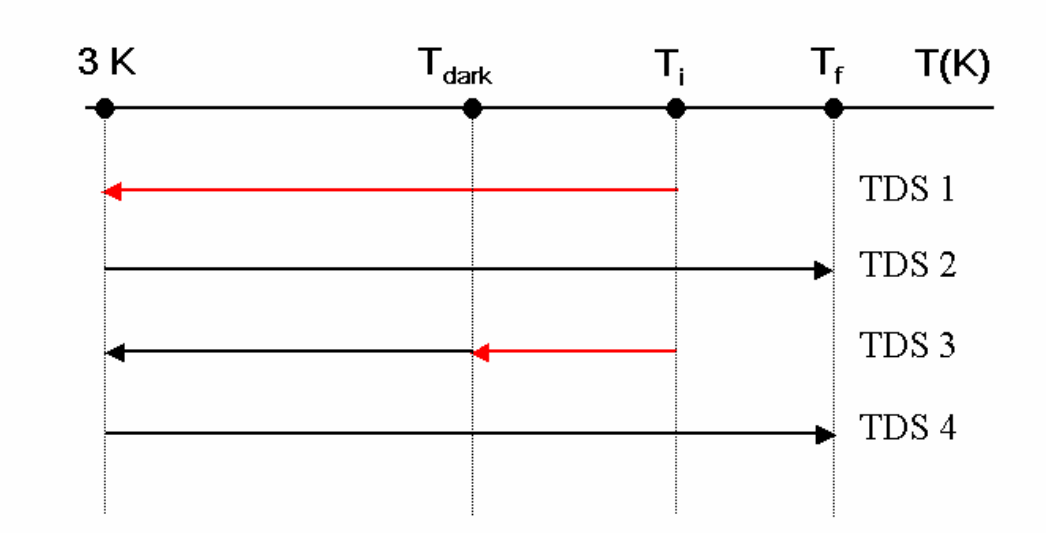

Fig. A1: Set of TDS protocols to monitor intrinsic absorbance changes of photoproduct IR bands.

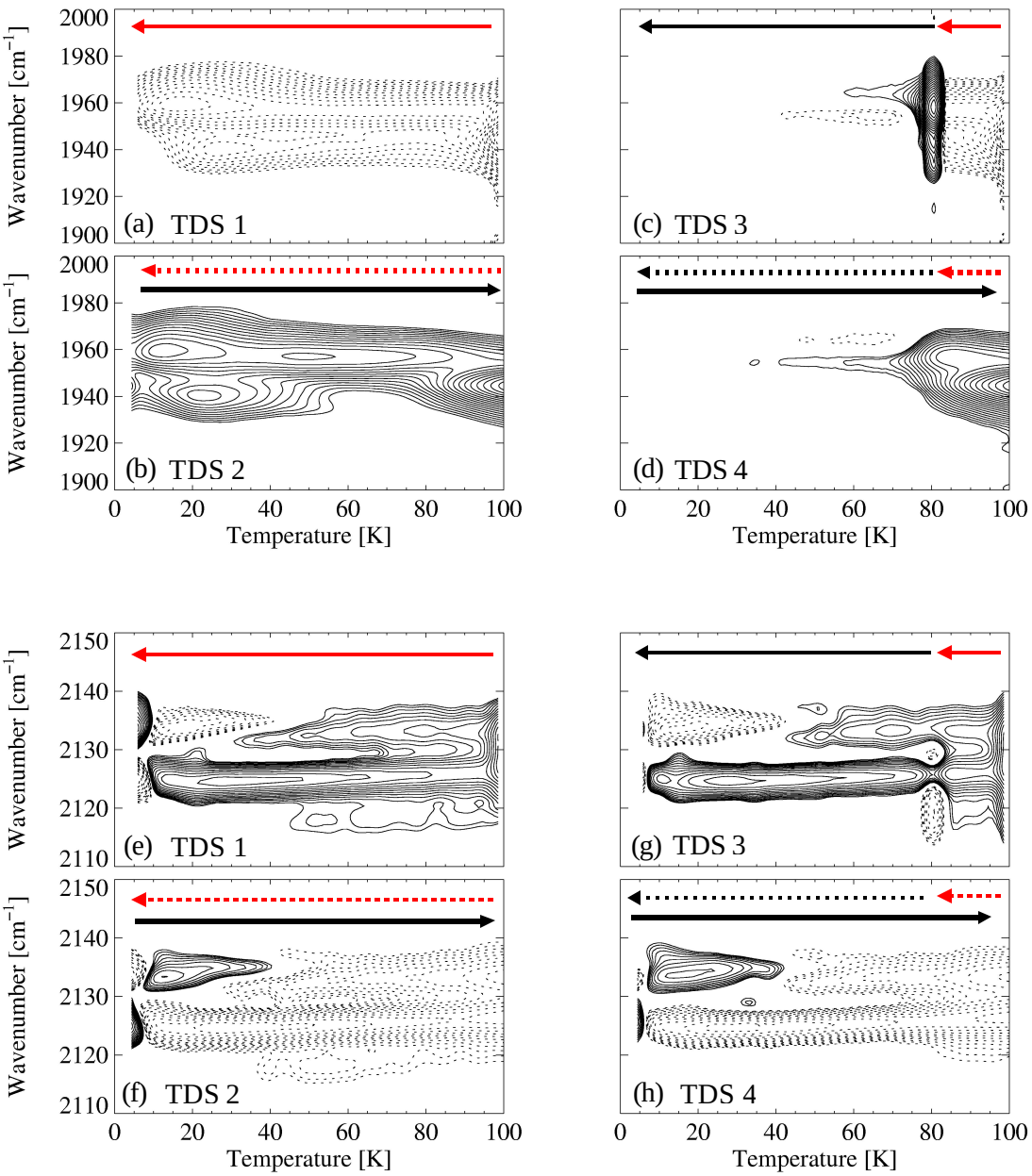

Fig. A2: TDS maps of L29W MbCO in 75%/25% glycerol/buffer applying different illumination protocols; (a–d) heme-bound CO, TDS experiments 1-4; (e–h) photolyzed CO, TDS experiments 1-4; arrows indicate the direction of the temperature ramp; red arrows: under illumination; black arrows: in the dark; solid arrows: actual protocol; dotted arrows: sample history.

The set of four consecutive TDS experiments was performed on L29W MbCO in 75%/25% glycerol/buffer (Fig. A2). In TDS 1, spectra were collected from T_i = 100 to 3 K, followed by TDS 2 from 3 to 160 K. In TDS 3, T_{dark} was set to 80 K. Finally, TDS 4 ran from 3 to 160 K. The temperatures T_{dark} = 80 K and T_i = 100 K were chosen to selectively populate intermediate state C' and to allow any CO ligands located at the initial docking site B to rebind immediately after switching off the light.

Panels a-d and e-h in Fig. A2 display absorbance changes in the bands of heme-bound and photodissociated CO, respectively. The data in the left column are associated with TDS experiments 1 and 2, the ones in the right column with experiments 3 and 4. Whereas the A substate map in panel d shows recombination mainly from C' to A_I, the photoproduct maps show a perplexing variety of solid and dotted contours over the whole temperature range, indicative of decreasing and increasing intensities of photoproduct bands associated with temperature changes only. Figure A3 displays the TDS photoproduct spectra of TDS 4 from 3

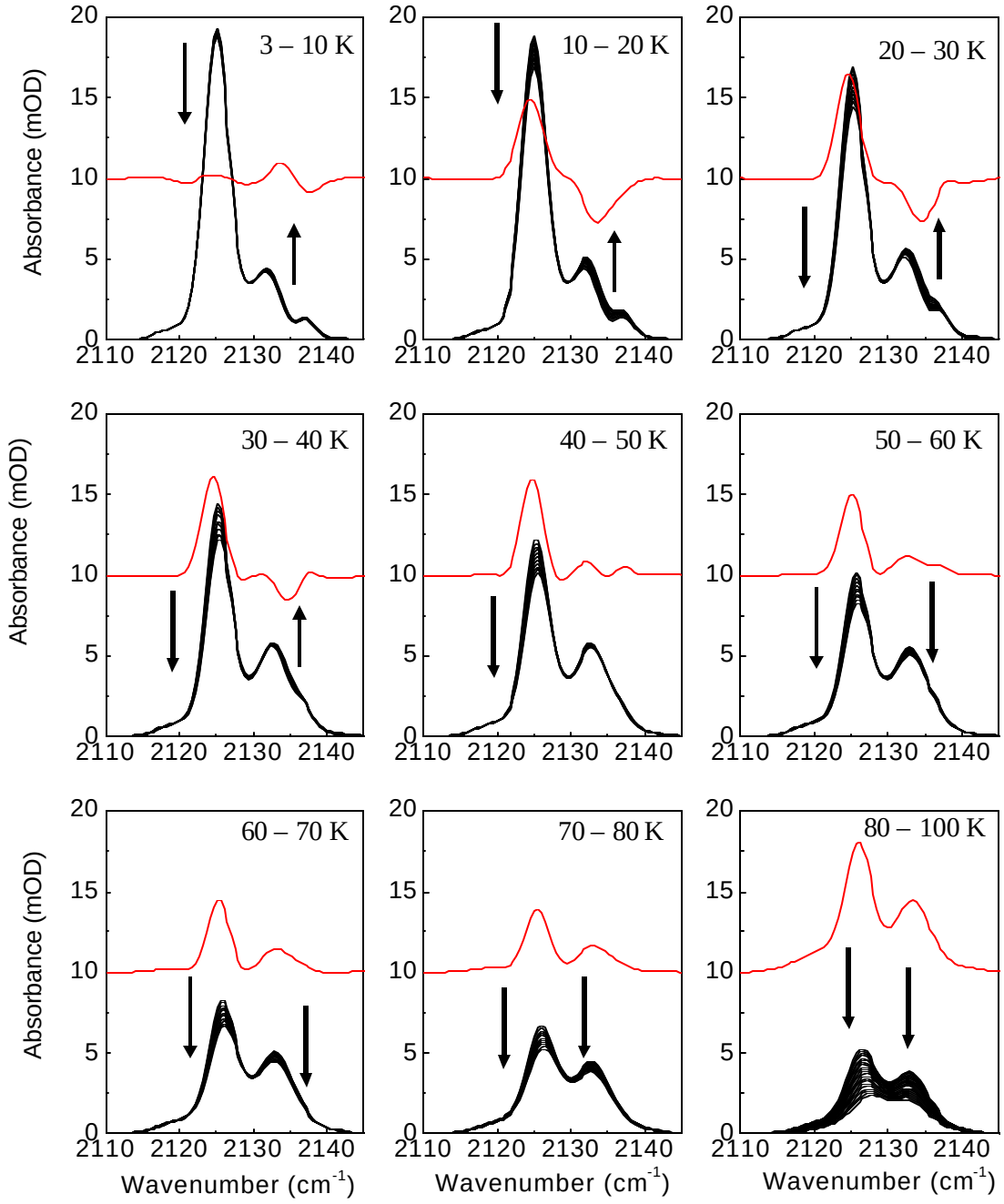

Fig. A3: Photoproduct spectra of intermediate C' of L29W MbCO as a function of temperature while increasing the temperature in the dark from 3 K to 100 K (TDS 4); red: overall difference within each temperature interval (shifted by 10 mOD); arrows: development with increasing temperature.

to 100 K. After correcting for the intrinsic absorbance changes by taking differences between the FTIR spectra of sets 1 and 3 and also 2 and 4, the contour maps in Fig. A4 exclusively display features due to photolysis (panel a, c) and recombination (panels b, d). Calculation of the absorbance difference across the recombination signal of A_{II} from 60 to 80 K gives the unaltered spectrum of $B(A_{II})$ with bands at 2118 and 2125 cm^{-1}.

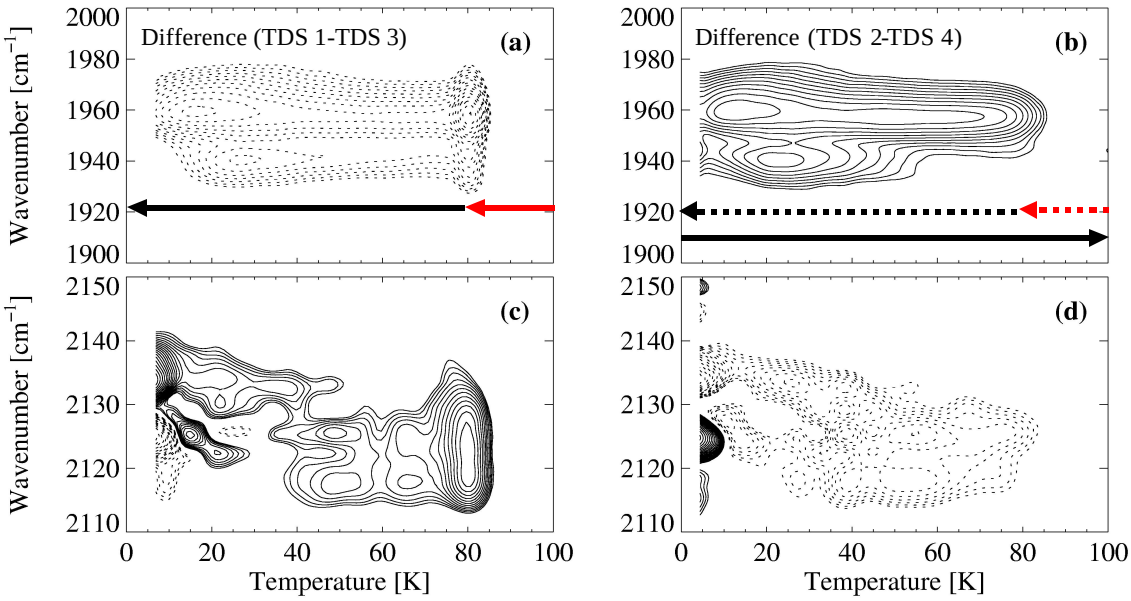

Fig. A4: TDS maps of L29W in glycerol/buffer corrected for temperature induced absorbance band changes; (a) difference between Fig. A2 a and c; (b) difference between Fig. A2 b and d; (c) difference between Fig. A2 e and g; (d) difference between Fig. A2 f and h.

An analogous set of four TDS experiments was performed on L29W MbCO dried in trehalose. In Fig. A5 a, b, we plot the TDS maps obtained while cooling under illumination from T_i =160 K to T_{dark} =100 K. When decreasing the temperature in the dark from 100 to 3 K, we observe a band shift in the A state bands (panel c). This is a consequence of the referencing procedure (compare section 2). The photoproduct bands, however, exhibit a gain in absorbance (panel d). Increasing the temperature reverses the spectral changes (panels e, f).

In Fig. A6, we present the TDS maps obtained with protocols 2 and 4. In the TDS maps e and f, the maps in panels a and b were corrected for the intrinsic absorbance changes apparent in c and d. This procedure yields a photoproduct spectrum for $B(A_{II})$ as well as one for $C'(A_I)$ that were not at all visible in the photoproduct contour map in panel b.

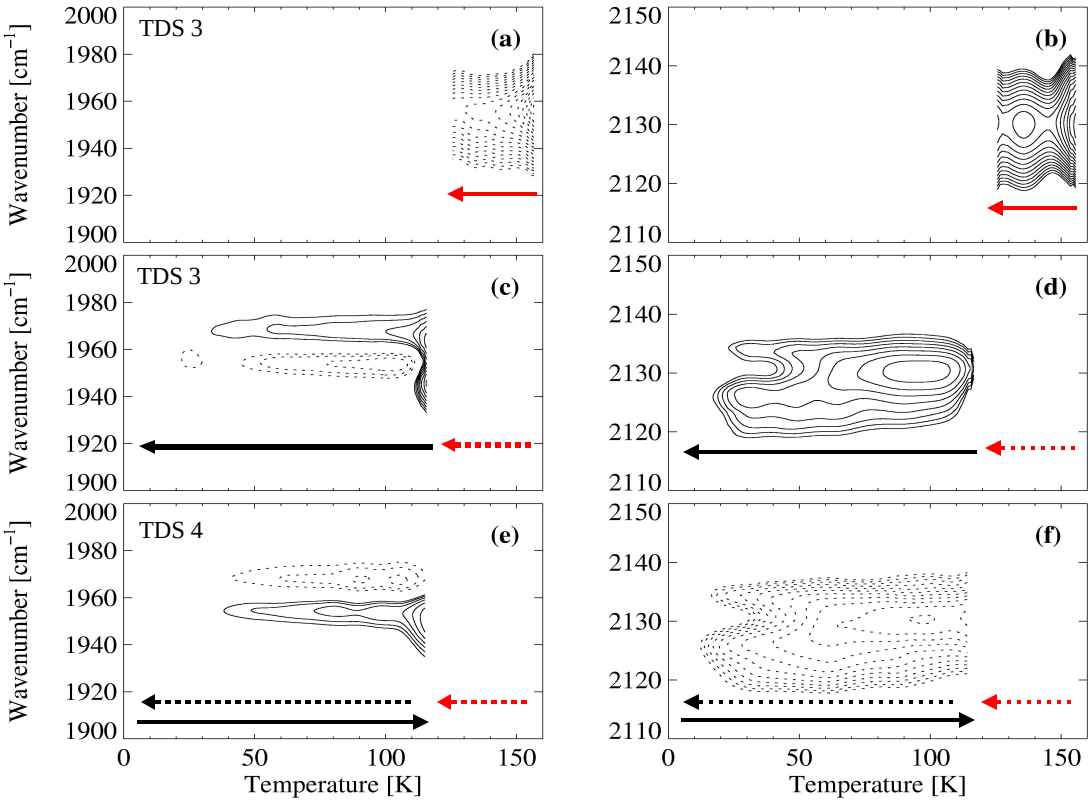

Fig. A5: TDS maps of L29W (dried trehalose) of (left) heme-bound and (right) photodissociated CO during different illumination prot ocols and temperature.

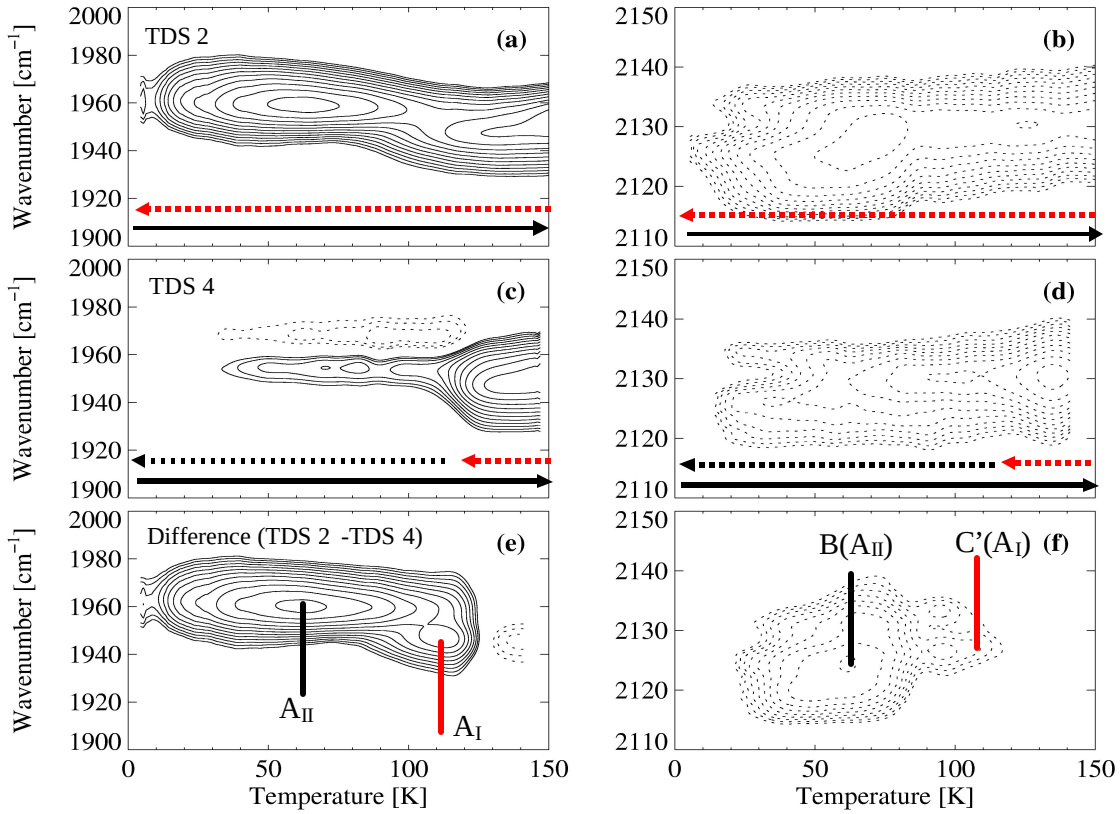

Fig. A6: TDS maps of L29W in dried trehalose obtained with (a, b) TDS protocol 2 and (c, d) TDS protocol 4; e, f: Difference TDS maps corrected for intrinsic band changes.

Mutant MbCO L29W/S108L presents another impressive example of the temperature dependence of photoproduct bands. In the TDS plots in Fig. 3.61, contours of two photoproduct bands at ~2125 and 2138 cm^{-1} are visible that stretch out over a temperature interval spanning more than 60 K. Fig. A7 shows data collected with TDS protocols 1 and 2, followed by contour plots from protocols 3 and 4 in Fig. A8. T_i was set to 100 K, T_{dark} to 80 K. Thus, we have selected exclusively the photoproduct bands of C'.

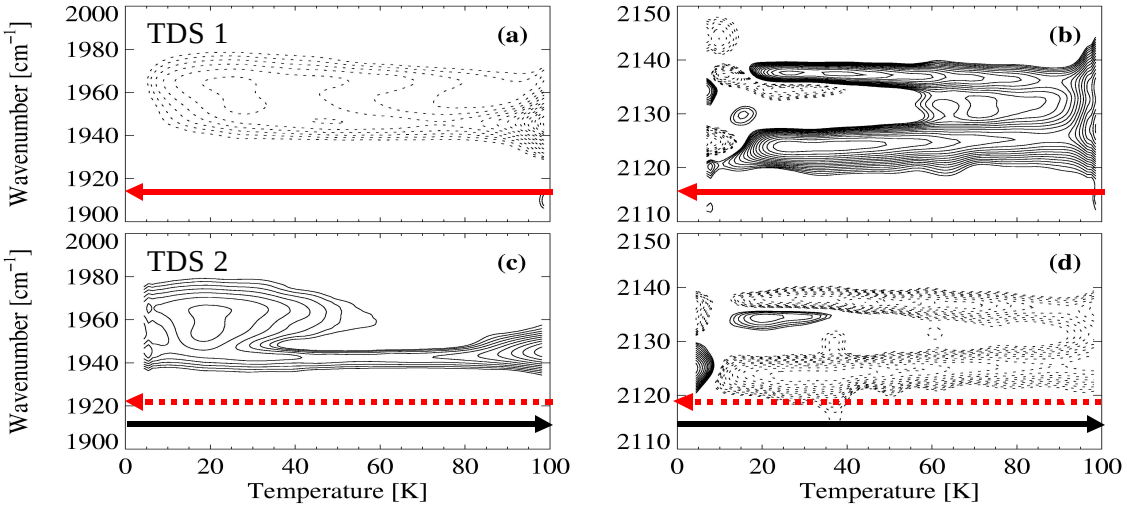

Fig. A7: TDS maps of L29W/S108L MbCO received with TDS protocols 1 and 2; T_i=100 K; T_{dark}=80 K.

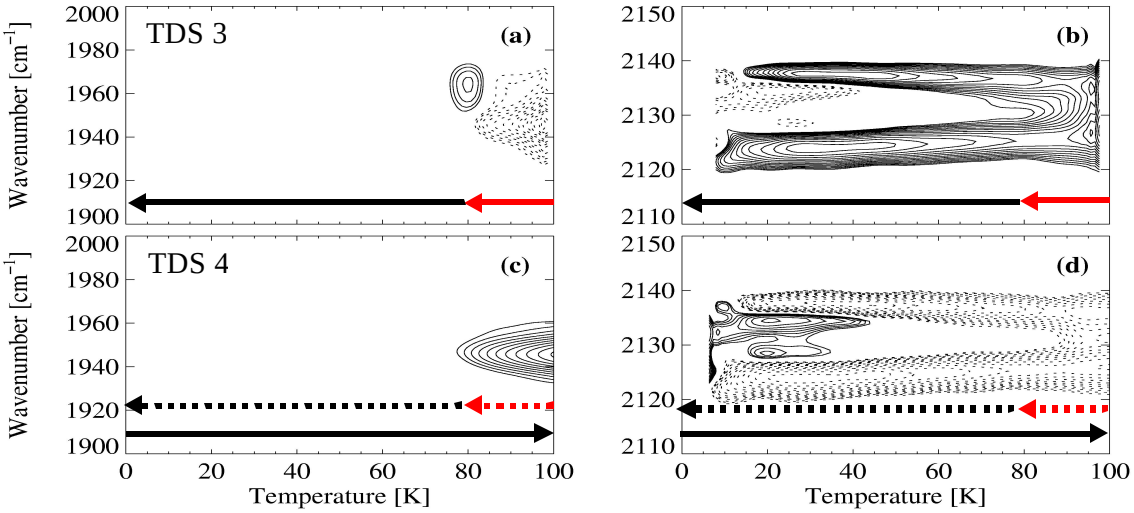

Fig. A8: TDS maps of L29W/S108L MbCO received with TDS protocols 3 and 4; T_i=100 K; T_{dark}=80 K.

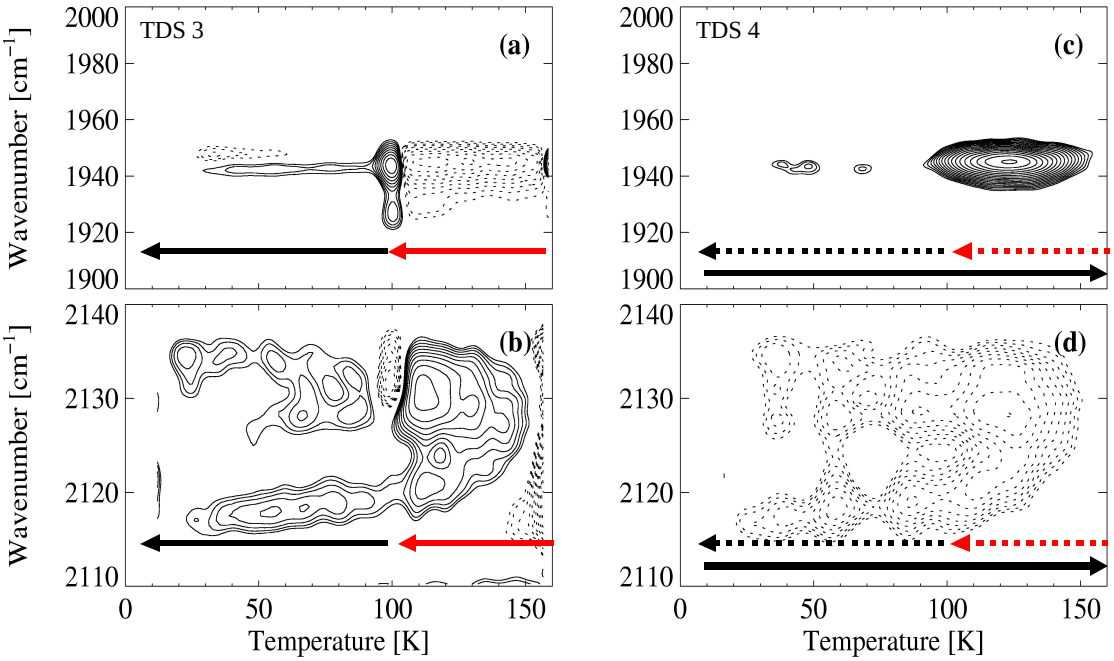

Fig. A9: TDS maps of I28W MbCO received with TDS protocols 3 and 4; T_i=160 K; T_{dark}=100 K.

This temperature effect is not at all a feature characteristic of L29W and its double mutants, as seen from the contour plots of I28W MbCO, collected with TDS protocols 3 and 4 (Fig. A9). For this mutant, T_i was set to 100 K, T_{dark} to 80 K. This choice of T_{dark} yields the photoproduct bands of intermediate D. The data show pronounced changes in B_{2119} with temperature, and we also see alterations of two bands at ~2128 and ~2135 cm^{-1}.

In this work, the IR bands of heme-bound and photolyzed CO have served as internal probes to monitor ligand binding and migration. In the TDS experiments, it is normally assumed that the observed changes in integrated absorbance are proportional to the population that either rebinds or migrates to another state during acquisition of two consecutive spectra. In this appendix, we have provided evidence of an intrinsic temperature dependence of the IR bands of photodissociated CO. This observation implies an additional complication in the quantitative analysis of TDS maps. A detailed modeling of these data yields insights into ligand dynamics within the cavities. This work is will be presented elsewhere.

Appendix B: FTIR Absorption Band Frequencies

Table 3.1: Stretch frequencies of heme-bound and photolyzed CO (site B) in WT MbCO and related mutants.

Mutant MbCO	**Frequency of Heme-bound CO (cm^{-1})**			**Frequency of Photodissociated CO (cm^{-1})**			
Substate	**A_3**	**A_1**	**A_0 (A_x)**	**B_2**	**B_1**	**B_0**	**$B(A_0)$**
WT (pH 7)	1928	1945		2119	2131	2149	
WT (pH 5.4)	1931	1948	1967	2119	2131		2127/2138
H64L			1965		2126		
H64V			1968	2124	2129		
V68S	1927	1945	(1967)	2118	2134	2159	
V68F (pH 9.3)	1928	1945	(1967)	2113	2138	2126	
V68F (pH 5.6)	1935	1948	1966	2113	2138		2121/2127
V68W	1928	1945	(1967)	2110	2138	2148	
I28F	1927	1945		2118	2130		
I28W	1927	1945		2118	2131		
L32H	1929	1946	(1966)	2119	2131	2149	
I107W	1933	1945		2108	2129	2151	
L104W	1924	1944		2118	2131	2149	
H64V/V68S			1970				2124/2130

Table 3.2: Stretch frequencies of heme bound and photolyzed CO (site B) in L29W mutant MbCO and related double mutants.

Mutant MbCO	**Frequency of Heme-bound CO at 3 K (cm^{-1})**			**Frequency of Photodissociated CO (cm^{-1})**	
Substate	**A_I**	**A_{II}**		**$B_2(A_I)$**	**$B_1(A_I)$**
L29W (glyc./buf.)	1945	1955		2122	2131
L29W (treh./buf.)	1945			-	-
L29W (dry treh.)		1955		-	-
L29W/L32T	1951	1961		2122	2131
L29W/L72F	1944	1959	1915	2122	2131
L29W/I107W	1941	1952		2118	2129
L29W/S108L	1946	1964		2122	2131
L29W/L104W	1945	1963		2122	2131

Appendix C: List of Figures

1 Introduction

1.1 Schematic presentation of the rugged energy landscape.
1.2 Van der Waals representation of myoglobin.
1.3 Absorbance spectra of L29W myoglobin in the UV-visible region of the spectrum.
1.4 Five-well-model to describe ligand recombination.
1.5 Three-well model introduced by Eaton and coworkers to describe the recombination kinetics of MbCO.
1.6 Schematic presentation of the two-dimensional reaction surface proposed by Agmon/Hopfield.
1.7 Schematic representation of the initial docking site B.
1.8 Three-dimensional sketch of mutant L29W.
1.9 FTIR absorbance difference spectrum of WT MbCO; sketch of the three-dimensional structure of taxonomic substates A_1 and A_0 at the active site.
1.10 Temperature dependence of FTIR absorbance spectra of mutant L29W MbCO; pH dependence of FTIR spectra of WT MbCO.
1.11 Schematic presentation of back bonding based on the valence bond formalism of Alben and Caughey.
1.12 FTIR absorbance difference spectrum of L29W MbCO at 3 K after 1-s illumination; three-dimensional structure of L29W around the active site.
1.13 Mutated residues in the close vicinity of the binding site A and the initial docking site B in L29W MbCO.
1.14 Mutated residues lining the Xe cavities of L29W MbCO; CO ligand is sketched at docking sites B, C and D.

2 Materials and Methods

2.1 Schematic presentation of the PCR (polymerase chain reaction) temperature protocol used for site-directed mutagenesis.
2.2 Principle of absorption spectroscopy.
2.3 Basic instrumentation of the FTIR spectrometer.
2.4 Transmission spectra of MbCO.
2.5 FTIR absorbance difference spectra of MbCO.
2.6 FTIR absorbance difference spectra presented as linearly spaced (left panel) and logarithmically spaced (right panel) contour plots on a temperature versus wavenumber surface.
2.7 Set of logarithmically spaced contour maps representing FTIR absorbance difference spectra.
2.8 FTIR absorbance difference spectra showing kinetic hole burning.
2.9 FTIR absorbance difference spectra showing an intrinsic temperature dependence .
2.10 Comparison of contour plots of TDS data, employing different referencing procedures.
2.11 Overview of different illumination protocols to prepare specific intermediates.
2.12 The principle of the slow-cool protocol.

3 Results

3.1 FTIR absorbance difference spectra of WT MbCO (pH 7 and pH 5.4) and mutants H64L and H64V recorded at 3 K after illumination for 1 s.

3.2 FTIR spectra of WT MbCO and mutants V68S, V68F and V68W recorded at 3 K after illumination for 1 s; insets: (upper left) structure near the active site, (lower right) V68F at pH 5.4.
3.3 FTIR absorbance difference spectra of WT MbCO and mutants V68S, H64V/V68S and H64V measured at 3 K after illumination for 1 s.
3.4 FTIR absorbance spectra of MbCO samples WT, I28F, I28W and L32H at 3 K after illumination for 1 s.
3.5 FTIR absorbance difference spectra of WT MbCO and myoglobin mutants I107W and L104W at 3 K after illumination for 1 s.
3.6 TDS contour maps of (a, b) WT MbCO (pH 7), (c, d) WT MbCO (pH 5.4) as well as mutants (e, f) H64L and (g, h) H64V after illumination for 1 s at 3 K.
3.7 TDS contour maps of WT MbCO (high pH) and mutants V68S, V86F and V68W after illumination for 1 s at 3 K.
3.8 TDS contour maps of MbCO mutant V68F at (a, c) high and (b, d) low pH after illumination for 1 s at 3 K.
3.9 TDS contour maps of MbCO mutant H64V/V68S after illumination for 1 s at 3 K
3.10 TDS contour maps of WT MbCO (pH 7) and mutants L32H, L104W, I107W and I28W after illumination for 1 s at 3 K.
3.11 FTIR spectra of WT MbCO and mutants H64L and H64V in the spectral region of photodissociated CO; top: after short illumination for 1 s at 3 K; bottom: after slow cooling from 160 to 3 K under illumination.
3.12 FTIR spectra of WT MbCO and mutants V68S, V68F and V68W in the spectral region of photodissociated CO; upper panel: after illumination for 1 s at 3 K; lower panel: after slow-cool from 160 to 3 K under illumination; inset: sketch of the active site.
3.13 FTIR spectra of WT MbCO and mutants H64V, H64V/V68S and V68S in the spectral region of photodissociated CO; top panel: after illumination for 1 s at 3 K; lower panel: after slow cooling from 160 to 3 K under illumination.
3.14 FTIR absorbance spectra of WT MbCO and mutants I28F, I28W and L32H in the spectral region of photodissociated CO; top panel: after illumination for 1 s at 3 K; lower panel: after slow-cool from 160 to 3 K under illumination.
3.15 FTIR spectra of the photoproducts of WT MbCO and mutants I107W and L104W; top panel: after illumination for 1 s at 3 K; lower panel: after slow-cool from 160 to 3 K under illumination.
3.16 TDS contour maps of WT MbCO (pH 7), WT(Xe) and related mutants L104W, I107W, I28W and L32H after slow cooling from 160 to 3 K.
3.17 TDS contour maps of mutants H64L and H64V after slow cooling from 160 to 3 K.
3.18 TDS contour maps for WT (pH 7) MbCO and mutants V68S, V68F and V68W after slow-cooling from 160 to 3 K.
3.19 TDS contour maps of MbCO mutants V68S, H64V/V68S and H64V after slow cooling from 160 to 3 K.
3.20 Active sites of L104W MbCO (pdb code 1CPW) and YQRF MbO_2.
3.21 Integrated absorbance differences $\int \Delta A dv$ calculated from the TDS experiments in Fig. 3.16 of WT, WT(Xe) and L104W as a function of temperature; left panel: A_1; right panel A_3
3.22 Integrated absorbance differences $\int \Delta A dv$ calculated from the TDS experiments in Fig. 3.16 of WT, L32H, I107W, I28F and I28W as a function of temperature; left panel: A_1; right panel A_3. The TDS plots of I28F are not shown.
3.23 Superposition of WT (pdb code 1ABS) depicted in blue and V68F MbCO (pdb code 1MJL) depicted in gray ;Superposition of V68F deoxy (pdb code 1MKL) depicted in red and V68F MbCO (pdb code 1MJL) depicted in gray.

3.24 Integrated absorbance differences $\int \Delta A dv$ calculated from the TDS experiments in Figs. 3.16, 3.18 of WT, V68S, V68F and V68W as a function of temperature; left panel: A_1; right panel A_3.
3.25 Integrated absorbance differences $\int \Delta A dv$ calculated from the TDS experiments in Figs. 3.17 of WT MbCO and mutants H64L and H64V) as a function of temperature.
3.26 Solid lines: integrated absorbance differences $\int \Delta A dv$ calculated from the TDS experiments in Figs. 3.19 of WT, H64V, H64V/V68S and V68S; dotted line: data after 1-s illumination of H64V/V68S.
3.27 FTIR absorbance bands for intermediates B, C and D of A_1 (left) and A_3 (right).
3.28 FTIR spectra of WT MbCO, WT(Xe), L104W and I107W recorded at 160 K after illumination at 185 K for two hours and slow cooling to 160 K under light. Inset: active site structure showing important residues.
3.29 FTIR spectra of WT MbCO and mutants L32H, I28W and V68W recorded at 160 K after illumination at 185 K for two hours and slow cooling to 160 K under light.
3.30 TDS contour maps for WT MbCO, WT(Xe), L104W and I107W after illumination at 185 K for two hours and slow-cool to 160 K.
3.31 TDS contour maps of MbCO mutants I28W, L32H and V68W after illumination at 185 K for two hours and slow cooling to 160 K.
3.32 FTIR absorbance difference spectra $-\log(I_{light}/I_{met})$ of WT at selected temperatures; spectra display the bound population at a given temperature.
3.33 Active site of sperm whale MbCO substate A_1 (left) and mutant L29W (right) substates A_I (red) and A_{II} (blue); the CO ligand is depicted in the bound state A and at intermediate locations B, C and D.
3.34 FTIR spectra of L29W MbCO and related double mutants at 3 K. Transmission spectra were referenced against 'met' spectra to determine the IR bands of the overall bound population.
3.35 Temperature dependence of IR spectra of samples (a) L29W in glycerol/buffer, (b) L29W(Xe) in glycerol/buffer and (c) L29W in buffer saturated with trehalose. Transmission spectra were referenced against a 'met' transmission spectrum; insets: temperature dependence of fractions n_I of A_I and n_{II} of A_{II}.
3.36 FTIR spectra of L29W MbCO and related double mutants in 75%/52% glycerol/buffer at 300 K; the FTIR transmission spectra were referenced against a 'met' transmission spectrum; the area was normalized for comparison.
3.37 Effect of xenon on the relative populations of A_I/A_{II} in IR spectra of three mutants of MbCO at 3 K; black lines: samples without xenon; red lines: samples equilibrated with 1 atm of xenon at 0°C.
3.38 FTIR spectra of L29W MbCO at 3 K (bottom) and 290 K (top) in different solvents.
3.39 Van't Hoff plots of the A_I/A_{II} equilibrium population ratios of three different L29W MbCO samples.
3.40 Four-state-model to explain the influence of xenon on the equilibrium ratio A_I/A_{II} in MbCO mutant L29W.
3.41 FTIR absorbance difference spectra of MbCO samples L29W and L29W(Xe) after illumination for 1 s at 3 K.
3.42 FTIR spectra of MbCO mutants L29W, L29W/L72F and L29W/L104W after illumination for 1 s at 3 K
3.43 FTIR spectra of MbCO mutants L29W, L29W/L32T, L29W/I107W and L29W/S108L after illumination for 1 s at 3 K.
3.44 TDS contour maps of (a, c) L29W and (b, d) L29W(Xe) after illumination for 1 s at 3 K.
3.45 FTIR/TDS absorbance differences calculated across the recombination features in the TDS maps after illumination for 1 s at 3 K in Fig. 3.41.

3.46 TDS contour maps of MbCO mutants L29W/L104W, L29W/L72F, L29W/S108L, L29W/L32T and L29W/I107W after illumination for 1 s at 3 K.
3.47 The active site of MbCO mutant L29W; the CO ligand is depicted at the initial docking site B (pdb code 1ABS); red: A_I, blue: A_{II}.
3.48 Schematic explaining how of CO populates the $B_{1,2}$ photoproduct sites after photodissociation.
3.49 Temporal development of FTIR spectra of L29W MbCO during illumination for 15,000 s at 3 K.
3.50 TDS contour maps of mutant L29W MbCO after illumination for 15,000 s at 3 K.
3.51 Temporal development of the CO stretch bands of MbCO mutant L29W at 80 K.
3.52 CO stretch bands of the A states and photoproduct C' of L29W MbCO.
3.53 Active site of L29W; the CO ligand is located in the Xe 4 cavity.
3.54 Normalized FTIR spectra of CO at site B in L29W and WT MbCO.
3.55 Temporal development of the integrated absorbance of L29W MbCO at 3 K, monitored in the A state bands after 1-s illumination at 3 K; inset: FTIR absorbance spectra; arrow: time progression; red: overall change during rebinding for 7,000 s.
3.56 Temporal development of the photoproduct populations at sites B and C' in L29W MbCO; red: integrated absorbance in A state bands with respect to time.
3.57 Temporal development of the FTIR absorbance bands of MbCO mutant L29W at 120 K during illumination for 15,000 s.
3.58 FTIR spectra of heme-bound and photodissociated CO of L29W, L29W/L72F and L29W/L104W after slow cooling under illumination from 160 to 3 K (solid lines) and of L29W after 1-s illumination at 3 K (dotted line).
3.59 FTIR spectra of heme-bound and photodissociated CO of MbCO mutants L29W, L29W/L32T, L29W/I107W and L29W/S108L after slow cooling from 160 to 3 K (solid lines) and of L29W after 1-s illumination at 3 K (dotted line).
3.60 CO stretch bands of MbCO mutants L29W, L29W/I107W and L29W/L104W after slow cooling under illumination from 160 to 3 K; solid lines: samples without xenon; dotted lines: the identical samples after equilibration with 1 atm of xenon.
3.61 TDS contour maps of L29W MbCO and related double mutants after slow cooling from 160 to 3 K under illumination.
3.62 TDS contour maps after slow cooling from 160 K to 3 K under illumination for MbCO mutants L29W, L29W/L104W and L29W/I107W, equilibrated with 1 atm of Xe at 0° C.
3.63 CO stretch bands associated with intermediates C' and C'' of L29W MbCO and related double mutants.
3.64 Temporal development of the CO stretch bands of MbCO mutant L29W at 160 K.
3.65 TDS contour maps of MbCO mutant L29W after illumination for 15,000 s at 160 K.
3.66 TDS contour maps of L29W MbCO in different cryo-solvents after slow cooling from 160 to 100 K under illumination.
3.67 TDS maps of YQR MbCO after illumination for 1 s at 3 K (a, b) and slow cooling under illumination from 140 to 3 K (c, d).
3.68 Superposition of the three-dimensional structures of C' (blue) and C'' (red) intermediates of YQR mutant MbCO.
3.69 Superposition of cartoons of YQR MbCO structures: C' (blue) ,C'' (red) and deoxy YQR (dark gray).
3.70 TDS maps of L29W MbCO and related double mutants collected while ramping the temperature from 100 to 220 K under illumination.
3.71 Temporal development of the IR stretch bands of (left column) heme-bound and (right column) photodissociated CO in samples L29W and L29W(Xe) at 180 K during 15,000 s of illumination and subsequent 50,000 s in the dark.

3.72 Temporal evolution of the integrated absorbances of the FTIR bands of heme-bound CO under illumination and during subsequent rebinding in the dark.
3.73 FTIR spectra of MbCO mutants L29W, L29W/L72F, L29W/I107W and L29W/L104W after illumination at 185 K for 2 h and slow cooling under light to 160 K.
3.74 FTIR absorbance difference spectra of MbCO mutants L29W, L29W/I107W and L29W/L104W after illumination at 185 K for 2 h and slow cooling under light to 160 K; solid lines: without xenon; dotted lines: samples equilibrated with 1 atm of xenon.
3.75 TDS maps of L29W MbCO and related double mutants after illumination for 2 h at 185 K and slow cooling to 160 K while illuminating the sample.
3.76 TDS maps of L29W MbCO and related double mutants equilibrated with xenon after illumination for 2 h at 185 K and slow cooling to 160 K.
3.77 FTIR spectra normalized to 1 ODcm^{-1} of intermediates C'' (L29W) and D for MbCO samples L29W, L29W(Xe) and L29W/L104W.
3.78 FTIR spectra of photoproduct D in L29W, L29W(Xe) and L29W/L104W.
3.79 FTIR/TDS absorbance difference spectra of (left column) heme-bound and (right column) photolyzed CO monitored in the spectral range of heme-bound CO in L29W MbCO after 15,000 s of illumination at 160 K.
3.80 L29W versus YQR.

4 The Role of Internal Cavities on the Binding Process

4.1 Sequential multi-well model of WT (substate A_1).
4.2 Sequential multi-well model of WT (substate A_3) and mutants I28F and I28W.
4.3 Superposition of structural cartoons of sperm whale myoglobin and horse heart myoglobin.
4.4 Sequential multi-well model of WT (substate A_1) and mutants H64L and H64V.
4.5 Sequential multi-well model of MbCO mutant L104W.
4.6 Two-dimensional scheme of ligand migration and recombination in WT MbCO.
4.7 Kinetic traces of WT MbCO and related mutants.
4.8 Energy landscape to describe physiological ligand binding.
4.9 Our scheme to explain ligand migration and recombination.
4.10 Three-dimensional structure of the active site of YQRF MbO_2 and deoxy YQRF.
4.11 Schemes for ligand migration and recombination in Mb (from Chatfield *et al.*).
4.12 Modified side path model (from Scott *et al.*)
4.13 Superposition of the three-dimensional structures of taxonomic substates A_1 of WT MbCO (blue) and A_I of L29W MbCO (red).
4.14 Flash photolysis kinetics of L29W MbCO at 60 and 80 K, measured in the CO stretch band of the A_I conformation at 1,945 cm^{-1}.
4.15 Ligand migration and recombination in L29W MbCO.
4.16 Sequential multi-well model of L29W MbCO.
4.17 Kinetic traces of MbCO mutant L29W and related double mutants.
4.18 Comparison of deoxy L29W (black) at room temperature, L29W MbCO (red) and L29W MbCO after photolysis above 180 K (blue).

Bibliography

1. Anfinsen, C. B. (1967) *Harvey Lect.* **61,** 95-116.
2. Dill, K. A., Chan, H.S. (1997) *Nat. Struct. Biol.* **4,** 10-19.
3. Wolynes, P., Luthey-Schulten, Z. & Onuchic, J. (1996) *Chem. Biol.* **3,** 425-432.
4. Wolynes, P. G. (1996) *Proc. Natl. Acad. Sci. U S A* **93,** 14249-14255.
5. Wolynes, P. G. (1997) *Proc. Natl. Acad. Sci. U S A* **94,** 6170-6175.
6. Goldbeck, R. A., Thomas, Y. G., Chen, E., Esquerra, R. M. & Kliger, D. S. (1999) *Proc. Natl. Acad. Sci. U S A* **96,** 2782-2787.
7. Levinthal, C. (1968) *J. Chim. Phys.* **65,** 44-45.
8. Ansari, A., Berendzen, J., Bowne, S. F., Frauenfelder, H., Iben, I. E., Sauke, T. B., Shyamsunder, E. & Young, R. D. (1985) *Proc. Natl. Acad. Sci. U S A* **82,** 5000-5004.
9. Parak, F. G.& Nienhaus ,G.U. (2002) *Chem. Phys. Chem.* **3,** 249-254.
10. Frauenfelder, H. & McMahon, B. H. (2001) *Biosystems* **62,** 3-8.
11. Petsko, G. A. (1994) *Nature* **371,** 740-741.
12. Kendrew, J. C., Dickerson, R.E., Strandberg, B.E., Hart, R.G., Davies, D.R., Phillips, D.R., Phillips, D.C. & Shore, V.C. (1960) *Nature* **185,** 422-427.
13. Brunori, M., Bonaventura, J., Bonaventura, C., Antonini, E. & Wyman, J. (1972) *Proc. Natl. Acad. Sci. U S A* **69,** 868-871.
14. Austin, R. H., Beeson, K. W., Eisenstein, L., Frauenfelder, H. & Gunsalus, I. C. (1975) *Biochemistry* **14,** 5355-5373.
15. Ostermann, A., Waschipky, R., Parak, F. G. & Nienhaus, G. U. (2000) *Nature* **404,** 205-208.
16. Chu, K., Vojtchovs ky, J., McMahon, B. H., Sweet, R. M., Berendzen, J. & Schlichting, I. (2000) *Nature* **403,** 921-923.
17. Brunori, M. (2000) *Biophys. Chem.* **86,** 221-230.
18. Brunori, M., Vallone, B., Cutruzzola, F., Travaglini-Allocatelli, C., Berendzen, J., Chu, K., Sweet, R. M. & Schlichting, I. (2000) *Proc. Natl. Acad. Sci. U S A* **97,** 2058-2063.
19. Srajer, V., Ren, Z., Teng, T. Y., Schmidt, M., Ursby, T., Bourgeois, D., Pradervand, C., Schildkamp, W., Wulff, M. & Moffat, K. (2001) *Biochemistry* **40,** 13802-13815.
20. Perman, B., Anderson, S., Schmidt, M. & Moffat, K. (2000) *Cell. Mol. Biol. (Noisy-le-grand)* **46,** 895-913.
21. Moffat, K. (1998) *Acta Crystallogr. A* **54,** 833-841.
22. Moffat, K. (1998) *Nat. Struct. Biol.* **5 Suppl,** 641-643.
23. Kendrew, J. C. (1963) *Science* **139,** 1259-1266.
24. Stryer, L. (1995) *Biochemistry,* Freeman Publications, San Francisco.
25. Gibson, Q. H. & Ainsworth, S. (1957) *Nature* **180,** 1416–1417.
26. Schoenborn, B. P., Watson, H. C. & Kendrew, J. C. (1965) *Nature* **207,** 28-30.
27. Tilton, R. F., Jr., Kuntz, I. D., Jr. & Petsko, G. A. (1984) *Biochemistry* **23,** 2849-2857.
28. Tilton, R. F., Jr., Singh, U. C., Weiner, S. J., Connolly, M. L., Kuntz, I. D., Jr., Kollman, P. A., Max, N. & Case, D. A. (1986) *J. Mol. Biol.* **192,** 443-456.
29. Brunori, M. (2001) *Trends Biochem. Sci.* **26,** 209-210.
30. Brunori, M. (2001) *Trends Biochem. Sci.* **26,** 21-30.
31. Frauenfelder, H., McMahon, B. H., Austin, R. H., Chu, K. & Groves, J. T. (2001) *Proc. Natl. Acad. Sci. U S A* **98,** 2370-2374.
32. Cleeter, M. W., Cooper, J. M., Darley-Usmar, V. M., Moncada, S. & Schapira, A. H. (1994) *FEBS Lett.* **345,** 50-54.
33. Olson, J. S., Mathews, A. J., Rohlfs, R. J., Springer, B. A., Egeberg, K. D., Sligar, S. G., Tame, J., Renaud, J. P. & Nagai, K. (1988) *Nature* **336,** 265-266.

34. Eaton, W. A., Hofrichter, J. (1981) in *Methods in Enzymology, Hemoglobins*, ed. Antonini, E. Rossi-Bernardi, L., Chiancone, E., Vol. 76, pp. 175-261.
35. Dong, A. & Caughey, W. S. (1994) *Methods. Enzymol.* **232,** 139-175.
36. Antonini, E. & Brunori, M. (1971) *Hemoglobin and Myoglobin in Their Reactions with Ligands*, North-Holland, Amsterdam.
37. Gibson, Q. H. & Ainsworth, S. (1959) *Biochem. J.* **71,** 293-303.
38. McMahon, B. H., Stojkovic, B. P., Hay, P. J., Martin, R. L. & García, A. E. (2000) *J. Chem. Phys.* **113,** 6831-6850.
39. Henry, E. R., Sommer, J. H., Hofrichter, J. & Eaton, W. A. (1983) *J. Mol. Biol.* **166,** 443-451.
40. Agmon, N. & Hopfield, J.J. (1983) *J. Chem. Phys.* **79**, 2042-2053.
41. Powers, L., Sessler, J.L., Woolery, G.L., & Chance, B. (1984) *Biochemistry* **23,** 5519-5523.
42. Chance, B., Powers, L., Zhou, Y.-H., & Naqui, A. (1986) *Bull. Am. Phys. Soc.* **31,** 386.
43. Ansari, A., Berendzen, J., Braunstein, D., Cowen, B. R., Frauenfelder, H., Hong, M. K., Iben, I. E., Johnson, J. B., Ormos, P., Sauke, T. B., Scholl, R., Schulte, A., Steinbach, P.J., Vittitow, J. & Young, R.D. (1987) *Biophys. Chem.* **26,** 337-355.
44. Srajer, V., Reinisch, L. & Champion, P. M. (1991) *Biochemistry* **30,** 4886-4895.
45. Steinbach, P. J., Ansari, A., Berendzen, J., Braunstein, D., Chu, K., Cowen, B. R., Ehrenstein, D., Frauenfelder, H., Johnson, J. B., Lamb, D. C. Luck; S., Mouranr, J.R., Nienhaus, G.U., Ormos, P., Philipp, R., Xie, A.& Young, R.D. (1991) *Biochemistry* **30,** 3988-4001.
46. Nienhaus, G. U., Mourant, J. R. & Frauenfelder, H. (1992) *Proc. Natl. Acad. Sci. U S A* **89,** 2902-2906.
47. Nienhaus, G. U., Mourant, J. R., Chu, K. & Frauenfelder, H. (1994) *Biochemistry* **33,** 13413-13430.
48. Hartmann, H., Zinser, S., Komninos, P., Schneider, R. T., Nienhaus, G. U. & Parak, F. (1996) *Proc. Natl. Acad. Sci. U S A* **93,** 7013-7016.
49. Teng, T. Y., Srajer, V. & Moffat, K. (1994) *Nat. Struct. Biol.* **1,** 701-705.
50. Schlichting, I., Berendzen, J., Phillips, G. N., Jr. & Sweet, R. M. (1994) *Nature* **371,** 808-812.
51. Srajer, V., Teng, T., Ursby, T., Pradervand, C., Ren, Z., Adachi, S., Schildkamp, W., Bourgeois, D., Wulff, M. & Moffat, K. (1996) *Science* **274,** 1726-1729.
52. Braunstein, D. P., Chu, K., Egeberg, K. D., Frauenfelder, H., Mourant, J. R., Nienhaus, G. U., Ormos, P., Sligar, S. G., Springer, B. A. & Young, R. D. (1993) *Biophys. J.* **65,** 2447-2454.
53. Lim, M., Jackson, T. A. & Anfinrud, P. A. (1995) *Science* **269,** 962-966.
54. Lim, M., Jackson, T. A. & Anfinrud, P. A. (1997) *Nat. Struct. Biol.* **4,** 209-214.
55. Alben, J. O., Beece, D., Bowne, S. F., Doster, W., Eisenstein, L., Frauenfelder, H., Good, D., McDonald, J. D., Marden, M. C., Moh, P. P., Reinisch, L., Reynolds, A. H., Shyamsunder, E. & Yue, K. T. (1982) *Proc. Natl. Acad. Sci. U S A* **79,** 3744-3748.
56. Scott, E. E. & Gibson, Q. H. (1997) *Biochemistry* **36,** 11909-11917.
57. Nienhaus, G. U., Chu, K. & Jesse, K. (1998) *Biochemistry* **37,** 6819-6823.
58. Frauenfelder, H. & McMahon, B.H. (2001) *BioSystems* **62,** 3-8.
59. Cotton, F. A. & Wilkinson, G. (1966) *Advanced Inorganic Chemistry*, Wiley, New York.
60. Alben, J. O. & Caughey, W. S. (1968) *Biochemistry* **7,** 175-183.
61. McCoy, S. & Caughey, W. (1970) *Biochemistry* **9,** 2387-2393.
62. Makinen, M. W., Houtchens, R. A. & Caughey, W. S. (1979) *Pro.c Natl. Acad. Sci. U S A* **76,** 6042-6046.

63. Shimada, H. & Caughey, W. S. (1982) *J. Biol. Chem.* **257,** 11893-11900.
64. Frauenfelder, H., Sligar, S. G. & Wolynes, P. G. (1991) *Science* **254,** 1598-1603.
65. Mourant, J. R., Braunstein, D. P., Chu, K., Frauenfelder, H., Nienhaus, G. U., Ormos, P. & Young, R. D. (1993) *Biophys. J.* **65,** 1496-1507.
66. Hong, M. K., Braunstein, D., Cowen, B. R., Frauenfelder, H., Iben, I. E., Mourant, J. R., Ormos, P., Scholl, R., Schulte, A. & Steinbach, P. J. (1990) *Biophys. J.* **58,** 429-436.
67. Potter, W. T., Hazzard, J.H., Choc, M.G., Tucker, M.P. & Caughey, W.S. (1990) *Biochemistry* **29,** 6283-6295.
68. Johnson, J. B., Lamb, D. C., Frauenfelder, H., Muller, J. D., McMahon, B., Nienhaus, G. U. & Young, R. D. (1996) *Biophys. J.* **71,** 1563-1573.
69. Muller, J. D., McMahon, B. H., Chien, E. Y., Sligar, S. G. & Nienhaus, G. U. (1999) *Biophys. J.* **77,** 1036-1051.
70. Urayama, P., Phillips, G. N. & Gruner, S. M. (2002) *Structure (Camb)* **10,** 51-60.
71. Tetreau, C., Novikov, E., Tourbez, M. & Lavalette, D. (2002) *Biophys. J.* **82,** 2148-2155.
72. Yang, F. & Phillips, G. N., Jr. (1996) *J. Mol. Biol.* **256,** 762-774.
73. Vojtechovsky, J., Chu, K., Berendzen, J., Sweet, R. M. & Schlichting, I. (1999) *Biophys. J.* **77,** 2153-2174.
74. Perutz, M. F. & Mathews, F. S. (1966) *J. Mol. Biol.* **21,** 199-202.
75. Tian, W. D., Sage, J. T. & Champion, P. M. (1993) *J. Mol. Biol.* **233,** 155-166.
76. Rohlfs, R. J., Mathews, A. J., Carver, T. E., Olson, J. S., Springer, B. A., Egeberg, K. D. & Sligar, S. G. (1990) *J. Biol. Chem.* **265,** 3168-3176.
77. Springer, B. A., Egeberg, K. D., Sligar, S. G., Rohlfs, R. J., Mathews, A. J. & Olson, J. S. (1989) *J. Biol. Chem.* **264,** 3057-3060.
78. Carver, T. E., Rohlfs, R. J., Olson, J. S., Gibson, Q. H., Blackmore, R. S., Springer, B. A. & Sligar, S. G. (1990) *J. Biol. Chem.* **265,** 20007-20020.
79. Elber, R. & Karplus, M. (1990) *J. Am .Chem. Soc.* **112,** 9161-9175.
80. Huang, X. & Boxer, S. G. (1994) *Nat. Struct. Biol.* **1,** 226-229.
81. Christian, J. F., Unno, M., Sage, J. T., Champion, P. M., Chien, E. & Sligar, S. G. (1997) *Biochemistry* **36,** 11198-11204.
82. Phillips, G. N., Jr., Teodoro, M.L., LI, T., Smith, B., and Olson, J.S. (1999) *J. Phys. Chem. B* **103,** 8817-8829.
83. Li, T., Quillin, M. L., Phillips, G. N., Jr. & Olson, J. S. (1994) *Biochemistry* **33,** 1433-1446.
84. Vogel, K. M., Kozlowski, P.M., Zgierski, M.Z. & Spiro, T.G. (1999) *J. Am. Chem. Soc.* **121,** 9915-9921.
85. Ray, G. B., Li, X-Y., Ibers, J.A., Sessler, J.L. & Spiro, T.G.. (1994) *J. Am .Chem. Soc.* **116,** 162-176.
86. Park, K. D., Guo, K. M., Adebodun, F., Chiu, M. L., Sligar, S. G. & Oldfield, E. (1991) *Biochemistry* **30,** 2333-2347.
87. Dubost, H. & Abouaf-Marguin, L. (1972) *Chem. Phys. Let.* **17,** 269-273.
88. Chackerian Jr., C. (1976) *J. Chem. Phys.* **65,** 4228-4233.
89. Anfinrud, P. A., Han, C. & Hochstrasser, R.M. (1989) *Proc. Natl. Acad. Sci. U S A* **86,** 8387-8391.
90. Nienhaus, G. U. & Nienhaus, K. (2002) *J. Biol.Phys.* **28,** 162-172
91. Springer, B. A. & Sligar, S. G. (1987) *Proc. Natl. Acad. Sci. U S A* **84,** 8961-8965.
92. Atkins, P. W. (1978) *Physical Chemistry* (Oxford University Press.
93. Jung, C. (2000) *J. Mol. Recognit.* **13,** 325-351.
94. Griffiths, P. R. & deHaseth, J.A. (1986) *Fourier Transform Infrared Spectroscopy*, Wiley, New York.

95. Berendzen, J. & Braunstein, D. (1990) *Proc. Natl. Acad. Sci. U S A* **87,** 1-5.
96. Quillin, M. L., Li, T., Olson, J. S., Phillips, G. N., Jr., Dou, Y., Ikeda-Saito, M., Regan, R., Carlson, M., Gibson, Q. H., Li, H. & Elber, R. (1995) *J. Mol. Biol.* **245,** 416-436.
97. Braunstein, D., Ansari, A., Berendzen, J., Cowen, B. R., Egeberg, K. D., Frauenfelder, H., Hong, M. K., Ormos, P., Sauke, T. B., Scholl, Schulte, R. A., Sligar, S. G., Springer, B. A., Steinbach, P. J. & Young, R. D. (1988) *Proc. Natl. Acad. Sci. U S A* **85,** 8497-8501.
98. Cao, W., Christian, J. F., Champion, P. M., Rosca, F. & Sage, J. T. (2001) *Biochemistry* **40,** 5728-5737.
99. Quillin, M. L., Arduini, R. M., Olson, J. S. & Phillips, G. N., Jr. (1993) *J. Mol. Biol.* **234,** 140-155.
100. Egeberg, K. D., Springer, B. A., Sligar, S. G., Carver, T. E., Rohlfs, R. J. & Olson, J. S. (1990) *J. Biol. Chem.* **265,** 11788-11795.
101. Carlson, M. L., Regan, R. M. & Gibson, Q. H. (1996) *Biochemistry* **35,** 1125-1136.
102. Sugimoto, T., Unno, M., Shiro, Y., Dou, Y. & Ikeda-Saito, M. (1998) *Biophys. J.* **75,** 2188-2194.
103. Nienhaus, K., Lamb, D. C., Deng, P. & Nienhaus, G. U. (2002) *Biophys. J.* **82,** 1059-1067.
104. Straub, J. E. & Karplus, M. (1991) *Chem. Phys.* **158,** 221-248.
105. Kushkuley, B. & Stavrov, S. S. (1997) *Biochim. Biophys. Acta.* **1341,** 238-250.
106. Liong, E. C., Dou, Y., Scott, E. E., Olson, J. S. & Phillips, G. N., Jr. (2001) *J. Biol. Chem.* **276,** 9093-9100.
107. Scott, E. E., Gibson, Q. H. & Olson, J. S. (2001) *J. Biol. Chem.* **276,** 5177-5188.
108. Ansari, A., Jones, C. M., Henry, E. R., Hofrichter, J. & Eaton, W. A. (1994) *Biochemistry* **33,** 5128-5145.
109. Powers, L., Chance, B., Chance, M., Campbell, B., Friedman, J., Khalid, S., Kumar, C., Naqui, A., Reddy, K. S. & Zhou, Y. (1987) *Biochemistry* **26,** 4785-4796.
110. Lamb, D. C., Nienhaus, K., Arcovito, A., Draghi, F., Miele, A. E., Brunori, M. & Nienhaus, G. U. (2002) *J. Biol. Chem.* **277,** 11636-11644.
111. Dantsker, D., Samuni, U., Friedman, A. J., Yang, M., Ray, A. & Friedman, J. M. (2002) *J. Mol. Biol.* **315,** 239-251.
112. Lambright, D. G., Balasubramanian, S., Decatur, S. M. & Boxer, S. G. (1994) *Biochemistry* **33,** 5518-5525.
113. Young, R. D., Frauenfelder, H., Johnson, J. B., Lamb, D. C., Nienhaus, G. U., Phillip, R. & Scholl, R. (1991) *Chem. Phys.* **158,** 315-328.
114. Phillips, G. N., Jr., Arduini, R. M., Springer, B. A. & Sligar, S. G. (1990) *Proteins* **7,** 358-365.
115. Waschipky, R., Thesis Universität Ulm, to be submitted
116. Schmidt, M. (private communications).
117. Caughey, W. S. (1970) *Ann. N Y Acad. Sci.* **174,** 148-153.
118. Caughey, W. S., Shimada, H., Choc, M. G. & Tucker, M. P. (1981) *Proc. Natl. Acad. Sci. U S A* **78,** 2903-2907.
119. Ostermann, A., Thesis: TU Munich.
120. Vallone, B. *unpublished data* .
121. Brunori, M., Cutruzzola, F., Savino, C., Travaglini-Allocatelli, C., Vallone, B. & Gibson, Q. H. (1999) *Biophys. J.* **76,** 1259-1269.
122. Hargrove, M. S., Krzywda, S., Wilkinson, A. J., Dou, Y., Ikeda-Saito, M. & Olson, J. S. (1994) *Biochemistry* **33,** 11767-11775.
123. Barrick, D. & Baldwin, R. L. (1993) *Biochemistry* **32,** 3790-3796.

124. Beece, D., Eisenstein, L., Frauenfelder, H., Good, D., Marden, M. C., Reinisch, L., Reynolds, A. H., Sorensen, L. B. & Yue, K. T. (1980) *Biochemistry* **19,** 5147-5157.
125. Zhou, H.-X., and Zwanzig, R. (1991) *J. Chem. Phys.* **94,** 6147-6152.
126. Zwanzig, R. (1992) *J. Chem. Phys.* **97**, 3587-3589.
127. Draghi, F., Miele, A. E., Travaglini-Allocatelli, C., Vallone, B., Brunori, M., Gibson, Q. H. & Olson, J. S. (2002) *J. Biol. Chem.* **277,** 7509-7519.
128. Chatfield, M. D., Walda, K. N., and Magde, D. (1990) *J. Am. Chem. Soc.* **112,** 4680-4687.

Summary

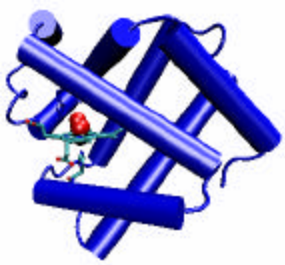

In the present postgenomic era, the quest for an understanding of functional processes that support the complex machinery of life continues to take center stage. Analogous to the successful high-throughput approach to gene sequencing, protein structure determination is currently being developed into a factory-style pursuit. However, a detailed understanding of how protein function is related to its structure is still elusive. The key problem is that proteins are dynamic entities that fluctuate among many different conformational substates with properties that may not be evident from the ground state average structures. Myoglobin (Mb) is as small, structurally well-characterized protein with a (comparatively) simple function. Therefore, is has served as a paradigm for structure-dynamics-function relations in proteins for many years. Its 153 amino acids are arranged in eight α-helices surrounding a heme prosthetic group. An iron atom in the center of the heme plane binds small ligands like O_2, CO, NO or H_2O. It was realized early on that the x-ray structure lacked an access pathway for the ligand to the active site; consequently, protein fluctuations that open transient channels must be essential for its function.

The iron ligand bond in myoglobin is photolabile and can be dissociated by a short laser pulse. The ensuing ligand binding reaction can be followed spectroscopically. This technique, called flash photolysis was employed by Frauenfelder and coworkers in the 1970s over wide time- and temperature ranges. They have shown a surprising complexity in the ligand binding reaction involving nonexponential rebinding and a number of discrete kinetic intermediates. Since then, huge piles of experimental data were amassed to elucidate the structural origins of these metastable states. Two classes of explanations were put forward, those involving protein conformational changes in response to breakage of the iron-ligand bond, and those assuming ligand migration to alternative locations within the protein before exiting. Only in recent years, a clear structural interpretation of the ligand binding reaction in myoglobin has begun to emerge. It is based on a concerted experimental approach, combining x-ray crystallography of photoproducts, time-resolved spectroscopy and protein engineering. The scientific results presented in this thesis provide important new insights in this area of research.

A dazzling array of crystal structures on ligand-bound and deligated (deoxy) myoglobins have been collected over more than 40 years. So far, only a few structures of metastable, light-induced intermediates (photoproducts) are available that were, however, pivotal for the understanding of the ligand binding reaction. After photolysis at liquid-helium temperatures, photolyzed ligands are found to reside in the primary docking site B in close vicinity of the heme-iron. Two additional secondary photoproduct sites C and D, characterized by CO ligands residing in two internal protein cavities could be resolved. Proteins are normally tightly packed structures, as empty volumes in the interior are costly in terms of the overall free energy of stabilization. However, a total of four cavities are known to exist in the Mb structure. They are spacious enough to accommodate a xenon atom and called xenon cavities 1 through 4. Xe 4 and Xe 1 were shown to house a CO molecule in low-temperature photoproduct structures, which suggests that they may have an important function in the physiological ligand binding.

The aim of this thesis research was to elucidate the dynamic aspects of the ligand binding reaction, especially the role of the xenon cavities. The key strategy was to remove or strongly modify the internal cavities. This was done by simple competitive binding of xenon, but more elegantly using modern tools of protein engineering. Specific alterations in the primary sequence were introduced by site-directed mutagenesis to selectively fill or block ligand access to specific xenon cavities, and therefore to alter their occupancy by ligands.

In this thesis, Fourier transform infrared (FTIR) spectroscopy was employed to follow the migration of CO molecules through the protein. This experimental technique combines sensitivity to local structure with time resolution, which is needed to observe the dynamics. The CO stretch bands of heme-bound, and more importantly, of photodissociated CO have served as powerful tools to probe the immediate vicinity of the CO molecule inside the protein matrix. CO-ligated myoglobin shows a few discrete stretch bands of the bound CO ligand. These multiple bands arise from the presence of different structural environments at the binding site that affect the bond order of the heme-bound CO ligand. Their study has provided valuable insights into structural details in the distal heme pocket. Photodissociated CO ligands that are trapped inside the protein matrix typically display multiple sharp IR lines, providing clear evidence that structurally well-defined ligand docking sites exist. From the study of a large number of mutants with modified internal cavities it became clear that each photoproduct state is characterized by a doublet spectrum, arising from internal electric fields in the protein splitting the CO stretch absorption into two bands associated with opposite orientations of the CO.

The spectroscopic work was done over a wide temperature range from 3 – 300 K. Temperature variation is advantageous because it allows one to change the rate of thermally activated processes by orders of magnitude. In these studies, both enthalpy barrier crossings by CO ligands as well as protein conformational changes were studied. To investigate the CO migration to or from different cavities separately, sophisticated photodissociation protocols were developed, involving temperature ramps under illumination, to selectively populate one or more photoproduct states.

The intermediate states were not only distinguished by their typical CO spectra, but also by their different temperatures (or rates) at which the CO escapes from the docking sites to rebind at the heme iron. Predominantly, temperature-derivative spectroscopy (TDS) at cryogenic temperatures was employed to monitor recombination of the photodissociated ligands sorted by their binding temperatures. The TDS data were frequently supplemented by isothermal perturbation and relaxation spectroscopy.

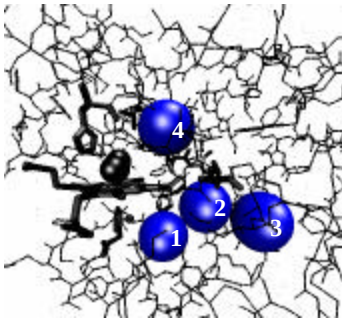

A large amount of myoglobin mutants was generated that provide an unprecedented wealth of experimental evidence of the involvement of the Xe cavities in ligand migration through the protein matrix. For the normal, or wild type (WT) MbCO and a whole family of single point mutants, a number of photoproduct states have been identified that are associated with ligands trapped in the different cavities in the protein. CO ligands were observed at the initial docking site B and at secondary sites C and D within the Xe 4 and Xe 1 cavities. No evidence was found for any involvement of Xe 2 and Xe 3 for transient storage of CO ligands. Local structural changes were shown to have significant effects on the accessibility of a particular site for CO. From the temperature dependencies and the yields of photoproducts upon illumination, the free energy barriers for accessing the cavities were estimated.

An important experience gained from studies with WT MbCO was that pronounced band shifts accompanying CO migration are more the exception than the rule. Only aromatic groups, like heme or aromatic amino acids (W, Y, F) in close vicinity to the photodissociated ligand were found to have a strong effect on the CO stretch frequency. Therefore, this research was extended to mutant L29W and a whole family of mutants with a second modification. In this protein, the strong interaction between the W29 indole side chain and the CO produces large spectral changes that have aided us enormously in relating these changes to ligand migration and protein dynamics. As a matter of fact, the results with L29W were pivotal for the correct interpretation of the rather subtle effects observed with the WT protein.

An extended FTIR/TDS study of L29W MbCO enabled us to unambiguously determine IR spectra of four photoproducts. In analogy to WT, three photoproducts were assigned to CO molecules at the initial docking site B and in cavities Xe 4 (C) and Xe 1 (D). For the fourth intermediate, however, a further docking site could not be found. A meticulous comparison of the CO photoproduct bands of many double mutants of L29W that were engineered to block access to specific xenon cavities prompted us to associate this additional photoproduct with a relaxation of specific sidechains in the close vicinity of the photolyzed ligand at site Xe 4. In this case, a protein relaxation from state C' → C'' was reflected in the spectral marker.

To connect the low-temperature spectroscopic data with physiological ligand binding, room temperature flash photolysis data were collected on several of the MbCO mutant samples. It was shown that the differences observed in the kinetic traces could be well understood with our FTIR/TDS experiments at cryogenic temperatures. A thermodynamic model of ligand binding was developed that considers the Xe cavities (photoproduct states C and D) as transient ligand storage sites. In this model, both bond formation and ligand entry and exit are slow processes compared with the equilibration among the internal sites. Docking site B serves as the first transient CO storage site after bond rupture; it is the key intermediate from which bond formation to the heme iron occurs. Subsequently, CO ligands equilibrate between geminate sites B, C and D on the nanosecond timescale. By fluctuating among these sites, the photolyzed ligands have a much lower probability of spending time at site B, from where they rebind. Hence, many more of them can take advantage of protein fluctuations and escape. The exact route(s) for ligand entry and exit remains obscure. Ligand exit solely through the Xe 1 site can be excluded, and it is likely that multiple pathways exist.

In L29W MbCO and all related double mutants, bimolecular recombination is significantly slowed (by factors ranging from 25 – 130) in comparison to WT. Our extensive low temperature studies have proven invaluable to elucidate the ligand binding mechanism in L29W MbCO. Only the detailed knowledge of the intricate interplay between the two conformations A_I and A_{II} with vastly different structural and functional properties has allowed us to develop a dynamic ligand binding model of L29W. Whereas the majority of molecules are in substate A_I at 200 K, essentially all adopt A_{II} at 293 K. The W29 indole sidechain in the A_{II} conformation not only occludes the initial docking site B, but also prevents access to the Xe 4 and Xe 1 cavities from the distal pocket. Consequently, no long-lived metastable photoproduct states exist in the predominantly A_{II}-type molecules at room temperature, and dissociated ligands will efficiently leave the protein. A transient conformational change from the A_{II}-like deoxy conformation to A_I is a prerequisite for any recombination, as state B remains the key docking site that mediates ligand binding. Therefore, bimolecular recombination is slowed substantially by the equilibrium deoxyA_{II}/deoxyA_I, which is shifted towards A_{II}.

This thesis has provided a glimpse of the stunning complexity involved in even the simplest biomolecular function. Proteins can assume many different conformational states with very different functional properties. Equilibria among these states can be shifted by external reagents so as to significantly alter the overall properties. Even within a single conformation, the reaction surface can be complicated by many short-lived intermediate states. Given the large number of proteins that exist on earth, it is clear that not every protein can be subjected to investigations at such a detail. However, by in-depth studies of the kind presented here on a few key systems, like myoglobin and hemoglobin, reaction centers, and bacteriorhodopsin, valuable insights can be obtained into the general principles governing the function of biological macromolecules.

Zusammenfassung

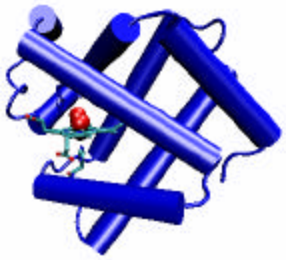

Auch nachdem das menschliche Genom entschlüsselt ist, steht die Suche nach dem Verständnis funktionaler Prozesse, die die komplexen Vorgänge des Lebens vorantreiben, im Mittelpunkt er Forschung. Analog der Vorgehensweise bei der Gensequenzierung, ‚high-throughput' heißt dort das Zauberwort, versucht man heutzutage, die Proteinstrukturbestimmung mit äußerstem Einsatz voranzutreiben, möglichst zu automatisieren, fast schon fabrikmäßig. Jedoch mangelt es immer noch an einem detaillierten Verständnis des Zusammenhangs von Proteinfunktion und Struktur. Das Hauptproblem besteht darin, dass Proteine dynamische Einheiten sind, die zwischen vielen Konformationssubzuständen fluktuieren, deren Eigenschaften aus dem Grundzustand, der mittleren Struktur, nicht ersichtlich sind. Myoglobin (Mb) ist ein kleines, strukturell gut charakterisiertes Protein mit einer vergleichsweise einfachen Funktion. Deshalb hat es viele Jahre als Musterbeispiel für Struktur-Dynamik-Funktionsbeziehungen in Proteinen gedient. Seine 153 Aminosäuren sind in acht α-Helices angeordnet, die eine Hämgruppe umschließen. Ein Eisenatom im Zentrum der Hämebene bindet kleine Liganden wie O_2, CO, NO oder H_2O. Man hat schon früh erkannt, dass die Röntgenstruktur keinen direkten Zugang an die aktive Stelle zeigt. Daher wurde vermutet, dass Proteinfluktuationen, die kurzzeitig Kanäle öffnen, unabdingbar für die Funktion sind.

In Myoglobin ist die Bindung zwischen Eisen und Ligand photolabil und kann durch einen kurzen Laserpuls gespalten werden. Die anschließende Ligandenbindungsreaktion kann spektroskopisch verfolgt werden. Unter Anwendung dieser Technik, der sogenannten Blitzphotolyse, haben Frauenfelder und seine Mitarbeiter in den 70-er Jahren eine überraschende Komplexität in der Ligandenbindungsreaktion nachgewiesen. Unter anderem beobachteten sie nicht-exponentielle Rückbindung über weite Zeit- und Temperaturintervalle. Außerdem detektierten sie eine Anzahl von diskreten kinetischen Intermediaten. Seither wurden riesige Datenmengen angesammelt, um die strukturellen Determinanten aufzudecken, die diesen metastabilen Zuständen zugrunde liegen. Es wurden zwei kontroverse Modelle diskutiert. Einerseits vermutete man an, dass Konformationsänderungen, hervorgerufen durch die Ligandendissoziation, neue metastabile Zustände erzeugen. Andererseits wurde Ligandenmigration innerhalb des Proteins als Ursache für die Entstehung von Intermediaten angenommen. Eine eindeutige Interpretation der Ligandenbindungsreaktion auf struktureller Basis zeichnet sich erst seit den letzten Jahren ab. Diese konnte nur durch den gleichzeitigen Einsatz von Röntgenkristallographie an photolysierten Myoglobinkristallen, zeitaufgelöster Spektroskopie und ‚protein engineering' erreicht werden. Die hier präsentierten wissenschaftlichen Ergebnisse geben neue E insichten in dieses Forschungsgebiet.

Eine verwirrende Anzahl von Kristallstrukturen, sowohl von ligandengebundenem als auch von ungebundenem (deoxy) Myoglobin, ist in mehr als vierzig Jahren publiziert worden. Im Gegensatz dazu existieren bisher nur einige wenige Röntgenstrukturen der metastabilen, lichtinduzierten Intermediate (Photoprodukte). Diese erwiesen sich jedoch als zentral für das Verständnis der Ligandenbindungsreaktion. Nach der Photolyse bei Flüssigheliumtemperaturen wurden die photolysierten Liganden in unmittelbarer Nähe des Hämeisens nachgewiesen, in der primären Andockstelle B. Zwei zusätzliche Photoprodukte C und D konnten bestimmt werden, welche durch CO-Liganden in zwei internen Proteinkavitäten charakterisiert sind. Proteine sind normalerweise dicht gepackte Strukturen, da freie Volumina im Innern energetisch ungünstig sind. Im Myoglobinmolekül kennt man jedoch vier Kavitäten, die groß genug sind, um ein Xenonatom aufzunehmen und daher Xenonkavitäten (Xe 1 bis Xe 4) genannt werden. Dabei waren Xe 4 und Xe 1 diejenigen Kavitäten, die bei den Tieftemperaturphotoproduktstrukturen mit je einem CO-Molekül

besetzt waren. Diese Tatsache läßt vermuten, daß die Kavitäten eine wichtige Funktion in der physiologischen Ligandenbindung innehaben.

Das Ziel dieser Forschungsarbeit war es, die dynamischen Aspekte der Ligandenbindungsreaktion aufzuklären. Besonderes Augenmerk galt dabei der Rolle der Xenonkavitäten. Die Strategie bestand darin, die internen Kavitäten entweder zu füllen und oder zumindest stark zu modifizieren. Dieses Ziel wurde einerseits durch einfache Zugabe von Xenon erreicht, welches mit den photolysierten Liganden um die freien Plätze in den Kavitäten konkurriert. Die viel elegantere Methode bestand jedoch darin, mittels moderner Mutationstechniken spezifische Änderungen in der Primärsequenz einzuführen. Kleine aliphatische Aminosäuren wurden durch aromatische Aminosäuren ersetzt, deren voluminöse Seitenketten den Zugang zu bestimmten Xenonkavitäten entweder blockierten oder zumindest erschwerten.

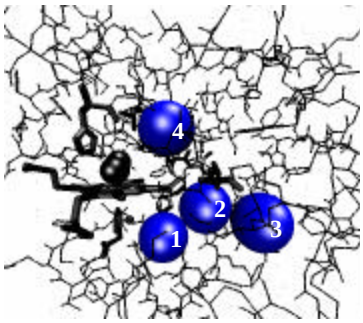

In dieser Arbeit wurde die Ligandenmigration durch das Protein mit Hilfe der Fourier- Transform-Infrarotspektroskopie verfolgt. Diese experimentelle Technik vereint die Empfindlichkeit für die lokale Struktur und die für die Beobachtung dynamischer Prozesse notwendige Zeitauflösung. Die Untersuchung der CO-Streckschwingungen des gebundene und, wichtiger noch, des photolysierten CO hat dabei wertvolle Aussagen über die direkte Umgebung des Liganden innnerhalb der Proteinmatrix geliefert. CO-ligandiertes Mb zeigt einige diskrete Absorptionsbanden des gebundenen CO, welche von unterschiedlichen strukturellen Umgebungen an der Bindungsstelle herrühren, die wiederum die Bindungsordnung des gebundenen CO beeinflussen. Diese Banden geben wertvolle Einsichten in die strukturellen Details in der distalen Hämtasche. Photodissoziierte Liganden, die in der Proteinmatrix gefangen sind, zeigen typischerweise ebenfalls mehrere scharfe Banden, die auf das Vorhandensein von strukturell wohldefinierten Andockstellen hinweisen. Nach Untersuchung einer großen Anzahl von Mutanten mit modifizierten Kavitäten wurde klar, das jedes Photoprodukt durch eine Doublette charakterisiert ist. Das interne elektrische Feld führt zu einer Aufspaltung der CO-Absorption in zwei Banden, die strukturell entgegengesetzten Orientierungen des CO zuzuordnen sind.

Die spektroskopischen Arbeiten wurden im Temperaturbereich von 3 - 300 K durchgeführt. Temperaturvariationen sind dahingehend von Vorteil, dass sie es erlauben, die Raten von thermisch aktivierten Prozessen um Größenordnungen zu ändern. Sowohl das Überwinden einzelner Enthalpiebarrieren durch den Liganden als auch Konformationsänderungen des Proteins wurden gezielt untersucht. Dazu wurden ausgeklügelte Photodissoziationsprotokolle entwickelt, die auch Temperaturrampen unter Beleuchtung einschlossen, um die Besetzung spezifischer Kavitäten zu erreichen.

Die Intermediate wurden nicht nur anhand ihrer typischen CO-Spektren unterschieden, sondern auch anhand der unterschiedlichen Temperaturen (oder Raten), bei denen das CO aus den Kavitäten entweicht und am Eisen rückbindet. Um die Rekombination in Abhängigkeit von der Temperatur aufzuzeigen, wurde in der Hauptsache die temperaturderivative Spektroskopie (TDS) bei tiefen Temperaturen eingesetzt. Die TDS-Daten wurden in vielen Fällen durch isotherme Störungs- und Relaxationsspektroskopieexperimente ergänzt.

Eine große Anzahl von Myoglobinmutanten wurde erzeugt, die eine unglaubliche Vielfalt an experimentellen Beweisen für die Beteiligung der Xenonkavitäten an der Ligandenmigration durch die Proteinmatrix lieferten. Für das unveränderte Wildtypmyoglobin (WT) sowie eine ganze Familie von Einzelmutanten konnten mehrere Intermediate identifiziert werden, die die Liganden in unterschiedlichen Kavitäten zeigen. CO-Moleküle wurden sowohl an der primären Andockstelle B als auch in den Kavitäten Xe 4 und Xe 1

nachgewiesen. Hinweise auf eine Besetzung von Xe 2 und Xe 3 ergaben sich nicht. Es zeigte sich, dass lokale strukturelle Änderungen wie Punktmutationen den Zugang zu den einzelnen Kavitäten in der Tat signifikant beeinflussen. Anhand der Temperaturabhängigkeiten und der lichtinduzierten Besetzung von Intermediaten konnten die freien Energiebarrieren für die Besetzung der Kavitäten abgeschätzt werden.

Eine wichtige Erfahrung, die aus den Studien an WT MbCO gewonnen werden konnte, war, dass deutliche Bandenverschiebungen durch CO-Migration eher die Ausnahme als die Regel sind. Nur aromatische Gruppen, wie Häm oder aromatische Aminosäuren (W,Y,F) in unmittelbarer Umgebung des photodissoziierten Liganden übten einen spürbaren Einfluss auf die CO-Streckfrequenzen aus. Daher wurden die Untersuchungen auf die Mutante L29W sowie eine ganze Familie von Doppelmutanten mit einer zusätzlichen zweiten Modifikation ausgedehnt. In diesem Protein verursachen die starken Wechselwirkungen zwischen der W29 Indolseitenkette und dem CO große spektrale Veränderungen, die uns enorm geholfen haben, diese Veränderungen sowohl auf Ligandmigration als auch auf Proteindynamik zurückzuführen. Im Nachhinein waren die Ergebnisse an L29W zentral für die korrekte Interpretation der eher subtilen Effekte, die beim WT Protein beobachtet wurden. Eine ausgedehnte FTIR/TDS-Studie an L29W MbCO gestattete es, IR-Spektren von vier Photoprodukten eindeutig zu bestimmen. Analog zum Wildtyp wurden drei der Photoprodukte CO-Molekülen an der Andockstelle B, sowie in Kavitäten Xe 4 (C) und Xe 1 (D) zugeordnet. Ein eingehender Vergleich der CO-Photoproduktbanden von vielen L29W Doppelmutanten, die synthetisiert worden waren, um den Zugang zu spezifischen Xenonkavitäten zu blockieren, bewirkte, dass wir das zusätzliche Photoprodukt einer Relaxation einer spezifischen Seitenkette in direkter Nachbarschaft des photolysierten Liganden in Xe 4 zuordnen konnten. In diesem Falle spiegelte sich die Proteinrelaxation vom Zustand C' in den Zustand C'' direkt im spektralen Marker, der CO-Bande, wider.

Um die Tieftemperaturspektroskopiedaten zur physiologischen Ligandenbindung in Relation zu setzen, wurden an verschiedenen MbCO-Mutanten Blitzphotolysedaten gesammelt. Es wurde gezeigt, dass die Unterschiede in den kinetischen Kurven anhand unserer FTIR/TDS-Experimente bei tiefen Temperaturen interpretiert werden konnten. Ein dynamisches Modell der Ligandenbindung wurde entwickelt, in welchem die Xenonkavitäten (Photoprodukte C und D) als transiente Ligandenspeicherplätze angesehen werden. Sowohl beim eigentlichen Bindungsprozess als auch bei Ligandenein und -austritt handelt es sich um vergleichsweise langsame Prozesse. Nach dem Bruch der Bindung dient die Andockstelle B als erste transiente CO-Speicherstelle. Hierbei handelt es sich um das wichtigste Intermediat, da nur von hier aus die Bindung an das Hämeisen stattfindet. Anschließend equilibrieren die CO-Liganden zwischen den internen Stellen B, C und D innerhalb von Nanosekunden. Durch die Fluktuation zwischen diesen Stellen wird die Wahrscheinlichkeit herabgesetzt, dass sich photolysierte Liganden tatsächlich an der Stelle B befinden, von wo aus sie zurückbinden. Daher können viele von ihnen Proteinfluktuationen ausnutzen und ins Lösungsmittel entweichen. Die exakte(n) Route(n) für Ein- und Austritt bleiben dagegen unklar. Ligandenaustritt allein durch die Kavität Xe 1 kann ausgeschlossen werden. Es ist daher wahrscheinlich, dass multiple Pfade aus dem Proteininneren ins Lösungsmittel führen.

In L29W MbCO und allen verwandten Doppelmutanten ist die bimolekulare Rekombination im Vergleich zum WT Protein signifikant verlangsamt (um Faktoren von 25 - 130). Unsere extensiven Tieftemperaturstudien haben sich als absolut notwendig herausgestellt, um den Ligandenbindungsmechanismus in L29W MbCO aufzuklären. Nur das detaillierte Wissen um das komplizierte Zusammenspiel zwischen den beiden Konformationen A_I und A_{II} mit ihren ausgesprochen unterschiedlichen strukturellen und funktionellen Eigenschaften hat es uns erlaubt, ein dynamisches Ligandenbindungsmodell für L29W zu entwickeln. Während die Mehrzahl der Moleküle sich bei 200 K im Subzustand A_I befinden, nehmen bei 293 K fast alle die A_{II}-Konformation ein. Die W29 Indolseitenkette der

A_{II}-Konformation blockiert nicht nur die primäre Andockstelle B, sie verwehrt auch den Zutritt zu den Kavitäten Xe 4 und Xe 1 von der distalen Tasche her. Folglich existieren keine langlebigen metastabilen Photoproduktzustände in den vorherrschend A_{II}-Typ Molekülen bei Zimmertemperatur, und dissoziierte Liganden verlassen effizient das Protein. Eine transiente Konformationsänderung von der A_{II}-ähnlichen Deoxykonformation nach A_I ist Voraussetzung für jegliche Rekombination, da B auch weiterhin die Schlüsselstelle bleibt, die die Bindung vermittelt. Daher wird bimolekulare Rückbindung durch das vorgelagerte Gleichgewicht Deoxy A_{II}/Deoxy A_I, welches nach A_{II} verschoben wird, spürbar verlangsamt.

Diese Arbeit hat einen Einblick in die überwältigende Komplexität gewährt, die selbst den einfachsten biomolekularen Funktionen zugrunde liegt. Proteine können viele verschiedene Konformationssubzustände mit sehr unterschiedlichen funktionellen Eigenschaften annehmen. Gleichgewichte zwischen diesen können durch externe Parameter verschoben werden. Schon innerhalb einer einzelnen Konformation kann die Reaktionsoberfläche durch viele kurzlebige Zwischenzustände kompliziert werden. Wenn man die große Anzahl von Proteinen, die auf der Erde existiert, in Betracht zieht, wird deutlich, dass nicht jedes Protein bis ins letzte Detail untersucht werden kann. Jedoch können weitreichende Studien wie diese, durchgeführt an ein paar Schlüsselsystemen wie Myoglobin, Hämoglobin, den Reaktionszentren oder Bakteriorhodopsin, wertvolle Einsichten in die allgemeinen Prinzipien liefern, die die Funktionen von biologischen Makromolekülen bestimmen.

List of Publications

Nienhaus, K., Stegger, P., Lehmann, G. & Schneider, J.R. (1986), Assessment of quality of quartz crystals by EPR and gamma -ray diffraction, *J. Cryst. Growth* **74,** 391-398.

Kriegl, J.M., Bhattacharyya, A.J., Nienhaus, K., Deng, P., Minkow, O. & Nienhaus, G.U. (2002), Ligand binding and protein dynamics in neuroglobin, *Proc. Natl. Acad. Sci. U S A.* **99**, 7992-7997.

Nienhaus, K., Lamb, D.C., Deng, P.& Nienhaus, G.U. (2002), The effect of ligand dynamics on heme electronic transition band III in myoglobin, *Biophys. J.* **82**, 1059-1067.

Lamb, D.C., Nienhaus, K., Arcovito, A., Draghi, F., Miele, A.E., Brunori, M.& Nienhaus, G.U. (2002), Structural dynamics of myoglobin: ligand migration among protein cavities studied by Fourier transform infrared/temperature derivative spectroscopy, *J. Biol. Chem.* **277**, 11636-11644.

Nienhaus, G.U. & Nienhaus, K. (2002), Infrared Study of Carbon Monoxide Migration among Internal Cavities of Myoglobin Mutant L29W, *J. Biol. Phys.* **28**, 163-172.

Nienhaus, K., Vallone, B., Renzi, F., Wiedenmann, J. & Nienhaus, G.U., Crystallization and Preliminary X-ray Diffraction Analysis of the Red Fluorescent Protein eqFP611, *Acta Cryst. D*, submitted.

Kriegl, J.M., Nienhaus, K., Deng, P., Fuchs, J. & Nienhaus, G.U., Ligand Dynamics in a Protein Internal Cavity, *Proc. Natl. Acad. Sci. U S A*, submitted.

List of Posters

Waschipky, R., Librizzi, F., Nienhaus, K., Cordone, L. & Nienhaus, G.U. (1998)
Infrared studies of ligand binding in myoglobin embedded in a trehalose glass
Biophys. J. **74,** A83-A83
42nd Biophysical Society Meeting, Kansas City, MS 1998.

Waschipky, R., Böhm, A., Nienhaus, K., Cordone, L. & Nienhaus, G.U. (1998)
Dynamische Eigenschaften von Myoglobin in einer Trehalosematrix
Jahrestagung der Deutschen Gesellschaft für Biophysik, Frankfurt, 1998

Waschipky, R., Böhm, A., Nienhaus, K. & Nienhaus, G.U. (1999)
Time-resolved infrared study of carbon monoxide binding to myoglobin mutants
Biophys. J. **76,** A419-A419
43rd Biophysical Society Meeting, Baltimore, MD 1999.

Lamb, D.C., Nienhaus, K. & Nienhaus, G.U. (2001)
Heme absorption band III as a marker of ligand migration in the distal heme pocket of myoglobin
Biophys. J. **80,** 1172
Biophysical Society Meeting, Boston, MA 2001.

Nienhaus, K., Lamb, D.C., Minkow, O., Waschipky, R. & Nienhaus, G.U. (2001)
Examining the role of protein internal cavities in ligand binding to myoglobin
Biophys. J.. **80**, 1431
Biophysical Society Meeting, Boston, MA 2001.

Lamb, D.C., Nienhaus, K., Deng, P., Arcovito, A., Brunori, M., Draghi, F.& Nienhaus, G.U. (2001)
Ligand Migration in YQR and YQRF Myoglobin Mutants
Jahrestagung der Deutschen Gesellschaft für Biophysik, Münster, 2001.

Nienhaus, G.U., Kriegl, J.M., Bhattacharyya, A.J., Nienhaus, K., Deng, P., Minkow, O. & Burmester, T. (2002)
Ligand binding and protein dynamics in neuroglobin
Biophys. J.. **82**, 2188
Biophysical Society Meeting, San Francisco, 2002.

Nienhaus, K., Lamb, D.C., Deng, P.C. & Nienhaus, G.U. (2002)
The effect of ligand dynamics on heme electronic transition band III in myoglobin
Biophys. J.. **82**,1059-1067
Biophysical Society Meeting, San Francisco, 2002.

Kriegl, J.M., Bhattacharyya, A.J., Nienhaus, K., Deng, P., Minkow, O. & Nienhaus, G.U., Structural Heterogeneity and Ligand Binding Properties of Neuroglobin (2002)
Jahrestagung der Deutschen Gesellschaft für Biophysik, Dresden, 2002.

Deng, P., Nienhaus, K., Kriegl, J.M., Bhattacharyya, A.J., Dewilde, S., Moens, L. & Nienhaus, G.U.
Ligand Binding and Migration in Cerebratulus lacteus Hemoglobin
Jahrestagung der Deutschen Gesellschaft für Biophysik, Dresden, 2002.

Talks:

Nienhaus, K., Stegger, P. & Lehmann, G.
Determination of the Quality of Quartz in Esr-Irradiation and Gamma-Irradiation Measurements
Z. Kristallogr. **170,** 140-141 (1985)
24. Diskussionstagung der Arbeitsgemeinschaft Kristallographie der Deutschen Mineralogischen Gesellschaft, Köln, 1985.

Parak, F.G., Nienhaus, G.U., Ostermann, A., Nienhaus, K., Gassmann, A. & Waschipky, R.
Structural fluctuations enable conformational changes in proteins
Biophys. J.. **78,** 2320
44th Biophysical Society Meeting, New Orleans, 2000.

Danksagung

Hiermit möchte ich mich bei allen bedanken, die zur Fertigstellung dieser Arbeit beigetragen haben.

Prof. Dr. Peter Bäuerle und Prof. Dr. Hartmut Seliger danke ich für ihre Breitwilligkeit, die vorliegende Arbeit zu begutachten, die in der Abteilung Biophysik angefertigt wurde.

Mein besonderer Dank gilt meinem Mann Uli. Er hat nicht nur den Anstoß zu dieser Arbeit gegeben, sondern auch auf die Fertigstellung gedrängt. Ich danke Dir für viele, oft leider abendfüllende Diskussionen, die Dir die wenige Freizeit (und den letzten Nerv) auch noch raubten. Du hast mir gezeigt, dass Forschung aus 99 % Frustration und nur 1 % Erfolg besteht. Und nur dieses eine Prozent zählt.

Don C. Lamb hat mich in die IR-Spektroskopie eingeführt. Seine Computerprogramme, oft meinen persönlichen Wünschen angepasst, waren eine große Hilfe bei der Datenanalyse. Thanks. Außerdem ist er seit vielen Jahren ein Freund der Familie. Wer sonst hätte Dinnereinladungen damit verbracht, mit drei Kindern Football zu spielen anstatt zu essen?

Pengshi Deng ist gleichzeitig mit mir in die Spektroskopie eingestiegen und hat viele FTIR-Messungen für mich durchgeführt. Vielen Dank dafür. Ich hoffe, ich kann mich revanchieren.

Charlie Röcker kann mit Fug und Recht als „ruhender Pol“ der Arbeitsgruppe bezeichnet werden. Sein guter Draht zu den Werkstätten hat oft dafür gesorgt, dass notwendige Reparaturen auch tatsächlich durchgeführt wurden. Sein Organisationstalent ist unübertroffen. Danke.

Vladimir Ens hat sich immer dann um meinen Computer „Madame Curie“ gekümmert, wenn ich die Dame wieder gar zu arg misshandelt hatte. Danke.

Uwe Theilen war eine große Hilfe bei der Proteinexpression und Aufreinigung. Vielen Dank. Und dabei sind in dieser Arbeit nur einige der Mutanten behandelt, es gibt noch viele mehr!

Jan Kriegl hat die meisten Blitzphotolysemessungen durchgeführt und mir die nachfolgende Analyse erklärt. Er war mein Anlaufpunkt für alle mathematischen Fragen. Danke.

Meine Kinder sollen nicht unerwähnt bleiben, mussten sie doch unter unzähligen „Frozen Pizza Dinners“ leiden. Haben sie eigentlich gelitten?

Und zuletzt der Dank an meine Eltern, die mir vor vielen Jahren mein Studium ermöglicht haben.

Curriculum Vitae

Karin Nienhaus

Zur Person

Geboren am 13. September 1959 in Rhede
Staatsangehörigkeit: Deutsch
Familienstand: seit April 1984 verheiratet mit Prof. Dr. Gerd Ulrich Nienhaus
Drei Kinder, geboren 1984, 1986 und 1988

Schulbildung

1966-1969	Overberg Grundschule, Rhede
1969-1975	Realschule Rhede
1975-1978	Besuch der Oberstufe des Gymnasium Remigianum, Borken 5. Juni 1978: Abitur

Studium

1978-1984	Studium der Chemie an der Westfälischen Wilhelms-Universität Münster 27. März 1984: Diplom in Chemie, Note: sehr gut
1984-1985	Wissenschaftliche Hilfskraft, Physikalische Chemie, Universität Münster
1996-2000	Freiwillige Mitarbeit in der Abteilung Biophysik der Universität Ulm
seit Sept. 2000	Wissenschaftliche Mitarbeiterin in der Abteilung Biophysik der Universität Ulm